ONE-DIMENSIONAL PLATINUM-BASED HYBRID NANOSTRUCTURES FOR HIGH PERFORMANCE ELECTRODES IN PROTON EXCHANGE MEMBRANE FUEL CELLS

By

Peter Mardle

A thesis submitted to the

University of Birmingham

for the degree of

DOCTOR OF PHILOSOPHY

Centre for Doctoral Training in Fuel Cells and their Fuels

School of Chemical Engineering

College of Engineering and Physical Sciences

University of Birmingham

ABSTRACT

To reduce the required high loading of Pt to catalyse the sluggish oxygen reduction reaction (ORR) at cathodes in proton exchange membrane fuel cells (PEMFC), much development has been made on increasing the efficiency of the catalyst material. However, there is big challenge to fully translate catalytic enhancements into higher performance catalyst electrodes in PEMFCs.

Pt nanowire (NW) array gas diffusion electrodes (GDEs) matches the promise of higher PEMFC performances. Alloying of Pt with a non-noble metal such as Ni, and using alternative carbonaceous supports such as carbon nanotubes (CNTs) are known methods of increasing ORR catalytic activity. This study applies both methods to improve the performance of the Pt NW array system and to better understand the mechanisms that influence real performance of PEMFC catalyst materials.

Herein, a facile method for the preparation of PtNi NWs supported on carbon is developed by an impregnation and annealing approach. The optimal PtNi NW/C catalyst is achieved at an annealing temperature of 150°C with a duration of 24 hrs, showing 1.78-fold mass activity enhancement with respect to the pure Pt NWs. However, very poor power performance is observed for the PtNi NW/C GDE in PEMFCs. This is ascribed to the increased mass transport resistance resulting from ionomer contamination within the catalyst layer caused by severe Ni dissolution from the PtNi NWs. An acid leaching step is therefore introduced in the fabrication of PtNi NW array GDEs and an optimised GDE gave a 1.07-fold of power density with respect to the Pt NW array GDE.

Finally, nitrogen-doped CNT arrays are fabricated directly onto the GDL surface by plasma enhanced chemical vapour deposition (PECVD) and active screen plasma treatment (ASP). These act as the catalyst support for Pt NW arrays where much enhanced power performance as compared to Pt NW array and Pt/C GDEs is attributed to an increase in

macropores with a diameter range of 315-360 nm, concluding that mass transport properties are the key to translating effective ORR catalysts into high performance PEMFC electrodes.

ACKNOWLEDGMENTS

LIST OF PUBLICATIONS

Peer-reviewed Journal Papers

1. **P. Mardle**, G. Thirunavukkarasu, S. Guan, Y, Chiu and S. Du, "A comparative study in the enhanced performance of PtNi nanowire array gas diffusion electrodes in half-cell measurement and PEMFC tests", *under preparation*.

2. **P. Mardle**, I. Cerri, S-San and A.E. Kharouf, "An examination into the disparity between the Nernst potential and open circuit potential of PEMFCs", *under preparation.*

3. **P. Mardle**, X. Ji, J. Wu, S. Guan, H. Dong and S. Du, "Thin film electrodes from Pt nanorods supported on aligned N-CNTs for proton exchange membrane fuel cells", *Appl. Catal. B. Environ.* **260** (2020) 118031–118038.

4. M. Wang, H. Zhang, G. Thirunavukkarasu, I. Salam, J.R. Varcoe, **P. Mardle**, X. Li, S. Mu and S. Du, "Ionic Liquid-Modified Microporous ZnCoNC- Based Electrocatalysts for Polymer Electrolyte Fuel Cells", *ACS Energy Lett.* **4** (2019) 2104–2110.

5. Z. Jiang, N.A. Arifin, **P. Mardle** and R. Steinberger-Wilckens, "Electrochemical Performance and Carbon Resistance Compaison between Tin, Copper and Silver-Doped Nickel/Yttria-Stabilized Zirconia Anodes SOFCs Operated with Biogas". *J. Electrochem. Soc.* **166**(6) (2019) F393–F398.

6. **P. Mardle** and S. Du, "Annealing Behaviour of Pt and PtNi Nanowires for Proton Exchange Membrane Fuel Cell", *Materials.* **11** (2018) 1473–1485.

7. **P. Mardle**, O. Fernihough and S. Du, "Evaluation of the Scaffolding Effect of Pt Nanowires Supported on Reduced Graphene Oxide in PEMFC Electrodes", *Coatings.* **8** (2018) 48–56.

Book Chapters and Reviewed Conference Papers

1. **P. Mardle** and S. Du, Adapting Pt nanowire catalysts for high performance PEMFC GDEs and CCMs, *EFCF 2019: Low-Temp. FUEL CELLS, ELECTROLYSERS & H_2 Processing* (2019), *proceedings under preparation*.

2. **P. Mardle** and S. Du, "Materials for PEMFC Electrodes", *Reference Module in Materials Science and Materials Engineering* (2017) 1–13.

Conference Presentations

1. "An examination into the disparity between the Nernst potential and open circuit potential (OCP) of PEMFCs". Toyota 2019 European Fuel Cell Research Workshop – Innovative solutions for future FCEV, 22nd October 2019. ***Oral presentation.***

2. P. Mardle and S. Du, Adapting Pt nanowire catalysts for high performance PEMFC GDEs and CCMs, EFCF 2019: Low-Temp. FUEL CELLS, ELECTROLYSERS & H2 Processing. 2nd–5th July 2019. ***Poster presentation.***

3. "Pt nanowire thin film catalyst coated membranes for PEMFCs". CCSHFC 2019: Hydrogen and Fuel Cells - Powering the Future. 19th March 2019. ***Poster presentation.***

4. "Considerations for PEMFC catalyst layer development through the adaptation of Pt nanowire thin film electrodes". H2FC SUPERGEN, 18th–19th December 2018. ***Oral presentation.***

5. "The development of aligned PtNi NW electrodes for PEMFCs". FCH2 Technical conference 2018, 14th March 2018. ***Oral presentation.***

6. "Towards the Scalable Synthesis of NiPt Nanowires for PEMFC Applications"- *oral presentation*. FCH2 Technical conference 2018, 31st May–1st June 2018. ***Oral presentation.***

7. "Towards NiPt nanowires for PEMFC applications". CARISMA 2017. 9th–12th April 2017. ***Poster presentation.***

8. "A Study in the Scalable Fabrication of NiPt Nanowires for PEMFC applications." ChemEngDayUK 2017, 27th–28th March 2017. ***Poster presentation (prize awarded).***

9. "NiPt nanowire catalyst electrodes for PEMFC applications". H2FCSUPERGEN 2016. 12th–14th December 2016. ***Poster and oral (3 minute thesis) presentation.***

10. "Ni@Pt Core shell nanowires as novel catalysts for the ORR in PEFCs". CINF Summer School 2016: Reactivity of nanoparticles for more efficient and sustainable energy conversion. 7th–12th August 2016. ***Poster and oral (3 minute thesis) presentation.***

11. "NiPt nanowires grown by a simple wet chemical route for PEMFC applications". FCH2 Technical conference 2016. 25th–26th May 2016. ***Poster presentation.***

TABLE OF CONTENTS

LIST OF FIGURES

xi

LIST OF TABLES

ABBREVIATIONS, SYMBOLS AND UNITS

1D	One-dimensional
A	Area / cm^2
A_{Pt}	Absolute Pt surface area / cm^2
ASP	Active screen plasma
AST	Accelerated stress test
b	Tafel slope / $V\ dec^{-1}$
BEV	Battery electric vehicle
C^0-C	Concentration gradient / $mol\ cm^{-3}$
C^0_{Red} / C^0_{Ox}	Equilibrium concentration of the reduced (Red) or oxidised (Ox) species / M
CL	Catalyst layer
CNT	Carbon nanotube
CO_2	Carbon dioxide
C_{Red} / C_{Ox}	Concentration of the reduced (Red) or oxidised (Ox) species / M
CTAB / CTAC	Cetyltrimethyl-ammonium bromide / chloride
CV	Cyclic voltammetry
CVD	Chemical vapour deposition
D^{eff}	Effective diffusion coefficient / $cm^2\ s^{-1}$
DFT	Density functional theory
DMF	Dimethylformamide
DoE	Department of energy
ECSA	Electrochemically active surface area / $m^2\ g_{Pt}^{-1}$
EDX	Energy dispersive X-ray spectroscopy
EIS	Electrochemical impedance spectroscopy

E_{Nernst}	Nernst potential. Thermodynamic maximum potential achievable / V
EV	Electric vehicle
EXAFS	Extended X-ray absorption fine structure
$E^{\ominus}_{298K}$	Standard cell potential / V
F	Faraday's constant / 96485 C mol^{-1}
FFT	Fast Fourier transform
GCE	Glassy carbon electrode
GDE	Gas diffusion electrode
GDL	Gas diffusion layer
GHG	Greenhouse gas
GO	Graphene oxide
GtCO$_2$e	Gigatons carbon dioxide equivalent
H$_{des}$	Hydrogen desorption
HFC	Hydrogen fuel cell
HFCV	Hydrogen fuel cell vehicle
HFR	High frequency resistance
HOR	Hydrogen oxidation reaction
i	Current / A
i_0	Exchange current / A
ICE	Internal combustion engine
ICP-MS	Inductively coupled plasma – mass spectroscopy
ICR	Internal contact resistance
i_k	Kinetic current / A
IPA	Isopropyl alcohol
J	Diffusion flux / mol s^{-1}
JCPDS	Joint Committee on Powder Diffraction Standards

K_{eq}	Equilibrium constant
LSV	Linear sweep voltammetry
$MA_{0.9V}$	Mass activity at 0.9 V vs. RHE / A mg_{Pt}^{-1}
MEA	Membrane electrode assembly
MPL	Microporous layer
n	Number of electrons transferred
N-CNT	Nitrogen doped carbon nanotube
NP	Nanoparticle
NSTF	Nanostructured thin film
NW	Nanowire
OCP	Open circuit potential / V
ORR	Oxygen reduction reaction
p	Partial pressure / atm
PCTE	Poly carbonate track etch
PECVD	Plasma enhanced chemical vapour deposition
PEM	Proton exchange membrane
PEMFC	Proton exchange membrane fuel cell
PGM	Platinum group metals
Pt/C	Commercial catalyst (TKK)
PTFE	Polytetrafluoroethene
PVP	Polyvinylpyrrolidone
Q_{Hdes}	Total charge transferred from hydrogen desorption / C
R	Gas constant / 8.314 J K^{-1} mol^{-1}
R	Resistance / Ω
$r.f.$	Roughness factor / cm_{Pt}^{-2}
RDE	Rotating disk electrode

RF	Radiofrequency
rGO	Reduced graphene oxide
RH	Relative humidity / %
RHE	Reference hydrogen electrode
R_{NF}	Non Fickian mass transport resistance / Ω
RRDE	Rotating ring disk electrode
$SA_{0.9V}$	Specific activity at 0.9 V vs. RHE / μA cm_{Pt}^{-2}
SEM	Scanning electron microscopy
STD	Standard conditions
STEM	Scanning transmission electron microscopy
T	Absolute temperature / K
TEM	Transmission electron microscopy
TGA	Thermo-gravimetric analysis
UPD	Underpotential deposition
v	Kinematic viscosity / $cm^2\ s^{-1}$
XPS	X-ray photoelectron spectroscopy
XRD	X-ray diffraction
α	Transfer coefficient
δ	Diffusion layer thickness / cm
ΔE_{Ohmic}	Voltage loss due to internal resistances / V
$\Delta G^{\ominus}_{298K}$	Gibbs free energy change at standard temperature and pressure / J mol^{-1}
η_{MT}	Overpotential from mass transport limitations / V
$\eta_{ORR/HOR}$	Overpotential for the ORR and HOR / V
ω	Angular rotation rate / rad s^{-1}

1. Introduction

1.1. Proton exchange membrane fuel cells (PEMFCs)

1.1.1. The need for PEMFCs

In 1769, James Watt patented his steam engine and as such is considered to have catalysed the industrial revolution [1]. It is no coincidence that around this time the CO_2 concentration in the atmosphere - a leading contributor to global climate change - began to exponentially rise to the record levels that it is today. In an historic move by world leaders, the Paris climate change agreement was made in 2016 with the long-term goal of limiting global temperature increases to well below 2°C from the pre-industrial level. In 2019, the world was already at 1°C with greenhouse gas (GHG) emissions as high as they have ever been at approximately 50 gigatons CO_2 equivalent ($GtCO_2e$) [2]. Therefore, to meet the 2°C target there must be an immediate and drastic reform of our energy systems.

Many sources of GHG emissions from the transport sector can be eliminated by a complete electrification of the energy network where electric vehicles (EVs) are the natural end point. In comparison to the battery electric vehicle (BEV), the H_2 fuel cell vehicle (HFCV) can provide a longer range and shorter refuelling time. The HFCV also has the potential to be green if a H_2 economy is established in which the H_2 is produced from electrolysis using sustainable electricity or from biomass. Therefore, for commercial vehicles, taxies, heavy duty vehicles, buses and trains, the hydrogen fuel cell (HFC) has been considered as the more favourable replacement for the internal combustion engine (ICE) [3,4].

For vehicle applications, the proton exchange membrane fuel cell (PEMFC) is favoured due to its low operating temperature, flexible scalability and quick start up/shut down. In PEMFC operation, molecular H_2 is split at the anode into 2 H^+ ions (or protons) and 2 e^- in a process called the hydrogen oxidation reaction (HOR) (Figure 1.1). The protons transfer to the cathode via the proton exchange membrane (PEM), which has a very high electrical resistance, forcing the electrons to travel via the external circuit and thus power the electrical

load. At the cathode, O_2 then combines with the protons and electrons via the oxygen reduction reaction (ORR) to produce H_2O. The PEMFC essentially is therefore the chemical formation of H_2O from its elements engineered in such a way that the transfer of electrons can be harnessed as electrical energy.

$$H_2 \rightarrow 2H^+ + 2e^- \quad \text{(Eq. 1)} \qquad 1/2O_2 + 2H^+ + 2e^- \rightarrow H_2O \quad \text{(Eq. 2)}$$

$$\text{Overall: } H_2 + 1/2O_2 \rightarrow H_2O \quad \text{(Eq. 3)}$$
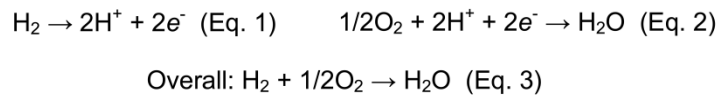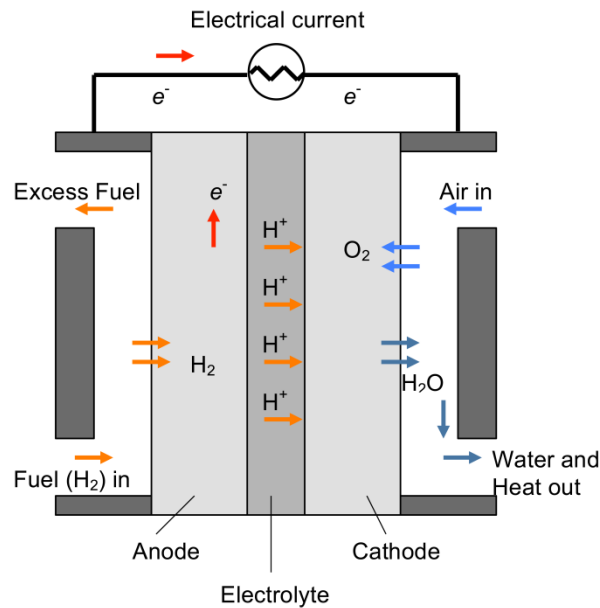
Figure 1.1: A schematic illustration of a typical PEMFC single cell [5].

1.1.2. PEMFC components

A PEMFC stack usually consists of multiple cells connected in series but the engineering challenges associated with this are beyond the scope of this thesis [6]. Rather, the focus is on single cells with the components illustrated in Figure 1.2. In the middle is the PEM. The material is highly conductive for protons but well insulating to electrons as well as impermeable to both H_2 and O_2. Ever since a breakthrough development in 1966 by Du Pont, the hydrated perfluoro-sulfonic acid polymer (with a commercial name as Nafion®) has been favoured [7]. Sandwiching to the PEM to make a membrane electrode assembly (MEA) are the cathode and anode. These can be gas diffusion electrodes (GDEs), consisting of a

catalyst layer (CL) deposited on-top of a gas diffusion layer (GDL). Alternatively, the CL can be directly fabricated onto the PEM to afford a catalyst coated membrane (CCM). The CL on both sides of the electrodes is conventionally a mixture of Pt nanoparticles (NPs) supported on a mesoporous carbon support (denoted as Pt/C) mixed with some proton conducting ionomer (e.g. Nafion®) to ensure adequate proton transport within the layer. The GDL is made from a carbon paper or cloth with a controlled porosity to ensure adequate reactant gas transport while maintaining a high electrical conductivity. It is usually treated with polytetrafluoroethene (PTFE) for good hydrophobicity so that H_2O generated during fuel cell operation does not accumulate in the pores (i.e. flooding) and hinder the effective transport of reactant gases. Gaskets are required to prevent lateral gas leaks and can be used to control the compression on the MEA [8]. Flow-field plates are required to transfer electrons, distribute the reactants evenly across the GDL and remove the liquid H_2O [9], all of which are heavily dependent on the flow field design [10]. The flow field plates commonly used are either metal (e.g. stainless steel with surface coating), which are cheaper and thinner but suffer from corrosion, or graphite which are more stable but brittle and expensive [11]. Finally, current collectors are required to connect the cell to external wiring.
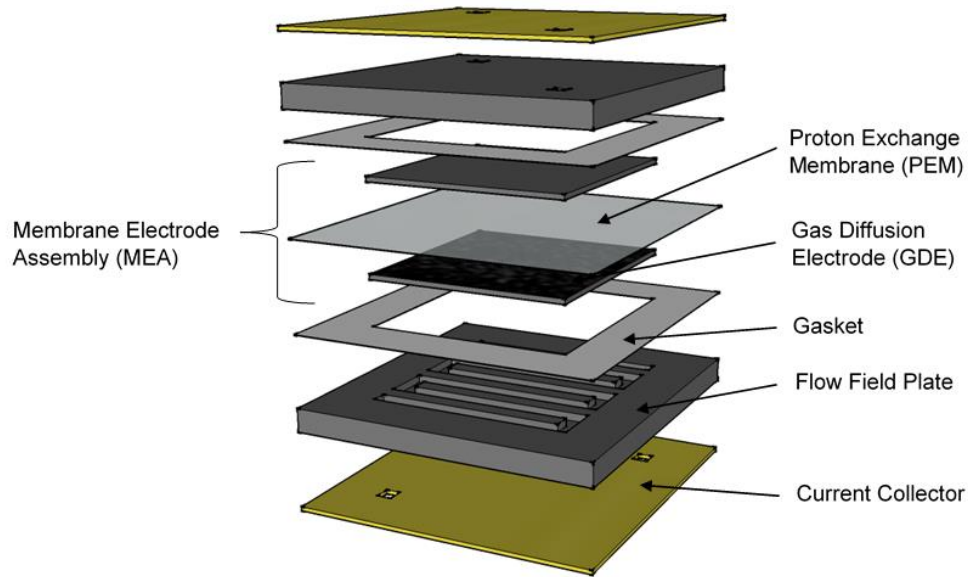
Figure 1.2: Illustration of the components required in a PEMFC single cell [5].

1.1.3. PEMFC polarisation

The overall reaction of liquid H_2O formation from H_2 and O_2 gases has a standard Gibbs free energy change ($\Delta G^{\ominus}_{298\ K}$) of -237 kJ mol^{-1} (at standard temperature and pressure, STD). This corresponds to a standard cell potential of 1.23 V (Equation 1.1).

$$\Delta G^{\ominus}_{298\ K} = -\mathrm{R}T\ln(K_{eq}) = -\mathrm{n}\mathrm{F}E^{\ominus}_{298\ K} \qquad \textbf{(Equation 1.1)}$$

R is the gas constant (8.314 J K^{-1} mol^{-1}), T is the temperature / K, K_{eq} is the equilibrium constant, n is the number of electrons, F is Faraday's constant (96485 C mol^{-1}) and $E^{\ominus}_{298\ K}$ is the standard cell potential / V.

Rearranging this equation and factoring in the empirically derived temperature dependency of $E^{\ominus}$, the theoretical maximum cell potential (E_{Nernst}) can be calculated:

$$E_{Nernst} = E^{\ominus}_{298.15\ K} - 0.000846(T - 298.15) + \frac{\mathrm{R}T}{n\mathrm{F}}\ln\left(pH_2{}^2 \cdot pO_2\right) \qquad \textbf{(Equation 1.2)}$$

pH_2 and pO_2 are the partial pressures of H_2 and O_2 respectively / atm.

Under STD, the electrochemical activities of O_2 and H_2 can be considered by their partial pressure with respect to 1 atm. With liquid H_2O in abundance, the activity is conventionally taken as unity.

Considering also the effect that relative humidity (RH) has on the partial pressures of the gas supply, a 3D plot can be constructed showing the effect of cell temperature, inlet pressure (assuming identical pressures and pure reactants) and RH have on the Nernst potential, E_{Nernst}:
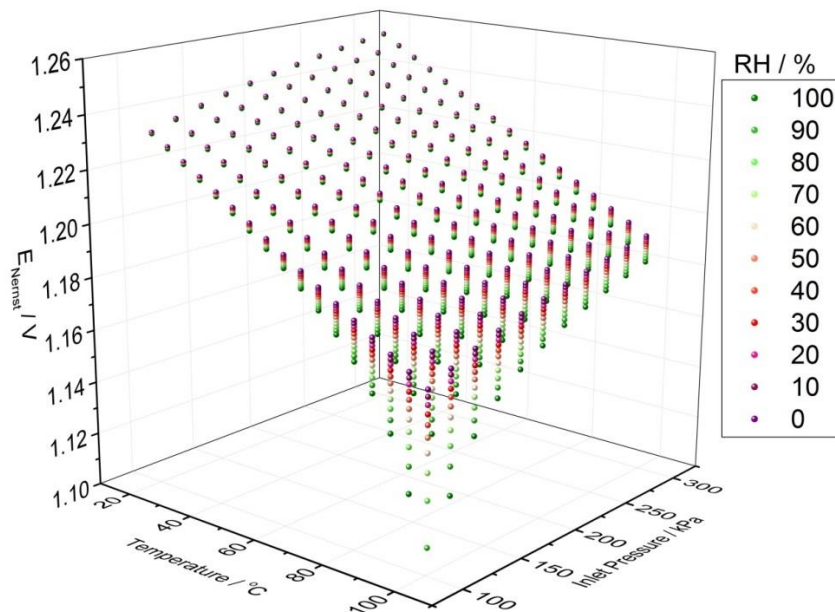
Figure 1.3: A 3D plot showing the calculated E_{Nernst} for different cell temperatures, inlet pressures and RH values. The electrochemical activity is modelled via partial pressure of reactants.

The Nernst potential only describes the theoretical maximum cell potential achievable. However, a polarisation curve demonstrates the progressive efficiency losses as more current is drawn from the PEMFC (Figure 1.4). Initial losses are a result of the overpotential

related to the kinetics of the HOR and ORR ($\eta_{ORR/HOR}$). Both reactions adhere to the Butler-Volmer kinetic equation on a heterogeneous catalyst [6]:

$$i = i_o \left(\left(\frac{C_{Red}}{C_{Red}^0} \right) \exp\left[\frac{\alpha n F \eta}{RT} \right] - \left(\frac{C_{Ox}}{C_{Ox}^0} \right) \exp\left[\frac{-(1-\alpha)n F \eta}{RT} \right] \right)$$ **(Equation 1.3)**

i is the current / A, i_0 is the exchange current / A. C_{Red} and C_{Ox} are the concentrations of the reduced and oxidised species respectively / M, C^0_{Red} and C^0_{Ox} are the equilibrium concentrations of the reduced and oxidised species respectively / M, α is the transfer coefficient and η is the overpotential / V.

This equation holds separately on the anode and the cathode, and when considering only the HOR and ORR, the respective Tafel equations apply:

$$\eta_{HOR} = \frac{RT}{\propto_{HOR} n F} \ln\left(\frac{-i}{i_{o,HOR}} \right)$$ **(Equation 1.4)**

$$\eta_{ORR} = \frac{-RT}{\propto_{ORR} n F} \ln\left(\frac{i}{i_{0,ORR}} \right)$$ **(Equation 1.5)**

These Tafel equations can be alternatively expressed as $\log_{10}(x)$ functions where the pre-logarithmic term is described as the Tafel slope, b / V dec^{-1}:

$$b = 2.3 \frac{RT}{\propto F}$$ **(Equation 1.6)**

The catalyst is required in the electrodes to speed up the reaction rate so that usable currents can be drawn. Two terms within the Tafel equation are attributable to the catalyst, the exchange current, i_0 and the Tafel slope, b. The exchange current corresponds to the reversible current at the catalyst surface at zero overpotential. The Tafel slope however is a function of the transfer coefficient, α which for a single electron transfer reaction can be described as the symmetry of the energy barrier [12]. For multi-electron processes with multiple steps, the transfer coefficient and thus the Tafel slope therefore depends on the symmetry of the energy barrier at the rate determining step [13]. The objective of PEMFC

catalyst development is to increase i_0 (or more specifically the exchange current density normalised to catalyst surface area, I_0), decrease b, and hence reduce $\eta_{ORR/HOR}$. I_0 for the HOR has a magnitude of 10^{-3} A cm_{Pt}^{-2} whereas the ORR is several magnitudes slower at 10^{-9} A cm_{Pt}^{-2} [6]. Therefore, the overpotential in the PEMFC is attributed primarily to the sluggish ORR at the cathode and so the measured cell potential corresponds to the potential of the cathode [14].

Oxidative currents due to the oxidation of impurities, of the catalyst itself and of the H_2 that permeates through the PEM (H_2 crossover) also contribute to the activation region of the polarisation curve [15]. These currents induce a compensating reaction and hence add to η_{ORR} as per Equation 1.7. Practically, these currents result in an open circuit potential (OCP) smaller than that predicted by the Nernst equation.

$$\eta_{ORR} = \frac{-RT}{\propto_{ORR}F}\ln\left(\frac{i+i_{ox}}{i_{0,ORR}}\right) \qquad \textbf{(Equation 1.7)}$$

i_{ox} is the oxidative current / A.

Internal resistances play a huge role in the PEMFC polarisation with a linear drop following Ohmic law (Equation 1.8). The internal resistances are a result of the combined electrical resistance in the flow field plates, electrodes and current collectors, their respective interfacial contact resistance (ICR) and most prominently the resistance of proton conduction across the PEM [16].

$$\Delta E_{Ohmic} = iR \qquad \textbf{(Equation 1.8)}$$

ΔE_{Ohmic} is the voltage loss due to internal resistances / V. R is the resistance / Ω.

Finally, at the large current density region, mass transport limitations occur where the rate at which reactants can reach catalyst sites is the limiting factor. A large contributor to this is the porosity of the GDL and CL where a high degree of porosity increases the effective

diffusivity, D^{eff} / cm^2 s^{-1}, a crucial component in the diffusion flux, J / mol s^{-1}, through the GDE [6,17].

$$J = \frac{D^{eff}A(C^0-C)}{\delta}$$

(Equation 1.9)

A is the area / cm^2 and δ is the diffusion layer thickness / cm.

The removal of produced H_2O is also vital where flooding of the GDL can adversely contribute to D^{eff}. Besides PTFE treatment, a microporous layer (MPL) also helps to alleviate this issue by providing a uniform contact between the CL and GDL. The H_2O produced is removed by capillary action where lower thicknesses and densities have been also shown to be beneficial [8]. Flow field plate design is also important where sufficient H_2O removal is required in lieu of effective reactant gas supply and even distribution across the entire fuel cell [10]. In particular with ultra-low catalyst loadings, local mass transport resistances dominate the effective diffusivity whereby the reactant gases must dissolve into and permeate through the ionomer/H_2O coating around catalytic sites [18].

When drawing a current, *i*, the required diffusion flux is given by:

$$J = \frac{i}{nF}$$

(Equation 1.10)

Hence a larger D^{eff} results in a reduced difference between *C* and C^0 for a given flux requirement at steady state. The effects of this concentration difference on mass transport induced overpotential, η_{MT} are two-fold: Firstly, the Nernst potential is reduced by virtue of reduced local reactant concentration at high currents (Equation 1.2). Secondly, the reaction rate can be further limited by reduced concentration leading to an increase in kinetic overpotential (Equation 1.3).
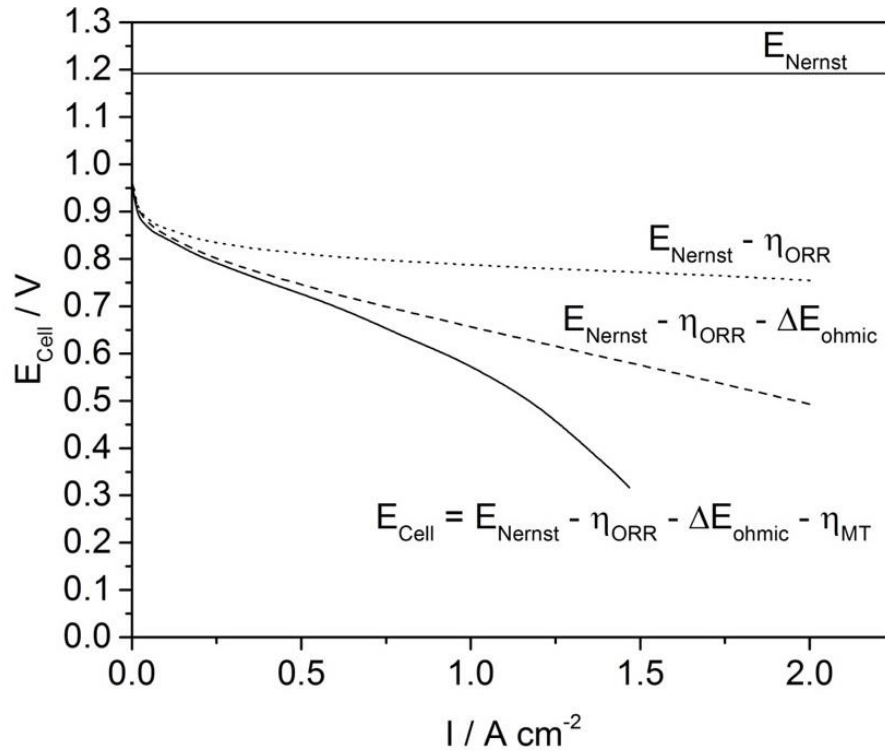
Figure 1.4: A typical polarisation curve for PEMFCs demonstrating the major losses which contribute to the deviation of the measured cell potential in comparison to the theoretical Nernst equation.

1.2. Challenges for the development of PEMFC electrodes

In past decades, a huge amount of effort in PEMFC development has been put to improve the catalytic performance of the electrodes. With a higher power performance, fewer cells need to be used for a given stack power output leading to reduced materials and overall cost. In particular, the high η_{ORR} with the cathode means that a significantly higher Pt loading (the current catalyst material of choice) is required than that at the anode. Currently, the commonly used catalyst loading is 0.2 mg_{Pt} cm^{-2} at the cathode and 0.05 mg_{Pt} cm^{-2} at the anode [19]. But, even with such low loadings, the catalyst accounts for about 40% of the overall stack cost [20]. This needs be reduced either by increasing the activity of Pt group metal (PGM) catalysts so that less is required, or by developing PGM-free catalysts that are sufficiently active towards the ORR and stable enough in PEMFC operational conditions.

For vehicle applications, the durability of PEMFCs needs to exceed 8000 hrs [20]. However, current estimates put the most durable PGM based catalysts at around 5000 hrs. The challenge is that in PEMFC operation, materials must undergo highly oxidative and acidic conditions at the cathode at a temperature of about 80°C. The durability also needs to be demonstrated under drive cycle conditions where high power loads and high voltages can be experienced.

1.3. Research strategies for the cathode development

The very high overpotential at the cathode has attracted much attention to work on the cathodic catalysts to improve their catalytic activities toward the ORR. The mostly widely adopted strategy is to alloy Pt with low cost transitional metals such as Ni or Co [21]. The alloyed metal reduces the bond strength of reaction intermediates on the Pt surface to a more optimal value and hence increases catalytic activities [22]. Alternative crystal structures have also been investigated whereby the preferential exposure of the more active facets of Pt can boost ORR activity [23]. PtM alloys have been frequently reported showing higher stability with the half-cell electrochemical measurement in liquid electrolytes. However, leaching of the transitional metal is facile in PEMFC operating environment [24]. For a full removal of the expensive PGM catalysts from the electrode, PGM-free materials have also been under considerable development. Although encouraging catalytic activities have been shown, their stability still needs to be much improved [21].

In addition, catalyst support can also contribute to enhanced ORR activities through improved electrical conductivity and metal-support interaction [25]. Much focus has been given to alternative carbonaceous supports such as carbon nanotubes (CNTs) [26] and graphene [27] along with non-carbonaceous supports such as metal oxides which avoid issues of carbon corrosion at high cell potential, in particular during fuel cell start-up [28].

The effects of the ionomer on the catalytic performance of electrodes have also been getting more appreciation where for example, shorter side-chained ionomers such as Aquivion have been reported showing better performance than Nafion® [29]. Alternative proton conducting materials such as ionic-liquids are also being investigated for enhanced ORR catalytic activities [30]. Another potential strategy is to remove the ionomer all together by using thin film CLs [31].

The strategy taken here is to adapt the synthesis of highly active one-dimensional (1D) Pt nanostructured catalysts for the fabrication of high-power performance electrodes with a thin CL. Previous works have shown success with the use of formic acid (HCOOH) as the reducing agent with chloroplatinic acid (H_2PtCl_6) precursor [32–35]. The aim of this thesis is to further this technology and develop cathodes with enhanced catalytic performance via alternative catalyst compositions (e.g. PtNi) or by incorporating novel support materials (e.g. CNTs), whilst maintaining the scalability of this approach.

Research objectives for this PhD research are listed as below:

1. To establish a method for the fabrication of PtNi nanowires (NW) supported on carbon utilising the formic acid reduction approach.
2. To adapt the methodology developed in 1 to fabricate PtNi NW array GDEs and evaluate the performance by using both ex-situ measurement in liquid electrolyte and in-situ in the MEA test in single fuel cells.
3. To fabricate and evaluate the performance and stability of GDEs made from 1D Pt nanostructures supported on N-doped CNT arrays.
4. To compare the two approaches in enhancing catalytic activities of the Pt NW array GDEs and establish the factors that affect real power performance of the 1D Pt-based hybrid nanostructure array electrodes in PEMFCs, hence providing knowledge aiding CL development in the wider community.

1.4. Thesis overview

Chapter 1 as described above gives a brief introduction into PEMFC technology; its role in society, basic materials and principles that result in a typical polarisation performance curve. This chapter also establishes some of the challenges facing the widespread adoption of this technology as well as some of the research strategies to overcome them, finalising in the objectives of this thesis.

Chapter 2 consists of a detailed review of the literature surrounding PEMFC cathode catalyst and CL development. The mechanism for the ORR is firstly explored including computational works focused on predicting the ideal catalyst material. Afterwards the focus moves to the physical development of the ideal catalyst with a focus on Pt-based nanoparticles and nanostructures, in particular 1D materials. The review then assesses developments in novel carbonaceous catalyst support materials for their impact on catalytic activity and performance in PEMFCs. Next, the review explores the translation of such novel and high potential materials into higher performance CLs in the PEMFC where Pt NW array GDEs are shown to be a very promising candidate.

Following the literature review, Chapter 3 describes the methods employed in this thesis. The source of all materials is detailed as well as the synthesis methodology of all novel materials used throughout this thesis. The parameters used in the physical characterisation of these samples are then detailed followed by the methods used to electrochemically assess the half-cell ORR catalytic activity and PEMFC performance of all materials. With a focus on the electrochemical properties of these materials, greater detail into the theory and analysis methodology is provided in the latter section.

Chapters 4-6 discuss the results of this thesis where two methods are adopted to improve power performance of the Pt NW array GDEs. In Chapter 4, a feasibility study in the impregnation and annealing of Ni into prior synthesised Pt NW catalysts to improve the

activities towards the ORR is shown. The NWs are grown on carbon spheres for ease of material handling and the evaluation of the ORR catalytic activities by the half-cell electrochemical measurement using the thin film rotating disk electrode (RDE) technique. With a focus on the effects of the annealing temperature and duration on the NW morphology and composition, enhanced catalytic activities are demonstrated in half-cell measurement but reduced overall performance in fuel cell tests.

Chapter 5 focuses on adapting this synthesis method for the scalable fabrication of PtNi NW array GDEs, with a structure analogous to those of the pure Pt metal. The effects of metal composition and alloying degree on the electrode performance are investigated by tuning the annealing and acid leaching parameters. The design principles for the PtNi NW array GDEs with improved power performances over Pt NW GDEs is explored in conjunction with half-cell measurements under the context of explaining the disparity between ORR catalytic activities measured and actual power performance recorded in the MEA test [23].

Chapter 6 demonstrates the use of nitrogen doped CNT (N-CNT) arrays grown directly on the GDL as the catalyst support for 1D Pt nanostructures to enhance the performance of array GDEs through a unique CL structure. By comparing the much greater enhancements with those of the previous two chapters, the final discussion in Chapter 7 therefore concludes the role that the CL structure has on overall electrode performance, as well as perspectives based on the advancements made in this thesis for a better development strategy of PEMFCs.

2. Literature Review

Chapter 1 provided a brief overview on the challenges and strategies for the development of proton exchange membrane fuel cell (PEMFC) electrodes in overcoming the sluggish oxygen reduction reaction (ORR) kinetics and reducing Pt group metal (PGM) content in PEMFCs. This chapter provides a deeper focus where firstly, recent progress in the fundamental understanding of the ORR mechanisms and their influence on the fuel cell power performance is reviewed. In respect of this, ORR catalyst development is then discussed with a focus on composition (i.e. PtM alloys), morphology (1D structure) and support (new carbonaceous support materials). The challenges in incorporating such developments to develop high performance electrodes are then explored alongside recent developments in thin catalyst layers (CLs). The goal is to establish the position of Pt nanowire (NW) array electrodes in this field as well as highlight the development trends that motivated the advances presented in this thesis.

2.1. The oxygen reduction reaction (ORR) mechanism

To aid the development of high performance electrodes for use as the cathode in the PEMFC, the mechanism for the ORR should be understood and hence our current understanding is briefly reviewed as follows:

The ORR occurs following the general equation below:

$$O_{2(g)} + 4H^+ + 4e^- \rightarrow 2H_2O_{(l)} \qquad \textbf{(Equation 2.1)}$$
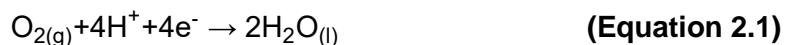
An early description of the ORR mechanism was provided by Wroblowa *et al.* [36] and a modified version is reproduced here as Figure 2.1 [37]. While O_2 can adsorb on the catalyst surface and react directly to form H_2O (k_1), it can also react via a 2-electron pathway with hydrogen peroxide (H_2O_2) as an intermediate species (k_2 and k_3). The 2-electron pathway is unfavourable in comparison to the 4-electron pathway because; (i) firstly, the H_2O_2 can desorb from the surface before completion to H_2O. This has half the standard Gibbs free energy change and thus reduces the cell potential by half. (ii) Secondly, H_2O_2 can

decompose to radical species via a Fenton type reaction and heavily degrade the fuel cell electrolyte membrane (e.g. Nafion®) [37].

By rotating ring-disk electrode (RRDE) electrochemical measurements, Paulus *et al.* found that on a Pt catalyst supported on Vulcan carbon, the ORR proceeded almost exclusively via the 4-electron pathway above 0.6 V vs. RHE in 0.5 M $H_2SO_{4(aq)}$ at 60°C. This is consistent with an earlier study by Yeager, who additionally stated that the 2-electron pathway was favoured on PGM free carbon and most transition metal oxide catalysts [38]. This latter fact was further demonstrated by Molina-García with single-heteroatom doped graphene catalysts, which showed an average electron transfer between 2.8-3.2 in alkaline electrolyte [39].

$$O_2 \longrightarrow O_{2,\,ads} \xrightleftharpoons[k_4]{k_2} H_2O_{2,\,ads} \xrightarrow{k_3} H_2O$$
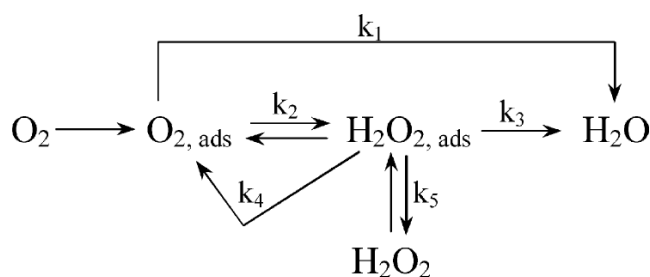
Figure 2.1: A scheme demonstrating the possible reaction pathways of the ORR [37].

Although the detailed ORR mechanisms are still in debate, it is widely accepted that the direct 4-electron pathway can be considered to proceed either by a dissociative mechanism or an associative one. The three mechanisms are outlined as follows, where the * denotes adsorption on the catalyst surface:

a) Dissociative mechanism (4-electron):

$$O_2 \rightarrow O_2^*$$
$$O_2^* \rightarrow 2O^*$$
$$2(O^* + H^+ + e^- \rightarrow OH^*)$$
$$2(OH^* + H^+ + e^- \rightarrow H_2O^*)$$

$$2(H_2O^* \rightarrow H_2O)$$

b) Associative mechanism (4-electron):

$$O_2 \rightarrow O_2^*$$

$$O_2^* + H^+ + e^- \rightarrow OOH^*$$

$$OOH^* \rightarrow O^* + OH^*$$

$$O^* + H^+ + e^- \rightarrow OH^*$$

$$2(OH^* + H^+ + e^- \rightarrow H_2O^*)$$

$$2(H_2O^* \rightarrow H_2O)$$
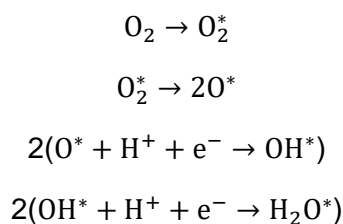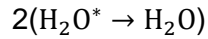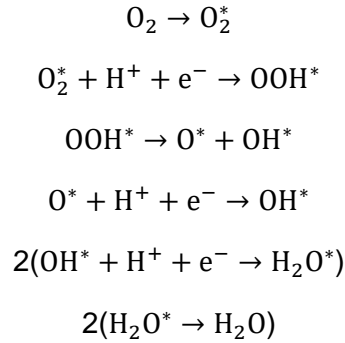
c) Peroxide mechanism (2-electron pathway):

$$O_2 \rightarrow O_2^*$$

$$O_2^* + H^+ + e^- \rightarrow OOH^*$$

$$OOH^* \rightarrow O^* + OH^*$$

$$OOH^* + H^+ + e^- \rightarrow HOOH^* \textcolor{red}{(\rightarrow HOOH)}$$

$$HOOH^* \rightarrow 2OH^*$$

$$2(OH^* + H^+ + e^- \rightarrow H_2O^*)$$

$$2(H_2O^* \rightarrow H_2O)$$
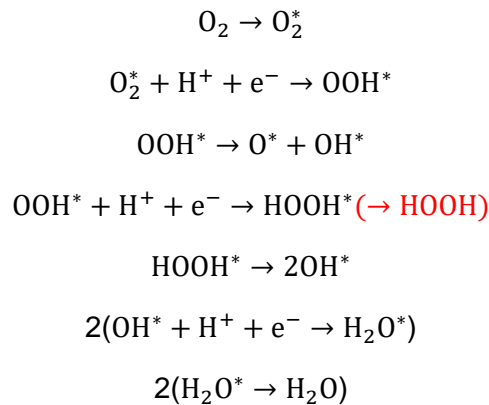
Based on these pathways, Nørskov *et al.* predicted the ideal catalyst material for the ORR by using density functional theory (DFT) to evaluate the free energy of each intermediate in the dissociative and associative mechanisms on metal (111) surfaces, and then determined the rate of each step by use of the Arrhenius equation [40]. For Pt, it was found that the associative mechanism dominated the reaction on the (111) surface at a potential below 0.8 V. An expansion on this work gave a similar result for the Pt(100) surface albeit with lower activities than that of the Pt(111) surface because of a stronger Pt-OH binding energy [41]. It is the binding energy of the catalyst to O that governs the ORR pathway where protonation of O* or OH* is the rate limiting step for strongly binding catalysts, and the protonation of O_2* is

the rate limiting step for those that are weakly binding [42]. This is an example of Sabatier's principle and thus for different metal catalysts the famous volcano plot between the M-O bond strength and catalytic activity was constructed (Figure 2.2):
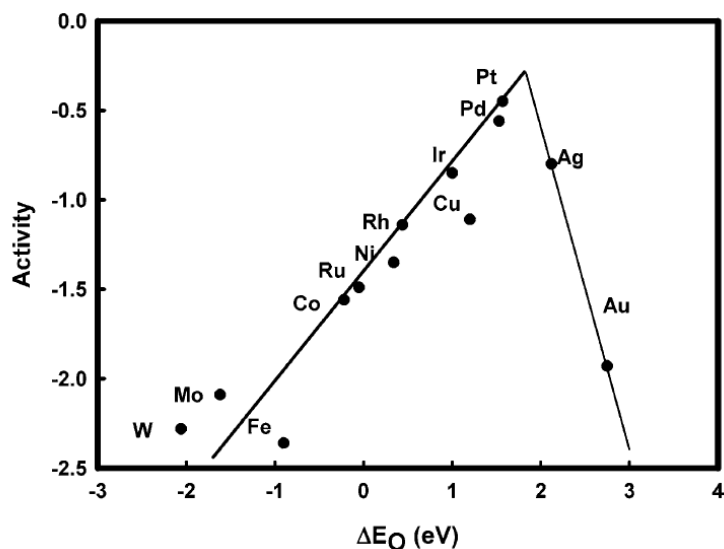
Figure 2.2: A volcano plot of the ORR activity for pure metal (111) surfaces as a function of the M-O binding energy [40].

Among commonly used pure metal surfaces, Pt was found to be closest to the peak of the volcano plot, explaining its prominence in PEMFC catalysis, although it is on the side of binding to O too strongly [40]. Hence, to improve the performance of the PEMFC cathode, it has been a key goal for researchers to develop ways of reducing the M-O bond strength on Pt surfaces.

One focus for this effort is through modifying the crystal structure of Pt based catalysts. For example, it was found that the (100) surface has a stronger binding energy in comparison to the (111) surface. For Au this is beneficial, but for Pt based catalysts who already bind too strongly to O, it is detrimental to ORR kinetics (Figure 2.3a) [41]. Based on this evidence, maximising the (111) facet exposure in comparison to the (100) through novel synthesis methods would result in a more active catalyst. In practical operation, adsorption of anions

such as bisulphate on the catalyst surface affects its activity and this also needs to be considered in modelling studies [43,44]. For example, in $H_2SO_{4(aq)}$ electrolyte the catalytic activity follows the opposite trend of Pt(111) < Pt(100) and so contrary to the original studies, Pt(100) facets should be maximised [45].

Aside from crystal structure, DFT was used in conjunction with RRDE measurements on polycrystalline Pt_3M films showing that alloying Pt with an alternative metal can also shift the binding energy to more optimal values [46,47]. Pt_3M compositions (M = Ni, Co, Fe or Ti) with a pure surface of Pt(111) and second layer of 50% Pt were analysed by DFT. A weakened M-O bond was measured for all alloys as a result of the downwards shift of the metal d-band centre, which led to a greater degree of filling of the antibonding orbitals. This is linked with lattice strain effects resulting from the lattice mismatch between Pt and the transition element such as Ni or Co. Due to the smaller atomic radius of the transition elements, this strain causes a contraction to the surface Pt and thus a reduction in bond length, in turn leading to a reduced Pt-O bond strength [22]. In particular, alloys of Pt with Ni were indicated to give the best catalytic activities over the other compositions (coinciding with the comparison of experimental Pt 'skin' structures in Figure 2.3b [48]) determining its selection in this thesis (Chapters 4 and 5).
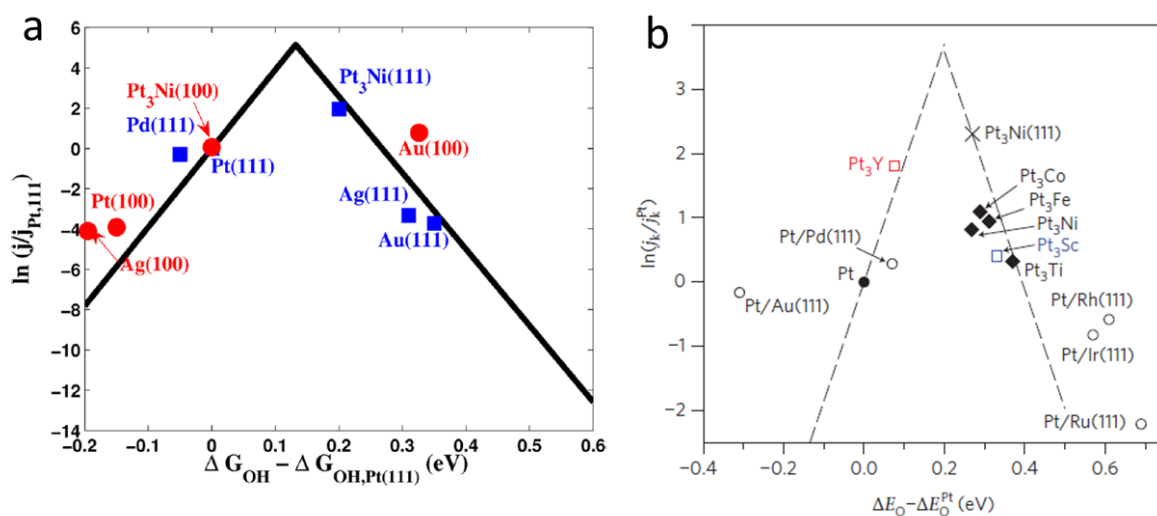
Figure 2.3: (a) Volcano plot indicating the activity vs. M-OH binding energy for PGM surfaces relative to Pt(111) [41]. **(b)** Kinetic current densities for a range of alloy catalysts with Pt skins on the surface. The dashed line represents calculated values [48].

Theoretical models of the ORR have since been refined to include solvation effects in greater detail [48–51], but crucially, a scaling relationship has also been found between the bond strength of the two intermediates, *OH and *OOH: Both intermediates contain a single Pt-O bond, and so a reduction of bond strength in one intermediate coincides with a reduced bond strength in the other [41]. Considering the difference of adsorption free energy of 3.2 eV between both intermediates, indications are therefore of a minimum overpotential for the ORR, which cannot be avoided unless this scaling relation can be circumvented. While further exploration of this subject is of great interest to researchers, the leaps made in understanding the ORR mechanism has guided the synthesis of the highly active and novel electrocatalysts reviewed in the next section.

2.2. ORR catalyst development

Based on the results from the DFT calculations, the vast majority of ORR catalyst development has been focused on the alloying and surface alteration of Pt [21]. At the same time, the high cost and the scarcity of Pt drive the research on alternative PGM-free catalysts with very promising candidates in metal-carbon-nitrides [52]. However, despite reasonable ORR activities, the poor stability of the PGM-free catalysts is still a big challenge for practical applications in PEMFCs. Considering the focus of this thesis is on improving the performance of Pt based electrodes, this review is limited to highlighting notable developments of Pt-based ORR catalysts through alteration of composition, structure and support.

2.2.1. Pt and PtM alloy nanoparticles

When considering heterogeneous catalysis, in particular where the catalyst material is as expensive and scarce as Pt, the particle size effect needs to be well considered. To maximise use of any catalyst material, the surface to bulk ratio needs to be as large as possible. Considering that the available surface area of the catalyst is inversely proportional to the particle size, smaller particle sizes are therefore favoured. However, Kinoshita recognises that for crystalline Pt, the surface sites are more active in comparison to the edge and corner sites [53]. With a larger particle, the ratio of surface to edge/corner sites increases and as such so does the specific activity (the catalytic activity normalised to the surface area) as shown in Figure 2.4a. Considering both effects, a peak in ORR mass activity (normalisation of catalytic activity to the mass) is found for Pt particles in the size range 3.5–5 nm (Figure 2.4b). This is supported by early experimental data from Sattler and Ross [54].
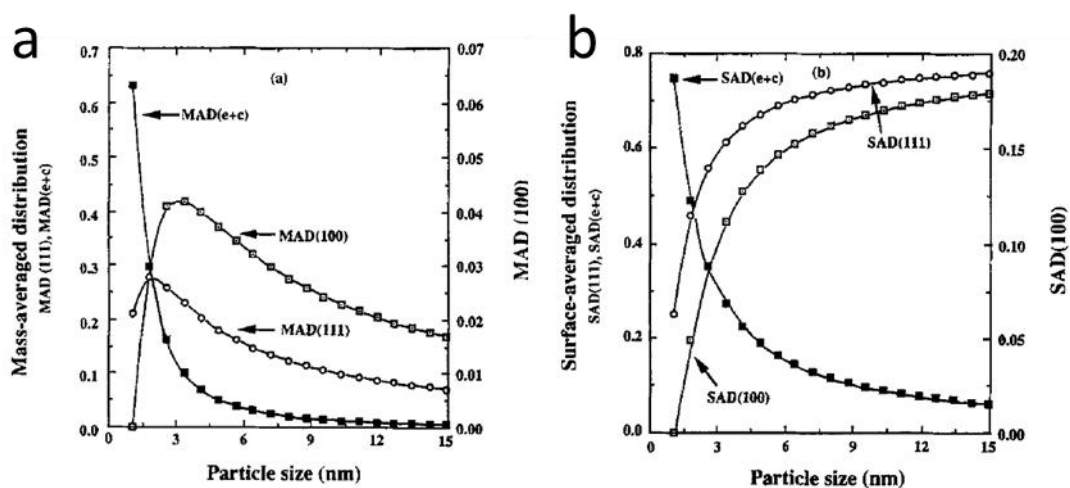
Figure 2.4: Graphs indicating the relationship of **(a)** mass activity and **(b)** specific activity as a function of the particle size of single crystalline Pt [53].

Asides from activity, stability is also of vital importance to catalysts. The high surface energy of smaller particles results in more facile aggregation into larger particles [55]. Ostwald ripening is another prime degradation mechanism for the small catalyst particles where Pt from the smaller particle dissolves in solution and redeposits on the larger particle surface (Figure 2.5). Pt mobility on a support surface also means that coarsening/sintering is possible and hence different catalyst supports have different susceptibilities to this process. For example, Padgett *et al.* reported reduced particle coarsening of Pt on porous carbon supports in comparison to solid ones such as Vulcan [56]. Therefore, particle size control is required from the synthesis methodology for its clear impact on both catalyst activity and stability.
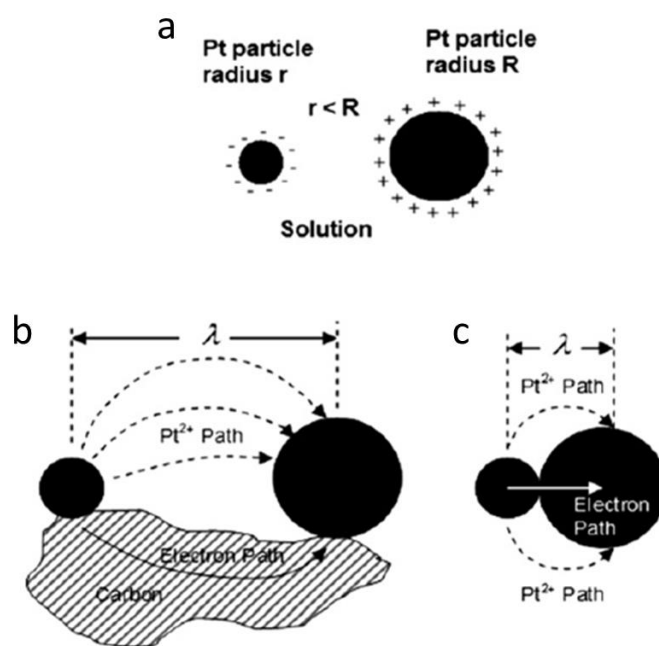
Figure 2.5: Depiction of particle growth mechanisms of **(a)** two particles in solution with different relative charges, **(b)** Ostwald ripening of two separate particles on a carbon surface and **(c)** sintering of two particles in contact [55].

Accordingly, much effort has been made towards highly controllable synthesis of Pt nanoparticles (NPs) [57]. Two common approaches for NP preparation are aqueous reduction and polyol synthesis. In the former, a Pt salt such as chloroplatinic acid (H_2PtCl_6) or potassium hexachloroplatinate (K_2PtCl_6) is dissolved in an aqueous solution and chemically reduced by a strong reducing agent such as sodium borohydride ($NaBH_4$) or Zn [58–63]. The fast reduction using a strong reducing agent allows the energy barrier for homonucleation to be overcome and well dispersed small NPs can be formed. In the polyol process, ethylene glycol (for example) acts as both the solvent and reducing agent [64]. In order to reduce the reaction time and to achieve a small particle size, microwave-assisted synthesis is often utilised [65,66]. Size control can also be achieved through the use of capping agents such as oleic acid, or polyvinylpyrrolidone (PVP) [67,68].

For example, Wang *et al.* synthesised unsupported Pt NPs by injecting iron pentacarbonyl into a reaction mixture of Pt(II) acetylacetonate, octadecene, oleic acid and oleylamine at various temperatures (Figure 2.6) [69]. At 180°C, 3 nm polyhedral Pt was obtained, whereas 5 nm truncated cubic Pt was obtained at 160°C. Finally, 7 nm cubic Pt was obtainable by using an initial injection temperature of 120°C and slowly increasing this to 200°C. Because of the increased proportion of Pt(100) facets, the 7 nm nano-cubes demonstrated enhanced ORR catalytic activity over the two other catalysts in $H_2SO_{4(aq)}$ electrolyte, thereby further demonstrating the importance of structural control.
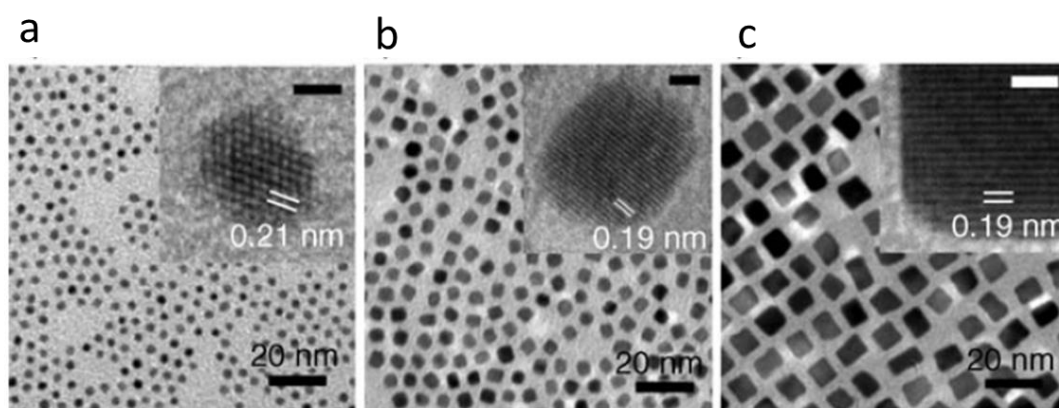
Figure 2.6: TEM images of **(a)** 3 nm polyhedral, **(b)** 5 nm truncated cubic and **(c)** 7 nm cubic Pt NPs [69].

Expanding on Kinoshita's work and in addition to the DFT studies reviewed in the previous section, a study by Tritsaris *et al.* further highlighted the relationship of catalyst structure to activity through the development of a mathematical model to consider and evaluate the catalytic activities of the step sites on catalyst surfaces [70]. Step sites were shown to have significantly higher activation energies for the ORR in comparison to surface sites, by virtue of more strongly bound intermediates, and so it can be concluded that a catalyst surface with extended facets can be more active. This is further demonstrated in Section 2.2.2 where extended Pt surface structures such as NWs are reviewed. Loukrakpam *et al.* have also

considered the aforementioned effects of preferential facet exposure, where Pt nanocubes demonstrated higher ORR activities as a result of a significant exposure of Pt(100) faces [71].

In Section 2.1 it was also shown how the alloying of Pt with a transitional metal can increase both the ORR mass and specific activities of the catalyst. To synthesize PtM alloy catalysts, co-reduction of the transitional metal salt with Pt is by far one of the simplest methodologies. PtM alloys with M = Cr [72], Ni [59,61], Co [60] and Cu [73] among a litany of bi/tri-metallic Pt based catalysts that have been reported [74]. A simple procedure was developed by Yu *et al.* who demonstrated the synthesis of monodisperse PtM NPs with a variety of compositions by simply reacting the salts (acetylacetonate) with oleylamine at 300°C [75]. Stamenkovic *et al.* on the other hand combined their previous experimental validation of the volcano plot (Figure 2.2b) [46,48] and Wang *et al.*'s exceptional size and structure tuning process [69] to synthesise homogenous Pt_3M catalysts to study the ORR catalytic activity of Pt_3M catalysts [76]. Pt_3M where M = Fe, Co and Ni were investigated with all NPs demonstrating much improved catalytic activity in comparison to pure Pt, with the performance order of Pt_3Co > Pt_3Ni > Pt_3Fe > Pt. Clearly material composition and control of facets have been shown to be a winning combination in the pursuit of more efficient Pt based catalysts for the ORR. As such octahedral Pt_3M have also received considerable attention [77–79]. In particular, Cui *et al.* used DMF to synthesise octahedral Pt_3Ni NPs, which demonstrated roughly 10-fold increases in both mass and specific activity (*cf.* Pt/C catalysts) through a combination of extended (111) surface structure and the benefits of sub-surface Ni [80].

Although Pt_3M alloy NPs show much higher ORR catalytic activities than Pt/C, leaching of the transitional metal has serious implications for fuel cell operation. In comparison to the RRDE measurement which are usually conducted at room temperature, PEMFCs typically operate at 80°C and so the dissolution of the transitional metals is a constant issue [81]. After dissolution, the transitional metal can deposit inside the Nafion® membrane leading to ion

exchange thus reducing the proton conductivity. Furthermore, for Fe, a Fenton type reaction in which H_2O_2 is decomposed to free radicals is possible, which can also physically decompose the electrolyte polymer [82–84]. One strategy to combat this - with the added bonus of minimising the amount of inactive Pt in the bulk NP - is through the protection of the transitional metal core with a Pt dominated surface in a core-shell structure [85].

In one early example, Zhang reduced an "almost dry slurry of carbon and metal salts" using H_2 gas at a high temperature of 600 – 850°C [86]. Followed by electrochemical Cu under-potential deposition (UPD) and then displacement of Pt a further monolayer was achieved on the surface of the NPs (Figure 2.7). A key factor here is the annealing step where the high reaction temperature and reductive atmosphere prompted a surface segregation because of the difference in free energy, where Pt typically segregated to the surface [87]. In-situ STEM analysis was used to study surface segregation in real time and experimental studies showed a high temperature dependency where for Pt_3Co, a Pt rich surface formed at temperatures up to 350°C but disappears at higher temperatures [88].

Chen *et al.* reported a direct approach for the synthesis of NiPt core-shell NPs through staggering the introduction of the two metal salts in a polyol reduction procedure [67]. By controlling the amount of precursor, different compositions were achieved. A monolayer of Pt was found to be both the most active and stable under potential cycling towards the ORR.
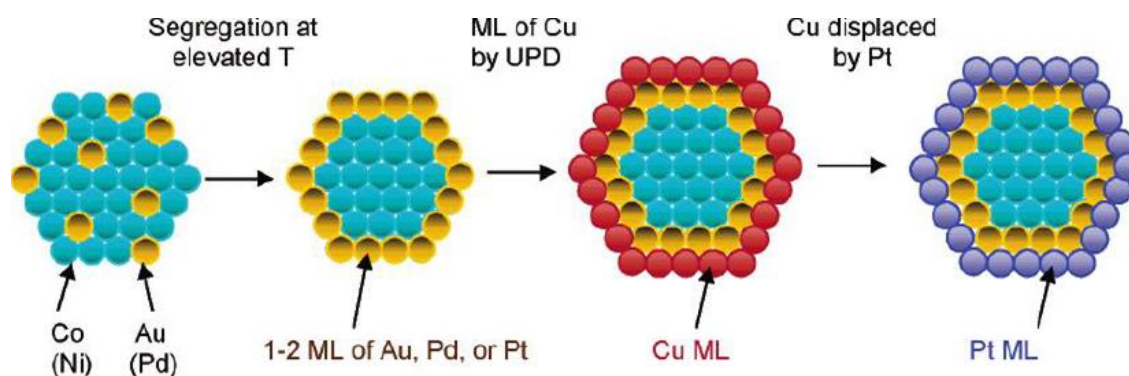
Figure 2.7: A schematic of the route to a core-shell NP with tuneable shell thickness utilising Cu UPD [86].

In addition to the sequential reduction method to synthesise the NiPt core-shell NPs [89], the combination of de-alloying and temperature induced surface segregation (i.e. thermal annealing) are also commonly reported to yield a core-shell structure. For example, Strasser *et al.* produced core shell PtCu NPs through the de-alloying of PtCu alloys [90]. The de-alloying was achieved electrochemically through potential cycling. In the MEA test, this electrochemical de-alloying process was supplemented by an ion exchange procedure whereby Cu^{2+} ions in the membrane were replaced with protons by soaking in H_2SO_4 [91]. This procedure was found to give comparable performance to that of chemical de-alloying. Still, concerns over Cu film deposition in the anode prompted a study of other bimetallic and tri-metallic systems, all prepared using this method, where Ni systems were found to be more resistant to the electrochemical de-alloying process, suggesting greater stability to leaching during PEMFC operation in comparison to the other alloy compositions [92].

Nevertheless, Ni dissolution from Ni rich PtNi alloys was utilised by Snyder *et al.* to produce nanoporous PtNi nanostructures [93]. $PtNi_3$ NPs were synthesised with controllable sizes and then electrochemically de-alloyed. For particles over a critical size of 15 nm diameter, nanoporosity was left in the final nanostructures resulting in an enhanced ORR catalytic activity (4 times that of Pt/C) through an increase in the surface/volume ratio and also an increase in the attempt frequency (the frequency that the O_2 collides into the catalyst surface)

through the nano-confinement of reactant molecules. Further improvements were also shown with the encapsulation of a protic hydrophobic ionic liquid to increase the catalytic sites with the nanoporous structures [94].

In all of these systems, enhanced ORR catalytic activity was found despite surface roughening from the de-alloying process. As described earlier in this Chapter, corner and edge sites are unfavourable in ORR catalysts and rather a smooth crystalline surface gives better performance. Therefore with the aim of refining bimetallic synthesis, Wang and Stamenkovic *et al.* mimicked the de-alloyed PtNi structures by sputtering Pt clusters onto a PtNi film [95]. By utilising surface rearrangement during annealing (Figure 2.8), they showed that a reduction in under-coordinated Pt sites resulted in an increase in the ORR activity that more than compensates for a loss in active surface area, a result typical of extended Pt surfaces.
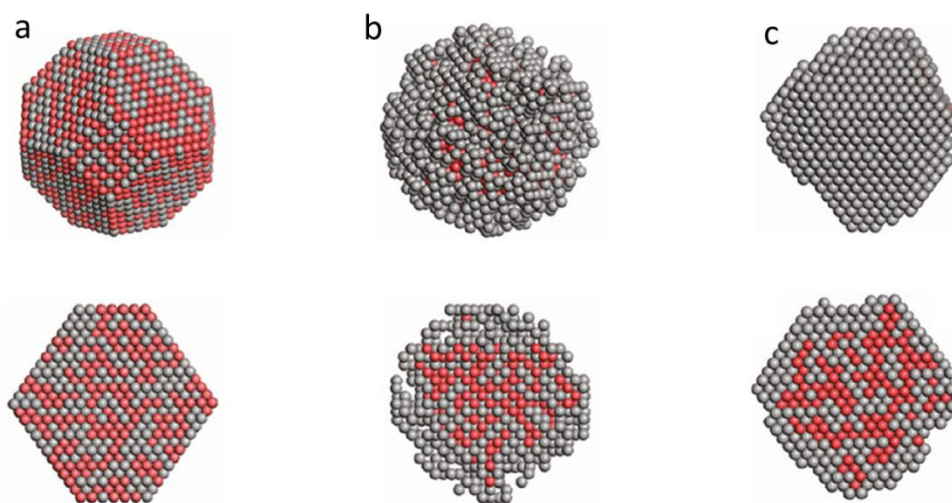
Figure 2.8**:** Simulation of a PtNi NP **(a)** as prepared, **(b)** acid treated and **(c)** acid treated and annealed with the presence of pristine facets post annealing [95].

2.2.2. Extended Pt surface structures

While NPs benefit for their unmatchable surface areas, the extended surface of other Pt structures have demonstrated considerable improvements in the specific activity that can

offset the disadvantage caused by a lower Pt surface area [23]. For example, Huang and co-workers have recently reviewed the polyol synthesis methodology in obtaining a wider variety of highly active ORR catalysts [96]. In particular PtPb/Pt core/shell hexagonal nanoplates were synthesised with an extended biaxial strained Pt(110) surface showing a mass activity of 4.3 A mg_{Pt}^{-1}, 9.8 fold higher than the US Department of Energy (DoE) 2020 target [97].

In another example, Chen *et al.* demonstrated Pt_3Ni nanoframes with a 36-fold mass activity enhancement to Pt/C [98]. Starting from $PtNi_3$ polyhedra synthesised utilising the oleylamine reduction method, after 'free-corrosion' of Ni with dissolved O_2 over a 2-week period the catalysts were transformed into Pt_3Ni nanoframes (Figure 2.9). Defects in the surface were thus smoothed by the post thermal treatment to form a highly optimised Pt-skin structure where the outermost Pt is just two monolayers thick.
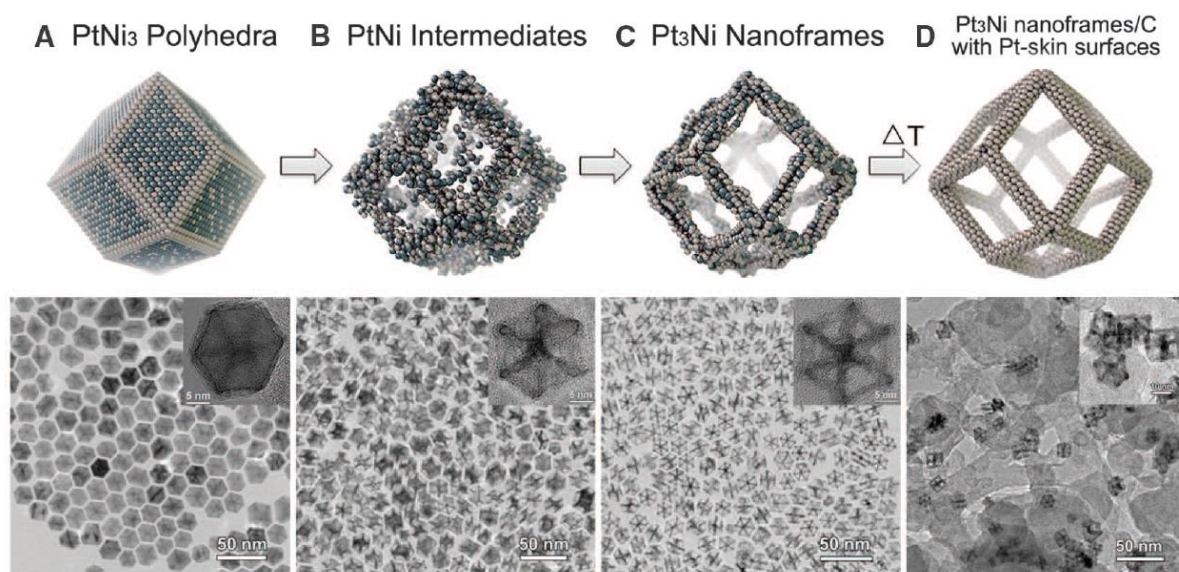
Figure 2.9: Illustration and TEM images of the formation of Pt_3Ni nanoframes over time. The final step to form a Pt skin structure is of thermal annealing [98].

1D Pt nanostructures have also gained considerable attention as ORR catalysts because of several inherent advantages [99]: Firstly, single crystal 1D nanostructures can offer preferential exposure of highly crystalline facets and fewer surface defect sites resulting in

increased surface specific activities. In addition, the 1D morphology enables a high porosity in the CL leading to enhanced mass transport characteristics in an operating fuel cell. Stability is also often improved where the bulk characteristics make 1D nanostructure more resistant to the degradation mechanisms such as dissolution, aggregation and Ostwald ripening.

Pt nanowires (NWs) are the largest group of 1D structures and can be broadly classified into two groups: polycrystalline and single crystalline, where the former offers simpler preparation techniques such as using a template [33]. For example, Choi *et al.* used a poly carbonate track etch membrane (PCTE) as the template to produce NWs up to 6 μm long with an average diameter of 47 nm. At first, an Au film was coated by sputtering onto one side of the PCTE to allow for the electrodeposition of Pt in the pores. Dichloromethane was then used to remove the PCTE template leaving behind an array of NWs. The catalysts were loaded onto a GCE for electrochemical measurement and better mass activities were found than Pt NPs for the methanol oxidation reaction, but mainly at higher loadings [100]. A silica template has also been used for preparing bimetallic parallel PtRu NWs (diameter 7–8 nm) that are linked by metallic bridges [101], but hydrofluoric acid (HF) was required to remove the template. Piao *et al.* demonstrated the use of an alumina template to produce highly ordered NWs with a diameter of 90 nm. As with all template routes a removal step is required at the end, and in this case NaOH was used (Figure 2.10) [102]. In addition, electrodeposition is often required in the preparation of NWs, further limiting the scalability of the template approach.
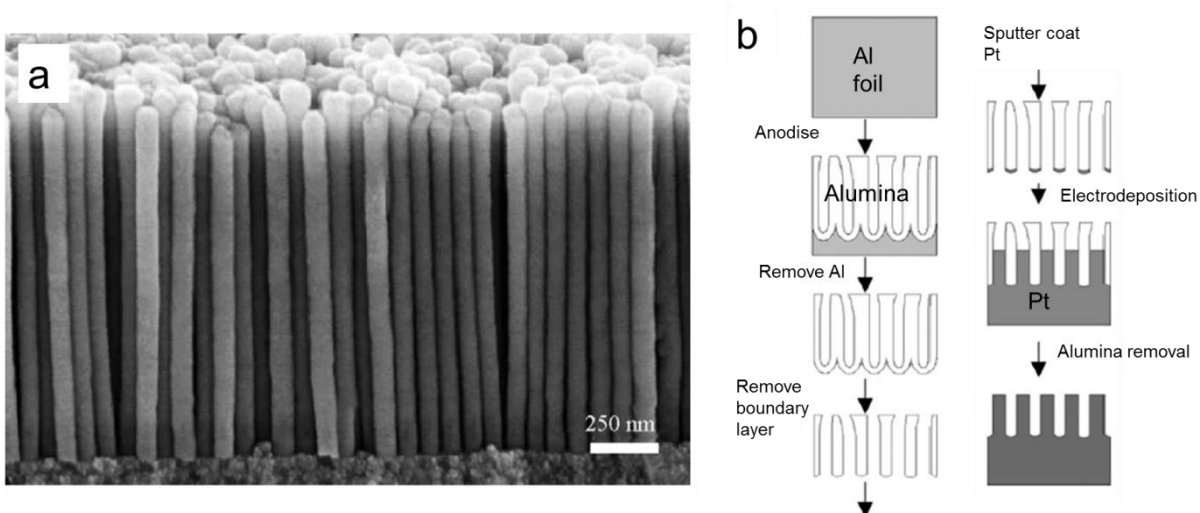
Figure 2.10: (a) Side view scanning electron microscopy (SEM) image of Pt NWs after electrodeposition utilising an alumina template and **(b)** a schematic of the fabrication procedure [102].

Song *et al.* demonstrated the use of a soft template to prepare ultra-thin polycrystalline Pt NWs with an average diameter of 2.2 nm reaching an ECSA of 32.4 m^2 g_{Pt}^{-1} (Figure 2.11) [103]. Networks of cetyltrimethyl-ammonium bromide (CTAB) were encapsulated in chloroform ($CHCl_3$) droplets dispersed in H_2O. These provided channels to entrap Pt complexes, which were then reduced by $NaBH_4$ and undertook the shape of the template. Unlike the hard templates, only distillation was required to remove the soft template here.
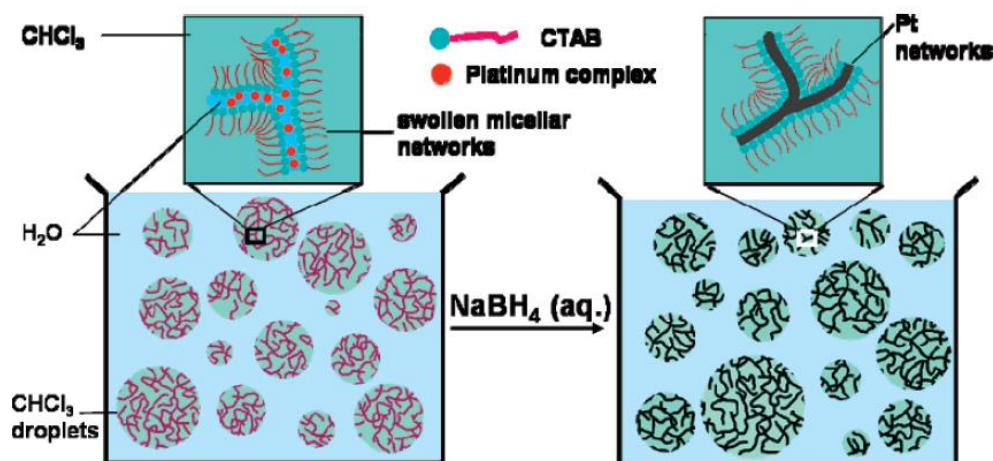
Figure 2.11: Schematic of the formation of Pt NWs by using a soft template [103].

Compared to template approaches, template-free methodologies have gained more interest for PEMFC catalyst development because single crystalline growth can be achieved, leading to a highly active catalyst surface towards the ORR. For example, Chen modified the polyol process for NP synthesis by adding trace amounts of $FeCl_2$ or $FeCl_3$ and allowing exposure to air [104]. In so doing, reduced Pt(0) could be re-oxidised by the Fe species so that the reaction rate was significantly slowed. As a result, instead of small NPs, Pt nanowires with crystal growth along the <111> direction were formed at the end of the reaction but large agglomerates were achieved rather than dispersed NWs.

Alternatively, Sun *et al.* developed a simple aqueous synthesis method where formic acid (HCOOH) was used to reduce H_2PtCl_6 in aqueous solution [105]. In this initial work, the reaction mixture was stirred at room temperature. After 16 hrs, "flower like structures" with diameters 150–400 nm were produced. These structures consisted of Pt NWs with an average length of 120 nm and diameters of approximately 4 nm. High resolution TEM showed that like the modified polyol process, single crystal Pt NWs grown along the <111> direction were achieved because the reaction rate had sufficiently slowed down. When the reaction temperature was 80°C, only NPs were obtained, indicating that the growth

mechanism was kinetically determined by the activation energies of homonucleation and heteronucleation along the different crystal faces [106].

This 'formic acid reduction' approach was then used to grow ultra-thin Pt NWs directly onto carbon black support, e.g. Vulcan XC-72R [107]. In the reduction, Pt NPs were first formed on the carbon black surface, which then acted as crystal seeds for the slow NW growth over the course of a 72 hr period. The resultant NWs exhibited a short length of 10–30 nm with a good distribution and stability on the support surface (Figure 2.12a–d). The Pt NW/C was tested as the cathode catalyst in the MEA in PEMFCs where enhanced catalytic activity was demonstrated towards the ORR in comparison to Pt/C nanoparticle catalysts. In addition, an optimal Nafion®:C ratio of 3:1 was demonstrated - much higher than that of Pt/C catalysts (typically around 1:1) - for good dispersion of the proton conducting ionomer and hence optimal proton conductivity within the rough Pt NW/C CL. Later, half-cell RDE experiments in 0.5 M $H_2SO_{4(aq)}$ were conducted to evaluate its inherent ORR catalytic activity [108]. The Pt NW/C catalyst exhibited an ECSA of 22.1 m^2 g_{Pt}^{-1}, around half of that for Pt/C. However, a 3-fold increase in the specific activity to around 611 µA cm_{Pt}^{-2} led to a larger mass activity than the Pt/C catalyst. The increases in activity were attributed to improved diffusion of O_2 along the 1D structure, fewer surface defects and the preferential exposure of highly active facets through the growth mechanism in the <111> direction. In addition, the durability of the Pt NW/C and unsupported Pt NW catalysts was compared to that of Pt/C where it was found that the 1D structure reduced the susceptibility of the NWs to dissolution, Ostwald ripening and aggregation (Figure 2.12e). The unsupported Pt NW catalyst was also shown to have minimal degradation under accelerated cycling because without a carbon support, carbon corrosion leading to catalyst detachment does not occur.
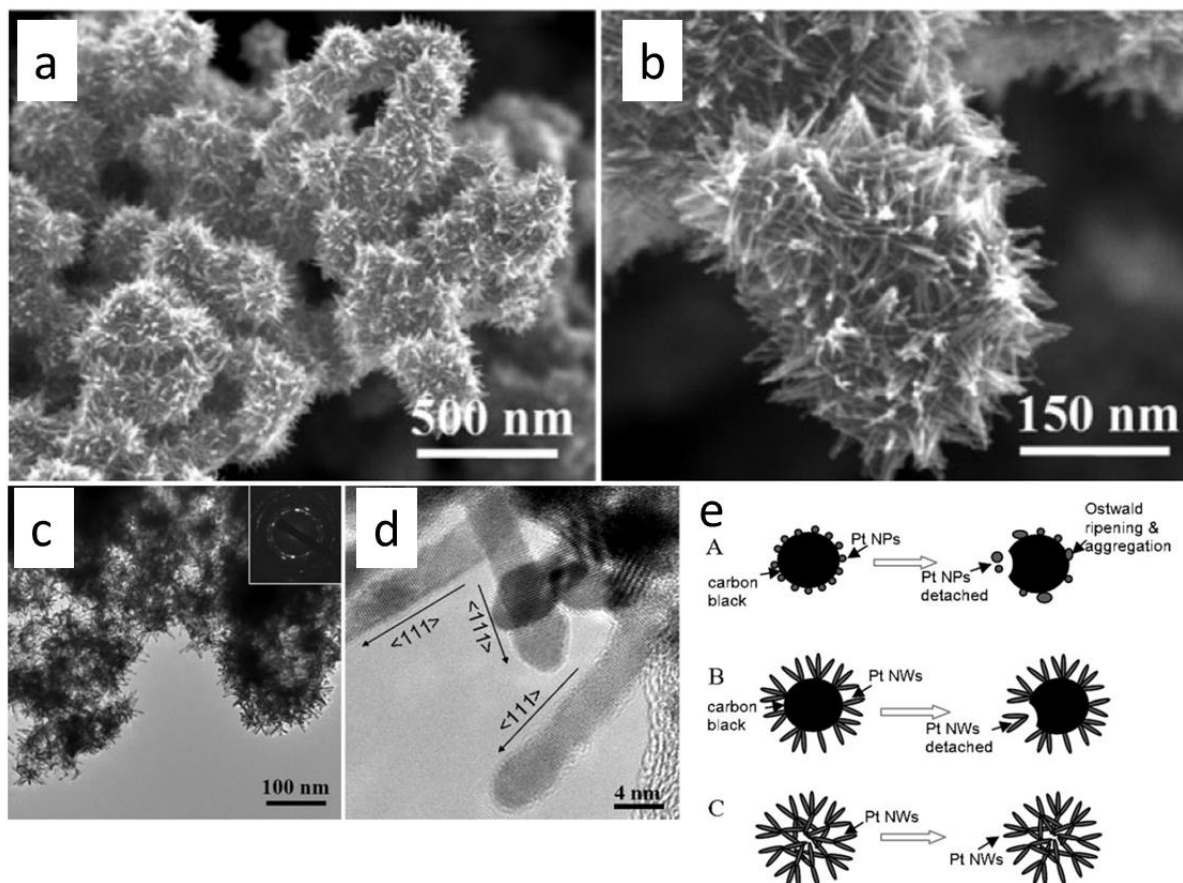
Figure 2.12: (a)–(b) SEM and **(c)–(d)** TEM images of Pt NW/C formed by the formic acid reduction method [107]. **(e)** A schematic showing the degradation mechanisms of Pt NP/C, Pt NW/C and unsupported Pt NWs [108].

In order to clarify the mechanisms behind the Pt NW growth, Meng *et al.* conducted a detailed investigation to all parameters involved in the reduction process. It was found that with regards to the Pt precursor, the higher aspect ratios followed the sequence of H_2PtCl_6 > K_2PtCl_6 > $(NH_4)_2PtCl_6$, indicating that while thought of as spectator species, the cations disrupted the growth mechanism [109]. A more substantial finding was that a decrease in the pH of the solution led to the formation of NWs with an increased anisotropic ratio because the CO produced from the dehydration of HCOOH bound much more strongly on other Pt facets such as (100) compared to (111). The thermal stability of the NWs under a flow of H_2/Ar was also examined and it was found that coarsening of the Pt NWs occurred at a

temperature above 200°C, which is used as an important consideration for the thermal annealing employed to similar systems in Chapters 4 and 5.

While the formic acid reduction approach provides a facile and simple route to synthesise highly active ORR catalysts, Pt_3M alloy NWs prepared through an organic oleylamine reduction process has led to record breaking ORR activities. In a procedure, $Pt(acac)_2$ was simultaneously reduced with the alloyed metal in a mixture of oleylamine and glucose with CTAC as the structure driving agent [110]. An initial formation of the Pt NWs superseded the reduction of Ni, eventually forming a highly flexible, crystalline Pt_3Ni alloy NW with lengths of hundreds nm and an average diameter of 9 nm (Figure 2.13). The measured ECSA are 67.5 m^2 g_{Pt}^{-1} for the pure Pt NWs and 43.4 m^2 g_{Pt}^{-1} for the Pt_3Ni alloy NWs. As a result of the highly crystalline surface, ideal Pt_3Ni composition for lattice strain and high ECSA, a mass activity of 4.15 A mg_{Pt}^{-1} at 0.9 V vs. RHE was recorded for the Pt_3Ni NWs supported on carbon in half-cell RDE measurement in 0.1 M $HClO_{4(aq)}$ electrolyte. This was 34.6 fold larger than a commercial Pt/C catalyst. Stemming from this initial research, Huang *et al.* also developed a variety of analogous PtM NW catalysts which all showed exceptional catalytic activities toward the ORR and various alcohol oxidation reactions, although all results are limited to half-cell measurement in liquid electrolytes [96,111–115].
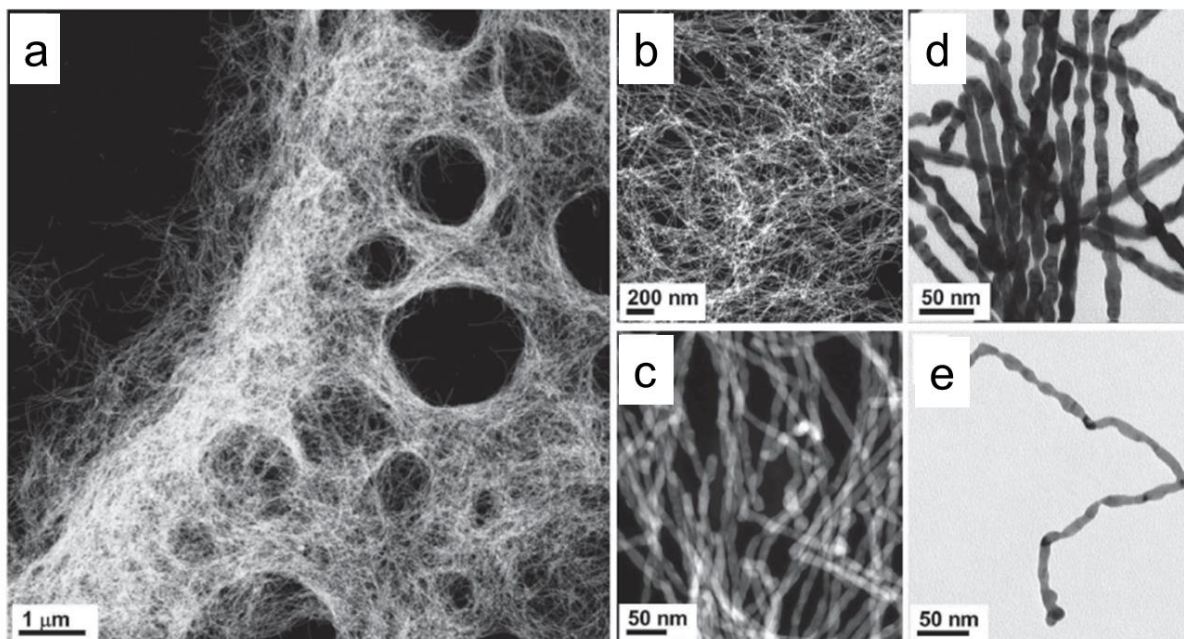
Figure 2.13: (a)–(c) STEM and **(d)–(e)** TEM images of Pt$_3$Ni NWs [110].

Currently, the highest reported mass activity for the ORR is 13.6 A mg$_{Pt}^{-1}$ for Pt NWs with jagged surfaces [116]. Firstly, Pt/NiO core/shell NWs were synthesised in a mixture of 1-octadecene and oleylamine, loaded onto carbon black and then annealed under a flow of H$_2$/Ar at 450°C to produce PtNi alloy NWs with a Pt:Ni ratio of 15:85. Electrochemical de-alloying finally produced the jagged Pt NW catalysts with a small diameter of around 2 nm achieving a high ECSA of 118 m^2 g$_{Pt}^{-1}$. The ultra-high catalytic activity towards the ORR was attributed to the high density of surface rhombi (4 atoms in 2 equilateral triangles with a shared edge) of the jagged NWs, in particular those that are under-coordinated. These sites were found by simulation and EXAFS to have a high degree of stress leading to a weakening of the Pt-O bond strength and thus increasing the catalyst activities as per the volcano plots described in Section 2.1. However, the real catalytic performance of this jagged Pt NW catalyst in PEMFCs has not yet been evaluated.

2.2.3. Catalyst support materials

The catalyst support also has a big influence on the catalyst catalytic performance. An ideal catalyst support requires the following 7 properties [25]: good electrical conductivity, catalyst-support interaction, high surface area, meso-porosity to allow ionomer distribution, good water handling properties, resistance to corrosion and easy catalyst recovery.

Carbon blacks have long been and the most common support of choice for PEMFC catalysts. Carbon blacks are primarily electrically conductive graphite nanospheres with size up to 50 nm. When they are made into catalyst layer, these spheres provide a continual porous network providing the required porosity for H_2O and gas flow without hindering electrical conductivity. Catalyst loading onto these supports is also relatively simple with techniques such as the wet chemical surface deposition, sputter deposition [117], electrochemical deposition [118] or impregnation [119].

Various types of carbon blacks have been investigated as supports with the main variable feature being the micro-porosity in the carbon itself. Very recently General Motors (GM) published their study on the impact of the internal porosity of carbon black supports on the kinetic and mass transport properties of the embedded PtCo NPs (Figure 2.14) [120]. PtCo was supported by three types of mesoporous carbon with differing amounts of micro-porosity where the kinetic performance, ECSA and local O_2 transport resistance were evaluated in PEMFC tests. As a solid carbon support, Vulcan has very little porosity so the catalyst NPs are often embedded on the surface. This enables a high catalyst utilisation, but the overall kinetic activity is inhibited by ionomer adsorption on the catalyst surface [121]. For highly porous carbons such as Ketjen black, catalyst NPs embedded in the micropores are reliant on ionomer free proton transport mechanisms as well as prompting added tortuosity for reactant transport to those catalytic sites. Those catalytic sites that are active however do not suffer from ionomer poisoning. Therefore, the ideal carbon black support was found to be

one with an intermediate porosity whereby catalyst utilisation and mass transport properties are not compromised, and ionomer adsorption is avoided.
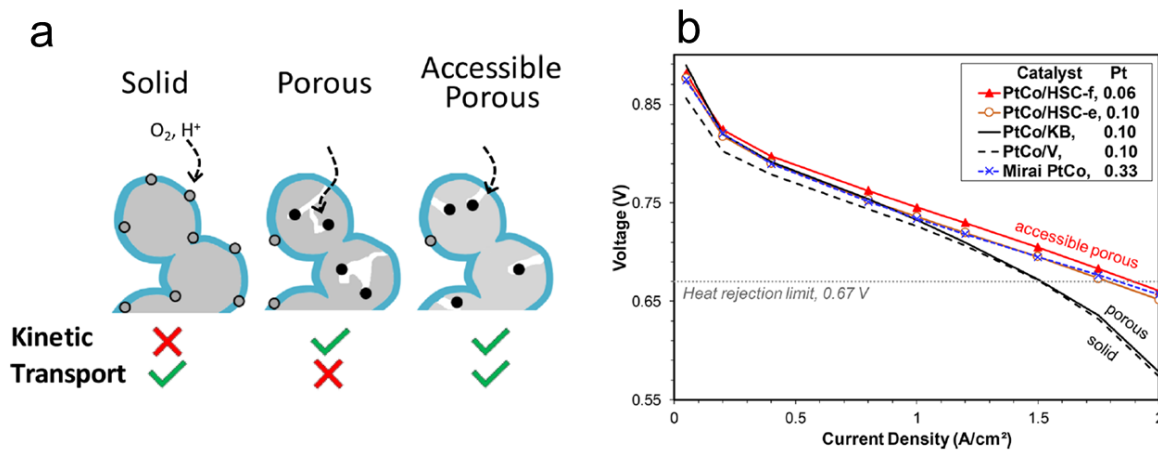
Figure 2.14: (a) Illustration of three types of carbon black supports and their relative performance with regards to kinetic activity and mass transport properties. **(b)** Polarisation curves of the three types of carbon supports demonstrating the traits described in (a) [120].

In addition to the catalytic properties, the carbon support porosity was also shown to help mitigate the ECSA loss mechanism of particle coalescence for a better retention of PEMFC performance in long-term operation [56]. However, carbon corrosion remains a prominent issue in PEMFCs which is exacerbated by the high potentials during the frequent start-up and shut-down [122]. This leads to NP detachment and hence the loss of ECSA. As such multiple non-carbonaceous supports have been investigated such as metal oxides which show a good stability to oxidised corrosion at a high potential. However, the low electrical conductivity of metal oxide supports presents a great challenge for their practical application [28].

Alternative carbonaceous supports such as carbon nanotubes (CNTs) and graphene have been much considered. They demonstrate increased activities and stability as the support for catalysts through enhanced electrical conductivities and synergistic support-catalyst

interactions [26,27,123]. However, a significant disadvantage of these supports is that their pristine surface increases the difficulty of catalyst deposition and so prior functionalisation is often necessary [124]. This functionalisation can take the form of surface organic groups [125], metallic seeds [126,127] or heteroatom doping [39,128]. Functionalisation provides the additional benefits of enhancing the catalytic activity through the modification of the catalyst electronic structure [129] and providing some inherent catalytic activity of the support itself [130]. For example, Qu *et al.* fabricated N-doped graphene sheets utilising chemical vapour deposition (CVD) and demonstrated much enhanced catalytic activity in comparison to un-doped graphene by virtue of a switching from the 2-electron to the 4-electron ORR mechanism [131].

Additionally, reduced graphene oxide (rGO) can be used, where the functionalisation derives from the incomplete reduction of the GO precursor. While enhanced catalytic activity has been demonstrated in half-cell measurement, in the PEMFC environment it was found that aggregation and stacking of the graphene sheets blocked the catalytic sites and led to large mass transport losses [126,132]. In our group, NWs have been grown on the rGO surface with later help of Pd nanoseeds to help alleviate this stacking effect, similar to reported carbon black spacers [133]. However, only limited improvements were observed in PEMFC performance.

CNTs on the other hand do not have the same issue as 2D rGO due to their 1D morphology. Tang *et al.* utilised thermal CVD to produce CNT arrays on carbon paper acting as the support for Pt NPs (Figure 2.15) [134]. With a Pt loading of just 0.04 mg_{Pt} cm^{-2}, a maximum power density of 595 mW cm^{-2} was recorded under pure O_2 benefiting from the localised Pt distribution at the membrane-electrode interface and enhanced utilisation at the low catalyst loading. Liu *et al.* grew highly ordered CNT/Pt catalyst structures on quartz using CVD which were then transferred onto the Nafion® PEM where enhanced catalytic performance was also demonstrated in PEMFC tests [135]. Shen *et al.* also deposited ordered CNT/Pt catalyst

structures on an Al foil substrate for PEMFC application [136]. The very different performances observed for CNT, and for graphene supported Pt NP catalysts indicate that the electrode performance in PEMFCs is highly dependent on the CL structure, not just the improvements in catalyst activity. Therefore, a promising combination of CNT array support and Pt NWs became one of the avenues explored in this thesis to develop high performance GDEs, as detailed in Chapter 6.

The ORR activity of Pt supported on commercial Ni decorated CNTs was previously examined where an enhanced mass activity of 0.51 A mg_{Pt}^{-1} in 0.1 M $HClO_{4(aq)}$ electrolyte was recorded in half-cell tests [127]. The kinetic enhancement was attributed to the combination of anisotropic Pt nanostructure and synergism between the Pt and support Ni where contribution from the support was found to be negligible. Dai and co-workers showed that unlike non-doped CNTs, N-CNTs catalysed the ORR through a direct 4-electron pathway where carbon atoms adjacent to the N were activated through an increase in positive charge density leading to the adsorption of O_2 [137]. Excellent stability was also demonstrated in acid, conditions where CNTs doped with transition metals suffer from the facile oxidation and leaching of the metal [138]. Considering these benefits and the ease of N-doping by active screen plasma (ASP) nitriding treatment [35,139], N-CNTs were used for the aforementioned investigation described in Chapter 6 in this thesis. This choice has recently been further validated by Louisia *et al.*, who fabricated and characterised the electrochemical performance of Pt_3M/N-CNTs and Pt_3M/S-CNTs (M = Co or Ni), where enhanced catalytic performances towards the ORR were demonstrated for the N-doped support in comparison to the S-doped CNTs and a commercial carbon black [140].
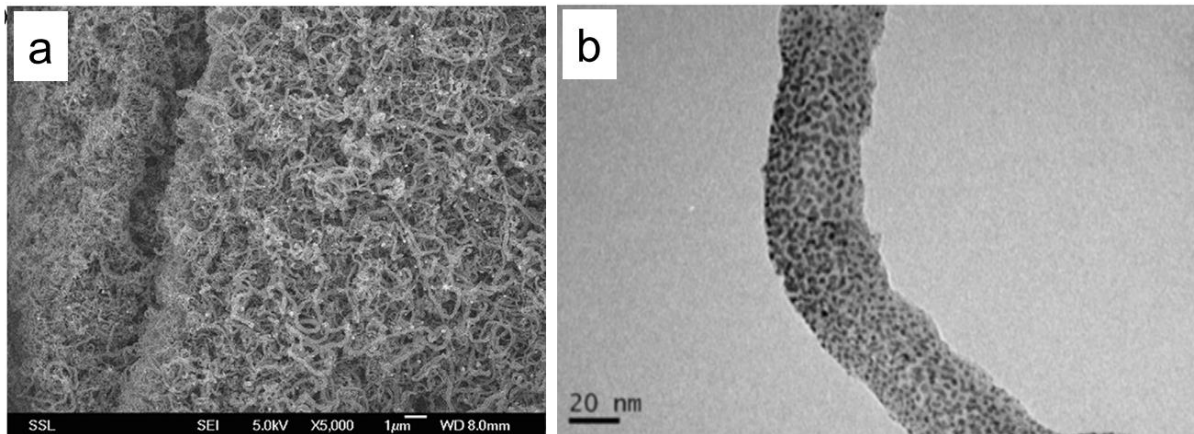
Figure 2.15: (a) SEM and **(b)** TEM images of Pt NPs deposited on CNTs grown on a GDL substrate by thermal CVD [134].

2.3. Catalyst layer development

For conventional catalysts in the spherical NP morphology, the development of novel catalysts with an enhanced ORR catalytic activity usually leads to an increased electrode performance in PEMFCs. However, different environmental conditions between PEMFC operation and the liquid electrolyte in half-cell measurements have presented some big challenges when trying to translate the ORR activity improvements of the latest generation of catalysts into real PEMFC performance enhancements. A review by Stephens, Rossmeisl and Chorkendorff commented that the highest fuel cell activity of only 0.76 A mg_{Pt}^{-1} (0.9 V) was recorded for the PtNi nanoframes that measured 5.7 A mg_{Pt}^{-1} in half-cell measurement [23]. Therefore, this section will review research that focuses on the real PEMFC performance of novel ORR catalysts and leading from this, the development of novel CL architecture, inspiring Pt NW array GDEs.

The poor translation of the excellent ORR activity of the Pt alloy nanostructures recorded in half-cell measurement to working PEMFCs is usually caused by the non-optimised distribution and/or serious decay of the proton conduction ionomer on the novel catalyst surface, reducing both proton conductivity and local O_2 permeability. For example, Alia and

42

Pivovar *et al.* developed a highly active Pt/Ni NWs catalyst by inducing galvanic displacement of Pt onto commercial Ni NWs [141]. In half-cell measurements the catalyst exhibited a high mass activity of 0.917 A mg_{Pt}^{-1} at 0.9 V vs. RHE as a result of the highly crystalline extended Pt surface and the strain effects induced by the Ni core. However, the Pt/Ni NW catalyst showed very poor performance in the single cell test due to heavy Ni contamination of the ionomer (Figure 2.16) [142]. Ni and Co, the two most popular transitional metals for bimetallic PtM catalysts, have a high propensity to be leached out of the alloy catalysts under PEMFC operation conditions via oxidation and dissolution [143]. The leached cations can cause fast membrane degradation, although this is not enough to fully explain the origins of the poor initial cell performance for the alloy catalysts. Rather the key difference between the half-cell measurement and MEA test environment is the requirement and presence of the ionomer coating over the catalyst nanostructures to provide sufficient proton conducting pathways. Okada *et al.* showed that the cation contamination of ionomer in Pt electrodes led to a reduction in ORR performance as a direct result of a decreased O_2 permeability [144]. Braaten *et al.* used a special in-house designed cell to decouple the effects of the ionomer from the rest of the MEA and could thus measure the O_2 transport resistance at different Co^{2+} contamination levels [145]. They reported an increased O_2 transport resistance with the increase of contamination resulting in cross-linking between sulfonate groups of ionomer and decreased uptake of H_2O. For Alia and Pivovar's work in particular, the Ni contamination was so severe that sulfonic acid groups were heavily blocked by Ni cations, and thus there was very limited proton transport through the catalyst electrode, resulting in the very small ECSA and very poor fuel cell performance [142]. This was somewhat mitigated by an ion exchange procedure with H_2SO_4 as shown in Figure 2.16b.
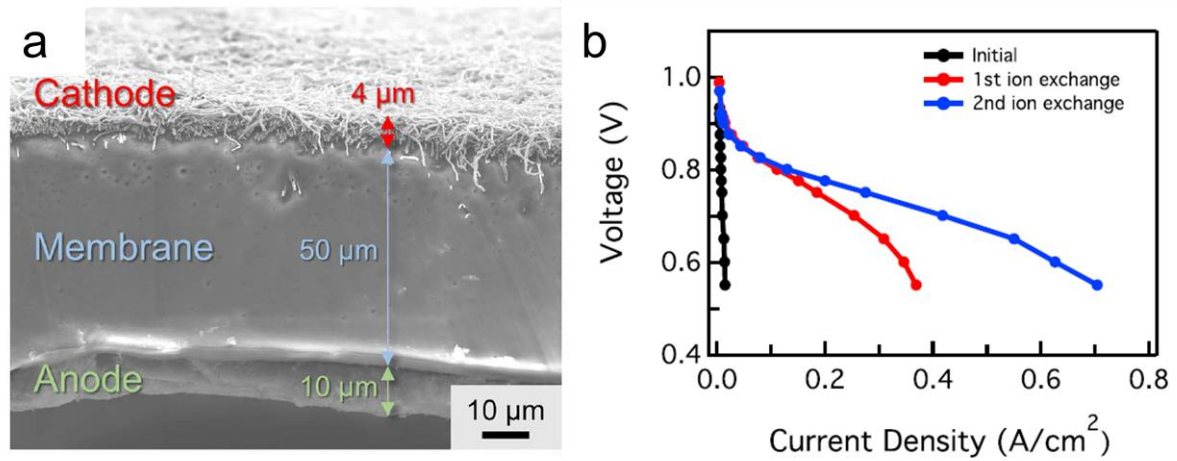
Figure 2.16: (a) Cross-sectional SEM of an MEA with PtNi NW catalysts. **(b)** MEA performance as fabricated and after ion exchange procedures [142].

Accordingly, to develop high power performance PEMFCs, the large current density region is receiving increased attention, in particular as the CL development is heading towards a low Pt loading. In the 1990's, a great advancement was made by the introduction of proton conducting ionomer to the electrode that allowed the MEA to be made with a 10-fold reduction in the Pt content from 4 to 0.4 mg_{Pt} cm^{-2} [146]. However, for full scale commercialisation of PEMFC vehicles the cathode catalyst loading needs to be further decreased to 0.05 mg_{Pt} cm^{-2} to reach 0.0625 g_{Pt} kW^{-1} (for a 90 kW_{gross}, 1 W cm^{-2} MEA) [19]. The challenges not only come from a pure kinetic limitation [147], but also an additional mass transport limitation now categorised as local O_2 mass transport losses. Researchers at Toyota Motors and GM suggested that this mass transport limitation is a result of the local O_2 transport resistance through the ionomer layer covering the catalyst surface [148–152]. They separated out the Fickian and non-Fickian components of the total transport resistance, where the non-Fickian contribution R_{NF} is a combination of components in the microporous layer (MPL); R_{NF}^{MPL}, CL; R_{NF}^{CL}, and the ionomer film; $\frac{R_{O2}^{Pt}}{r.f.}$, (Equation 2.2):

$$R_{NF} \approx R_{NF}^{MPL} + R_{NF}^{CL} + \frac{R_{O2}^{Pt}}{r.f.} \qquad \textbf{(Equation 2.2)}$$

Crucially from this equation, a low roughness factor exacerbates the mass transport resistance in the ionomer film, leading to a higher R_{NF} contribution to the total O_2 transport resistance. Therefore, one of the big advances in the PEMFC technology is development of ionomers with high O_2 permeability (Figure 2.17), or totally ionomer free CLs, allowing the use of very low Pt loadings. This also has the added benefit of a reduced mean free path for O_2 diffusion within the thin CL with a low catalyst loading - resulting in reduced Fickian transport resistances - key developments have been achieved with thin film CLs:
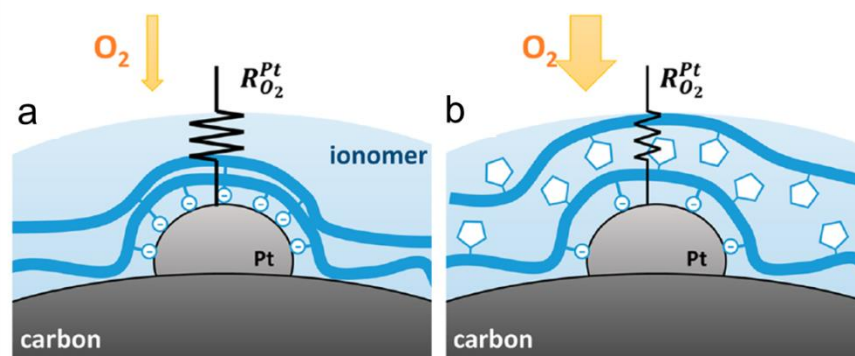
Figure 2.17: A schematic illustrating the local O_2 transport resistance through **(a)** a conventional ionomer film and **(b)** an ionomer film with a higher O_2 permeability [19].

One approach to fabricate the ionomer free thin film CLs is reported by Bizzotto and co-workers. They deposited Pt thin films directly onto Nafion® membrane: a Pt amine precursor solution was reduced to Pt metal on Nafion® by $NaBH_4$ where the reduction temperature and pH gradient were used to effectively confine the reduction close to the membrane surface [153,154]. Progressive refinements allowed the fabrication of multi-layer, monolayer and sub-monolayer Pt thin films on the Nafion® membrane surface. However, the thinness of these catalyst films caused severe water flooding issues in real PEMFC operation [155].

A second approach is the well-known nanostructured thin film (NSTF) catalysts proposed by 3M Company [31]. These catalysts consist of a thin film of Pt alloy sputter coated onto polymer whisker arrays of perylene red, with the inherent benefit that this polymer is stable to

electrochemical corrosion up to 2 V vs. RHE (Figure 2.18). Electrical conductivity is instead supplied by the coated continuous Pt alloy catalyst film. Multiple alloys have been investigated with the highest catalytic performance obtained with Pt_3Ni_7 [74,156]. Significant increases in the specific activity (approximately 10-fold) was obtained for the NSTF catalysts in comparison to the conventional Pt/C catalysts as a result of the highly crystalline nature of the polycrystalline catalyst film, where a square-truncated pyramid morphology enables a high exposure of the active (111) crystallographic facets [157]. Due to the hydrophilic surface feature of the Pt alloy catalysts, the pores formed between whisker arrays were then filled with water in fuel cell operation. These flooded water channels allowed protons to transport through water localised at the catalyst surface [158], enabling the NSTF CL to be operated with ionomer-free catalyst [159]. However, the water flooding also significantly increases the mass transport resistance. For example, Ni leached from the PtM alloy catalysts with high transitional metal content, and diffused into the membrane. Here it enhanced the net water transport from the anode to the cathode and exacerbated flooding in the cathode CL, impeding O_2 diffusion [156]. Therefore, effective water management is key for the use of NSTF CLs in PEMFC operation. Kongkanand *et al.* showed that by introducing a little ionomer, water mediation could be improved by virtue of the hydrophobic backbone of Nafion® ionomer [160]. Later work focused on elucidating the degradation mechanisms under large current density operation but also demonstrated that a hybrid layer of Pt/C catalysts between the NSTF CL and MPL showed positive effect towards water management [161,162]. While there are clear challenges with the implementation of ionomer-free NSTF CLs, the thin-CLs demonstrate enhanced mass transport properties in comparison to conventional Pt/C CLs within an operating PEMFC and are a key factor towards the high performance of the Pt NW array GDEs detailed in this thesis.
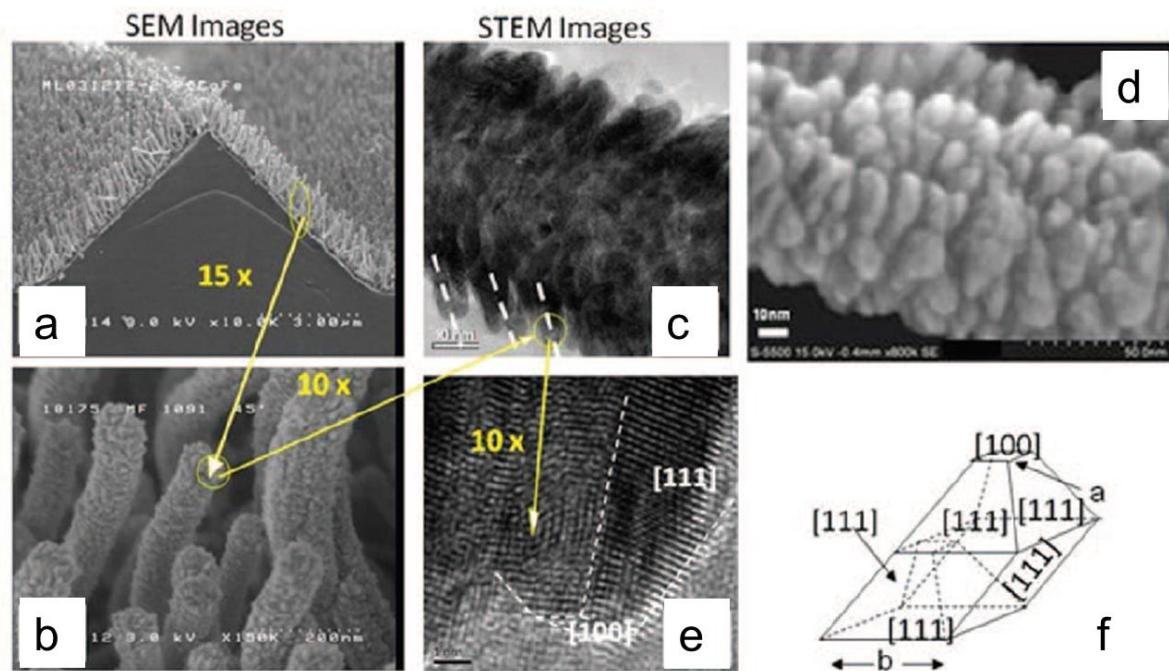
Figure 2.18: (a)–(b) SEM and **(c)–(e)** STEM images of the NSTF CL showing Pt alloy 'whiskerettes' deposited on the organic whisker substrate. **(f)** Schematic representation of the square-truncated pyramidal morphology after extended deposition [31].

2.4. Pt nanowire (NW) array gas diffusion electrodes (GDEs)

So far, this Chapter has shown 1D single crystal NWs, PtNi alloys, N-CNTs and thin CL technology to be promising avenues to improve the performance of the cathode in PEMFCs. Combining these advances, Pt NW array electrodes have been developed where the formic acid reduction method has been used to grow Pt NW arrays directly on the gas diffusion layer (GDL) surface. The collective works are reviewed here:

With carbon paper GDLs serving as the substrate for heteronucleation, arrays of Pt NWs of length 100–150 nm were grown at room temperature using HCOOH in an analogous method to that detailed in Section 2.2.2 [34]. Similar to Sun's work on carbon supported and unsupported Pt NWs [105,107,108], Pt NWs on the GDL also grew in the <111> direction and as such the preferential exposure of highly crystalline facets resulted in a smaller charge

transfer resistance as compared to the commercial Pt/C GDE. The high aspect ratio of the NWs together with the array structure improved the gas diffusion within the CL and enhanced power performance was hence achieved at the high current density region.

Unlike the NSTF CL, a careful study showed that a larger ionomer content is required for the Pt NW array GDEs in comparison to those made with commercial Pt/C nanoparticles, for optimal PEMFC performance [163]. This resulted from the less hydrophilic Pt NW surface (*cf.* the PtM alloy thin film catalyst) and the rough surface resulting from the ends of the NW arrays requiring a high ionomer content for maximal catalyst utilisation (Figure 2.19). The accelerated stress test (AST) demonstrated a faster degradation rate for the Pt NW array GDE than the commercial Pt/C GDE. Considering the inherently higher stability of the Pt NWs to major degradation mechanisms than nanoparticles as discussed in Section 2.2.2, the main degradation of the Pt NW GDE was ascribed to worse contact of the ionomer with the NW catalyst surface.
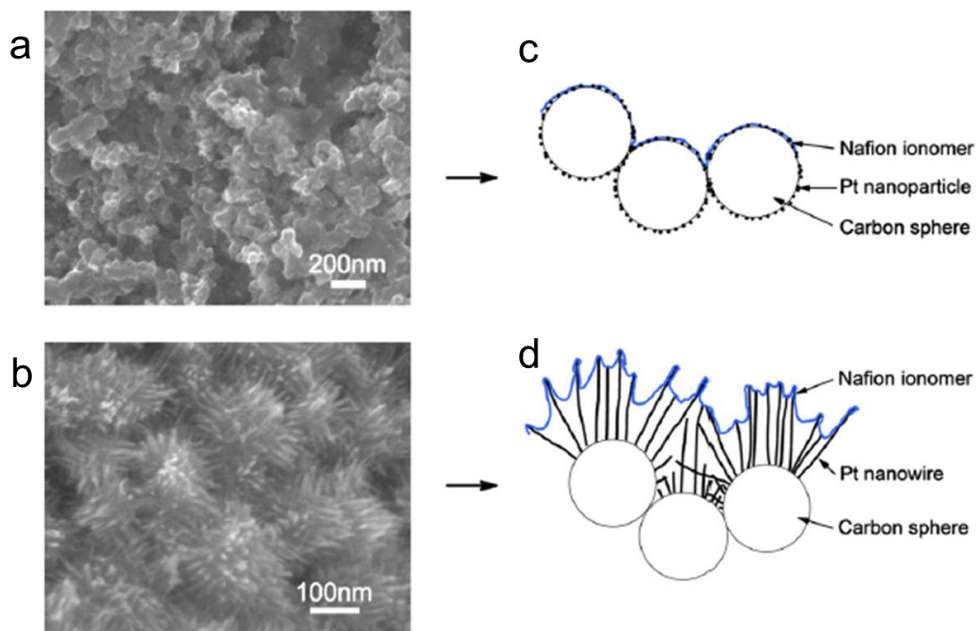
Figure 2.19: (a)–(b) SEM images of commercial Pt/C and Pt NW GDE, respectively, with **(c)** and **(d)** schematics of the Nafion® ionomer distribution on the catalyst surface [163].

To improve the NW distribution on the GDL surface, various seeding sites have been introduced to lower the activation barrier of heteronucleation. For example Pd nanoparticle seeds were introduced prior to NW growth [164]. Because of the more positive reduction potential, $PdCl_2$ was more easily reduced than H_2PtCl_6 and so these two precursors could simply be added together in the reaction solution. Notably a relationship was found where too much Pd resulted in too facile heteronucleation and so NPs were formed rather than NWs. An optimum content of 5 at% Pd (of PtPd) was found in terms of GDE performance primarily due to improved NW distribution. There is a trade-off when introducing seeds for NW growth; too many and the distribution is improved but with a significantly reduced anisotropic ratio and hence decreased catalytic benefits, but when the number of seeds is too few, agglomeration and poor distribution compromises ECSA despite the formation of long NWs.

Active screen plasma (ASP) treatment was also used to modify the MPL surface via nitriding to improve the NW distribution on the GDL surface [35]. Similar to the hetero-atom doping of pristine carbon supports, the ASP nitriding here resulted in increased defect sites and high surface activity for a better contact between the GDL surface and reaction solution in Pt NW growth, which led to a better distribution of Pt NWs and thus an enhanced electrode performance for ORR in PEMFC operation (Figure 2.20). A Pt/C functional layer prior to NW growth (0.005 mg_{Pt} cm^{-2}) has also been studied showing improved NW distribution and increased PEMFC performance [165].
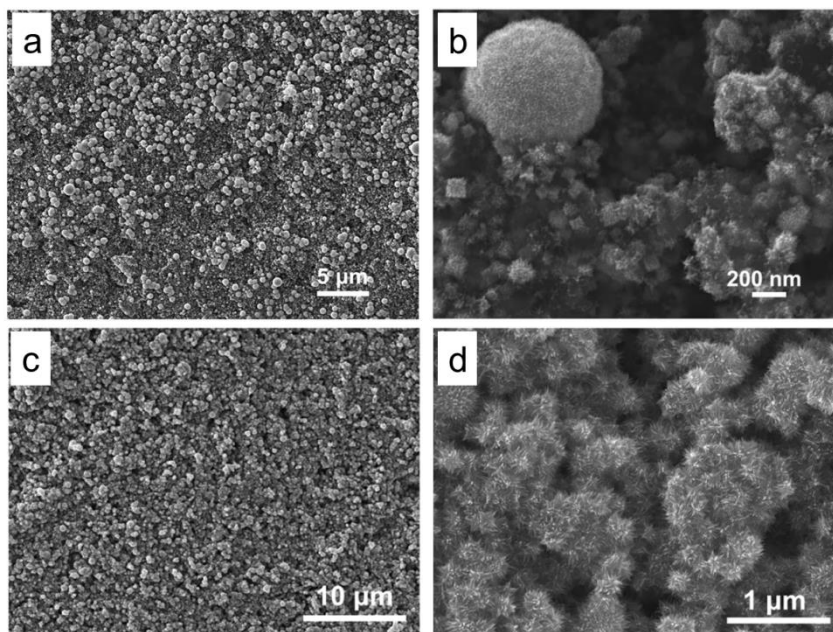
Figure 2.20: SEM images of Pt NWs grown on **(a)–(b)** the pristine GDL and **(c)–(d)** ASP nitrided GDL substrate [35].

Regarding the Pt NW array GDE, the temperature of NW growth has also been shown to have direct consequences on the Pt NW distribution, aspect ratio and electrode performance [32]. Because of the prior PTFE treatment in the GDL fabrication process, the surface is highly hydrophobic and so at room temperature the reaction solution only wet the GDL edge effectively, and finally the formed Pt NW were mainly concentrated at the edges of the GDE piece (Figure 2.21). In addition, the slow reduction rate results in the formation of large agglomerates of long Pt NWs protruding from the surface resulting in a reduced catalytic performance. A high temperature helps to improve the wettability of the GDL surface via a reduction in water surface tension, but at a relative high temperature (e.g. at 50°C) homonucleation dominates, leading to mainly NP formation. An optimum temperature of 40°C was determined by virtue of the best PEMFC performance where an array of well distributed Pt NWs was observed.
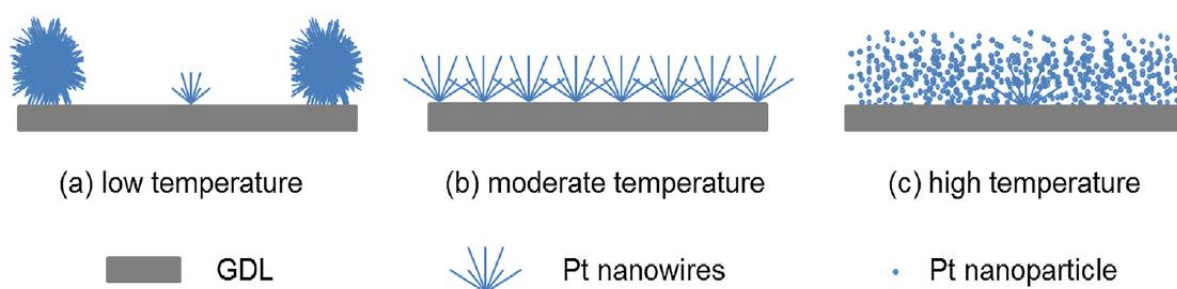
Figure 2.21: Schematic illustrating the CL structure with NWs grown at different temperatures [32].

2.5. Summary and perspectives

If PEMFC technology is to replace the internal combustion engine (ICE) in vehicle applications, then it needs to become much more cost effective. In particular the quantity of the expensive Pt catalyst needs to be reduced by either improving the catalytic performance or by using alternative cheap and abundant materials. It has been shown that for the sluggish ORR at the cathode in PEMFCs, Pt is inherently the best single metal catalyst because of the near optimal M-O binding energy. However, Pt lies on the strong binding leg of the volcano plot and so alloying with some transitional metals to induce lattice contraction or control over the exposed crystallographic facets have been discussed as promising methods to reduce the binding force to improve the catalytic activity. In particular, 1D materials have been shown to provide both avenues of improvement and are the source of the highest recorded ORR activities to date.

However, difficulties in translating these outstanding activities to real PEMFC performance improvements are not well understood. Some mechanisms such as ionomer contamination are discussed here, but further investigations into what causes this disparity in performance are needed. Additionally, it has been shown to achieve the required power outputs, mass transfer resistances need to be dramatically reduced where the thin film CL technology provides a promising solution.

In combining both enhanced mass transport properties and high ORR catalytic activity, Pt NW array GDEs grown on GDLs using the simple formic acid reduction method have shown considerable performance enhancements with respect to conventional NP technologies, where the emphasis has previously been on optimising NW distribution. With commercial PEMFC vehicles adopting Pt alloy catalysts in their MEAs, there is scope to expand the Pt NW array GDE technology through developing a fabrication method of PtM alloys. Therefore, in Chapter 4, a method of impregnation and annealing to prepare PtNi NW was firstly established on Pt NWs supported on carbon and subsequently adapted to the fabrication of PtNi NW array GDEs which will be described in Chapter 5. While performance enhancements are shown, it is through the adoption of a novel support material in N-CNT arrays deposited directly on the GDL surface (Chapter 6) that great improvements in the GDEs from Pt NW-based nanostructure arrays can be made. As such this thesis emphasises the CL structure over material composition when trying to achieve real PEMFC performance enhancements. Future work on these novel electrodes can then use these findings to focus on scaling these electrodes up to make industrial impact as well as establishing how these novel CL structures perform with ultra-low catalyst loadings.

3. Materials and Methods

This chapter firstly outlines the catalyst synthesis and gas diffusion electrode (GDE) fabrication procedures, followed by relevant preparation and testing parameters for all physical characterisation techniques employed. Details concerning the ex-situ component characterisation (rotating disk electrode (RDE) and ex-situ GDE) are then provided. Finally the methodology for all single cell tests is outlined. This chapter therefore provides all of the necessary details for interested parties to repeat any experiment detailed in this thesis.

3.1. Catalyst and GDE fabrication

3.1.1. Preparation of Pt NW/C and PtNi NW/C

To obtain sufficient Pt NW/C catalysts for physical characterisation and electrochemical measurements, 240 mg of Vulcan XC-72R (Fuel Cell Store) was initially dispersed in 750 mL H_2O by sonication bath (Ultrawave 300H, 35 W). All H_2O detailed in this thesis is deionised by a Millipore water system (18 MΩ). 9.0 mL of H_2PtCl_6 (8_{wt}% in H_2O, Sigma Aldrich) was then added. 48 mL of HCOOH (≥95%, Sigma Aldrich) was then added dropwise during a 25 min sonication step. Afterwards the reaction mixture was left to react for 72 hrs at room temperature before washing with H_2O twice and EtOH (Sigma-Aldrich) once by centrifugation (16000 rpm, 20 mins). The Pt NW/C was collected in EtOH and dried in an oven at 60°C. The final Pt loading was 60_{wt}% on C.

To impregnate Pt NW/C with Ni, 300 mg Pt NW/C catalyst was dispersed into a solution of 73 mg $NiCl_2.6H_2O$ (Sigma-Aldrich) in 180 mL 0.1 M NaOH aqueous solution (prepared in-house from 10 M, Fluka Biochemika). 80 mg $NaBH_4$ (Sigma-Aldrich) was dissolved in 40 mL of 0.1 M NaOH aqueous solution and this was added dropwise to the Pt NW/C dispersion under vigorous stirring. After 1 hr, the PtNi NW/C samples were collected as per the procedure for Pt NW/C.

Pt NW/C and PtNi NW/C catalysts were thermally annealed at 150, 250 and 350°C for 24 hrs under a flow of 50 mL min^{-1} 4% H_2/Ar in a tube furnace (Vecstar Ltd). The heating and

cooling rate was 2°C min^{-1}. PtNi NW/C was also annealed at 150°C for 72 hrs to study the influence of the annealing time.

A full schematic of the synthesis process is shown in Figure 3.1:
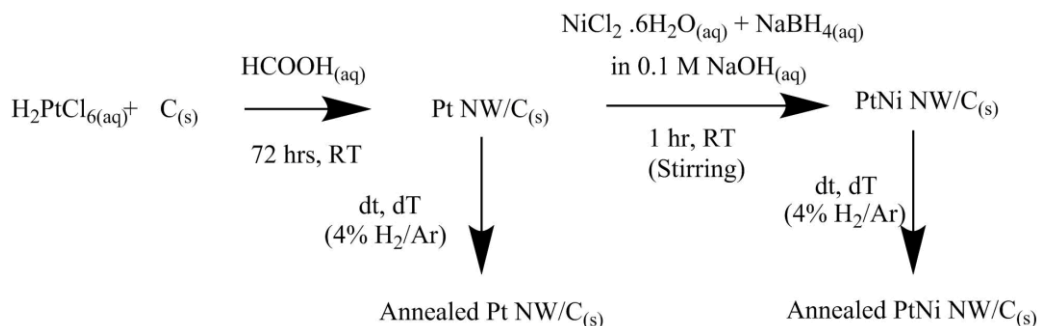
Figure 3.1: Schematic of the synthesis process of Pt NW/C and PtNi NW/C catalysts.

3.1.2. Preparation of Pt NW array and PtNi NW array GDEs

To prepare Pt NW array GDEs with a loading 0.4 mg cm^{-2}, a 10 cm by 10 cm square piece of Sigracet 39 BC gas diffusion layer (GDL) was cut and washed with H_2O, IPA and finally H_2O. This was then immersed in 66 mL H_2O in an equal sized square petri dish. 1.050 mL of H_2PtCl_6 (8_{wt}% in H_2O) was added followed by 3.3125 mL HCOOH. The petri dish was covered and after sonication for 1 min, left to react at 40°C for 72 hrs. The Pt NW array GDE was then washed with H_2O and IPA before drying in the oven at 40°C.

A typical Ni impregnation step for a precursor ratio of Pt_3Ni_4 is as follows: for a 16 cm^2 GDE cut from the 100 cm^2 piece, 10.4 mg of $NiCl_2.6H_2O$ was dissolved in 100 μL of H_2O and this was painted onto the GDE surface. 10.4 mg of $NaBH_4$ was dissolved in 0.1 M NaOH aqeous solution and added dropwise onto the GDE surface. The GDE was left for 2 hrs to ensure complete reaction. Then the PtNi NW array GDE was washed and dried in the same manner to the Pt NW array GDE.

Thermal annealing was carried out under the same conditions as the PtNi NW/C catalysts but with select temperatures of 150, 200 and 250°C. An acid leaching step was then

employed where the annealed PtNi NW array GDE was submerged in 0.1 M HNO_3 (diluted in-house from 70%, Fisher Chemicals) for 2 hrs before washing and drying.

A full schematic of the synthesis process is shown in Figure 3.2:
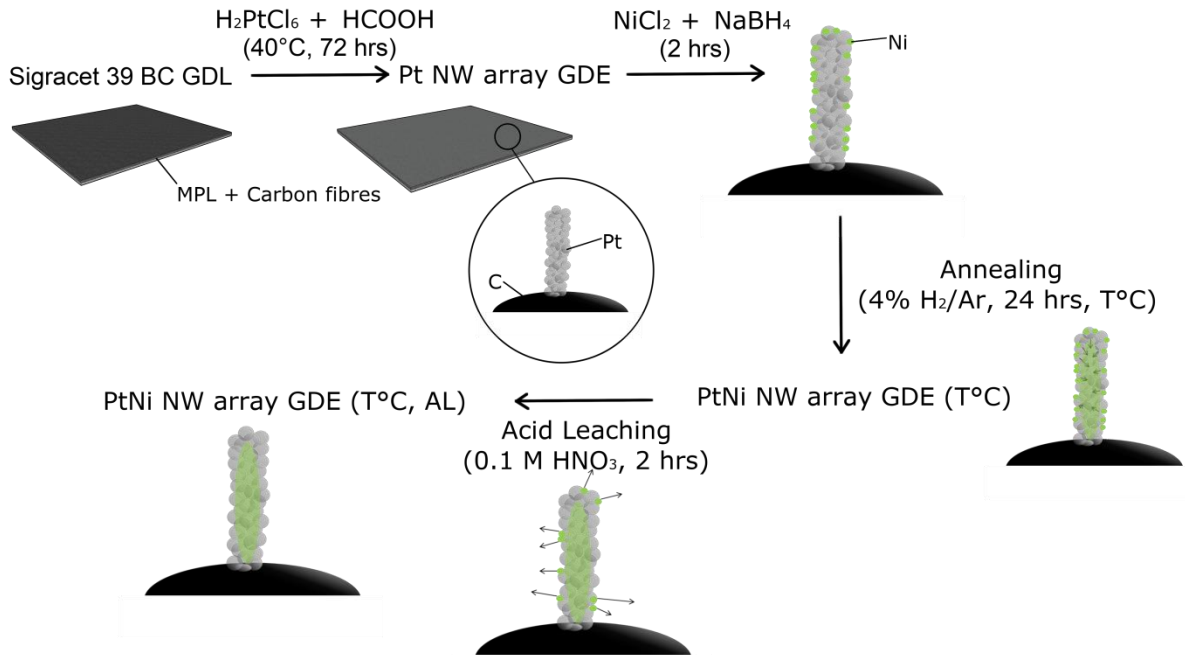
Figure 3.2: Schematic of the synthesis process of PtNi NW array GDEs.

3.1.3. Preparation of Pt/N-CNT GDEs

Plasma enhanced chemical vapour deposition (PECVD) was used to grow CNTs onto the GDL substrate. Figure 3.3 provides a schematic where a 16 cm^2 Sigracet 39 BC GDL as substrate was loaded onto the bottom worktable. The lid and substrate had a 10 mm separation distance. After assembly, a vacuum was introduced to the chamber where the base pressure was ensured to be below 1×10^{-5} mbar to avoid the interference of residual air. Gas mixtures of Ar (50 sccm) and H_2 (30 sccm) were then fed into the chamber. The plasma was then turned on with a radiofrequency (RF) power of 300 W. This was done for 10 mins in order to clean the GDL surface. Once the working temperature had stabilised, C_2H_2 gas was then fed into the chamber at a flow rate of 5 sccm. The flow of Ar remained at 50 sccm and

H_2 was reduced to 20 sccm. Deposition was then carried out with a gas pressure of 1 mbar and plasma RF power of 30 W for 30 mins. After deposition the Ar and H_2 flow was maintained but the C_2H_2 flow was switched off and the sample was left to cool down to room temperature.

The nitriding of the CNTs on the GDL surface was performed using a plasma of N_2 and H_2 with a ratio of 25:75%. This was carried out at 200°C for 10 mins to finally obtain N-CNTs. Pt NW growth was conducted in a circular petri dish using the procedure detailed in Section 3.1.2. H_2PtCl_6 (8 wt%), H_2O and HCOOH with the quantities of 168 µL, 8 mL and 530 µL were used, respectively, to achieve a loading of 0.4 mg_{Pt} cm^{-2}. The reaction temperature was 40°C.
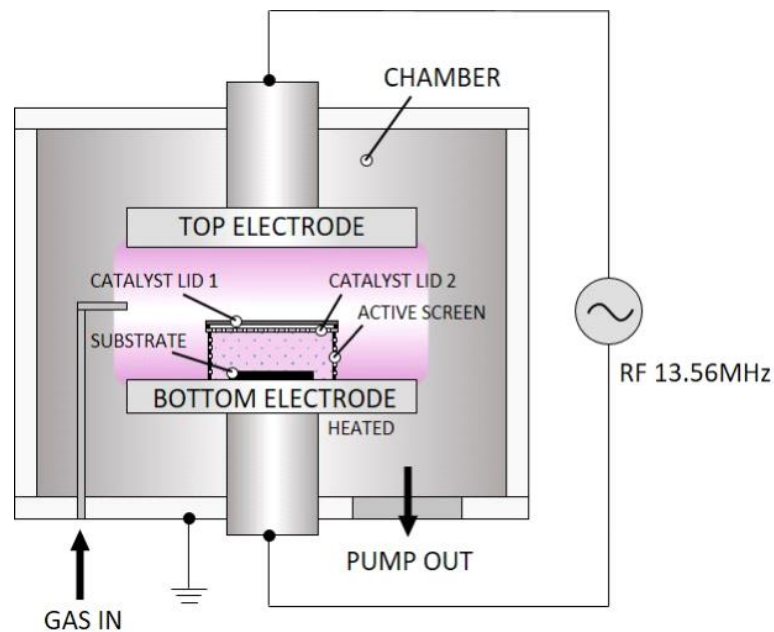
Figure 3.3: Diagram of the P500+ PECVD system and the active screen settings to deposit CNTs on the GDL substrate.

3.2. Physical characterisation

3.2.1. Scanning electron microscopy (SEM)

SEM throughout this thesis was mostly conducted with a JEOL 7000F SEM with an accelerating voltage of 20 kV except where noted. For the carbon supported catalysts, the powder was dispersed in EtOH and supported on Al foil. For the GDEs, sections were simply cut and loaded onto conductive carbon tape. For the SEM energy dispersive X-ray spectroscopy (EDX) on PtNi NW GDEs, a Hitachi TM3030Plus SEM was used with an accelerating voltage of 15 kV.

3.2.2. Transmission electron microscopy (TEM) and scanning transmission electron microscopy (STEM)

TEM and EDX analyses of the Pt NW/C and PtNi NW/C catalysts were conducted with a Jeol 2100 FEG-TEM at an accelerating voltage of 200 kV. STEM analysis of the PtNi NW GDEs and Pt/N-CNT GDEs was conducted with a FEI Talos F200 STEM with an accelerating voltage of 200 kV. All samples were prepared by dispersing the powder in H_2O and depositing onto a TEM grid. For the GDE samples, the catalyst was scraped from the electrode surface.

3.2.3. Inductively coupled plasma – mass spectrometry (ICP-MS)

A microbalance was used to measure out 0.5–1.0 mg of the Pt NW/C and PtNi NW/C catalysts or 1 cm^2 of the GDEs was cut for analysis. Digestion of the samples was conducted by firstly adding 10 mL of 25% aqua Regia solution and sonicating in boiling water for 2 hrs in the sonic bath to fully dissolve the samples. The aqua Regia solution was made in-house by diluting 18.9 mL of HCl (37%, Sigma Aldrich) and 6.6 mL HNO_3 (70%) in H_2O. After the samples had cooled down to room temperature, 20 mL of H_2O was added to provide an end concentration of approximately 2% HNO_3. 10 mL was then filtered through a 0.22 μm filter syringe into a 15 mL sample vial ready for characterisation.

A Perkin Elmer Nexion 300X with plasma strength of 1500 W was used and the analysis was conducted against appropriate calibration curves. For sample introduction, a SeaSpray™ nebulizer connected to a cyclonic spray chamber was used. The sample was pumped through at a rate of 0.3 mL min^{-1} using a peristaltic pump.

3.2.4. Thermo-gravimetric analysis (TGA)

A Netzsch TG209F1 TGA was conducted for the Pt NW/C and PtNi NW/C catalysts in the temperature range of 20–700°C at a heating rate of 10°C min^{-1} under a 40 mL min^{-1} flow of air. The analysis to GDEs was conducted by cutting out a 1 cm^2 piece and running TGA in the temperature range of 20–900°C at a heating rate of 10°C min^{-1} under air:N$_2$ gas flow mix (40:20 mL min^{-1}).

3.2.5. X-ray diffraction (XRD)

Samples for XRD measurement were prepared by creating a thin film of the catalyst power on a 1 cm^2 strip of Scotch Magic Tape, or directly using a 1 cm^2 piece of GDE. XRD patterns were recorded with a Bruker D8 Auto-sampler with a Cu Kα X-ray source (λ = 0.15406 nm). Scans were run with a step size of 0.02° and dwell time of 0.47 s.

3.2.6. X-ray photoelectron spectroscopy (XPS)

XPS samples were prepared by dispersing the catalyst powders (or sticking the GDEs) onto double-sided tape on-top of a Si wafer. A Thermo Fisher Scientific NEXSA spectrometer was used and the samples were analysed using a micro-focused monochromatic Al Kα source with a power of 72 W. The spot size was 300 μm by 300 μm. A combination of both low energy electrons and Ar ions were used to achieve charge neutralisation of the samples. CasaXPS software (version: 2.3.18PR1.0) was used for data analysis where sample charging was corrected by using the C1s peak at 284.5 eV.

3.2.7. Hg porosimetry

A Hg porosimeter (AutoPore IV, Micrometrics) was used to obtain pore size distributions of Pt/C (Tanaka Kikinzoku Kogyo (TKK), TEC10E50E, 46.2 wt_{Pt}%), Pt NW array and Pt/N-CNT GDEs. A piece of the GDEs of ca. 49–62 mg were cut into pieces and placed into a glass stem. After insertion into the porosimeter, the stem was slowly filled up with Hg up to a pressure of around 31.4 kPsi (corresponding to a pore diameter of around 5.77 nm where a higher pressure results in the filing of smaller pores) whereby the volume intrusion was measured. A plot of differential volume intrusion vs. pore diameter provides the pore size distribution.

3.3. Electrochemical measurement

3.3.1. Rotating disk electrode (RDE) preparation

In order to evaluate the inherent catalytic activities of Pt/C, Pt NW/C and PtNi NW/C, a standard 3-electrode setup was used with an Autolab PGSTAT302N potentiostat. Catalyst ink with a concentration 5 $mg_{catalyst}$ mL^{-1} was made up with H_2O:IPA:10$_{wt}$% Nafion solution at a volumetric ratio of 0.79:0.2:0.01, respectively. This was homogenised by using the sonication bath for 5 mins followed by the sonication probe (20% power for 10 mins in a 10 s on, 10 s off pulse sequence). The working electrode was made by pipetting 5 µL of the freshly made ink onto a 0.196 cm^2 Pine Instruments glassy carbon electrode (GCE) – pre-polished with alumina slurries down to 0.05 µm – and dried under a rotation rate of 600 rpm in air. An in-house prepared reference hydrogen electrode (RHE) and flame cleaned Pt gauze were used as the reference and counter electrodes, respectively. A 5 necked round bottom flask was used as the electrochemical cell. This was pre-cleaned by soaking in 1.67 g L^{-1} $KMnO_4$ and 0.33$_{vol}$% H_2SO_4 mixed solution for at least 1 day. The cell was then soaked in diluted H_2O_2 (3.5% in H_2O made from 35 %, Sigma-Aldrich) before multiple rinses with H_2O and finally 0.1 M $HClO_4$ solution (diluted in house from 70%, Honeywell). 0.1 M $HClO_4$ was

used as the electrolyte solution and a water jacket ensured a cell temperature of 25°C. A graphical representation of the RDE setup is shown in Figure 3.4:
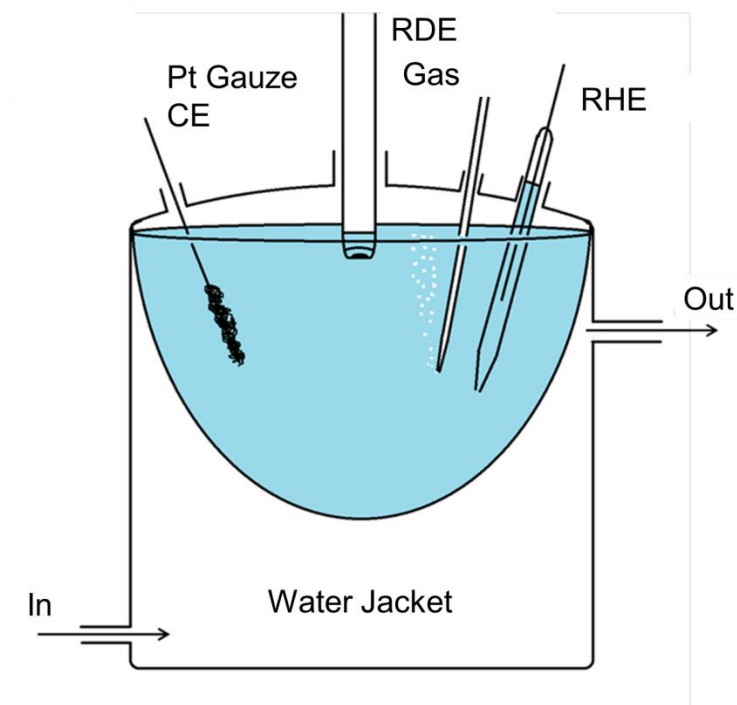
Figure 3.4: Schematic of the RDE testing apparatus.

3.3.2. RDE measurement

The cell was purged with N_2 for 20 mins before cyclic voltammetry (CV) was recorded in the potential range 0.05–1.2 V vs. RHE at a scan rate of 100 mV s^{-1}. This was undertaken to electrochemically clean the catalyst surface. Afterwards, 3 CVs were conducted at 20 mV s^{-1} the last of which was used to calculate the electrochemically active surface area using the following method:

The CV obtained for the Pt/C catalyst is shown below (Figure 3.5) where the region corresponding to the desorption of H from the Pt surface (H_{des}) is shown:
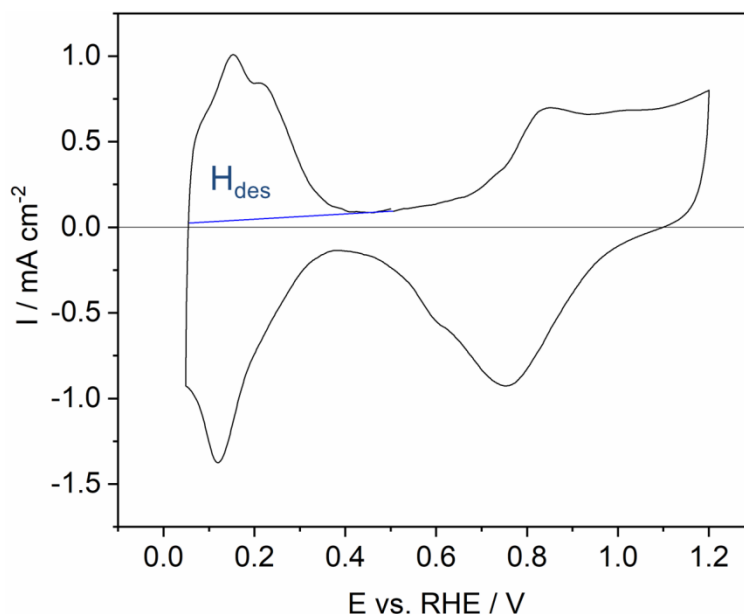
Figure 3.5: CV of the Pt/C catalyst recorded in the range 0.05–1.2 V vs. RHE at a scan rate of 20 mV s^{-1}. The H_{des} region is depicted.

A sloping background is used and the area – when converted to a current vs. time plot – corresponds to the charge associated with the process, Q_{Hdes} / C [166,167]. Assuming a full coverage on a polycrystalline surface, the absolute Pt surface area, A_{Pt} / cm^2 was calculated using Equation 3.1:

$$A_{Pt}= \frac{Q_{Hdes}}{210 \text{ μC cm}_{Pt}^{-2}}$$ **(Equation 3.1)**

The electrochemically active surface area (ECSA) / m^2 g$_{Pt}^{-1}$ can then be calculated by normalising to the mass of Pt on the working electrode (Equation 3.2):

$$ECSA= \frac{Area_{Pt}}{Mass_{Pt}}$$ **(Equation 3.2)**

Mass and specific activities are obtained by normalising the kinetic current at a set potential (e.g. 0.9 V) to the mass and ECSA of Pt, respectively. In this thesis, a full Koutecky-Levich analysis was used: linear sweep voltammetry (LSV) was conducted in N$_2$ saturated electrolyte from 0.05–1.2 V vs. RHE at a sweep rate of 20 mV s^{-1} and rotation rates of 400,

800, 1200, 1600 and 2000 rpm. Electrochemical impedance spectroscopy (EIS) analysis was conducted in N_2 saturated electrolyte at 0.5 V vs. RHE in the frequency range 10 kHz–0.1 Hz. The internal resistance was taken as the real part of the impedance when it crosses that axis of the Nyquist plot. The electrolyte was then saturated with O_2 for 25 mins and LSVs were then recorded. The electrolyte was purged with O_2 for 20 mins in between each run to ensure full saturation. Figure 3.6 shows the N_2, O_2, and corrected LSV plots where the N_2 LSV plot was treated as the background and the internal resistance, R_{int} / Ω was corrected for using Equation 3.4:
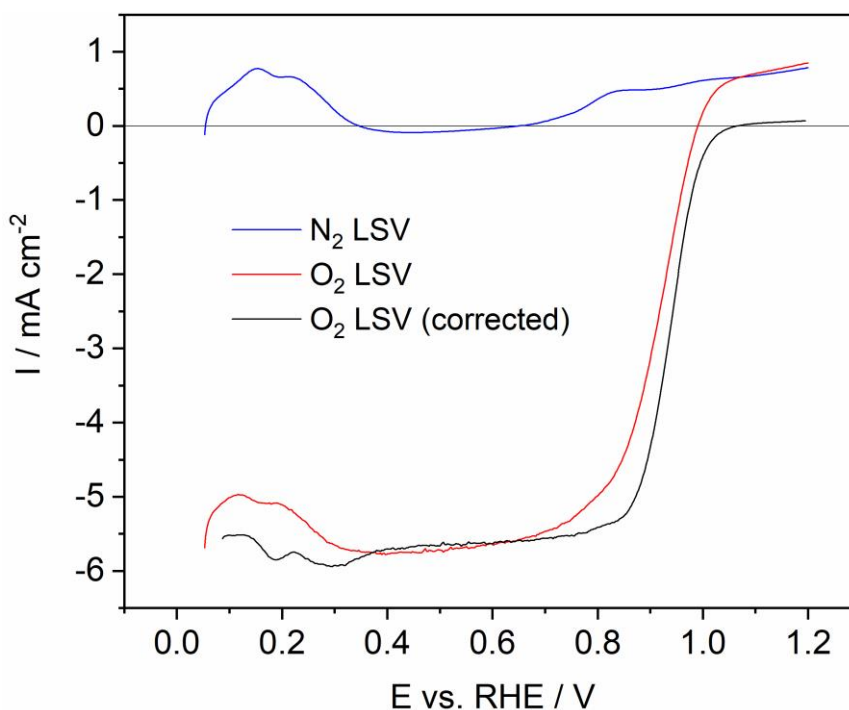
Figure 3.6: LSV plots of the Pt/C catalyst recorded in the range 0.05–1.2 V vs. RHE at 1600 rpm and a scan rate of 20 mV s^{-1}. N_2 or O_2 saturation is indicated as well as an LSV where background and internal resistance corrections have been made.

$$E_{corrected} = E_{meas} - (i \cdot R_{int}) \qquad \textbf{(Equation 3.4)}$$

$E_{corrected}$ is the internal resistance corrected potential vs. RHE / V, E_{meas} is the measured potential vs. RHE / V and i is the measured current / A.

To obtain a kinetic current, a Koutecky-Levich plot was made from the corrected LSV plots at various rotating rates:
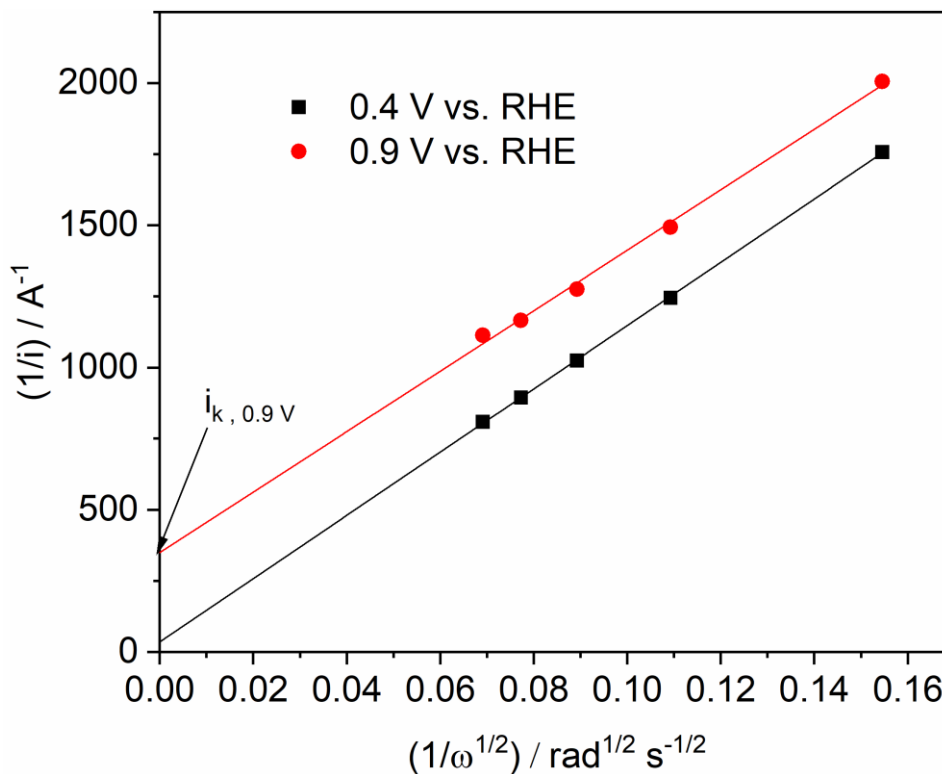
Figure 3.7: The Koutecky-Levich plot for the Pt/C catalysts at potentials of 0.4 and 0.9 V vs. RHE. The kinetic current as the intercept of the extrapolated line of best fit with infinite rotation rate is shown.

The Koutecky-Levich equation (Equation 3.5) implies that the intercept of the plot corresponds to the kinetic current, i_k / A, at the specified potential, i.e. what the current would be if the rotation rate was infinite and hence zero mass transport limitations.

$$\frac{1}{i} = \frac{1}{i_k} + \left(\frac{1}{0.620 \cdot n \cdot F \cdot A \cdot D^{2/3} \cdot v^{-1/6} \cdot C}\right) \omega^{-1/2} \qquad \textbf{(Equation 3.5)}$$

A is the electrode surface area / cm^2, D is the diffusion coefficient / cm^2 s^{-1}, v is the kinematic viscosity cm^2 s^{-1}, C is the reactant concentration / mol cm^{-3} and ω is the angular rotation rate / rad s^{-1}.

The kinetic current at 0.9 V was then used to obtain mass (MA) and specific activities (SA) using the follows two equations:

$$MA_{0.9\ V} = \frac{i_{k,\ 0.9\ V}}{m_{Pt}} \qquad \textbf{(Equation 3.6)}$$

$$SA_{0.9\ V} = \frac{i_{k,\ 0.9\ V}}{A_{Pt}} \qquad \textbf{(Equation 3.7)}$$

3.3.3. Ex-situ GDE measurement

For the NW GDEs, ex-situ GDE measurement was conducted using a FlexCell polytetrafluoroethene (PTFE) from Gaskatel. Figure 3.8 shows a schematic illustration of the cell. Both Pt NW and PtNi NW GDEs (precursor ratio Pt_3Ni_4, annealed at 200°C, acid leached) were tested both without ionomer and with a loading of 0.6 mg_{Naf} cm^{-2}. Ionomer coating was applied by painting a solution of 85.7 µL 10_{wt}% Nafion® suspension dispersed in 200 µL IPA and leaving to dry in ambient conditions. The GDE was wetted with H_2O before inserting into the FlexCell gas compartment where it was held by O-rings of active area 3 cm^2. The main and reference electrode compartments were filled with 0.1 M $HClO_4$ aqueous solution and a pipette was used to purge and dislodge any bubbles within the luggin channel (the channel that links the RHE with the main electrolyte compartment as close to the GDE as possible). The gas behind the electrode piece was set at a constant flow of 189 mL min^{-1}. A Pt coil counter electrode was in built into the cell and a commercial HydroFlex RHE (Gaskatel) was used as the RHE. Temperature was controlled by two heating plates inserted into the side of the PTFE cell, connected to a thermocouple.
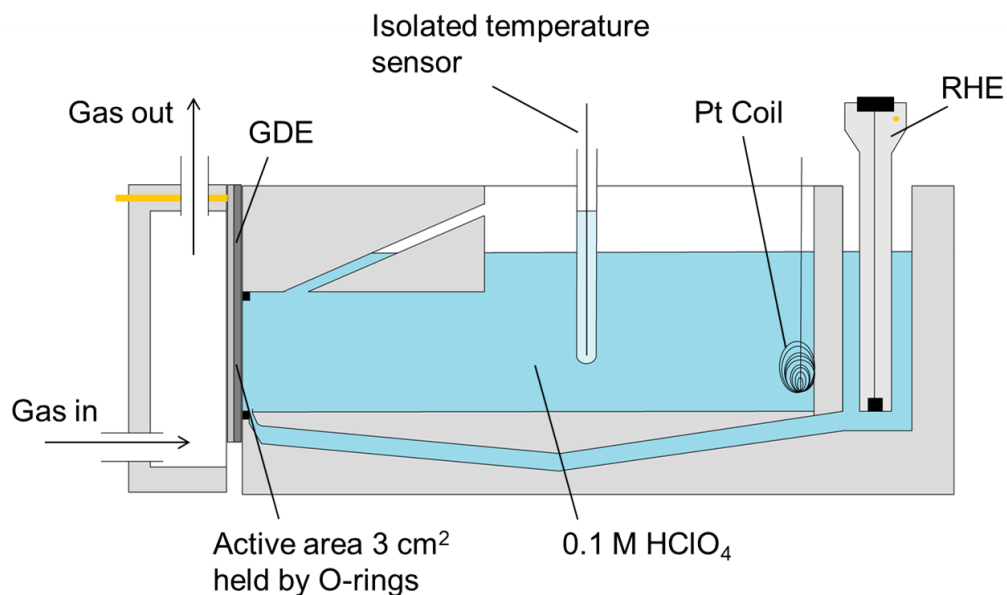
Figure 3.8: Schematic of the FlexCell used for ex-situ GDE measurement.

The Pt NW GDE and PtNi NW GDEs were initially measured at 25°C with N_2 gas flowed behind the GDE for 20 mins before running 100 CV cycles in the range 0.05–1.2 V vs. RHE at 100 mV s^{-1} in order to electrochemically clean the surface. 2 CV cycles were then conducted at 20 mV s^{-1}, the last of which was taken for ECSA measurement as described in Section 3.3.2. The gas was then switched to O_2 and the open circuit potential (OCP) measured until a stable value was reached for at least 200 s, indicating the electrolyte was saturated. An LSV was then recorded from 1.2–0.05 V vs. RHE at 10 mV s^{-1}. EIS was conducted at 0.9 V vs. RHE in the frequency range of 10 kHz–0.1 Hz with the real impedance at the high frequency intercept taken as the internal resistance. Double layer charging was accounted for by shifting the LSV up so that the current at the measured OCP was equal to 0 A. Internal resistances were corrected for as per Section 3.3.2. The cell temperature was then changed to 50°C and all measurements re-run.

3.3.4. Membrane electrode assembly (MEA) fabrication

For the Pt/C and Pt NW/C catalysts, the required catalyst for 0.4 mg_{Pt} cm^{-2} was measured and dispersed in 90.5 µL 10_{wt}% Nafion® aqueous solution and 0.5 mL IPA by use of the sonication bath for 5 mins, followed by sonication probe at 20% power for 10 min in a 10 s on / 10 s off pulse sequence. The ink was then painted onto a 4×4 cm GDL substrate (Sigracet 35 BC) and left to dry in ambient conditions. For NW array GDEs and Pt/N-CNT GDEs, Sigracet 39 BC GDLs (the new brand name of 35 BC) were used. Ionomer (for a loading of 0.6 mg_{Naf} cm^{-2}) was applied by painting a solution of 91.4 µL 10_{wt}% Nafion® in 200 µL IPA onto the GDE surface.

JM Pt/C GDEs (0.4 mg_{Pt} cm^{-2}) coated with an ionomer layer of 0.6 mg_{Naf} cm^{-2} were used the anodes to make MEAs. FuelCellStore Pt/C GDEs with 0.2 mg_{Pt} cm^{-2} on carbon paper were used for making MEAs used in Chapter 5 – Section 5.4.2. Nafion® 212 membrane was used as the proton exchange membrane (PEM) for all MEAs. The cathode and anode were hot pressed at either side of the PEM at 135°C under 4.9 MPa for 2 mins.

3.3.5. Single fuel cell performance testing

For all single cell tests, a PaxiTech-Biologic FCT-50S PEMFC test stand was used (Figure 3.9). PTFE gaskets with a thickness 254 µm were used. Graphite flow field plates with single serpentine tracks were arranged in counter flow. The single cell was tightened with a force of 3.5 Nm. The cell was tested at 80°C. Initially for membrane break-in, the cathode/anode were fuelled with air/H_2 with an absolute pressure of 1.5/1.5 bar at a stoichiometry of 1.5/1.3 and 100%/100% relative humidity (RH), respectively. The cell was held at 0.6 V overnight (minimum of 8 hrs) or until a constant current was measured. The gas was switched to the following at the cathode/anode respectively, corresponding to those specified by the US department of energy (DoE) protocol for the activity measurement [97]: O_2/H_2, 1.5/1.5 bar absolute pressure, 2/9.5 stoichiometry and 100%/100% RH. Cell break in and polarisation

curve acquisition followed the methods defined by the harmonised EU testing protocols [168].
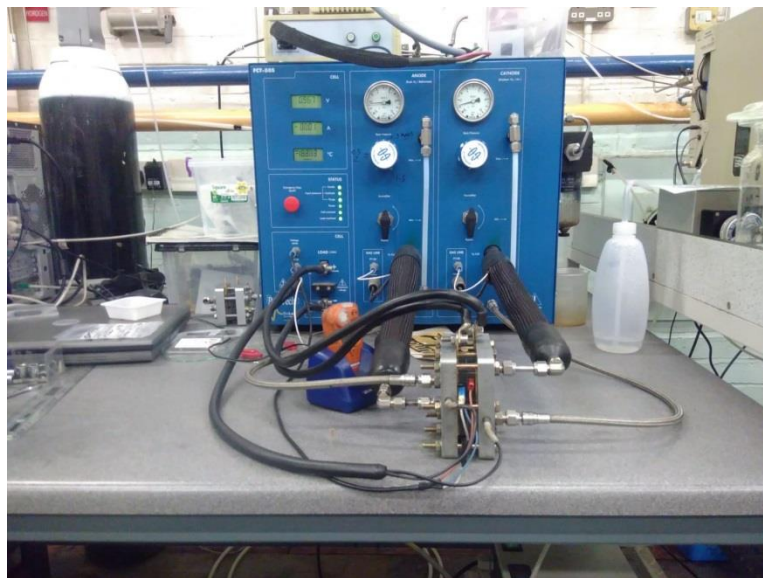
Figure 3.9: PaxiTech Biologic FCT-50S PEMFC test stand with single cell hardware.

Figure 3.10a shows the voltage and current outputs of a MEA with Pt/C electrodes when cycling between high (0.8 V) and low (0.4 V or as close to as possible) potentials to electrochemically clean the surface. The polarisation curve acquisition consisted of galvanostatic measurements as outlined in Table 3.1 and shown in Figure 3.10b. The potential and current in the last 25 s of each step was averaged to plot the polarisation curve in Figure 3.10c. EIS was run at 30 mA cm^{-2} with amplitude 72 mA (for 16 cm^2 MEA) in the frequency range of 10 kHz–0.1 Hz. The real impedance value at the high frequency intercept was taken as the internal resistance to correct the O_2 polarisation curve and the H_2 crossover current was also added onto the polarisation curve (acquisition method described shortly). The correction is also shown in Figure 3.10c. The current at 0.9 V was taken for mass and specific activity calculations.
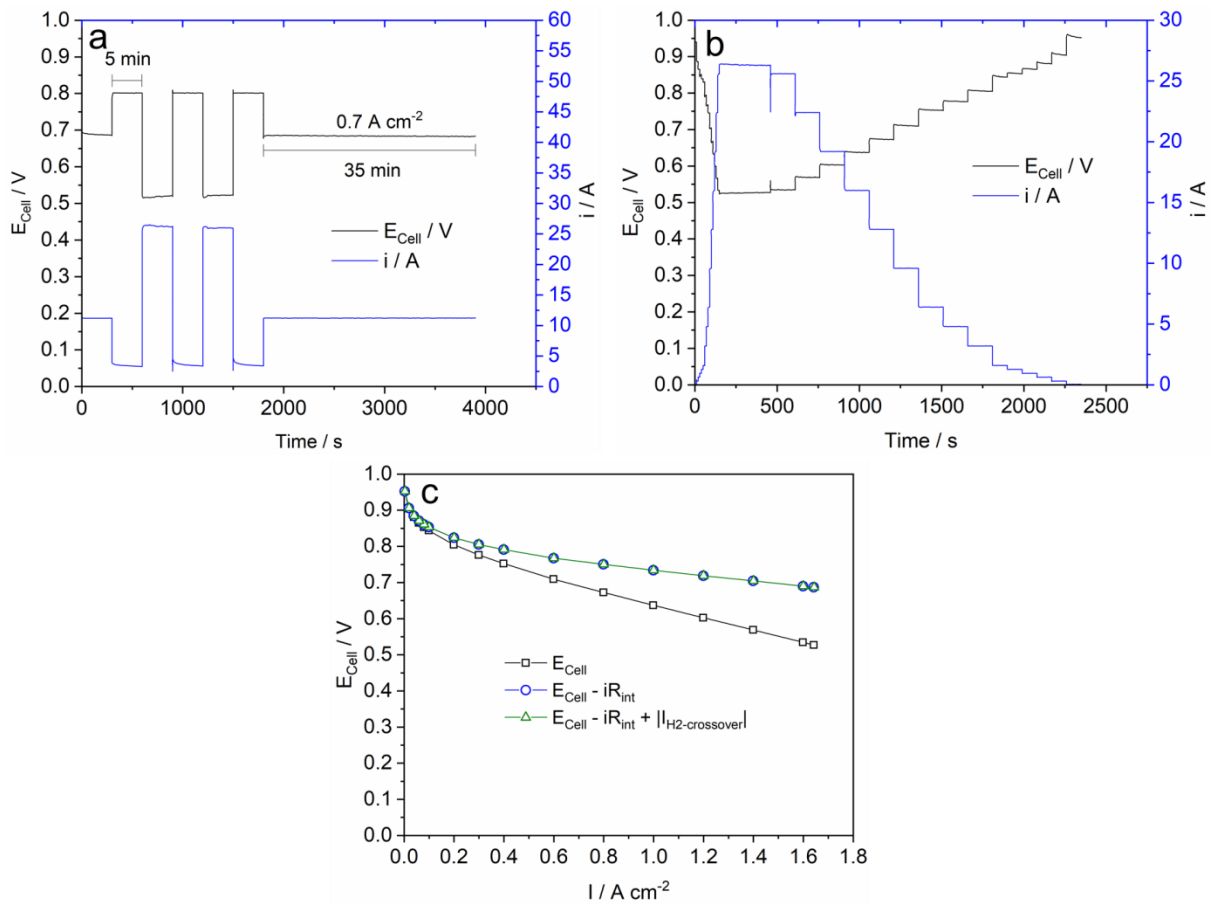
Figure 3.10: Data for a MEA with Pt/C electrodes showing **(a)** the break in procedure, **(b)** polarisation curve acquisition and **(c)** internal resistance and H_2 crossover corrections made on the O_2 polarisation curve.

Table 3.1: The protocol to acquire polarisation curves.

Step #	I / A cm^{-2}	Time / s	Step #	I / A cm^{-2}	Time / s
1	0.00	10	18	1.80	150
2	0.02	10	19	1.60	150
3	0.04	10	20	1.40	150
4	0.06	10	21	1.20	150
5	0.08	10	22	1.00	150
6	0.10	10	23	0.80	150
7	0.20	10	24	0.60	150
8	0.30	10	25	0.40	150

9	0.40	10	26	0.30	150
10	0.60	10	27	0.20	150
11	0.80	10	28	0.10	90
12	1.00	10	29	0.08	90
13	1.20	10	30	0.06	90
14	1.40	10	31	0.04	90
15	1.60	10	32	0.02	90
16	1.80	10	33	0.00	90
17	2.00	150			

For cathode CV and the measurement of the hydrogen crossover, the cathode gas was switched to N_2 and the potential held at 0.6 V for 1 hr. An EZstat-Pro system (NuVant Systems) was used for these tests where initially 6 cleaning CVs were conducted in the potential range of 0.05–1.2 V vs. RHE at 50 mV s^{-1}, followed by 3 CVs at 20 mV s^{-1}, which were used for Pt surface area measurements. The potential was then held at 0.5 V vs. RHE for 30 mins and the final current value taken as the hydrogen crossover current.

The polarisation curves of the MEAs under realistic automotive application conditions were recorded with the cathode/anode conditions as below: air/H_2, 2.3/2.5 bar absolute pressure, 1.3/1.5 stoichiometry and 30%/50% RH, respectively. Cell break in and polarisation acquisition were conducted with the same procedure as for the O_2 tests. EIS was recorded in the frequency range 10,000–0.1 Hz at 30 mA cm^{-2} (72 mA amplitude), 0.65 V (10 mV) and 0.5 V (10 mV).

3.3.6. Accelerated stress testing (AST) of the MEAs

AST was performed to evaluate the electrode stability. The gas settings were changed back to those used for the N_2 testing and 3000 CV cycles were run in the potential range of 0.6–1.2 V vs. RHE at 100 mV s^{-1}. Performance testing after AST followed the same method as in Section 3.3.5.

4. PtNi nanowires supported on carbon as electrocatalysts for oxygen reduction reaction

Some data has been re-analysed and acquired since publication

This chapter focuses on developing a method for alloying Ni into Pt nanowires (NWs) in a way that is translatable to other Pt structures and distributions, such as Pt NW array electrodes. The method employed is impregnation with subsequent thermal annealing. The effects of the thermal treatment temperature on the structure and morphology of the catalysts is evaluated, and the resultant oxygen reduction reaction (ORR) catalytic activities and single PEMFC performance are discussed.

4.1. Introduction

In Chapter 2 it was shown that the alloying of Pt with transition metals e.g. Ni and the extension of highly active crystal facets in 1D Pt nanostructures have both been confirmed as effective methods of improving the catalytic activity of Pt towards the ORR. Therefore, by combining both approaches into 1D PtM alloy nanostructures, ultra-high ORR catalytic activities can potentially be obtained. For example, Huang and co-workers have refined a solvothermal method for synthesising highly active PtNi NW/C for a variety of electrochemical reactions [110,112,113]. Their catalysts reached a mass activity of 3.96 A mg_{Pt}^{-1} using the half-cell electrochemical measurements in 0.1 M $HClO_4$ [110]. However, as of now, no result has been reported for this type of 1D PtNi electrocatalyst using the PEMFC single cell test. Single cell testing of such novel catalysts is increasingly important because of a well-known disparity between the catalytic activities recorded using the single cell test and the liquid half-cell measurement (i.e. RDE) [23]. A lack of understanding surrounding this is preventing such catalysts to becoming of practical use for commercial PEMFCs. In an example to stress the importance of proceeding to single cell PEMFC tests, Pivovar and co-workers used the spontaneous galvanic displacement of Pt on commercial Ni NWs to synthesise a catalyst with mass activity 0.92 A mg_{Pt}^{-1} [141]. Later work then focused on adapting these catalysts for use in PEMFCs by means of employing thermal treatment [11] and acid leaching techniques [170]. However, despite improvements, achieving high

performance in a single cell has been difficult due to the initial high Ni content causing serious contamination of the surrounding ionomer [171].

Previously, Du and co-workers demonstrated that a Pt NW array GDE, produced by a very simple wet chemical reduction of chloroplatinic acid can outperform a commercial Pt/C GDE in a working PEMFC as a result of an increased intrinsic catalyst activity and reduced mass transport limitations [32,35]. Inspired by the impressive increases in the catalytic activities to the ORR by alloying Pt with Ni, further enhancements are hypothesised for a similar NW array but with a Pt_3Ni alloy in place of pure Pt. While the aforementioned PtNi NW preparation methods have been shown to give highly active catalysts to the ORR, such approaches are difficult to adapt for NW array formation without sacrificing simplicity and scalability in the approach. Therefore, the development of a simple method of impregnating and annealing Ni into pre-existing Pt NWs supported on Vulcan XC-72R to form Pt_3Ni NWs, for the later adaption to Pt NW arrays forms the core objective of this work. A similar method has been shown before by Elvington *et al.* who reported improved specific activity of PtNi NWs supported on carbon nanotubes (CNTs) in comparison to the pure Pt control after Ni was impregnated and annealed into the Pt structure at 200°C [172]. However, the use of hydrazine monohydrate is highly toxic and so $NaBH_4$ was favoured as the reducing agent to then impregnate the surface of the NWs with Ni. To induce the surface segregation of Pt and thus alloying of the Ni, thermal annealing in a reductive atmosphere (4% H_2/Ar) is employed and the effects of temperature and duration of annealing on morphology, degree of alloying, catalytic and single cell behaviour are discussed in detail expanding on this method towards PtNi NWs.

4.2. Morphology Changes during the Thermal Annealing

To visualise the synthesised Pt and PtNi NW/C samples as well as to evaluate morphological changes during the thermal annealing, transmission electron microscopy (TEM) analysis was performed. Figure 4.1 shows the Pt NW/C catalysts initially synthesised by the formic acid reduction method. The images show that most of the Pt NW formation occurred in large, cubically shaped agglomerates with an average size of about 120 nm on the diagonal. Such agglomeration has been reported before on pure carbon supports and is thought to result from an underlying cubic seed whose facets provide the anchoring sites for Pt growth [165]. Some individual wires on the carbon support can still be seen amongst various particles which form in the early hours of the synthesis when reactant concentration is high [107]. While the agglomeration is known to reduce the ECSA of the catalysts and is the primary reason for the modest mass activities reported later in this chapter, the decision was made to prepare all Pt NW/C and PtNi NW/C catalysts in this study from the same large initial batch of the Pt NW/C catalysts. Therefore, whilst compromising catalytic performance, the trends in activity in this work can reliably be attributed to the control factors such as annealing temperature and time. The NWs within the agglomerates were found to have an average diameter of 3.40 nm, as expected from previous works [107,108]. From Figure 4.1d an inter-lattice spacing of 0.22 nm was also found, indicating NW growth in the <111> crystallographic direction and thus the preferential exposure of facets highly active towards the ORR.
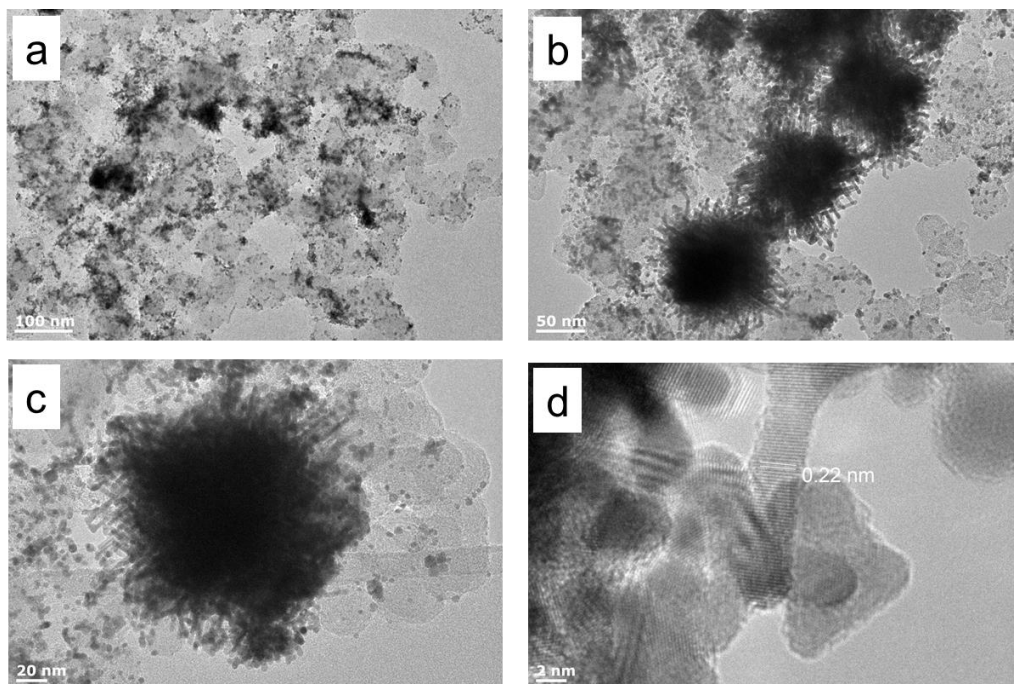
Figure 4.1: (a)–(d) TEM images of Pt NW/C catalysts.

Figure 4.2 shows the TEM images of the NWs upon impregnation of Ni (PtNi NW/C). Similar agglomerates to the Pt NW/C sample were observed with distinguishable NWs both singular on the carbon support and protruding from the agglomerate surface. On addition of Ni, the average diameter of the wires was found to be slightly higher than Pt NWs at 3.59 nm but the inter-lattice spacing remained at 0.22 nm, indicating no measurable lattice contraction for this sample.
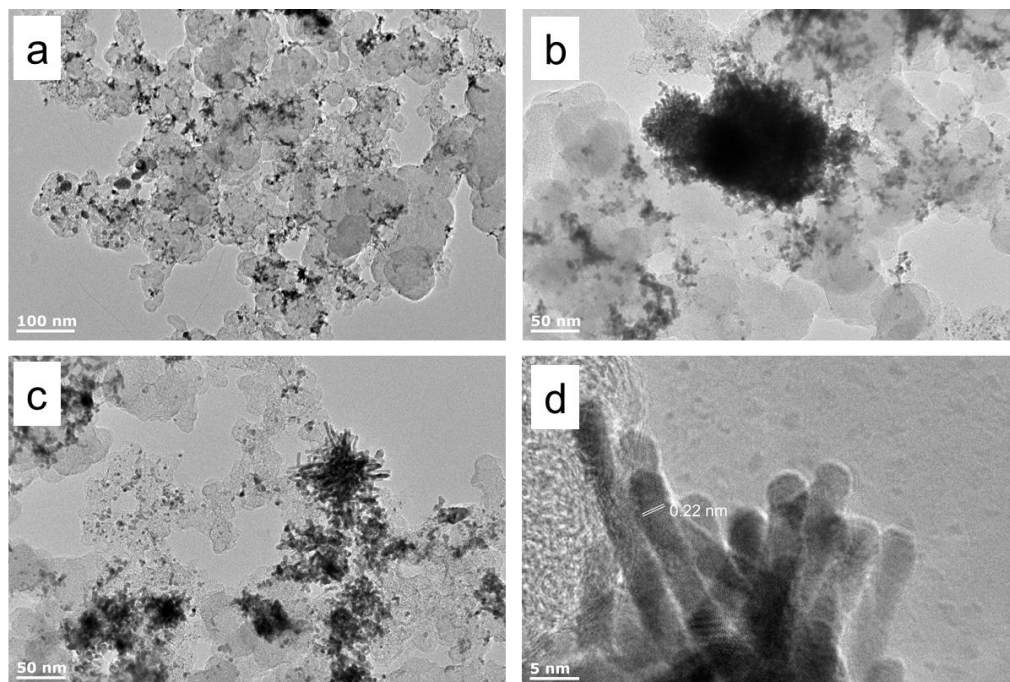
Figure 4.2: (a)–(d) TEM images of PtNi NW/C catalysts.

Both Pt NW/C and PtNi NW/C were annealed at temperatures of 150, 250 and 350°C for 24 hours and the change in morphology at these low annealing temperatures is significant. Figure 4.3 shows the changes to the Pt NW/C and PtNi NW/C samples after annealing at these different temperatures. Even at the lowest temperature of 150°C, slight sintering was observed for the Pt NW/C catalysts (Figure 4.3a) where some agglomerates had lost the protruding NWs to form Pt bulk crystals, and the NWs left over had grown in diameter to 5.06 nm. At 250°C and 350°C (Figure 4.3b and 4.3c, respectively) no NWs were present indicating a high degree of sintering. Figure 4.3c indicates that the agglomerates had also begun to coalesce resulting in even larger bulk structures. For the PtNi NW/C sample, after annealing at 150°C (Figure 4.3d) the NW structure appears much the same as the catalysts prior to annealing with an average NW diameter of 3.56 nm. After annealing at 250°C the vast majority of PtNi NWs had sintered. However, in contrast to the Pt NW catalyst, instances of NWs were observed with an average diameter of 8.58 nm (Figure 4.3e). As seen in Figure 4.3f, at 350 °C all of the PtNi NW/C catalysts had sintered into particles indicating that

despite a higher thermal stability for the PtNi NW/C catalyst in comparison to the Pt NW/C, the ultra-high annealing temperatures of up to 900°C used to alloy PtM nanoparticles cannot be used for the ultrathin NWs presented here if the morphology is to be retained [173,174]. This hampers the degree that Ni can segregate into the Pt NW structure. However, Pt alloy skin structures have been shown to be more active in comparison to bulk alloys where Ni enrichment in the second layer provides the greater weakening of the Pt-OH$_{ads}$ bond [87,175,176].
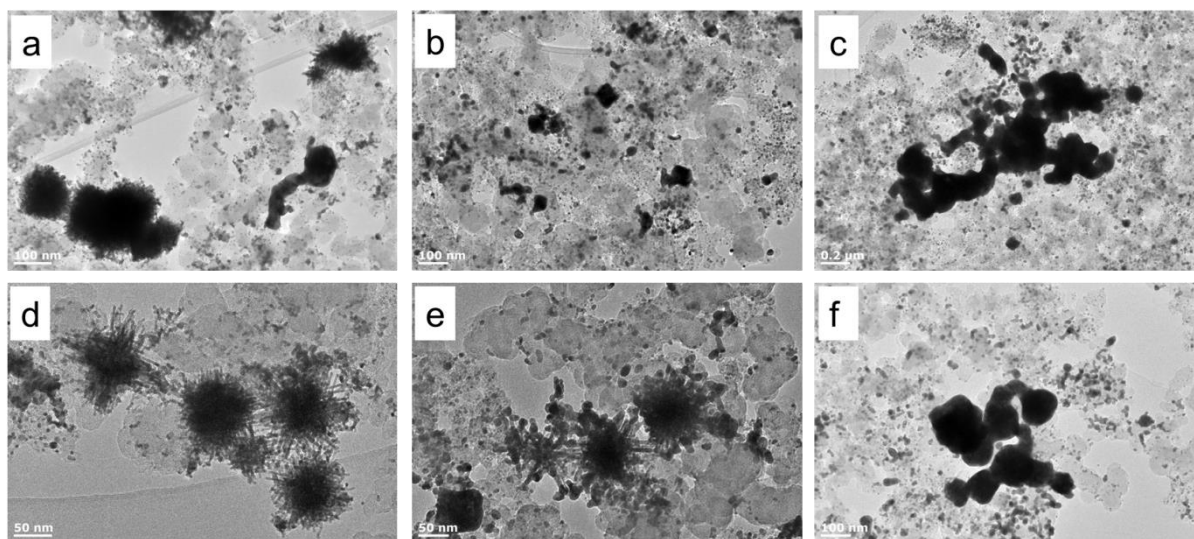
Figure 4.3: TEM images of Pt NW/C annealed for 24 hrs at **(a)** 150°C, **(b)** 250°C, **(c)** 350°C and PtNi NW/C annealed for 24 hrs **(d)** 150°C, **(e)** 250°C, **(f)** 350°C.

STEM-EDX mapping was conducted on the PtNi NW/C catalysts annealed at 150°C (Figure 4.4a–c) and 350°C (Figure 4.4d–f). However, the low Ni content means that this technique can only indicate the successful incorporation of Ni into the Pt structures by use of NaBH$_4$. Pt$_x$Ni was measured with values of x = 7.89 and 3.63 for samples annealed at 150 and 350°C, respectively. The high dependency of this technique on the spot area, material size and acquisition number means that ICP-MS is favoured for obtaining the accurate Pt$_x$Ni composition.
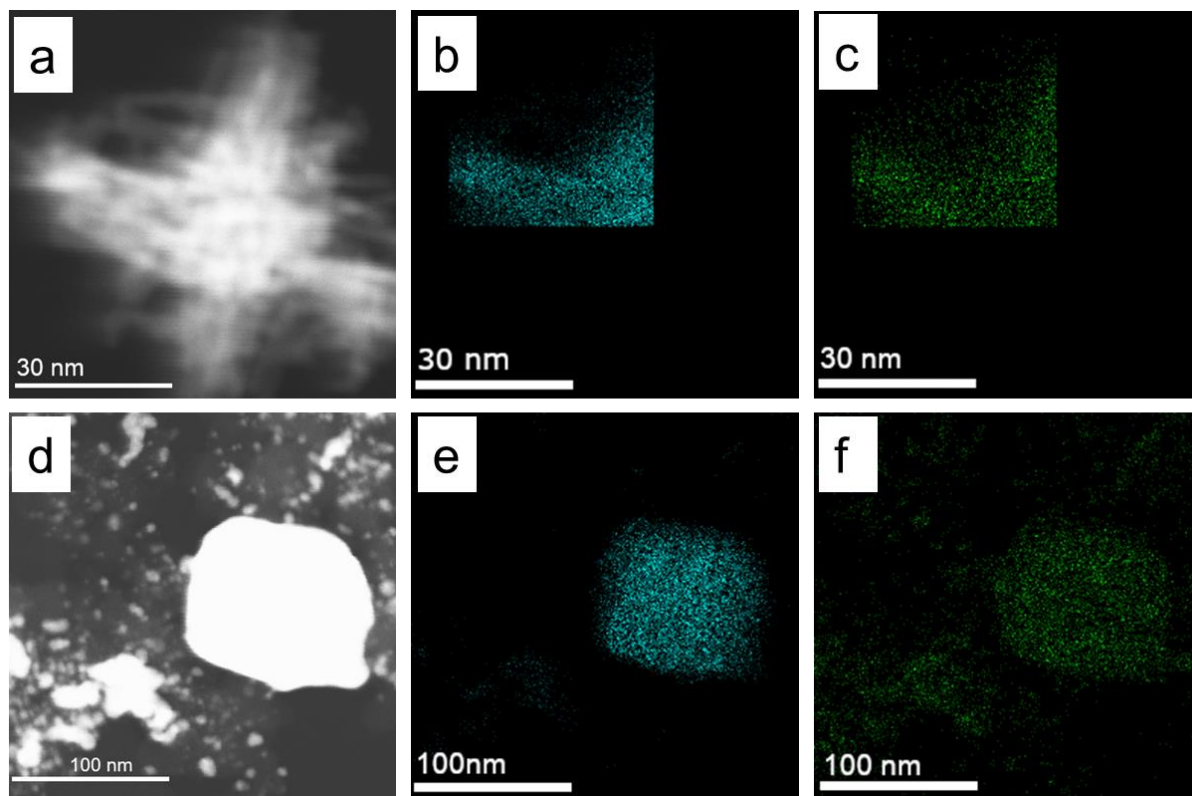
Figure 4.4: STEM images ((a) and (d)) and EDX mapping of Pt (Cyan (b) and (e)) and Ni (Green (c) and (f)) of **(a)–(c)** PtNi NW/C (150°C) and **(d)–(f)** PtNi NW/C (350°C).

Besides annealing temperature, the duration was also investigated. After annealing the PtNi NW/C at 150°C for 72 hrs, huge agglomerate structures were observed indicating a high degree of coarsening over the extended time period (Figure 4.5). While the average NW diameter remained low at 3.53 nm - indicating very high stability of PtNi NW/C at 150°C — the micron scale structures suggest that the coarsening is substantial at even this modest temperature. This knowledge is of importance if considering these catalysts for use in intermediate and high temperature PEMFCs which can run up to 180°C, as agglomeration could then overtake Ostwald ripening as the primary degradation mechanism [56,177].
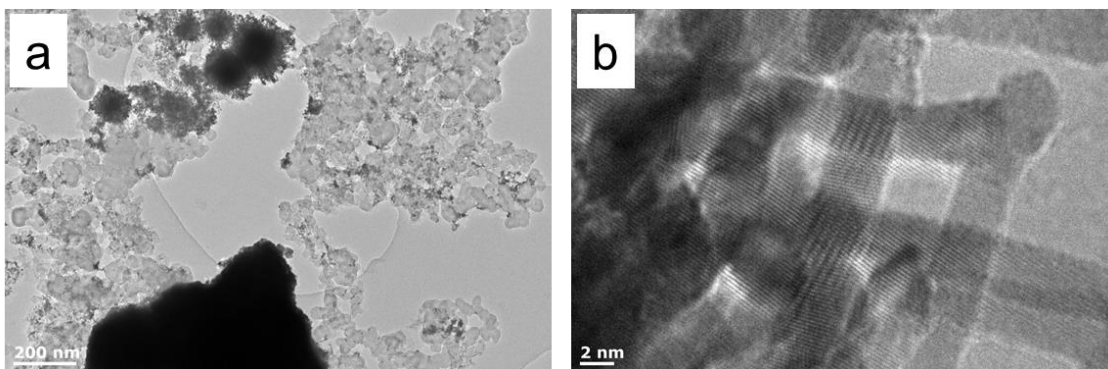
Figure 4.5: (a)–(b) TEM images of PtNi NW/C (150°C, 72 hrs).

Scanning electron microscopy (SEM) analysis was also conducted on the Pt NW/C catalyst to show the morphological change of the Pt NWs after thermal annealing at the higher temperature of 350°C for 24 hrs. Figure 4.6a shows that before thermal annealing the cubic formation of NWs has a spikey morphology where the wires protrude from the bulk's surface. These localised concentrations of Pt are not ideal for PEMFC operation where maximal Pt distribution is optimal for reactant mass transport, but are indicative of Pt NW growth at room temperature [32]. After annealing at 350°C, sintering of the NWs results in very smooth cubic particles of Pt (Figure 4.6b), which are later shown (Section 4.4) to have a 48% smaller surface area for a given Pt mass.
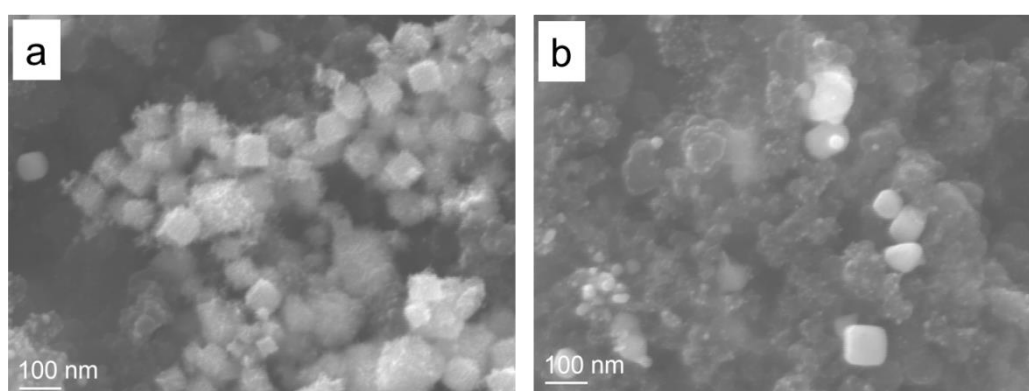
Figure 4.6: SEM images of **(a)** Pt NW/C and **(b)** Pt NW/C (350°C).

ICP-MS was used to accurately determine the Pt_xNi ratio in the catalysts: Table 4.1 shows the obtained Pt_xNi ratio for each catalyst with Ni in, as well as the Pt NW/C sample for a baseline. The baseline result shows minimal Ni contamination in the sample whereas the other results give an average Pt_xNi composition of $Pt_{2.7}Ni$ suggesting that the majority of Ni precursor was successfully reduced by the $NaBH_4$ giving a near optimal Pt_3Ni ratio for ORR performance [22,87,178].

Table 4.1: The Pt_xNi ratio as determined from ICP-MS.

Sample	Pt_xNi Ratio
Pt NW/C	1360.6
PtNi NW/C	2.5
PtNi NW/C (150°C)	2.7
PtNi NW/C (250°C)	3.0
PtNi NW/C (350°C)	2.5
PtNi NW/C (150°C, 72 hrs)	3.0

.

4.3. Degree of alloying and oxidation states of PtNi NW/C

To investigate the crystallographic nature of the synthesised catalysts and Ni alloying degree after thermal annealing, X-ray diffraction (XRD) was performed on the Pt NW/C and the PtNi NW/C catalysts after annealing at the different temperatures. All samples show the typical peaks that can be indexed to the Pt face centred cubic (FCC) structure (Joint Committee on Powder Diffraction Standards, JCPDS-04-0802), as indicated in Figure 4.7a. A positive peak shift in 2θ values for the PtNi NW/C catalysts can be clearly seen as the annealing temperature increases. As a result, using the well-defined (111) and (200) peaks, the lattice constant becomes smaller with the increase of the annealing temperature (Figure 4.7b). This lattice contraction is indicative of an increased alloying of Ni to Pt at the higher temperature

because it implies that the smaller diameter Ni atoms have successfully occupied Pt sites in the crystal lattice structure. The successful incorporation of Ni into the Pt NW structure is also suggested by the lack of Ni characteristic diffraction peaks in the spectra. Of importance to note is the fact that the observed shift in the lattice constant for the PtNi NW/C alloys here is much smaller than those reported in other studies [61,95], suggesting that the alloyed Ni remains close to the NW surface and is insufficient to obviously change the bulk lattice structure as also found by Elvington *et al.* [172]. For the longer annealing duration of 72 hrs at 150°C, the lattice parameter shifted to almost the same value as the PtNi NW/C annealed at 350°C for 24 hrs suggesting that a higher degree of alloying can be accomplished with an extended annealing duration.
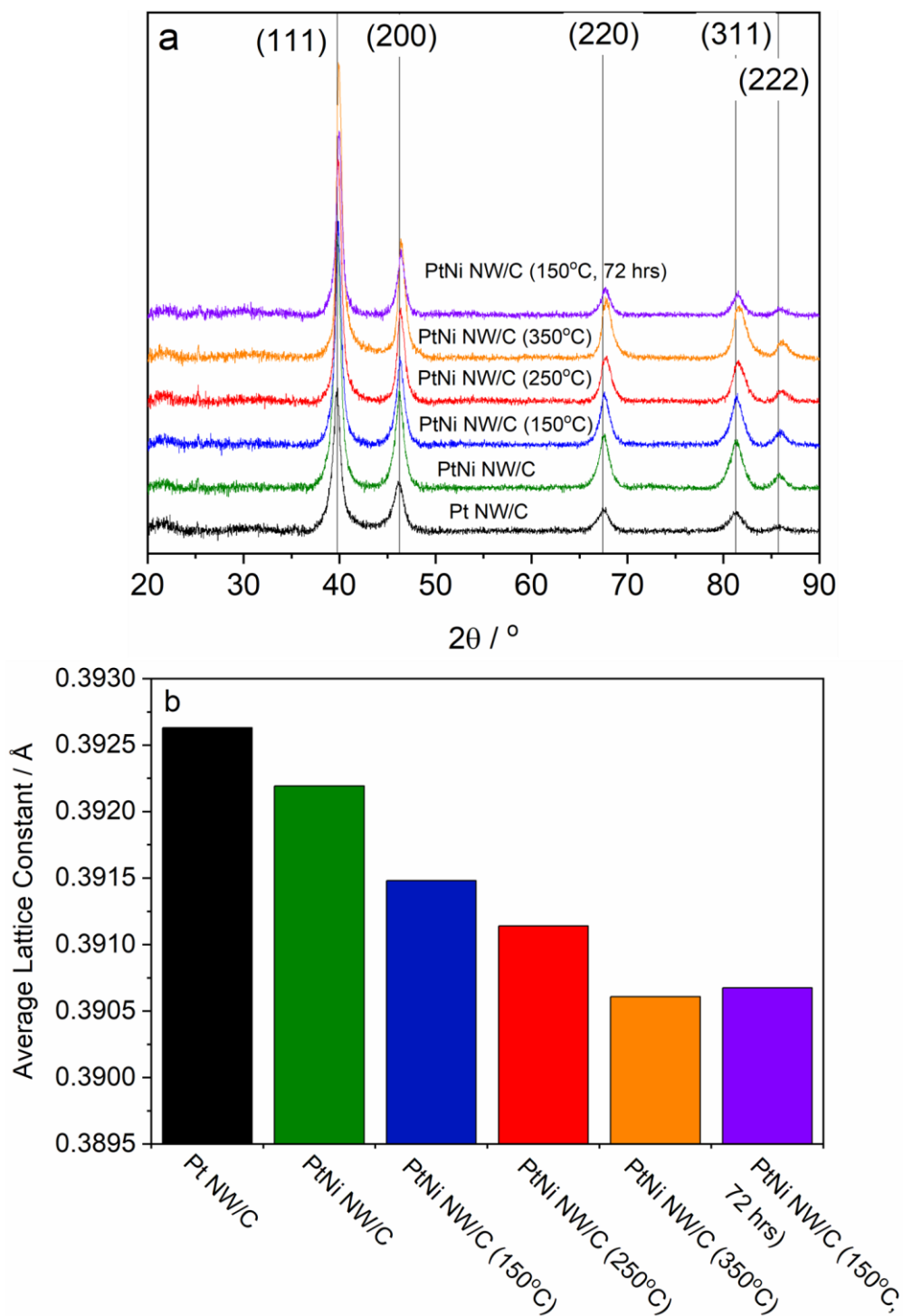
Figure 4.7: (a) XRD patterns of Pt NW/C and PtNi NW/C catalysts and **(b)** Average lattice constants calculated using the (111) and (200) peaks.

X-ray photoelectron spectroscopy (XPS) was conducted on the Pt NW/C and the PtNi NW/C catalysts so that the nature of the Pt and Ni species can be investigated. The prime difference in the survey spectra (Figure 4.8) is the presence of Ni 2p 3/2 and 1/2 spin orbital peaks in the binding energy (B.E.) range 845–890 eV. The intensity of these peaks for those catalysts containing Ni follows the order PtNi NW/C > PtNi NW/C (150°C) > PtNi NW/C (250°C) > PtNi NW/C (350°C). XPS resolution is highly surface sensitive and so this suggests that the Ni present is progressively more subsurface at the high annealing temperatures, supporting the XRD where the high annealing temperature induced a greater degree of surface segregation.
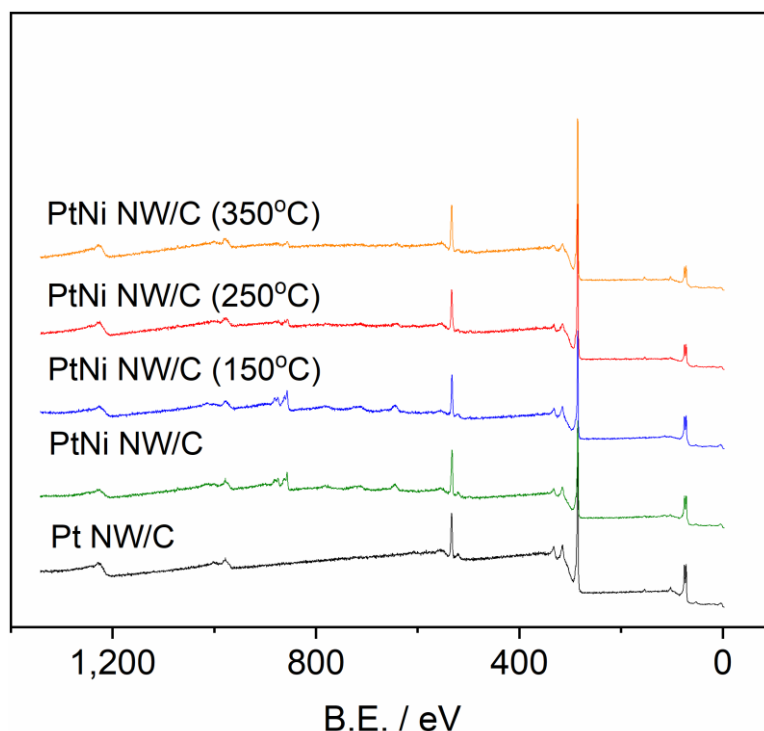
Figure 4.8: XPS survey scan of Pt NW/C and PtNi NW/C catalysts.

High resolution Pt 4f scans were conducted and are shown in Figure 4.9. Fitting of Pt XPS can be conducted with either the inclusion of Pt(II) and Pt(IV) peaks or through a single asymmetric peak attributable to metallic Pt. While the prior method was adopted for the associated publication [179], throughout this thesis it was found for the NW catalysts that it is

more appropriate to fit the peaks with the two Pt metallic peaks associated with the 7/2 and 5/2 spin states with spin-orbit coupling ≈ 3.33 eV [180,181]. At the high annealing temperatures it was found that the Pt peaks shifted to more negative binding energies, from 71.58 eV for the PtNi NW/C to 71.01 eV for the PtNi NW/C (350°C). This shift can be ascribed to alteration of the Pt electronic structure [182] or perhaps the reduction of any Pt oxide contribution to the single peak fitting. Within Pt 4f region, the overlap of Ni 3p peaks are also observable for all of the PtNi NW/C catalysts, and similar to the Ni 2p region in the survey spectra, decreased in intensity with higher annealing temperatures.
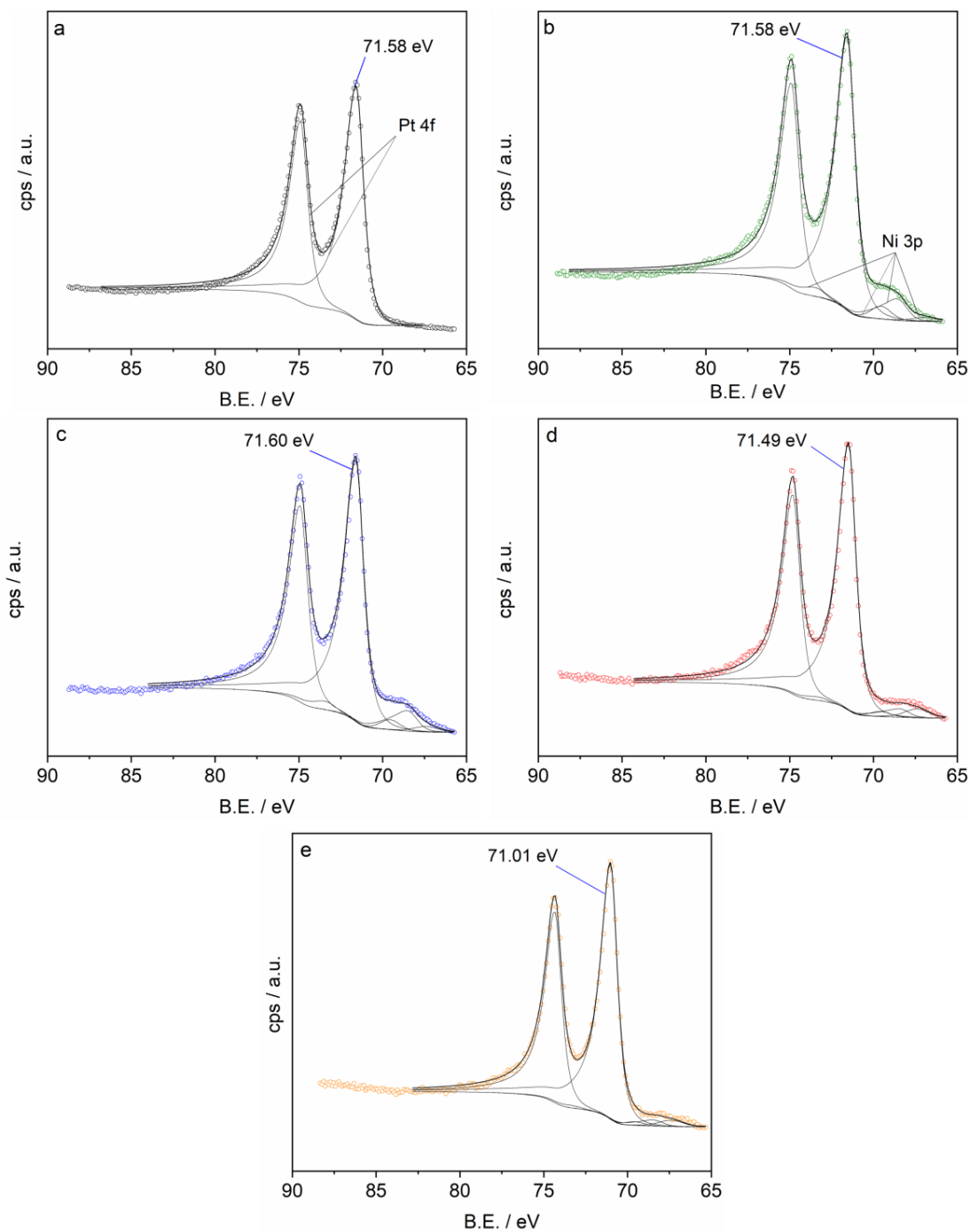
Figure 4.9: Pt 4f XPS spectra for **(a)** Pt NW/C, **(b**) PtNi NW/C, **(c)** PtNi NW/C (150°C), **(d)** PtNi NW/C (250°C) and **(e)** PtNi NW/C (350°C).

High resolution Ni 2p spectra were also obtained. Previously, fitting was conducted with peaks for metallic Ni, NiO, Ni(OH)$_2$, Ni(OOH) and a generic Ni satellite peak [59,179]. This has been simplified here, with fitting including just the Ni and more generalised Ni^{2+} species

with their respective satellite peaks (Figure 4.10). With this simplified fitting it can more clearly be seen that at the high annealing temperatures, the proportion of Ni to Ni^{2+} visibly increased suggesting a greater degree of reduction from the H_2/Ar gas during the annealing process.
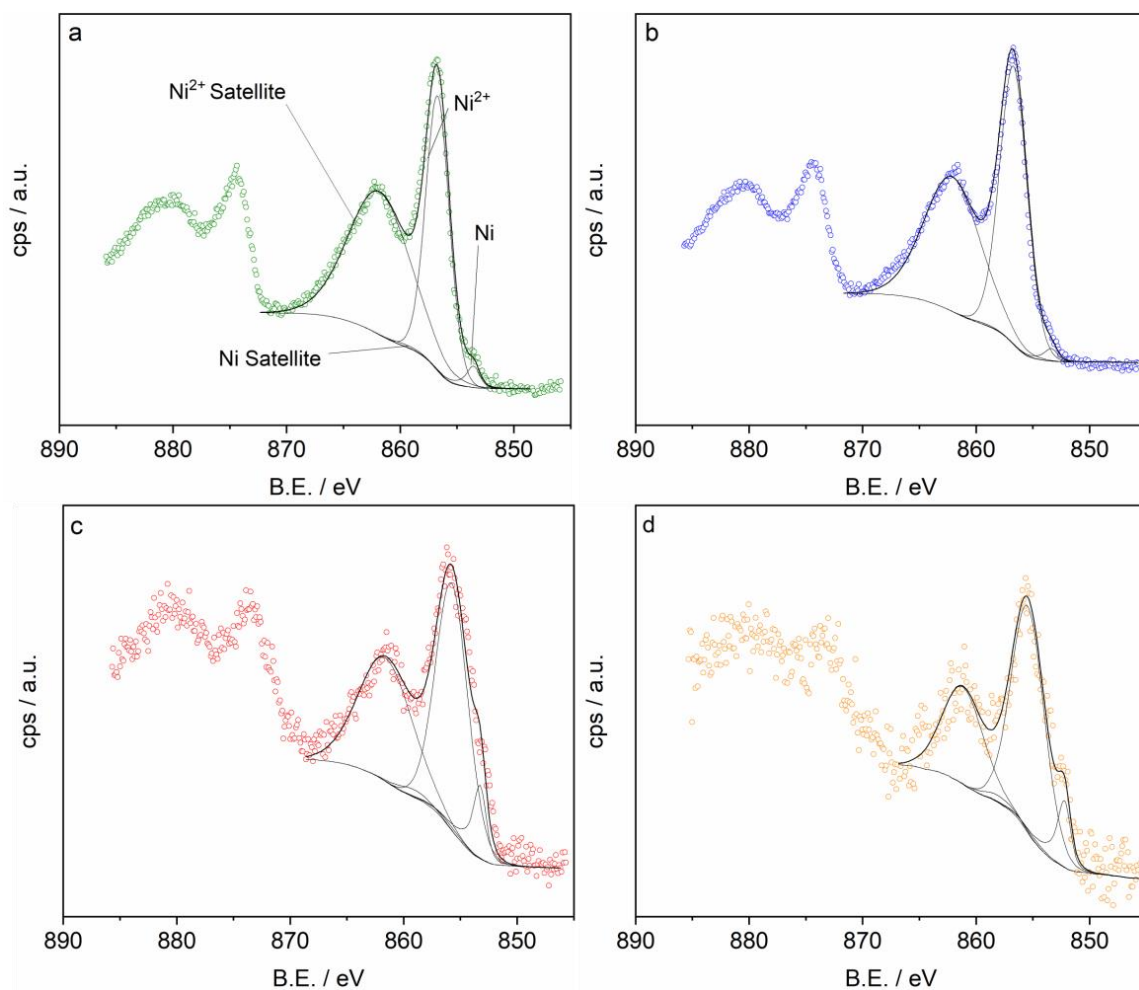
Figure 4.10: Ni 2p XPS spectra for **(a)** PtNi NW/C, **(b)** PtNi NW/C (150°C), **(c)** PtNi NW/C (250°C) and **(d)** PtNi NW/C (350°C).

XPS analysis was also conducted on PtNi NW/C after annealing at 150°C for 72 hrs and the XPS spectra suggests little change in oxidation states compared to the catalyst annealed at 150°C for 24 hrs (Figure 4.11). Considering that the lattice contraction is close to that seen for the sample annealed at 350°C by the XRD pattern, it appears that Ni reduction does not

completely cause effective segregation and alloying even though it can assist in the process [87]. It is known that a few layers of Ni beneath the surface or Ni on the surface can present in its oxidised form when exposed to ambient conditions and thus it could be these species inducing the lattice contraction in the PtNi NW/C (150°C, 72 hrs) [174].
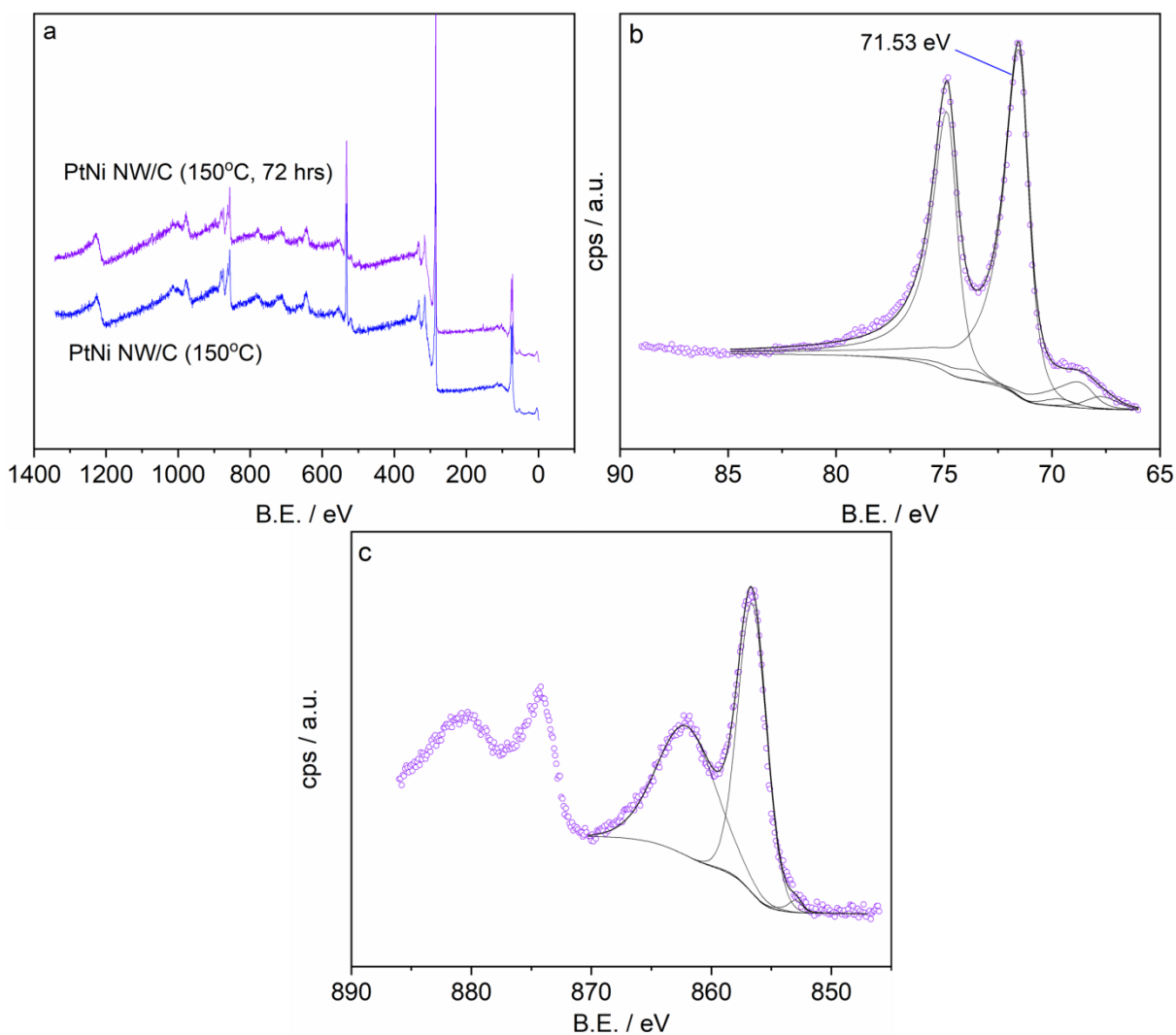
Figure 4.11: XPS spectra of PtNi NW/C (150°C, 72 hrs): **(a)** Survey spectrum including PtNi NW/C (150°C), **(b)** Pt 4f scan and **(c)** Ni 2p scan.

Thermogravimetric analysis (TGA) was run to evaluate the catalyst loading of the materials and to further evaluate the nature of Ni in the catalysts (Figure 4.12). For the PtNi NW/C

catalysts, an initial drop in residual mass was observed between 200–300°C which can be attributed to the decomposition of surface Ni hydroxide species [183]. The degree of this drop decreases with the increase of the annealing temperature coinciding with the drop of the Ni^{2+} proportion shown in the XPS analysis. With no clear hydroxide decomposition in the PtNi NW/C (350°C) catalyst, the residual masses of 61.0% for Pt NW/C and 64.3% for PtNi NW/C (350°C) (Pt loading of 58.4% assuming Pt_3Ni), indicates that the Pt loadings of 60% for Pt NW/C and 56.6% for PtNi NW/C (assuming Pt_3Ni) are valid.
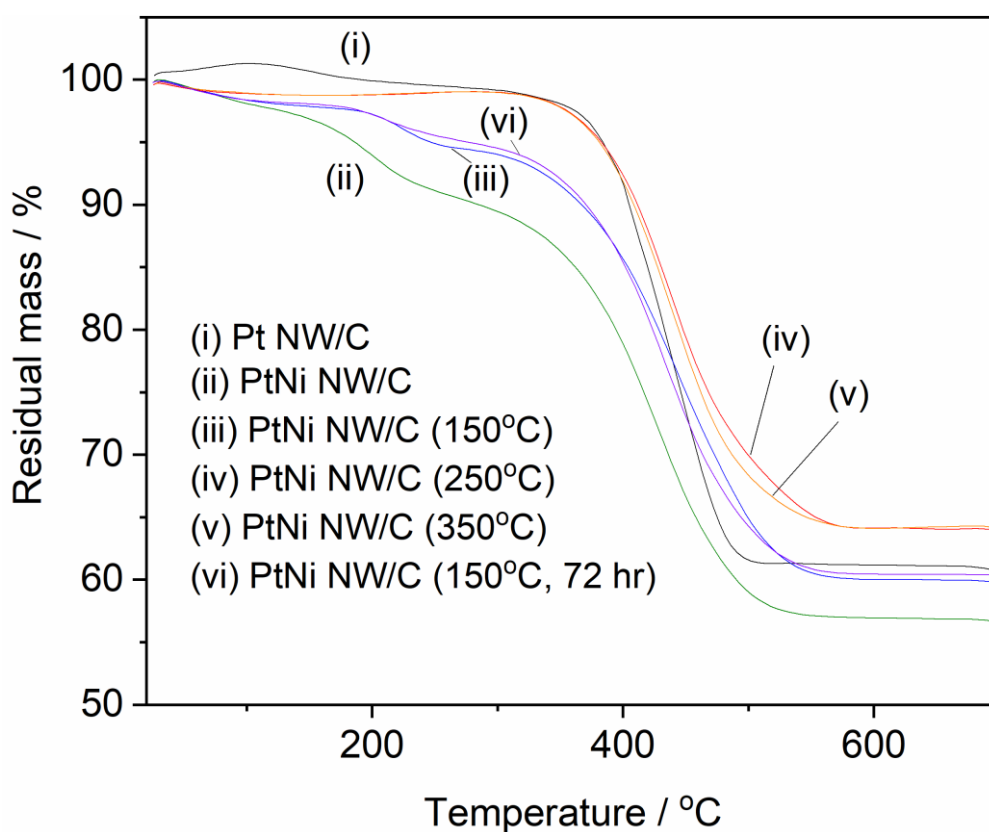
Figure 4**.12: Fast Fourier transform (FFT) 5 point smoothed TGA of Pt NW/C and PtNi NW/C catalysts.**

4.4. ORR Catalytic Activity Evaluation by Half-cell Measurements

To evaluate the inherent ORR catalytic activity of the synthesised catalysts, a half-cell RDE experiment was employed. It is important to note that while it is convention to use the mass

transport correction to obtain kinetic currents, a full Koutecky-Levich analysis was favoured in this work because the current at 0.9 V vs. RHE was frequently larger than the current at the half wave potential [167,184]. After the initial catalyst cleaning cycles, three CVs in the potential range of 0.05–1.2 V vs. RHE were run at 20 mV s^{-1} and the hydrogen desorption (H$_{des}$) region was used to evaluate the electrochemically active surface area (ECSA). Figure 4.13 shows the obtained ECSAs for the catalysts that did not undergo annealing alongside the obtained specific activities. For the commercial Pt/C nanoparticle catalyst, an ECSA of 85.7 m^2 g$_{Pt}$$^{-1}$ and a specific activity of 292 µA cm$_{Pt}$$^{-2}$ were obtained, meeting the expected standard and thus validating this test [167]. For Pt NW/C the heavy agglomeration seen in the TEM analysis resulted in a small ECSA of 13.1 m^2 g$_{Pt}$$^{-1}$. Surface Ni impregnation reduces this further to 8.0 m^2 g$_{Pt}$$^{-1}$ by the blocking of active Pt sites from the surface Ni hydroxide species, as previously indicated by the XPS analysis and TGA. Despite Ni mainly being present as hydroxides (and oxides), an enhanced specific activity of 769 µA cm$_{Pt}$$^{-2}$ was recorded for PtNi NW/C in comparison to 536 µA cm$_{Pt}$$^{-2}$ for Pt NW/C. While for Pt NW/C activity enhancements are attributable to the inherent benefits of the 1D morphology, even on the surface the Ni appears to contribute to a boost in ORR activity via the small lattice contraction observed in the XRD [46,99].
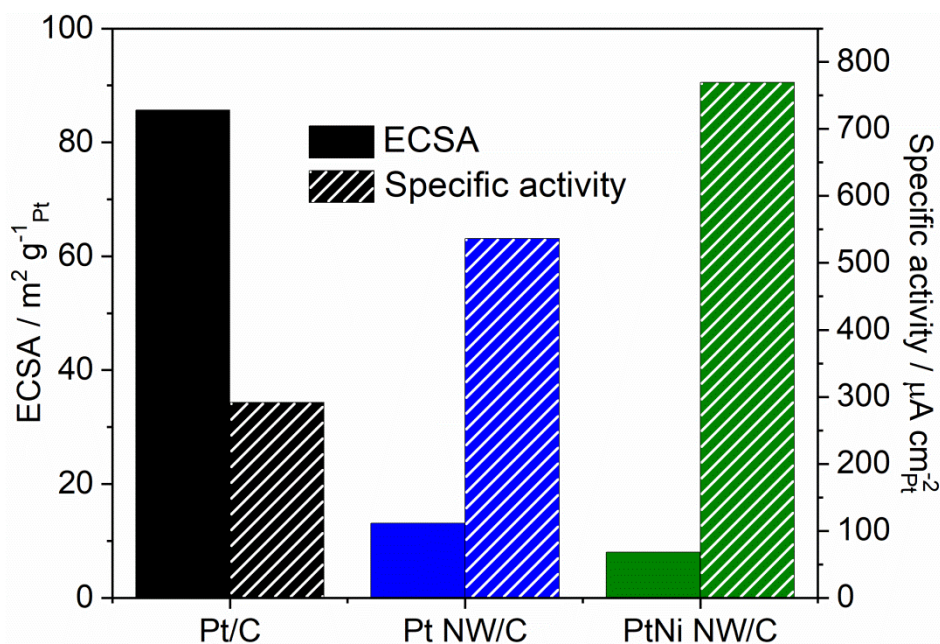
Figure 4.13: ECSA and specific activities for Pt/C, Pt NW/C and PtNi NW/C determined by RDE measurements.

With regards to the ECSAs after annealing, at 150°C the ECSA of PtNi NW/C increased to 11.1 m^2 g_{Pt}^{-1} (Figure 4.14). The surface segregation of Ni into the Pt would have freed some of the previously blocked catalytic sites resulting in this increase. After the extended annealing time of 72 hrs the coarsening resulted in a drop of ECSA to 9.3 m^2 g_{Pt}^{-1}. At higher annealing temperatures of 250 and 350°C, smaller ECSAs of 4.8 and 4.2 m^2 g_{Pt}^{-1} were recorded, respectively, as a result of the sintering process destroying the NW morphology and removing the access for reactants to catalytic sites originally between the wires. For Pt NW/C a similar progressive drop in ECSA was found for an increase of annealing temperature where values of 8.1, 7.6 and 6.1 m^2 g_{Pt}^{-1} were obtained for temperatures of 150, 250 and 350°C, respectively. The ECSAs of the PtNi NW/C catalysts at the high annealing temperatures were lower than the Pt NW/C counterparts. A contributing factor could be underestimation of the ECSAs due to the modification of the Pt surface electronic properties whereby other adsorption/desorption processes may overlap with the hydrogen desorption peak and the capacitive charging may not hold the same charge as on polycrystalline Pt

[166]. However, it is thought that surface hydroxides/oxides of Ni blocking Pt surface sites is the more likely cause.
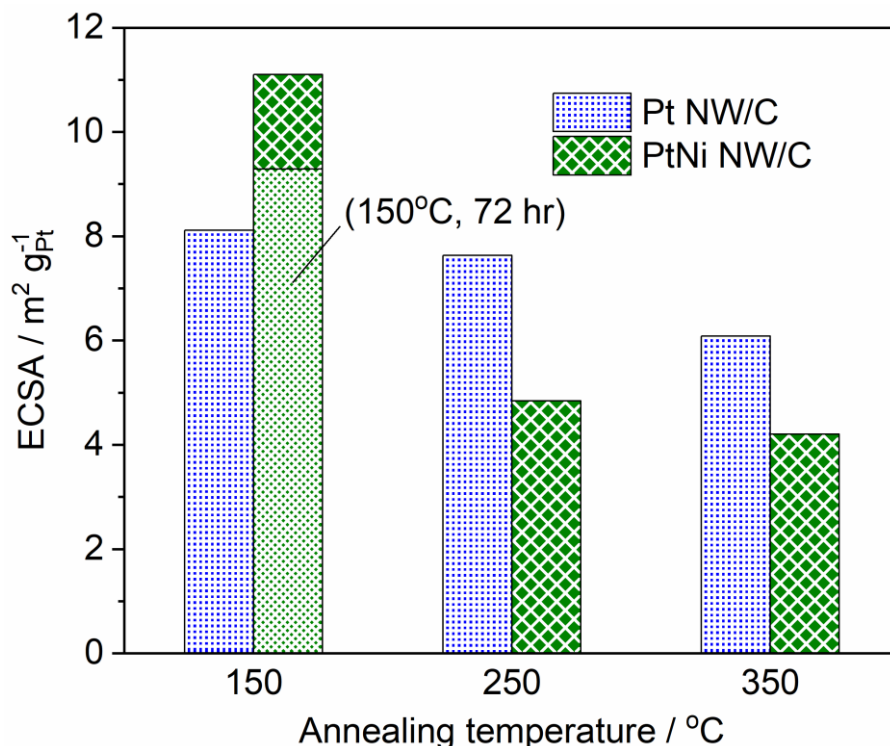
Figure 4.14: ECSA for the annealed Pt and PtNi NW/C catalysts as determined from the RDE measurement.

After thermal annealing at 150°C for 24 hrs, the specific activities of Pt NW/C and PtNi NW/C increased to 808 and 1123 $\mu A\ cm_{Pt}^{-2}$, respectively (Figure 4.15). The increase for the Pt NW/C catalyst can be attributed to the sintering of defect sites giving a more consistent crystalline surface. However, at 250°C a smaller specific activity even than the sample prior to annealing was found (561 $\mu A\ cm_{Pt}^{-2}$) presumably due to the loss of NW morphology and the specificity of the exposed facets. The highest specific activity for the Pt NW/C catalysts was found after annealing at 350°C with a value of 968 $\mu A\ cm_{Pt}^{-2}$ and is most likely due to the particle size effect where larger particles have a smaller proportion of corner and defect sites in comparison to the more active crystal faces than smaller sized particles [53].
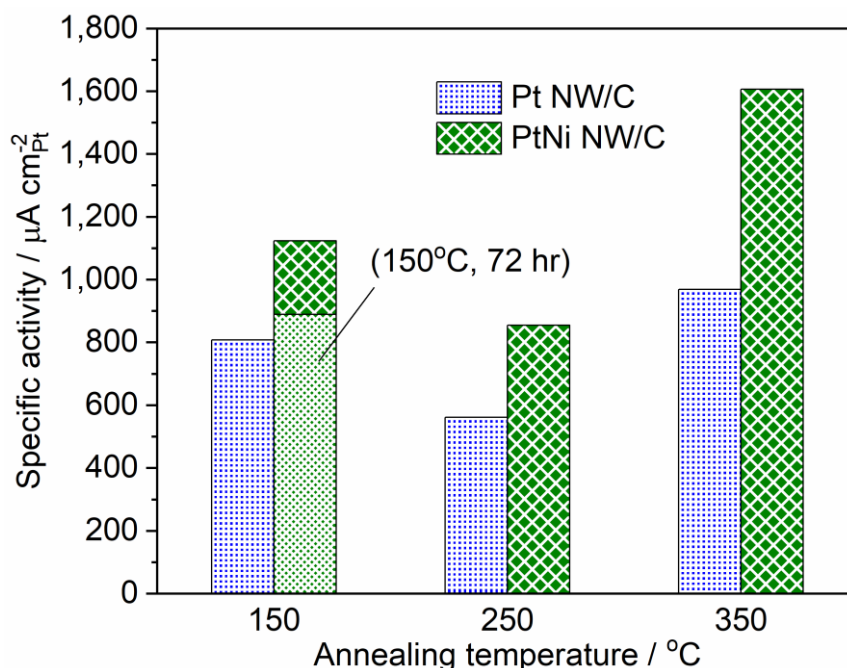
Figure 4.15: Specific activities for the annealed Pt and PtNi NW/C catalysts as determined from the RDE measurement.

For the PtNi NW/C catalysts, a similar trend to the Pt NW/C catalysts was seen for the specific activities where after 24 hrs annealing at 150, 250 and 350°C activities of 1123, 855 and 1606 μA cm_{Pt}^{-2} were measured, respectively. All PtNi NW/C catalysts demonstrated higher specific activities in comparison to the Pt NW/C equivalents showing that the slight alloying induced by the thermal annealing procedure increased the inherent catalytic activity of the NWs towards the ORR. Notably the differential between PtNi NW/C and Pt NW/C increased with annealing temperature as a result of the increased degree of alloying. For the PtNi NW/C annealed at 150°C for 72 hrs a specific activity of 889 μA cm_{Pt}^{-2} was obtained in spite of the increased degree of alloying suggested by the XRD analysis. Even though consistency in thin-film preparation was ensured, the current at 0.9 V is not completely absent of local mass transport limitations as is required for the kinetic currents to truly represent the catalytic activity of the NWs [185]. It could therefore be that the agglomeration

of the NWs after extended annealing times induced a greater mass transport resistance in the thin film and thus reduce the apparent activity of the catalyst surface.

The mass activities recorded for all NW catalysts were low in comparison to the commercial Pt/C (TKK) nanoparticle catalyst (Figure 4.16). This mainly derives from the much lower ECSAs than that previously reported for Pt NW/C resulting from the large batch synthesis, in addition to the lower surface/bulk ratio in comparison to nanoparticles [108]. Comparing different NW catalysts however shows a slight increase in the mass activity for the catalysts with high annealing temperatures. A 1.78-fold mass activity improvement was measured for the PtNi NW/C catalyst annealed at 150°C for 24 hrs in comparison to the initial Pt NW/C catalyst. This is due to the improvement in the specific activity and the retention of ECSA by the resistance to sintering at 150°C. The coarsening process and the lower specific activity for the PtNi NW/C catalyst annealed for 72 hrs resulted in a smaller mass activity than PtNi NW (150°C), but it is still higher than that of the Pt NW/C catalyst. These RDE experimental results therefore show that PtNi NW/C annealed at 150°C for 24 hrs can be a promising candidate for the preparation of high performing PtNi NW PEMFC electrodes.
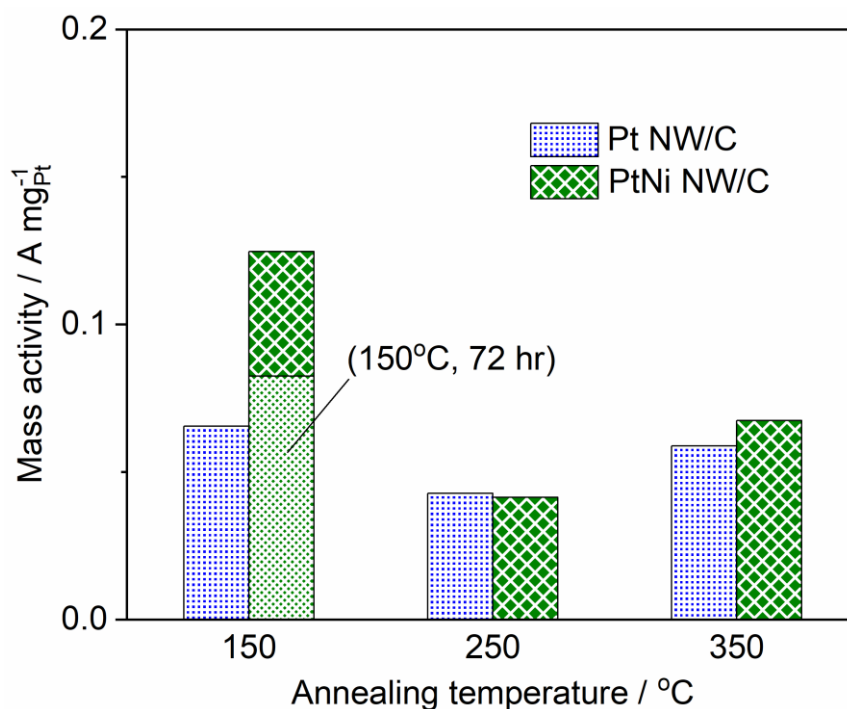
Figure 4.16: Mass activities for the annealed Pt and PtNi NW/C catalysts as determined from the RDE measurement.

4.5. Performance of the PtNi NW/C Catalysts in the PEMFC Single cell test

A key component for the development of PEMFC catalysts is to test them in the single cell where the effects of the ionomer, membrane and porosity are included. All of the as-prepared catalysts above were prepared into 16 cm^2 GDEs, hot pressed into MEAs with commercial GDEs as the anode and tested in the single cell PEMFC. In the single cells the OCP of all GDEs were comparable to each other and notably the specific activity of the catalysts at 0.9 V (in H_2/oxygen under DOE testing conditions) were not enhanced by the inclusion of the Ni (Figure 4.17). Therefore, in this work the disparity between activities recorded using the RDE measurement and MEA test for PtNi catalysts is also found.
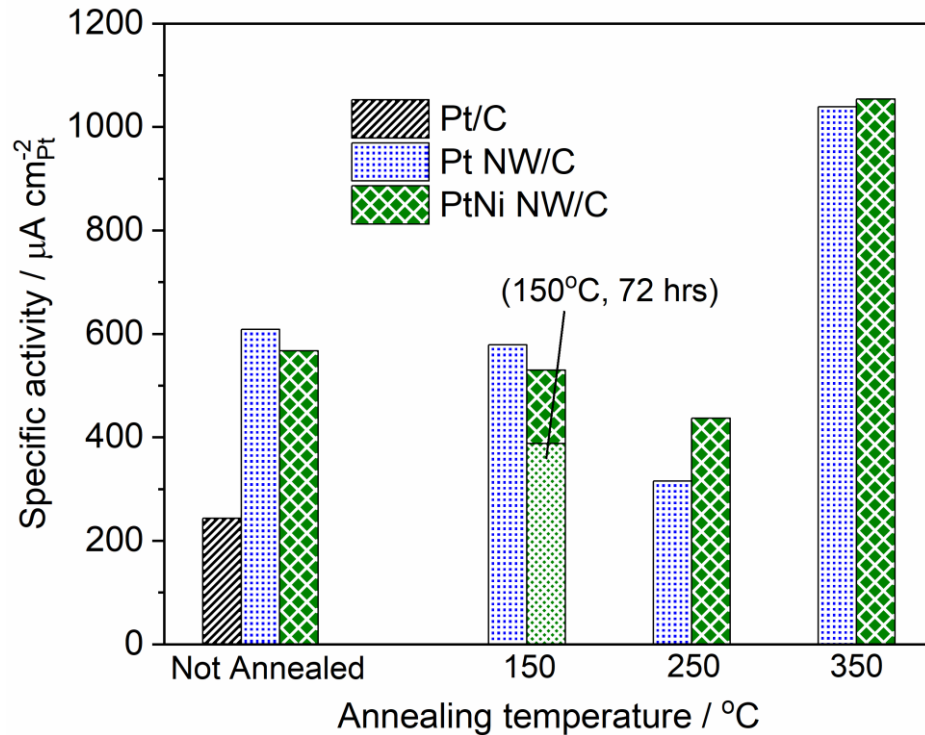
Figure 4.17: The specific activity at 0.9 V of the Pt/C, Pt NW/C and PtNi NW/C MEAs under DOE testing conditions.

Some of the explanation can be derived from the polarisation performance curves where there was a progressively higher drop in the cell potential on increase in the current density for the PtNi NW/C catalysts in comparison to the Pt NW/C catalysts (Figure 4.18). For the Pt NW/C catalysts it appears that the sintering and coarsening processes did not change the single cell performance as much as might be expected. When considering the agglomeration of the NWs, the Nafion® ionomer in the catalyst layer (CL) is thought to be unable to access all of the NWs and so mass transport characteristics appear to be more dependant of the larger structure size and distribution than the spacing between the individual NWs [163]. This result reiterates the importance of the NW dispersion in increasing overall PEMFC performance of 1D catalysts. This fact is illustrated further by the higher mass transport losses for the PtNi NW/C catalyst annealed at 150°C for 72 hrs in comparison to the sample

annealed for 24 hrs despite similar charge transfer resistances (Figure 4.19). The increased

coarsening despite similar NW diameters is the cause of this effect.
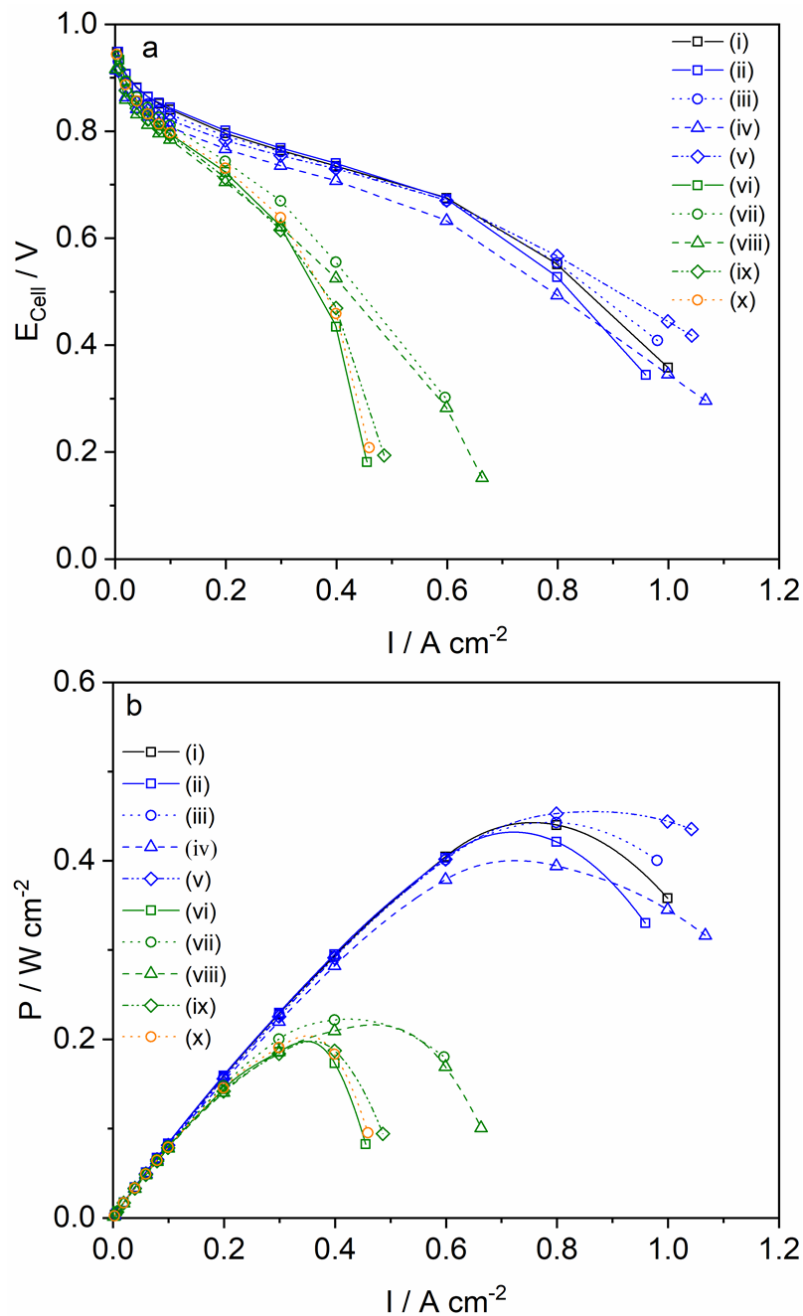
Figure 4.18: (a) Polarisation curves and **(b)** power density curves for the MEAs with the

electrodes of; (i) Pt/C, (ii) Pt NW/C, (iii) Pt NW/C (150°C), (iv) Pt NW/C (250°C), (v) Pt NW/C

(350°C), (vi) PtNi NW/C, (vii) PtNi NW/C (150°C), (viii) PtNi NW/C (250°C), (ix) PtNi NW/C

(350°C) and (x) PtNi NW/C (150°C, 72 hrs).

As previously mentioned the biggest difference in fuel cell performance was observed when comparing the PtNi NW/C catalysts to those made of pure Pt. After Ni impregnation both charge transfer and mass transfer resistances were found to increase in the electrochemical impedance spectra (EIS) despite the improved catalytic activities recorded in the thin film RDE measurements (Figures 4.19). In part this is because in the RDE measurement the thin film CL is designed to minimise all mass transport losses as much as possible, but these effects are more prominent in the single cell test because the ionomer thin film on the catalyst surface results in a local oxygen mass transport resistance [19]. From the XPS analysis it is apparent that even though the high annealing temperatures result in more subsurface Ni, there is always a significant contribution from Ni oxides and hydroxides that can be assumed to lie on or near the surface of the Pt NWs. Considering the low acidic dissolution potential of -0.26 V vs. RHE for Ni, surface Ni can be assumed to dissolve and contaminate the ionomer during PEMFC operation [169,186].

Early work by Okada *et al.* showed that cation contamination (those of alkali metals were tested) of ionomer coated Pt electrodes resulted in decreased ORR catalytic performance by virtue of decreased O_2 permeability [144]. More recently, Braaten *et al.* studied the effects of Co^{2+} contamination on the ionomer where increased O_2 transport resistances were attributed to a combination of cross-linking between the sulfonate groups and decreased water content [145]. Therefore, probable Ni contamination of the ionomer means that even at 0.9 V an increase in local O_2 transport resistance is reducing the catalytic activity of the PtNi NW/C catalyst. At the high current density region where mass transport losses dominate, the effects are more pronounced.

Another factor for the disparity from the RDE measurements and single cell test can be ascribed to the different stabilities of Ni towards dissolution in each environment namely due to the increased temperature in the PEMFC environment. As such any initial mass activity benefits that the Ni may produce can be quickly mitigated by dissolution in the time frame

that the cell hydration and break-in procedures occur. Jia *et al.* have shown that this effect can be circumvented by employing PtNi alloys with a high Ni content so that Ni dissolution actually increases catalytic activity over the course of the catalyst lifetime [24]. However, this does not consider the aforementioned negative effects of Ni dissolution.

It has been previously reported that a thick Pt surface layer can protect the sub surface Ni in the PEMFC operational environment [19]. While other methods following the thermal annealing to stabilise subsurface Ni such as galvanic displacement [187] and acid leaching [170] may improve the performance of the synthesised PtNi NW/C catalysts, these MEA tests serve in elucidating some of the disparity between the catalytic performances from the RDE and single cell of PtNi alloys. These results were therefore instrumental in the adaptation of the PtNi NW synthesis technique for PtNi NW array GDEs as discussed in Chapter 5.
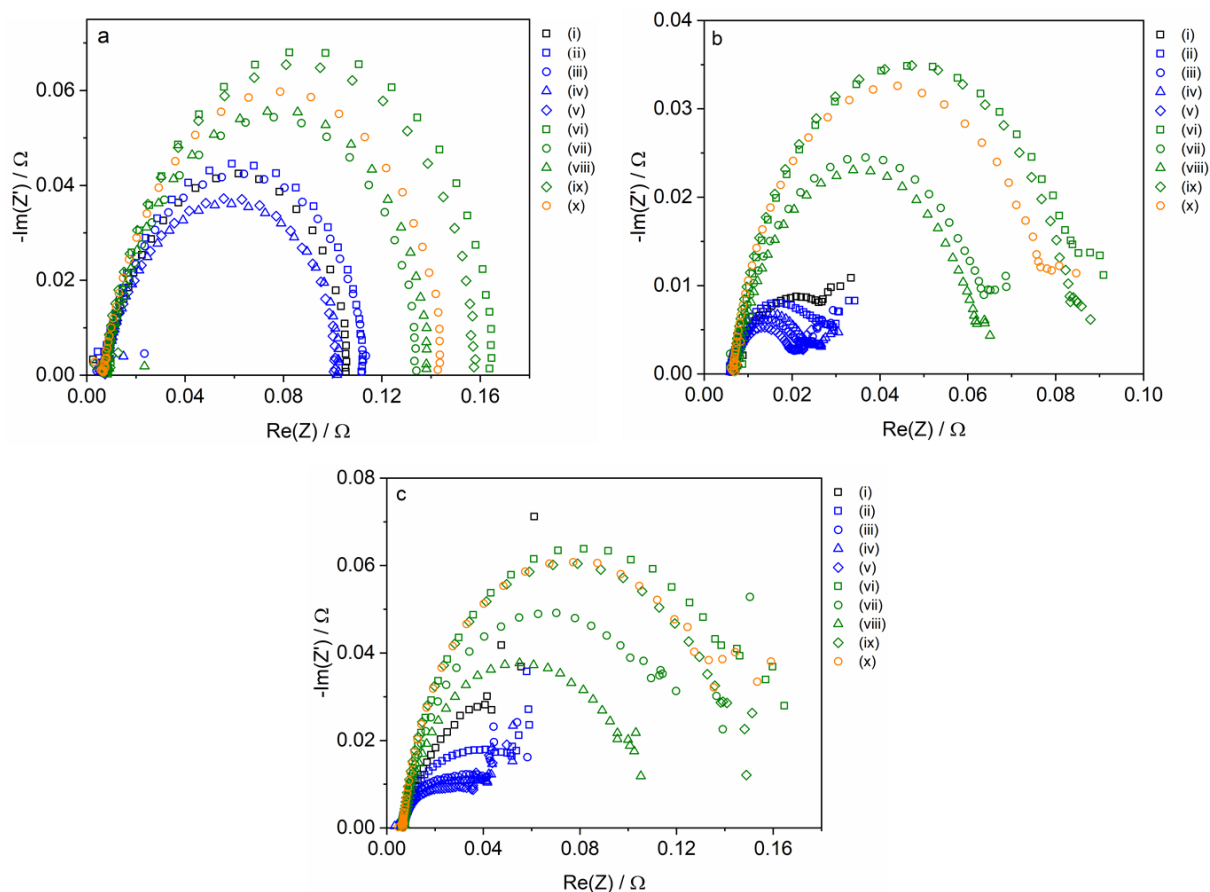
Figure 4.19: (a)–(c) EIS conducted at 30 mA cm^{-2}, 0.65 V and 0.5 V, respectively, for the MEAs with the electrodes of; (i) Pt/C, (ii) Pt NW/C, (iii) Pt NW/C (150°C), (iv) Pt NW/C (250°C), (v) Pt NW/C (350°C), (vi) PtNi NW/C, (vii) PtNi NW/C (150°C), (viii) PtNi NW/C (250°C), (ix) PtNi NW/C (350°C) and (x) PtNi NW/C (150°C, 72 hrs).

4.6. Conclusions

In this Chapter a simple and adaptable impregnation and subsequent annealing method for fabricating PtNi NWs supported on carbon was demonstrated. A more thorough investigation was conducted on the effects of the annealing temperature and time on the PtNi NW/C catalysts. It was found that while Pt NW/C sinters irreversibly at temperatures as low as 150°C, PtNi NW/Cs have a better thermal stability during this process. However, the coarsening mechanism remains to be a prominent artefact dependent primarily on the time of annealing. Physical characterisation including XRD, XPS and TGA analyses in conjunction

with the thin film RDE measurements showed that while the high annealing temperatures can increase the degree of alloying between the Pt and impregnating Ni, the best catalytic activity enhancements of 1.78-fold mass activity improvement for PtNi NW/C over Pt NW/C is obtained with the retention of NW morphology at 150°C. However, despite the differences in the intrinsic catalytic activities observed between the catalysts, in the single cell test the effects are dampened by the amount that Nafion® ionomer can access the gaps between the individual catalyst nanowires. Therefore, the importance of NW dispersion is stressed. In addition, worse power performance was found for the PtNi NW/C in comparison to the Pt NW/C catalysts and it can be ascribed to a combination of reduced Ni stability to dissolution in the PEMFC environment, and the contamination of the Nafion® ionomer on the catalyst surface inducing larger localised O_2 mass transport resistances. These results therefore help to explain the disparity between RDE results of novel ORR catalysts and their single cell performance as well as provide the groundwork to the fabrication procedure of PtNi NW array GDEs in the following work described in next Chapter.

5. PtNi nanowire array gas diffusion electrodes

The work presented in this chapter is unpublished at the time of writing

This chapter focuses on the fabrication of PtNi nanowire (NW) array gas diffusion electrodes (GDEs) based on experiences and knowledge obtained from the PtNi NW catalyst shown in Chapter 4. Pt NW array GDEs are fabricated at first and Ni is impregnated on top. Thermal annealing is again employed as well as a subsequent acid leaching step to obtain the PtNi NW array GDEs. Further optimisation of the annealing temperature as well as the Ni and ionomer content are demonstrated for improved power performance in comparison to the pure Pt NW array GDEs. Ex-situ GDE testing is also employed to evaluate the oxygen reduction reaction (ORR) activities of the PtNi NWs in the GDEs as a comparison to the membrane electrode assembly (MEA) test.

5.1. Introduction

In Chapter 4 a method of synthesising PtNi NW/C was shown through a three step process of Pt NW growth, Ni impregnation and thermal annealing. The effects of the annealing temperature and time on the catalyst composition, morphology, ORR catalytic activities and MEA performance were analysed in depth where an annealing temperature of 150°C for 24 hrs was found to give the best catalytic activity enhancements for PtNi NW/C over Pt NW/C by alloying of the Ni and retention of the NW morphology. However, the MEA performances of all catalysts with Ni were poor, especially at the high current density region due to the presence of surface Ni hydroxide species, which contaminate the ionomer in the catalyst layer (CL) [145,179,188].

Analogously, Pivovar *et al*'s development of PtNi NW catalysts also demonstrated similar issues: An initial publication reported the synthesis of PtNi NWs by the galvanic displacement of commercial Ni NWs (with an average diameter of 150–200 nm and length of 100–200 μm), and through ex-situ RDE tests a high mass activity of 0.917 A mg_{Pt}^{-1} was demonstrated towards ORR at 0.9 V vs. RHE [141]. Atomic layer deposition (ALD) was also later investigated with even greater performance enhancements [189]. Durability concerns over Ni

dissolution prompted further investigations into firstly oxidative annealing whereby a Ni oxide layer is induced in the core Ni NW, trading improved durability for reduced initial catalytic activity [169]. Later, more vigorous post-treatment optimization was conducted where firstly hydrogen annealing was employed to improve the PtNi alloying and thus increase the catalytic activity of the PtNi NWs further [170]. Secondly, acid leaching (followed by another oxidative annealing process) was conducted on the catalysts prior to MEA fabrication with the result of further durability enhancements.

Since this work, focus shifted towards the optimization of MEAs containing the PtNi NWs. The PtNi NWs which underwent just hydrogen annealing exhibited a minimal catalytic activity in the MEA test and hence an ion exchange step was necessary by soaking the MEA in sulphuric acid [142]. Other improvements were made by reducing the ionomer content in the CL and pre-leaching the PtNi NW catalysts prior to MEA fabrication—which was also shown to be more effective in comparison to the ion exchange procedure where some Ni remained dispersed in the Nafion® ionomer as "atomic or ionic clusters" [190]. Through analysis of the rate limiting currents, it was shown that these procedures worked by mitigating Ni contamination of the ionomer and polymer electrolyte membrane where ion exchange with protons resulted in an increased oxygen transport resistance via dehydration of the polymer matrices.

This collection of works is one of the most thorough investigations illustrating why there is a significant disparity between the ORR catalytic activity and performance of novel PtM catalysts in the RDE measurement and MEA test environment [23]. In this chapter, an alternative catalyst system is presented whereby the PtNi NW/C synthesis methodology presented in Chapter 4 is adapted for the simple and scalable fabrication of the PtNi NW array GDEs. An emphasis on the optimisation of MEA performance is provided in this study where acid leaching is shown to be crucial for the removal of surface Ni as well as Ni particles deposited throughout the entire GDE. The annealing temperature is further refined

along with the PtNi precursor ratio and ionomer content. With all optimisations considered, modest improvements in PEMFC performance are shown for the PtNi NW array GDEs in comparison to the pure Pt NW array GDEs. Ex-situ GDE testing is also employed to demonstrate the inherent ORR catalytic performance of the GDEs with significant improvements observed for the PtNi NW GDE. This work therefore provides some explanation as to the RDE/MEA disparity as well as proposing some mitigation strategies.

5.2. Morphology, composition and Ni distribution in PtNi NW array electrodes

Pt NW GDEs were fabricated and Ni was subsequently deposited onto the surface by reducing Ni precursor with $NaBH_4$. To fabricate the Pt NW array GDEs, the formic acid reduction approach was run at 40°C as per optimizations conducted in our group [32]. While the reduction reaction does occur in the absence of any substrate at room temperature to produce 1D Pt clusters [105], homo-nucleation - whereby the initial Pt seed is formed – tends to have a higher activation energy barrier in comparison to heteronucleation [106]. Therefore in the presence of a gas diffusion layer (GDL) substrate, where the rough surface provides nucleation sites, clusters of Pt NWs tend to form on the GDL surface much like the clusters shown in Chapter 4 and the literature [179]. In addition, greater surface tension on the GDL surface prompted by its hydrophobicity leads to a better contact between the aqueous reaction solution with the edges of the GDL piece compared to the centre area. A higher reaction temperature therefore has the effect of providing a more even distribution of Pt NWs on the GDL surface. Too high however, and the homo-nucleation becomes more prominent and nanoparticles form in the solution instead of NWs on the GDL surface. Using fuel cell performance as a metric, 40°C was previously found to be the optimal reaction temperature and so this was adopted here.

SEM analysis was used to image the surface of the Pt NW GDE. The images show that even at 40°C, Pt agglomerates tend to form on the GDL surface (Figure 5.1a–b). It has been shown that distribution could be improved through active screen plasma (ASP) nitriding of the GDL surface prior to the Pt NW growth on the surface. However, this was not adopted in this work due to the increase in complexity [35]. EDX line scan is conducted on the GDE and the result is shown in Figure 5.1c where the Pt density in the clusters appears to be approximately 2–3 times higher in comparison to the rest of the area.
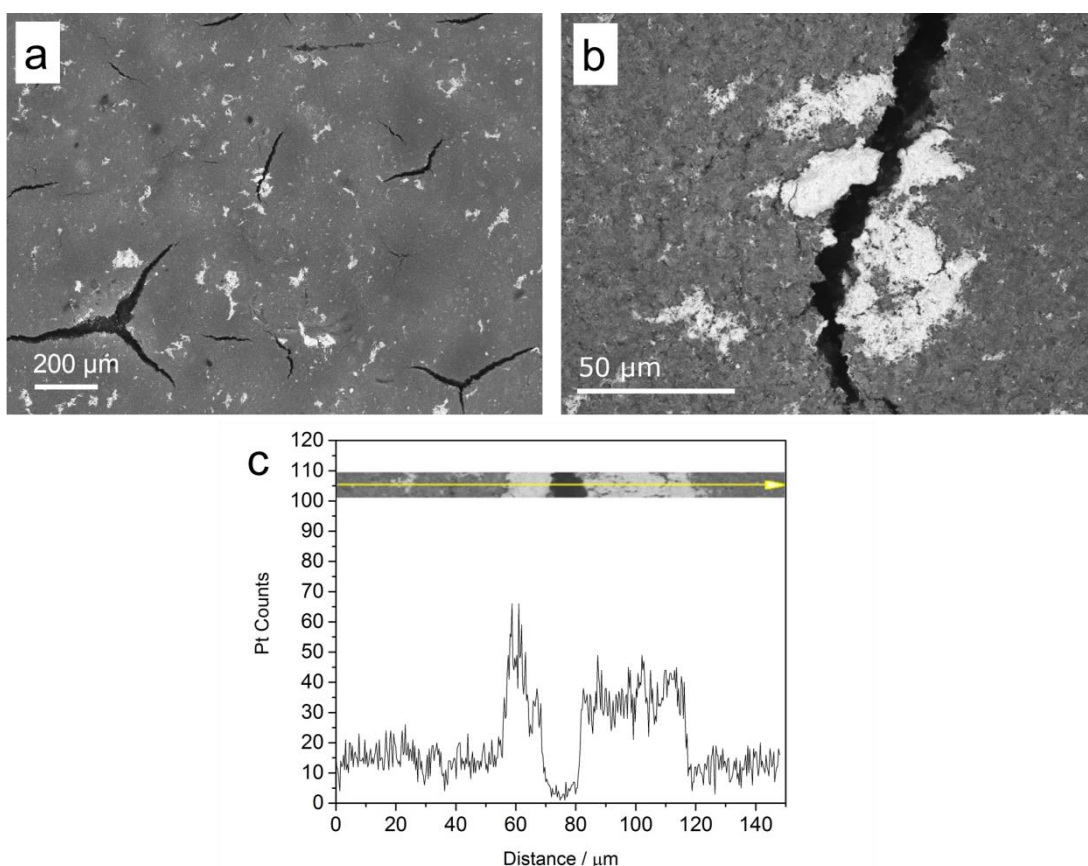
Figure 5.1: (a)–(b) SEM images of the Pt NW GDE surface and **(c)** EDX line scan map showing the Pt distribution in agglomerate regions as well as the bulk GDE surface and cracks in the GDE.

After Ni deposition, three different annealing temperatures were investigated in a narrower range compared to the previous study (Chapter 4) with values of 150, 200 and 250°C

followed by an acid leaching step. SEM-EDX analysis was conducted on the surface of these GDEs, and the maps indicate that Ni density is slightly larger in the Pt agglomerates (Figure 5.2a–c). This is not as visible for the GDE prior to acid leaching (Figure 5.2d) thus indicating that post thermal treatment, Ni deposited on the Pt agglomerates is better protected from the leaching.
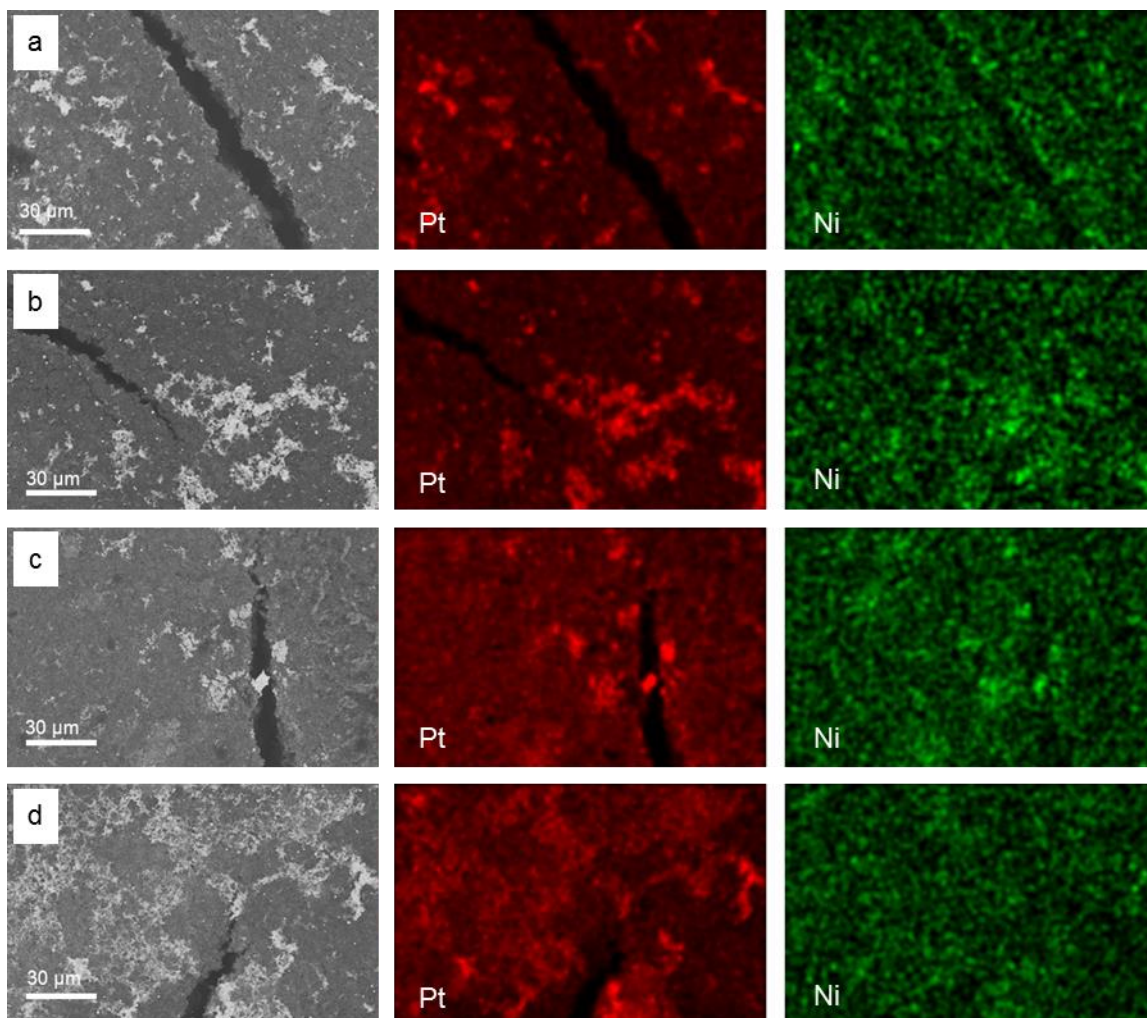
Figure 5.2: SEM images (left), Pt (middle) and Ni (right) EDX maps of the surface of **(a)** PtNi NW (150°C, AL), **(b)** PtNi NW (200°C, AL), **(c)** PtNi NW (250°C, AL) and **(d)** PtNi NW (200°C) GDEs.

To examine the distribution of Ni in the CL after the impregnation step, cross-sectional SEM-EDX mapping of the PtNi NW GDE annealed at 200°C was conducted. Sigracet 39 BC GDL

comprises of a mesoporous carbon layer (MPL) coated onto a fibrous carbon paper backing, both of which treated with polytetrafluoroethylene (PTFE) to ensure hydrophobicity [191]. The cross-sectional EDX maps (Figure 5.3a-b) indicate that most of the Ni deposited at the interface of the carbon paper backing layer and the MPL. In the Ni impregnation procedure, the Pt NW GDE was firstly wetted to ensure that $NiCl_2.6H_2O$ solution coats evenly on the GDE surface prior to reduction. The SEM-EDX map indicates that the super hydrophobicity of the fibrous backing layer in comparison to the MPL keeps the $NiCl_2.6H_2O$ solution from soaking into its pores. Therefore, during the impregnation step, much of the reduced Ni is away from the Pt NWs. This is exacerbated by the fact that the reduction by $NaBH_4$ is so quick that Ni is reduced on location with only a slight preference for the Pt surface. The subsequent acid leaching procedure is shown by the EDX map to be effective in removing the Ni at the backing layer/MPL interface leaving consistently low counts among the entire GDE with a slight increase visible at the CL surface (Figure 5.3c). This is later shown to have a positive effect on PEMFC performance.
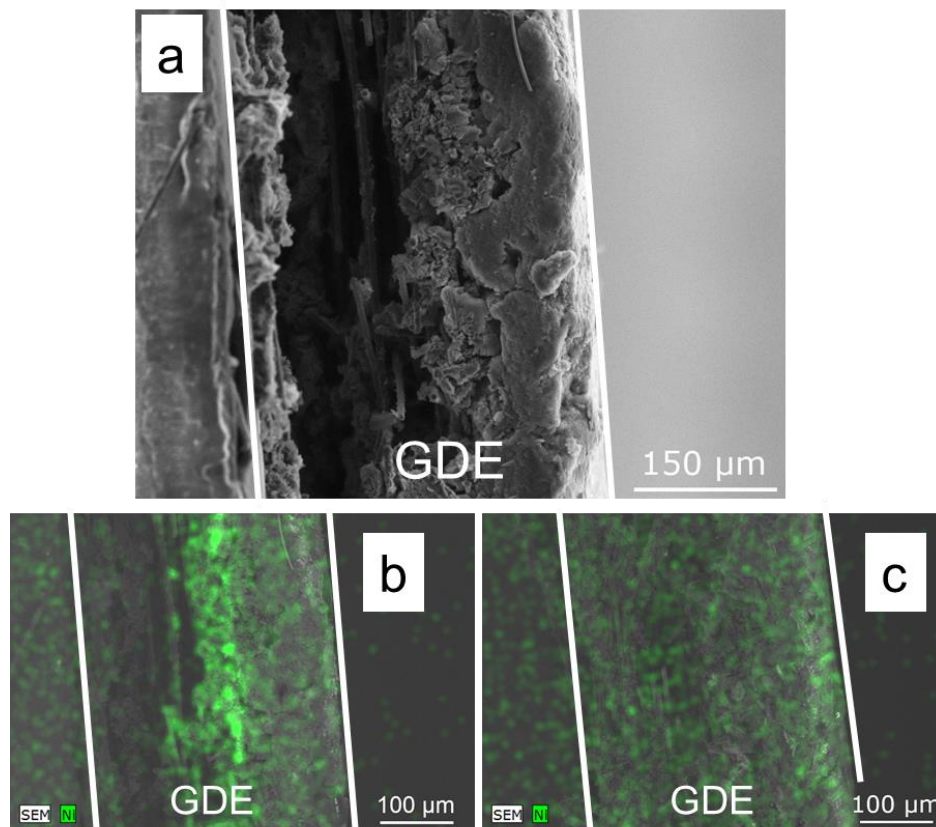
Figure 5.3: (a) Cross sectional SEM image of the PtNi NW GDE (200°C) and Ni EDX maps of **(b)** PtNi NW (200°C) and **(c)** PtNi NW (200°C, AL) GDEs.

To examine the fine structure of the synthesised NWs, high resolution SEM (HR-SEM) was firstly conducted on the PtNi NW (200 °C) and PtNi NW (200 °C, AL) GDEs. Both images (Figure 5.4a–b) show the cubic morphology of Pt NW agglomerates with a 'spikey' nature much like that shown for the NWs on carbon black. This appears to remain unchanged after the acid leaching step.
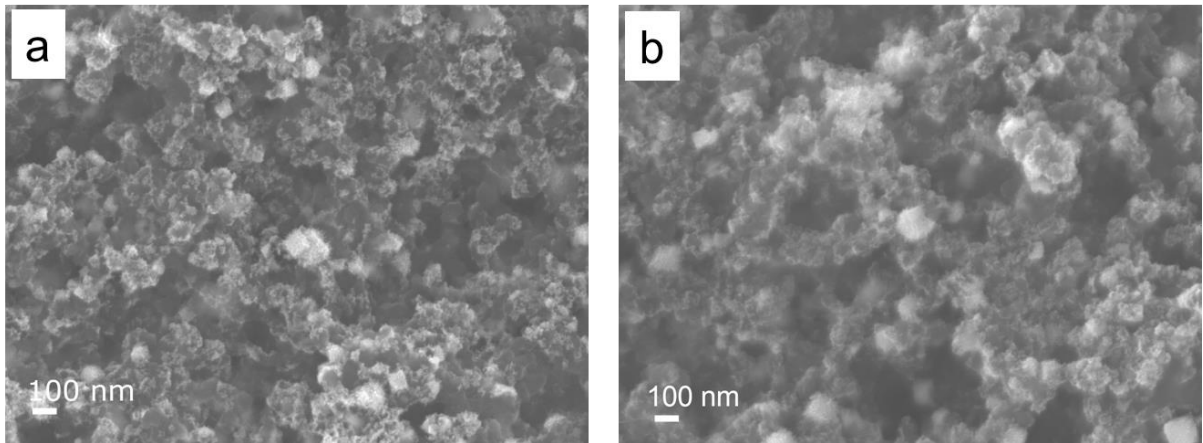
Figure 5.4: HR-SEM images of **(a)** PtNi NW (200°C) and **(b)** PtNi NW (200°C, AL) GDEs.

TEM analysis of the Pt NW GDEs has been extensively reported before [32,35] and so analysis was just conducted on the annealed and acid leached PtNi GDEs to monitor the changes in NW size and lattice spacing. In the previous study (Chapter 4 and [179]), the NW growth on Vulcan XC-72R was shown to produce cubic agglomerates with an average size of 121 nm on the diagonal. Primarily due to higher the reaction temperature and a rougher carbon with the MPL than the pristine Vulcan XC-72R [56], NW distribution was found to be much improved on the GDL surface as indicated by the agglomerate distribution profile (Figure 5.5), where there was only one instance of an agglomerate larger than 100 nm.
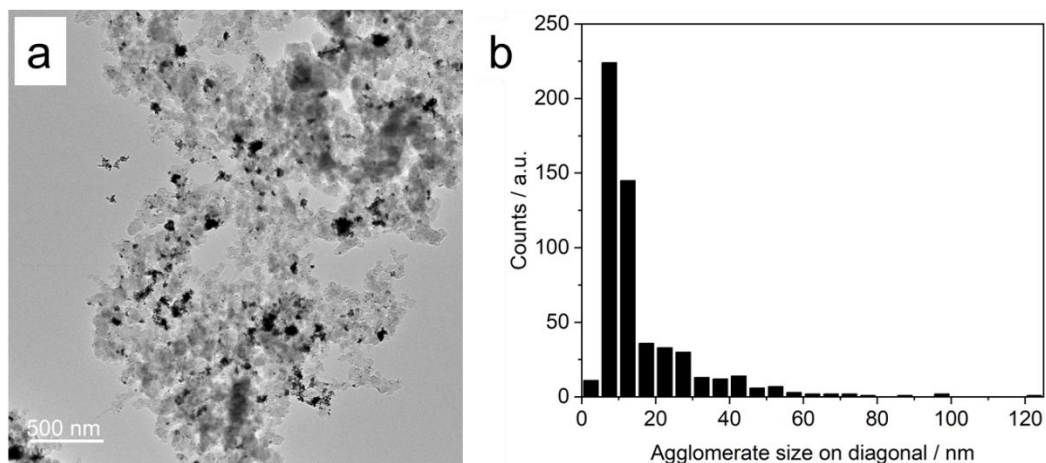
Figure 5.5: (a) TEM image of the top scrapings of the PtNi NW (200°C, AL) GDE and **(b)** the corresponding agglomerate size distribution.

Representative catalyst TEM images of the PtNi NW GDEs annealed at different temperatures and acid leached are shown in Figure 5.6a–d. As with the Pt NW/C catalysts, many nanoparticles and short NWs formed, indicating the anisotropic growth as expected by the formic acid reduction method. Accurate sizing of the NWs is difficult due to the agglomeration, however, lengths were measured to range up to around 25 nm which is consistent with previous analysis of Pt NW GDEs fabricated at 40°C [32]. The average diameter of the various NWs are nearly the same and within the standard deviation of each. A total average NW diameter of ≈3.9 nm was measured, slightly higher than the Pt NW/C samples (≈3.5 nm) presumably due to the elevated reaction temperature encouraging less anisotropic growth. Importantly the unchanged diameter with the annealing temperature and acid leaching indicates that these NWs have a stable morphology in the temperature range tested. For Pt NW/C it was shown that sintering begins as low as 150°C, but can be stabilised by the inclusion of Ni. The fact that these NW samples are stable is a clear indication of the successful incorporation of Ni into the fine Pt NW structure. The NWs remain stable after acid leaching and do not form a nanoporous structure as the diameter is well below the 15 nm critical NP radius found by Snyder *et al.* for the formation of nanoporous PtNi NPs [93]. The lattice fridge images indicate a spacing distance of around 0.22 nm along

the NW (Figure 5.6e), confirming anisotropic growth in the <111> direction. Differences between the catalysts are within the standard deviation of all sites measured (Figure 5.6f).
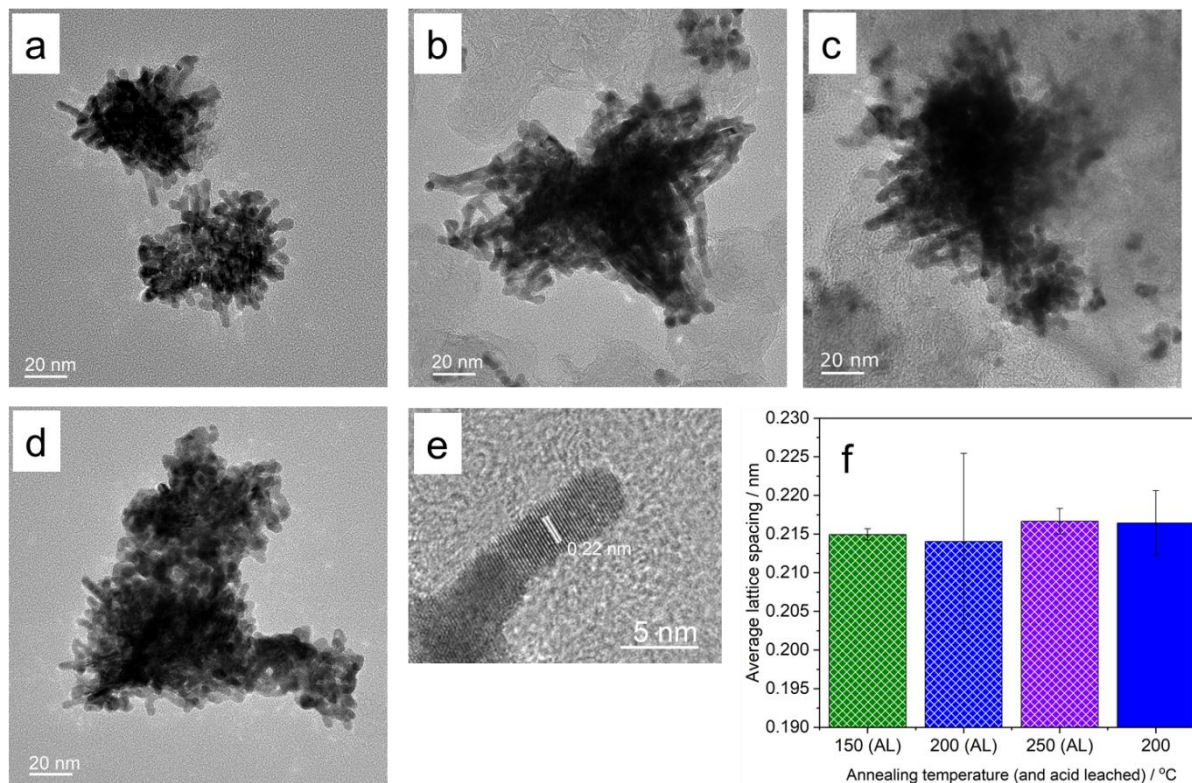
Figure 5.6: HR-TEM images showing NW agglomerate structure for **(a)** PtNi NW (150°C, AL), **(b)** PtNi NW (200°C, AL), **(c)** PtNi NW (250°C, AL) and **(d)** PtNi NW (200°C) CL scrapings. **(e)** PtNi NW (150°C) and **(f)** average lattice spacing with standard deviation given as the error.

To ascertain whether the Ni was successfully impregnated and annealed into the NW CL, and whether the Pt in the wire protected Ni from leaching out, STEM-EDX analysis was conducted on PtNi NW (200°C, AL). Figure 5.7a shows the HAADF image of a PtNi NW as well as the EDX maps of Pt and Ni. These images categorically show that Ni is successfully incorporated into the Pt NWs in a manner that is stable enough to resist the acid leaching procedure in 0.1 M HNO_3 (room temperature, 24 hrs). The STEM-EDX maps also indicate that neither a Pt@Ni nor Ni@Pt core-shell structure can be concluded but rather the NWs

more likely consists of an alloy where Ni is incorporated into the lattice structure. Figure 5.7b indicates that the impregnation of Ni into the Pt NWs is consistent throughout the catalyst structure, but also some individual Ni nanoparticles remain.
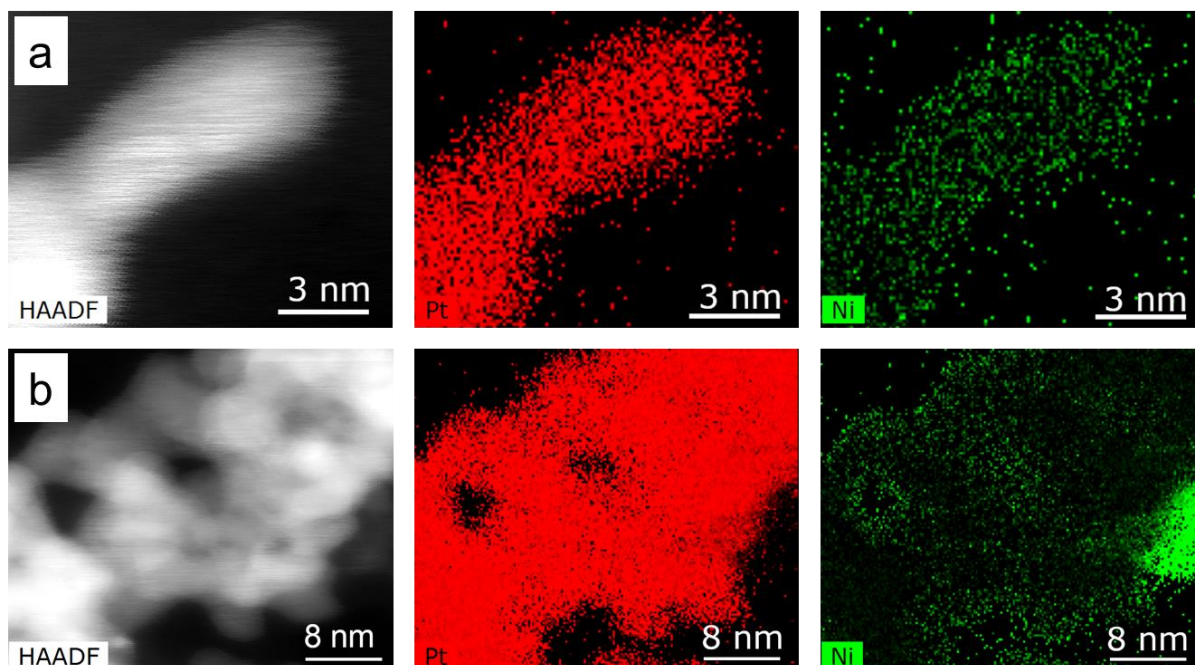
Figure 5.7: STEM-EDX mapping of PtNi NW (200°C, AL) with (left) HAADF, (middle) Pt EDX map and (right) Ni EDX map for **(a)** an individual wire and **(b)** the agglomerate structure.

ICP-MS was used in favour of STEM-EDX to obtain accurate Pt_xNi ratios in the GDEs when different annealing temperatures are used (for the precursor ratio of Pt_3Ni_4). This was conducted both before and after the acid leaching step so as to quantify the amount of the Ni protected by the Pt coverage. In addition, ICP-MS was conducted on the CL (only) of all GDEs to give a further description of the distribution of Ni after the reduction step. Figure 5.8 shows the obtained Pt_xNi ratios where an average value of 1.11 ± 0.20 was obtained prior to the acid leaching. Assuming 100% Pt is reduced and grown on the GDL surface, this equates to a yield of 67% for the reduction of Ni in the GDE whereas the remainder was reduced in the solution and immediately washed away. After acid leaching, an average Pt_xNi ratio of 4.55 ± 0.76 was found indicating that during acid leaching, 76% of the Ni was

removed. The analysis was conducted on the CL of the identical GDEs before and after acid leaching where average Pt_xNi ratios of 4.59 ± 0.49 and 4.34 ± 0.69 were measured, respectively. Within error, the PtNi composition of the CL before and after acid leaching is nearly the same as the entire GDE after acid leaching. Alongside the cross sectional SEM-EDX mapping (Figure 5.3) clear indications are that the acid leaching removes the Ni that is present in the interface of the backing layer/MPL whereas Ni present in the CL is protected. This protection occurs from the annealing procedure where surface segregation results in surface Pt, highly resistant to dissolution by the HNO_3 and thus protecting the alloyed Ni atoms. A further investigation into the optimal acid, concentration and temperature would be of interest although the milder conditions of the dilute HNO_3 used here have been successful in removing the Ni species that do not contribute to increased ORR activity [170].
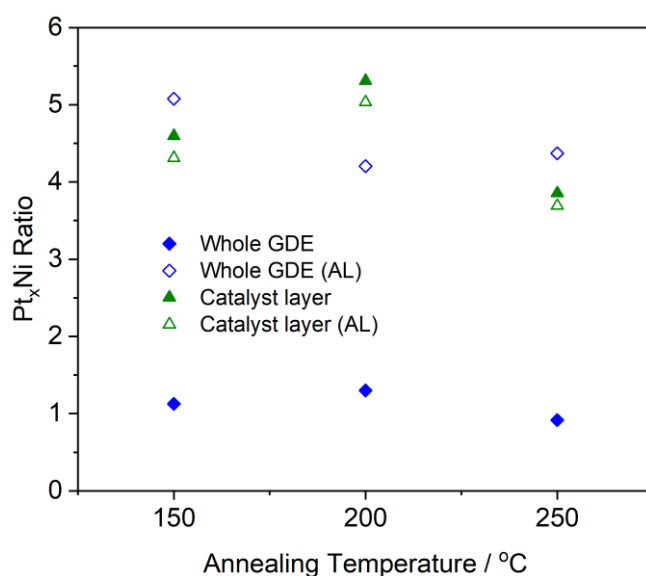
Figure 5.8: ICP-MS of Pt_3Ni_4 NW GDEs and CL with and without acid leaching (AL) after annealing at 150, 200 and 250°C for 24 hrs.

In addition, ICP-MS allowed for the determination of the catalyst loading where across all GDEs an average loading of 0.312 mg_{Pt} cm^{-2} with a standard deviation of 0.026 mg_{Pt} cm^{-2} was measured. As with Chapter 4 and later Chapter 6, thermogravimetric analysis (TGA)

was also used to obtain catalyst loadings. However, instabilities with the equipment provided highly variable results with the same Pt NW GDE. Therefore, for this study the loadings determined using ICP-MS analysis were used for ECSA and mass activity calculations in the electrochemical tests.

5.3. Degree of alloying in PtNi NW GDEs

As with the PtNi NW/C catalysts, X-ray diffraction (XRD) was conducted to assess Pt lattice contraction by the alloying with Ni and hence evaluate the effect of annealing temperature on the degree of alloying. Figure 5.9a shows the full XRD spectra of the GDE materials before acid leaching. Because of the low Pt loadings on the GDEs, the intensity of the Pt peaks is low but they can still be indexed accordingly (JCPDS-04-0802). The intensity is higher for the NW GDEs in comparison to the Pt/C nanoparticle GDE, indicating a high degree of crystallinity. The intense peak at 26.6° is the (002) plane for the graphitic carbon in the GDL [192]. A focus on the Pt(111) peak for the PtNi NW GDEs (Figure 5.9b) shows a positive peak shift with an increase in the annealing temperature similar to Chapter 4 and the literature [179]. Here a shift of +0.08° was observed between the PtNi NW GDE and that annealed at 250°C, indicative of the smaller lattice constants and hence lattice contraction induced by the surface segregation of Pt and the alloying of smaller Ni atoms. As with the PtNi NW/C GDEs, the lattice contraction is smaller here compared to other reported values because of the comparatively low annealing temperature required to maintain NW morphology [61,95,172]. The lower annealing temperature limits the ability of the Ni to alloy with the bulk Pt and reside predominantly at the surface (further confirmed through XPS analysis below). In addition, the lower Ni content in the PtNi NW GDEs compared to the PtNi NW/C provided a smaller contraction.
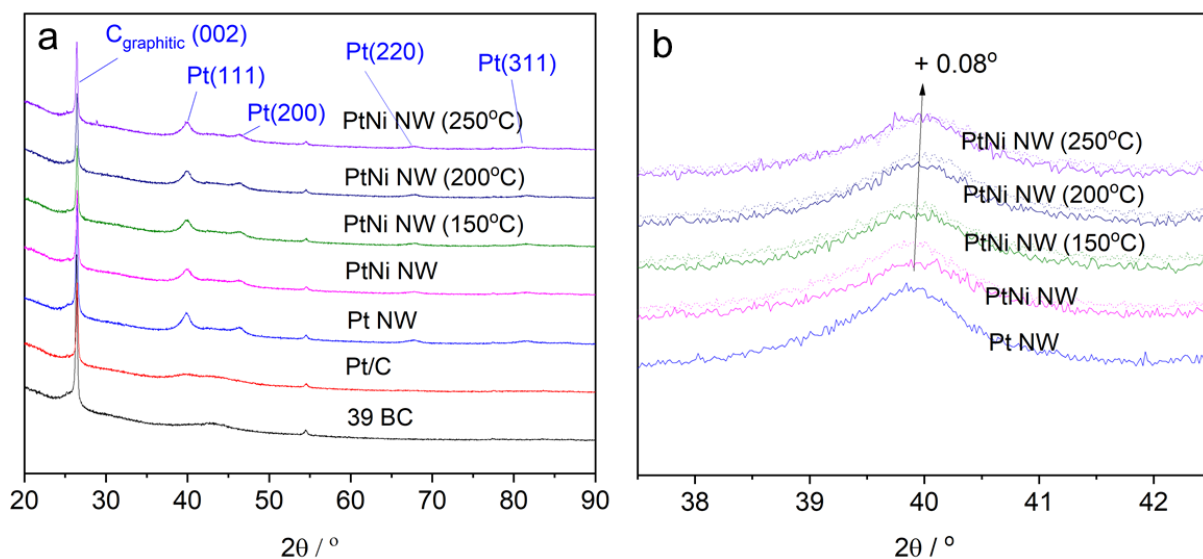
Figure 5.9: XRD patterns of the GDEs **(a)** before acid leaching (solid) and **(b)** magnification showing the shift after annealing, including GDEs after acid leaching (dotted).

XPS was used to evaluate the nature of Pt and Ni elements in the GDEs. The survey spectra (Figure 5.10) appear very similar for all GDEs with one exception, at 1072 eV, those GDEs with Ni impregnated but not acid leached show a peak for Na1s. This originates from $NaBH_4$ used in the initial impregnation and so indications are that this is not washed out post-impregnation with H_2O or IPA. Through quantification of the survey spectra, the average Na_xPt ratio was found to be 0.56 before acid leaching and 0.09 afterwards, indicating nearly complete removal. However, prior to acid leaching Na would undoubtedly have an adverse effect on PEMFC performance through cation exchange similar to dissolved Ni ions [144].
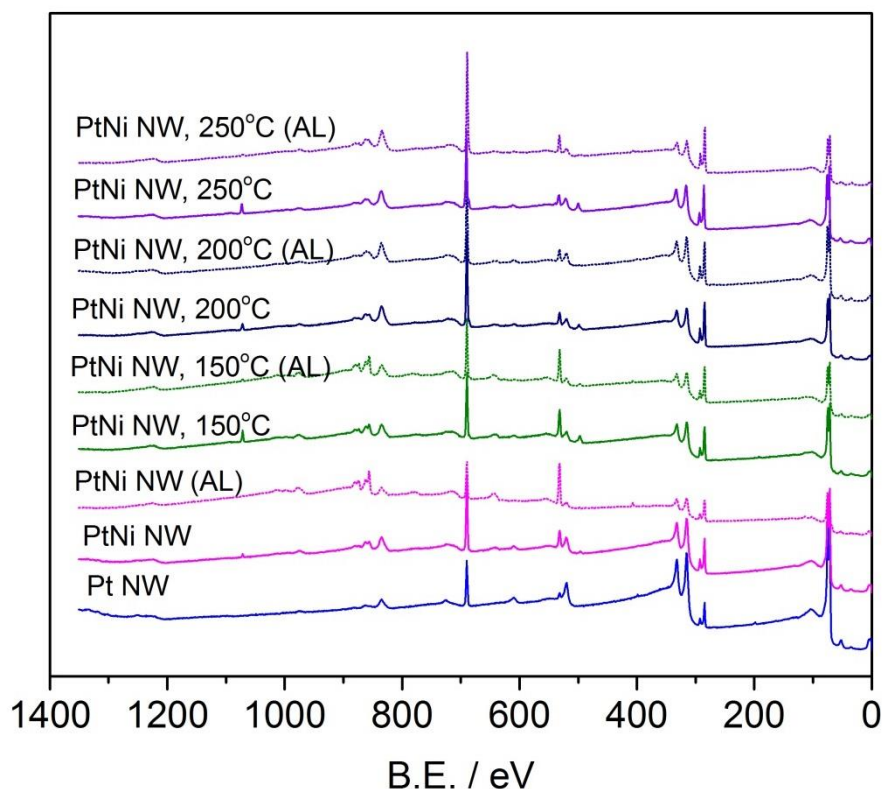
Figure 5.10: Survey XPS spectra of the Pt NW and PtNi NW GDEs annealed at various temperatures. GDEs that underwent acid leaching are labelled (AL).

The Pt 4f spectra for all samples are shown in Figure 5.11 where all were fitted with peaks for Pt in the 7/2 and 5/2 couplet spin states as well as Ni 3p peaks in the PtNi NW GDEs. All Pt 4f spectra (a–i) are similar where differences in intensity are thought to be caused by difference spot locations. For the PtNi NW GDEs, the Ni 3p peak size shows two trends. Firstly, as with the PtNi NW/C system in Chapter 4, the Ni 3p peak size decreases with the increase of the annealing temperature indicating surface segregation into the NWs. Secondly, the peaks increase after the acid leaching process. Alia *et al.* commented that when forming a Ni oxide layer in their PtNi NW system, XPS indicated surface segregation of the Ni oxide where under certain conditions (300°C annealing) very little Pt was present on the surface [169]. Therefore, when considering the surface sensitivity of XPS, it is reasonable

to conclude the oxidation of the Ni by the acid induces the segregation of Ni in the PtNi alloy back to the surface layers.
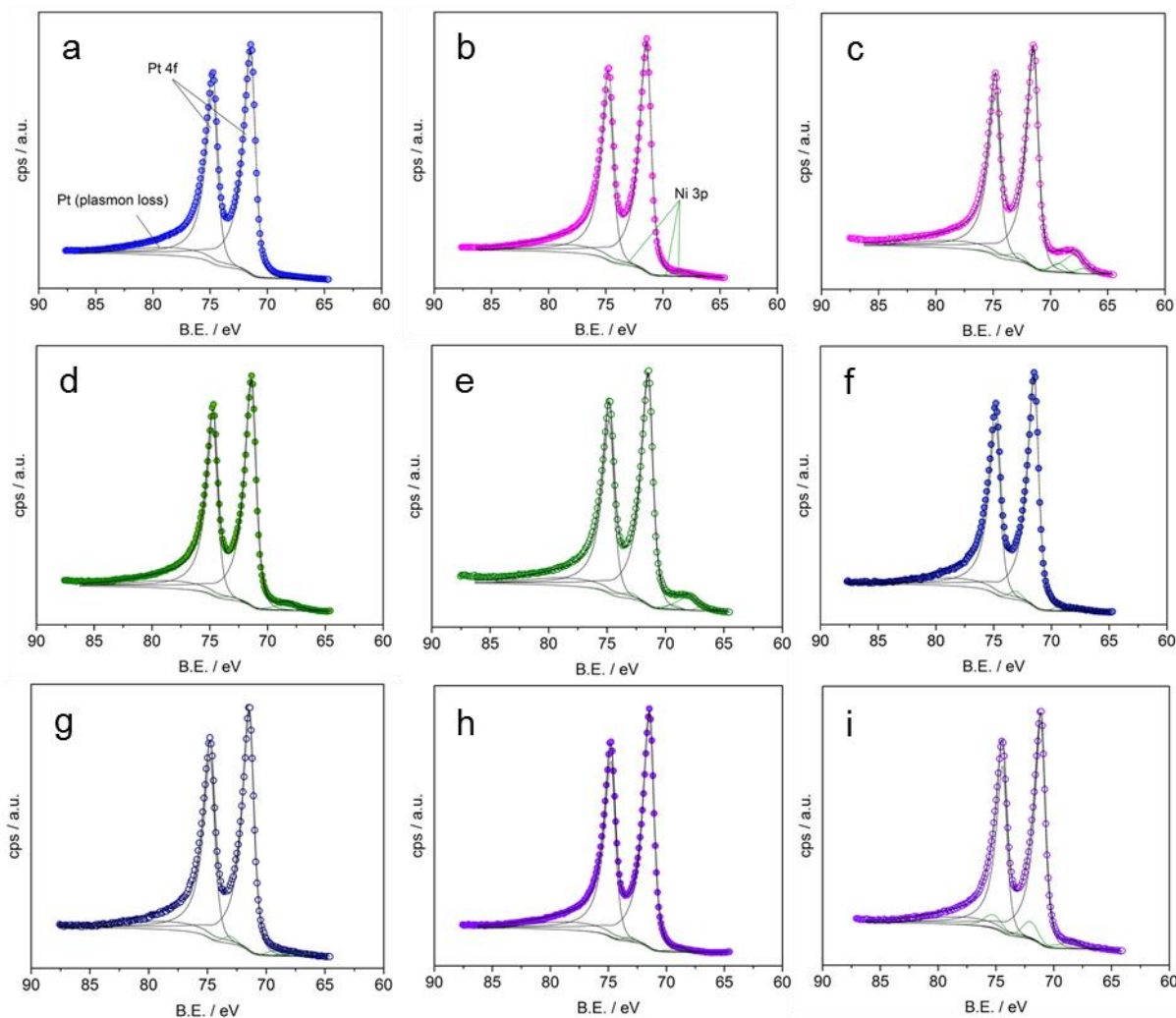
Figure 5.11: Pt 4f XPS spectra for **(a)** Pt NW, **(b)** PtNi NW, **(c)** PtNi NW (AL), **(d)** PtNi NW (150 °C), **(e)** PtNi NW (150°C, AL), **(f)** PtNi NW (200°C), **(g)** PtNi NW (200°C, AL**), (h)** PtNi NW (250°C) and **(i)** PtNi NW (250°C, AL) GDEs.

Oxidation of Ni in the PtNi NWs is further confirmed in the Ni 2p XPS spectra, where after fitting the 3/2 spin couplet the ratio of Ni/Ni oxides tends to decrease after acid leaching (Figure 5.12). This suggests that while the original Ni oxides are being removed, the subsurface Ni is being oxidised by the acid as they segregate back to the surface. In fact, at

the low annealing temperatures very little metallic Ni was observed indicating minimal protection to the acid as well as potentially a relative high proportion of Ni in the outermost surface layers. As in Chapter 4, there is a high proportion of metallic Ni/Ni oxides ratio at the high annealing temperature indicative of greater reduction by the H_2 during the annealing process and potentially greater surface segregation (of Pt to the surface).
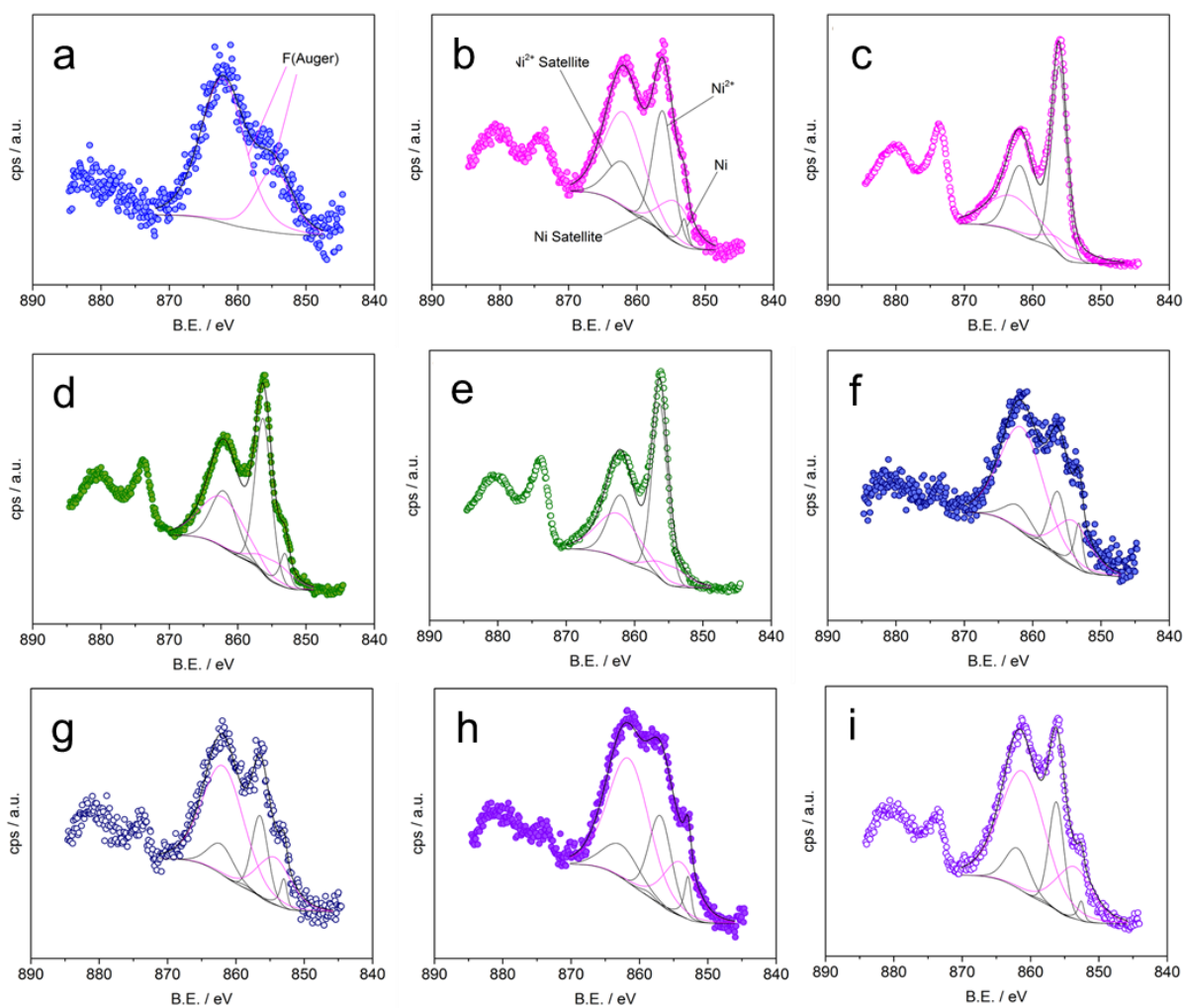
Figure 5.12: Ni 2p XPS spectra for **(a)** Pt NW, **(b)** PtNi NW, **(c)** PtNi NW (AL), **(d)** PtNi NW (150°C), **(e)** PtNi NW (150°C, AL), **(f)** PtNi NW (200°C), **(g)** PtNi NW (200°C, AL), **(h)** PtNi NW (250°C) and **(i)** PtNi NW (250°C, AL) GDEs.

5.4. Performance and optimisation of PtNi NW array GDEs.

5.4.1. Requirement of acid leaching

In Chapter 4, the PEMFC single cell performance of the PtNi NW/C catalysts was worse than the Pt NW/C catalysts as a result of ionomer contamination. Therefore, an acid leaching step post annealing was employed to remove surface Ni and individual Ni nanoparticles deposited in the GDE. Crucially, this leaching step was conducted on the GDEs before MEA fabrication thereby avoiding the entrapment of Ni clusters in the ionomer [190]. The polarisation performance of the PtNi NW GDE (200°C) was found to be similar to that of the PtNi NW/C catalysts where mass transport limitations result in a reduced performance at the high current density region (Figure 5.13a). The acid leaching step much improved the MEA performance whereby exposed Ni, not protected by the Pt surface layers was removed, which mitigated contamination of the ionomer and membrane.

The large mass transport loop on the Nyquist plot obtained at 0.5 V (Figure 5.13d) and the sudden drop in performance for PtNi NW (200°C) array MEA (Figure 5.13a) demonstrates large mass transport losses for this GDE. This can be attributed to ionomer contamination and hence a reduction in O_2 permeability. However, a significant difference for both GDEs is that the internal resistance was reduced during the acid leaching step, as shown in all three Nyquist plots (Figure 5.13b–d). A big contributor to the internal resistance is the proton conductivity of the Nafion® proton exchange membrane (PEM) [16]. Mauger *et al.* reported larger high frequency resistances (HFR) for those PtNi NW samples that did not undergo ion exchange in comparison to those that did, and likened the result to the blocking of sulphuric acid groups in the PEM [142]. By having a greater affinity to these groups, i.e. Ni^{2+} than protons, the PEM ionic conductivity is reduced [193].

Of note however is a slightly higher open circuit potential (OCP) and smaller charge transfer resistance for the MEA with the PtNi NW array (200°C) GDE compared to that of the acid

leached sample, indicating that acid leaching reduces the ORR catalytic activity of the PtNi NW arrays. This was also confirmed by the specific activities for the prepared and acid leached GDEs, which were 549 and 326 $\mu A\ cm_{Pt}^{-2}$, respectively, measured under DoE O$_2$ testing conditions [97]. Although limited, acid leaching would have removed some of the Ni alloying in the NWs and thus the beneficial effects of lattice contraction would have also been reduced. In particular, Jia *et al.* experimentally verified that if the PtM$_x$ ratio is higher than optimal, and thus the Pt-O bond is too weak, then dissolution of metal 'x' would actually result in an increase in the ORR catalytic activity through a strengthening of the bond [24]. However, if the initial Ni content is lower than the optimal then any dissolution would result in a decreased ORR activity. For the PtNi NW arrays presented here it appears that the catalyst resides on the strong leg of the activity vs Pt-O bond strength volcano plot.
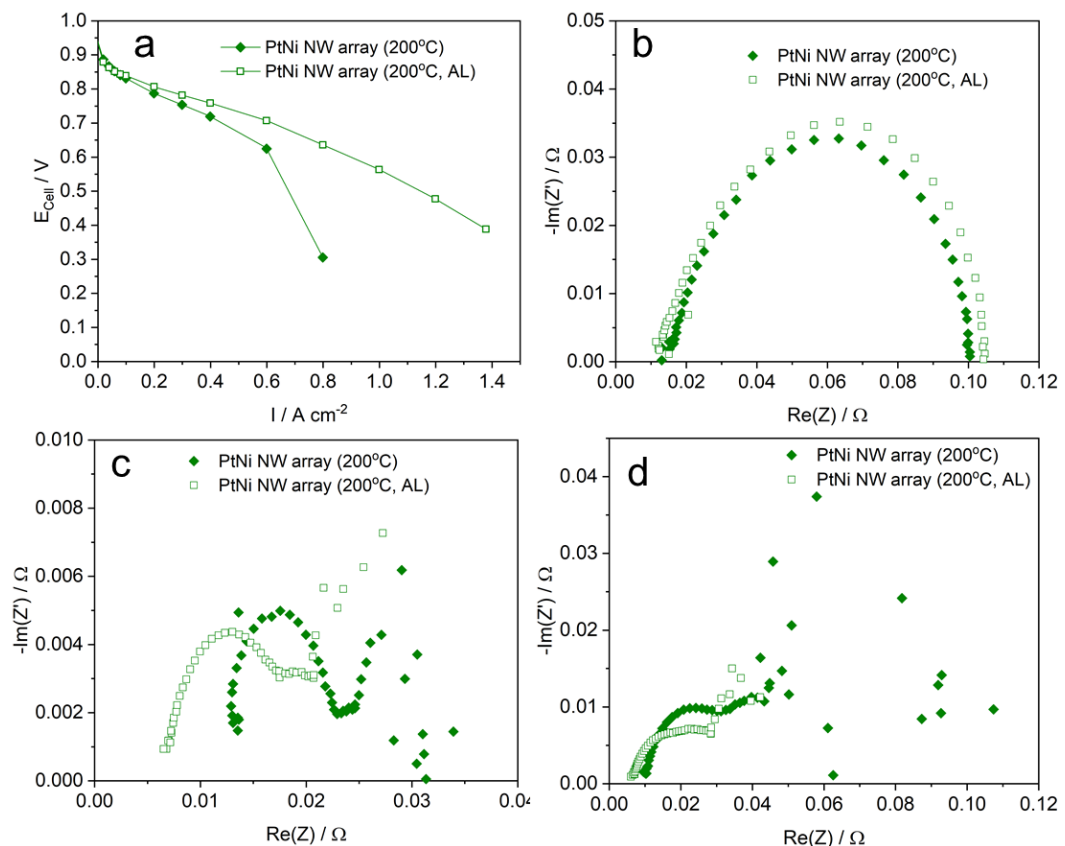
Figure 5.13: (a) Polarisation curves and EIS conducted at **(b)** 30 mA cm^{-2}, **(c)** 0.65 V and **(d)** 0.5 V for MEAs with the cathodes of PtNi NW (200°C) and PtNi NW (200°C, AL) GDEs.

5.4.2. Optimisations – Ni content, temperature and ionomer content

Throughout this chapter the precursor ratio of Pt_3Ni_4 was investigated because during optimisation it was found that this gave the best single cell performance (Figure 5.14a). Any catalytic enhancements to the Pt NWs must firstly overcome the negative effect of ionomer Ni contamination, to give an overall improvement in PEMFC performance. While an increase in the Ni content can achieve higher activities, if too much is added, then ionomer contamination would be too detrimental to the overall performance as per Section 5.4.1 (Figure 5.14a). The annealing temperature was also investigated further in order to expand and refine on the work shown in Chapter 4. The optimum performance for these PtNi NW array GDEs was found at the annealing temperature of 200°C because of a higher degree of alloying compared to 150°C and less morphological change compared to 250°C (Figure 5.14b). Finally, the amount of ionomer required for the PtNi NW array GDE was also optimised where a reduced loading of 0.4 mg_{Naf} cm^{-2} was found to provide the best performance (Figure 5.14c). With too little (0.2 mg_{Naf} cm^{-2}), the ECSA of the GDE was reduced by around 37%. While high ionomer contents are required for the Pt NW GDEs [163], reduced amounts were found to be optimal for the PtNi NW GDEs because of the higher O_2 permeation resistance due to contamination, and the increased hydrophilicity of the PtNi NW surface as compared to pure Pt [194].
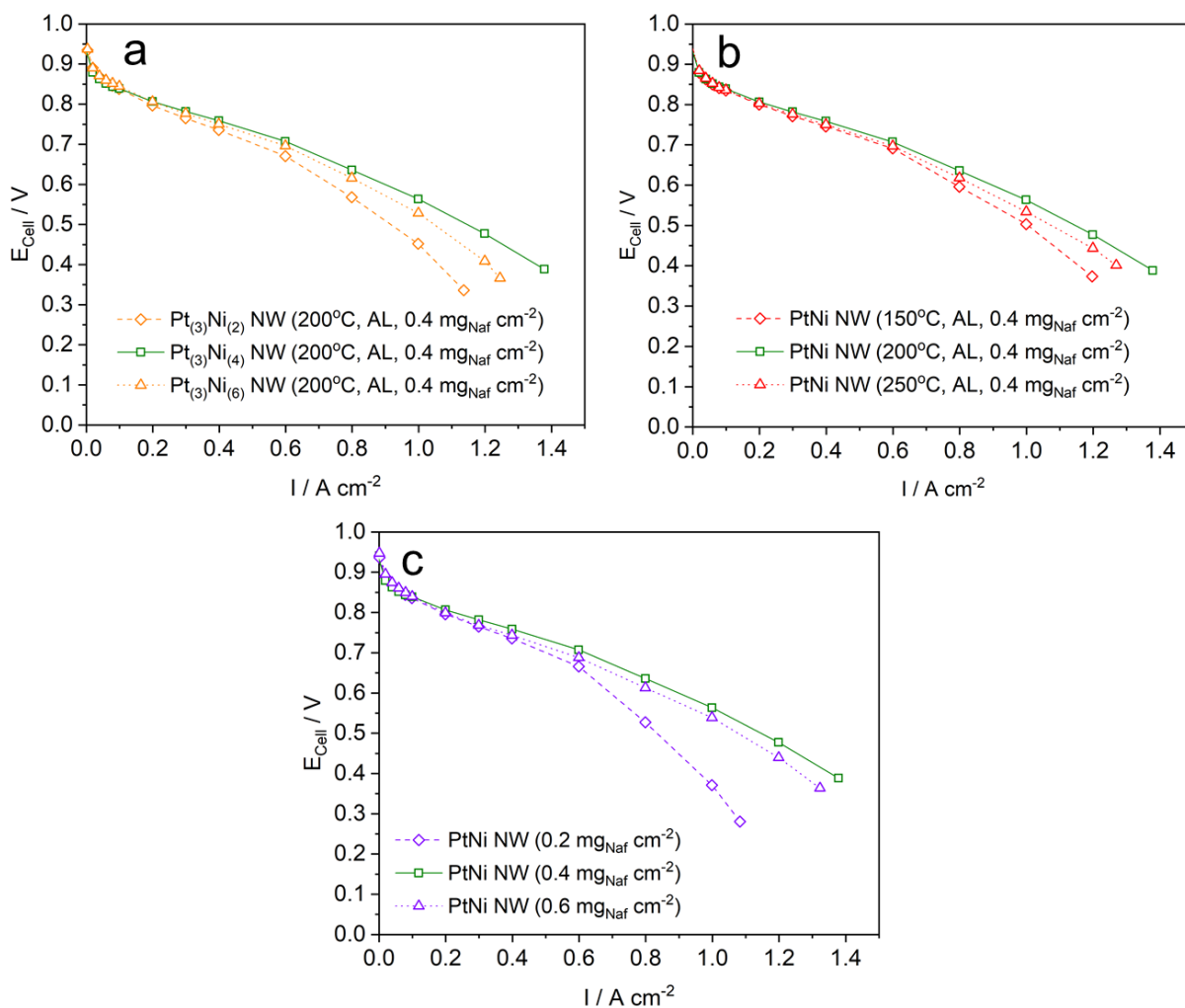
Figure 5.14: Polarisation curves showing the optimisation of the PtNi NW GDEs based on the **(a)** precursor content, **(b)** annealing temperature and **(c)** ionomer content.

5.4.3. Performance of optimised PtNi NW array compared to Pt NW array and Pt/C GDEs

The polarisation and power density curves for Pt/C, Pt NW array and the optimum PtNi NW array ($Pt_{(3)}Ni_{(4)}$ precursor ratio, 200°C annealing temperature, acid leached and 0.4 mg_{Naf} cm^{-2}, herein denoted as PtNi NW array*) GDEs are shown in Figure 5.15a. A clear performance trend of PtNi NW array* > Pt NW array > Pt/C can be seen with power densities at 0.6 V of 0.541, 0.504 and 0.442 W cm^{-2}, respectively. Fuel cell performance is highly dependent on the available effective catalyst surface area and so the H_{des} region of CVs run on the

cathodes was used for quantification [147]. Figure 5.15b shows the recorded CVs where the absolute Pt surface area is quoted in the legend. Assuming 0.312 mg_{Pt} cm^{-2} for each NW GDE based off the ICP-MS data, ECSAs of 40.1 m^2 g_{Pt}^{-1}, (Pt/C with a loading of 0.4 mg_{Pt} cm^{-2}), 21.8 m^2 g_{Pt}^{-1} (Pt NW arrays) and 16.7 m^2 g_{Pt}^{-1} (PtNi NW arrays) were obtained. The lower ECSAs for Pt NW arrays is due to the 1D morphology whereby the surface to bulk ratio is reduced, and is expected based on previous studies on this catalyst system [35]. More importantly the PtNi NWs showed a slightly reduced surface area to Pt compared to the Pt NW arrays, and so the minor improvement in fuel cell performance can only be ascribed to the contribution of the alloyed Ni.

To elucidate the performance enhancement, electrochemical impedance spectroscopy (EIS) analysis was conducted in the low, medium and high current density regimes with Nyquist plots shown in Figures 5.16. All GDEs exhibited a near identical HFR indicative of the similar proton conductivity of the PEM and negligible blockage of sulphuric acid groups for the PtNi NW array GDE. In the low current density region (Figure 5.16a) MEAs from the Pt NW arrays and Pt/C nanoparticles exhibited very similar Nyquist plots with near identical charge transfer resistances. One difference is a reduced slope for the Pt NW array GDE compared to Pt/C nanoparticle GDE in the mid-high frequency range. This can be potentially indicative of a higher ionic resistivity in the Pt NW array CL (*cf.* Pt/C), as a result of sub-optimal ionomer-NW contact [163,195]. The PtNi NW GDE, however, shows a similar trend to the Pt/C GDE in this region which could suggest improved contact between the NWs and ionomer because of the increased hydrophilicity of the PtNi NW surface [158]. More distinctly is a smaller charge transport resistance for the PtNi NW array GDE confirming the improved ORR catalytic activity for the PtNi NW GDE compared to both the Pt/C and Pt NW array GDEs.
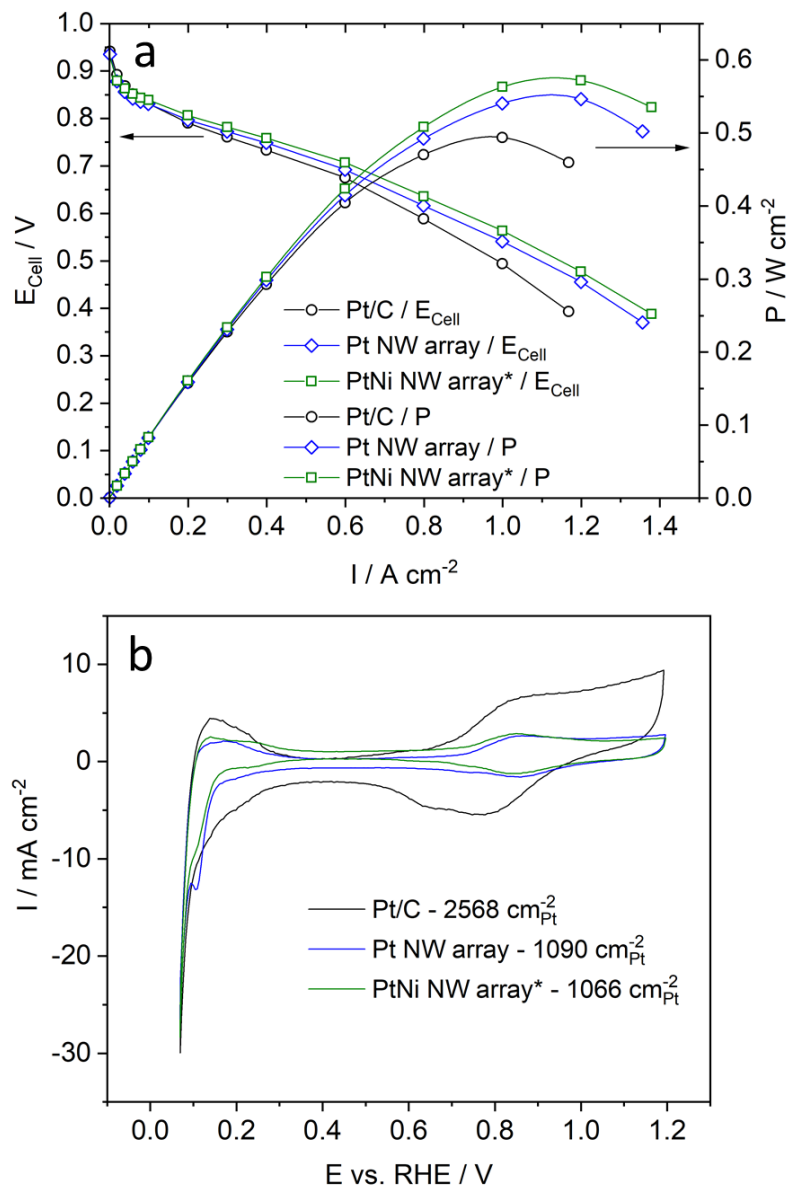
Figure 5.15: (a) Polarisation and power density curves and **(b)** CVs for the Pt/C, Pt NW array and PtNi NW array* GDEs. Number in the legend of **(b)** indicates the absolute Pt surface area.

At large currents (low voltage 0.65 and 0.5 V), the charge transfer resistances for the MEAs with the Pt and PtNi NW array GDEs are both equally smaller than that of the Pt/C GDE. An explanation is proposed: While the half-cell rotating disk electrode measurement is frequently used to quantify the ORR activities, it is limited to this quantification near OCP where there are very few mass transport limitations [167]. Zalitis *et al.* developed a 'floating electrode'

technique, which allows the measurement of kinetic performance at higher overpotential by providing an ideal mass transport environment [196]. In so doing, modifications to the "double-trap model" were proposed to include the effect of adsorbed peroxide intermediates at higher over-potentials [197]. This work helps to confirm the proposed switching of a dissociative ORR mechanism to an associative one [40]. Therefore, different catalyst materials will have different kinetic ORR activities at different cell potentials. As such, the charge transfer resistance loops here suggest that while the PtNi NW shows slightly enhanced ORR performance at the high cell potential, at the low potential the difference is negligible.
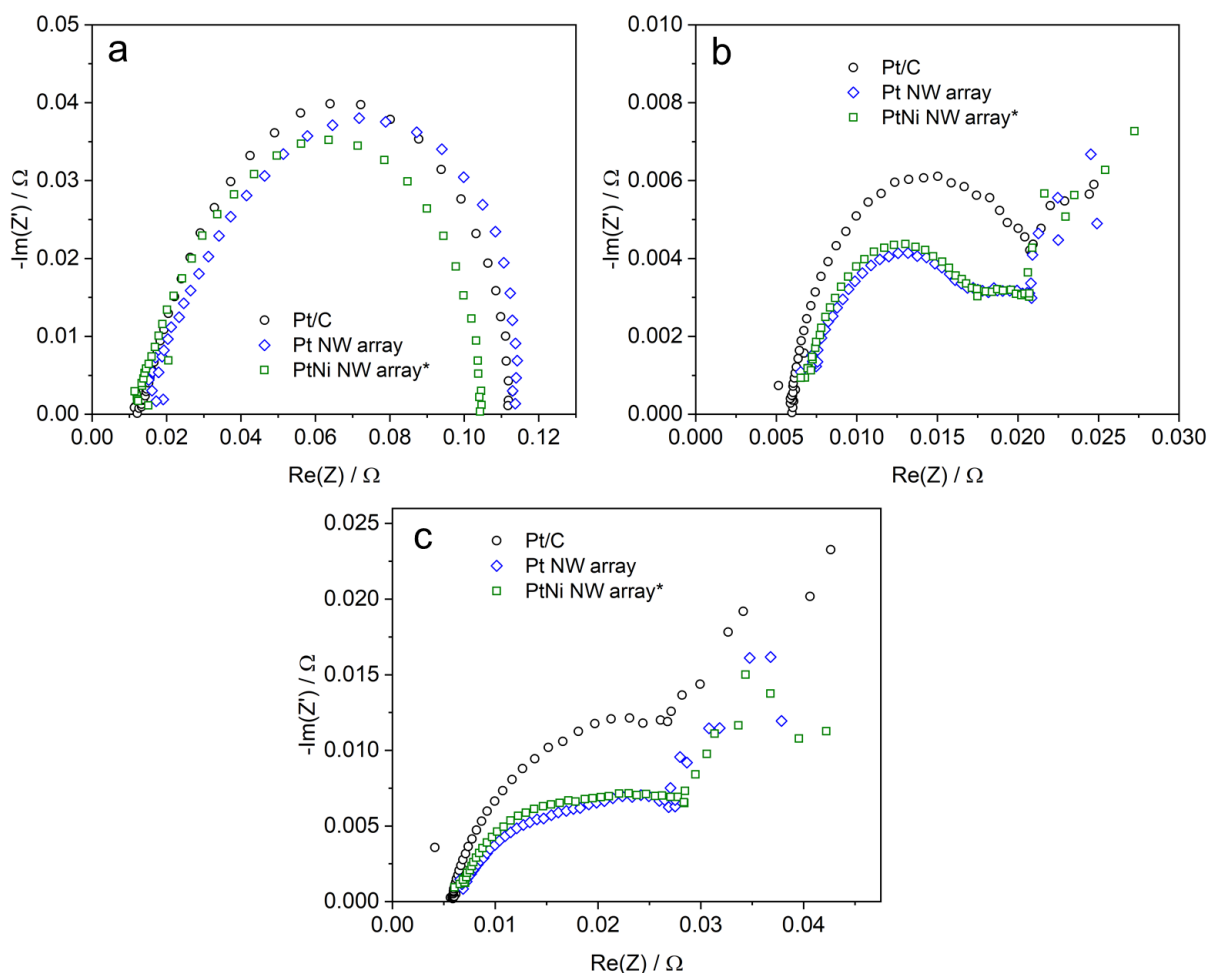
Figure 5.16: EIS conducted on the Pt/C, Pt NW array and PtNi NW array* GDEs at **(a)** 30 mA cm^{-2}, **(b)** 0.65 V and **(c)** 0.5 V.

To minimise the influence of mass transfer losses in the MEA test and focus on the ORR catalytic activity in the near OCP region, polarisation curves were run in O_2 under standard DoE testing protocol. These were corrected for internal resistances and hydrogen crossover and presented as a Tafel plot in Figure 5.17. Both MEAs with the NW GDEs exhibited lower OCPs in comparison to that of Pt/C as a result of their lower Pt surface area and as such the mass activity at 0.9 V increased modestly from 0.060 A mg_{Pt}^{-1} for Pt/C to 0.062 and 0.070 A mg_{Pt}^{-1} for Pt NW arrays and PtNi NW arrays*, respectively. Specific activities of 326, 285 and 150 µA cm_{Pt}^{-2} at 0.9 V were also obtained to give the respective ORR kinetic performance of PtNi NW arrays* > Pt NW arrays > Pt/C. The enhanced specific activity is due to the preferential exposure of active facets for the NW catalysts [198] and with Ni, the addition of lattice strain effects [22]. Reduced Tafel slopes of 44 mV dec^{-1} (Pt NW array) and 38 mV dec^{-1} (PtNi NW array) were found for the NW array GDEs in comparison to the Pt/C GDE which has a Tafel slope of 69 mV dec^{-1}. The reduced Tafel slope for these GDEs with low Pt loadings here indicates a positive contribution from NW array CL structure [32,147,199]. Coinciding with R_{CT} from the EIS in Figure 5.16, the PtNi NW array* GDE exhibited a larger Tafel slope (96.4 mV dec^{-1}) in the low potential region to the Pt NW array GDE (81 mV dec^{-1}). While the difference is small, evidence is of different kinetic performance for these catalysts for the different ORR mechanisms.
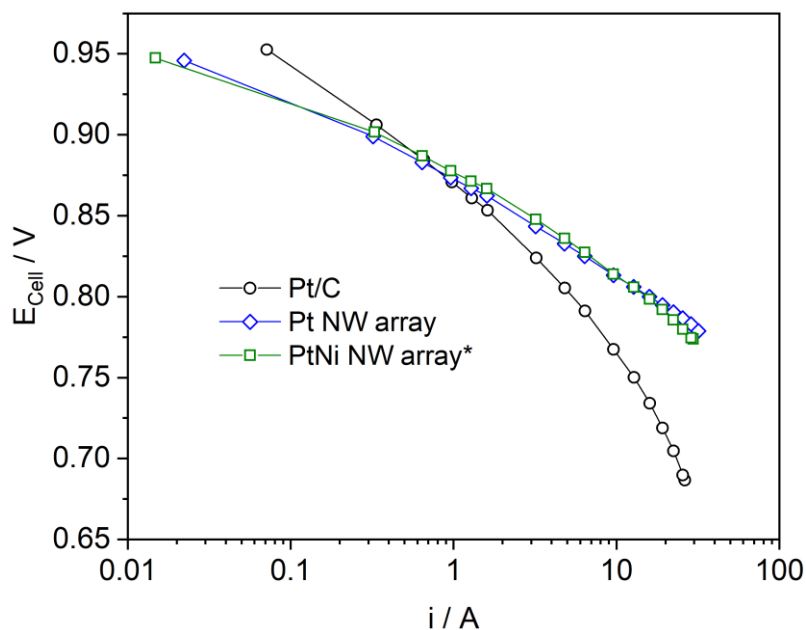
Figure 5.17: Tafel plot based on the corrected polarisation curves for the MEAs with the Pt/C, Pt NW array and PtNi NW array* GDEs using standard DoE testing protocol.

5.4.4. Stability test of the Pt/C, Pt NW GDE and PtNi NW GDEs

To evaluate the stability of the best performing PtNi NW array* GDE, AST was conducted whereby 3000 CV cycles were run under an N_2 atmosphere in the potential range 0.6–1.2 V vs. RHE in comparison to both the Pt NW and Pt/C GDEs. The Pt/C GDE suffered an ECSA loss of 76% (Figure 5.18). The Pt NW array electrode on the other hand only suffered an ECSA loss of 51%, which is consistent with previous studies that show higher resistance of 1D Pt nanostructures to the common degradation mechanisms of Ostwald ripening and Pt dissolution [108,200]. The PtNi NW array* GDE however incurred an ECSA loss of 60%, slightly higher than that of pure Pt NWs. This further indicates the decay of the ionomer because of the ion exchange resulting in reduced number of sites with proton accessibility, decreasing the triple phase boundary and ECSA [142]. Alternatively, Ni in the catalyst could also adversely affect the dissolution mechanism of Pt in the MEA environment.
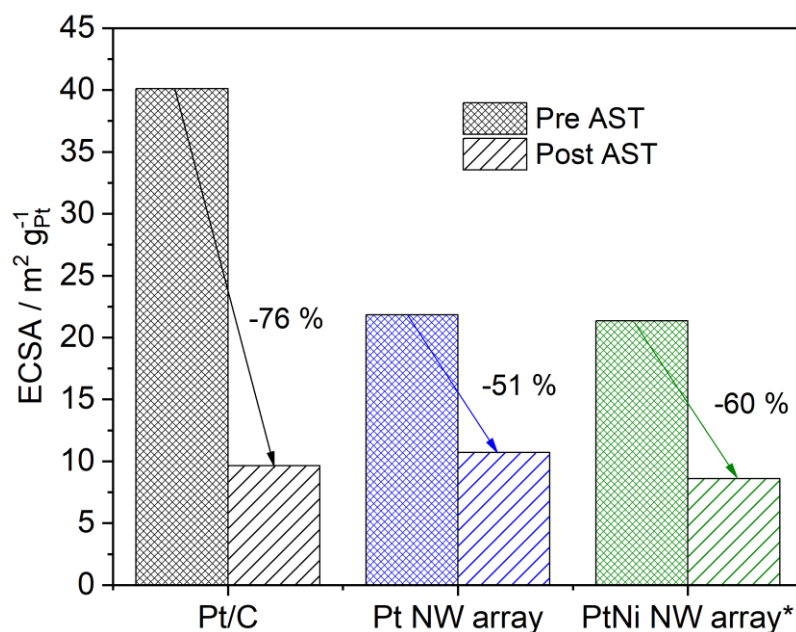
Figure 5.18: Histogram showing the ECSA of the Pt/C, Pt NW array and PtNi NW array* GDEs before and after the AST.

With regards to power performance, after AST the power densities at 0.6 V were 0.308, 0.393 and 0.390 W cm^{-2} for the MEAs with the Pt/C, Pt NW array and PtNi NW array* GDEs, respectively (Figure 5.19), corresponding to losses of 30, 22 and 28%. For the PtNi NW array* GDE, one of the major contributing factors is the ECSA loss as demonstrated in Figure 5.18, and the ionomer contamination further negatively affected the fuel cell performance. An additional performance loss can also be attributed to Ni leaching and hence activity loss, resulting in an almost overlapping polarisation curve as that of the Pt NW GDEs. Nevertheless, both NW array GDEs still show improved stability in comparison to the one made with the commercial Pt/C catalyst.
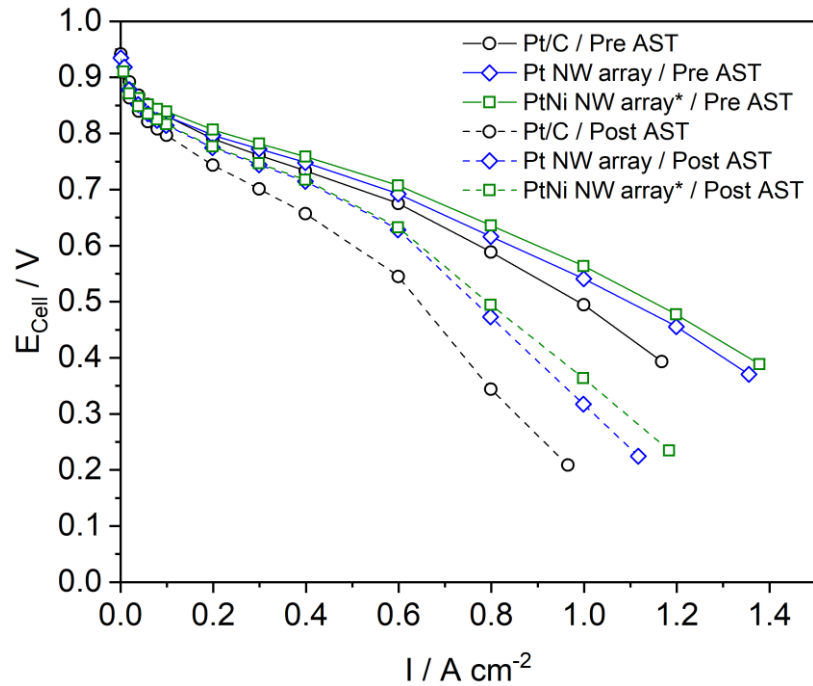
Figure 5.19: Polarisation curves for the MEAs with the Pt/C, Pt NW array and PtNi NW array* GDEs before and after AST.

5.5. Ex-situ GDE testing

After all optimisations, the PtNi NW array* GDE demonstrated only moderately improved power performance in the fuel cell test as compared to the Pt NW GDE. The conclusion is that in the single cell, Ni is leached out of the PtNi NWs and contaminates the local ionomer thus increasing local O_2 mass transport resistance and proton conductivity. To support this, ex-situ GDE measurements were run on the Pt NW array and PtNi NW array* GDEs where the ORR catalytic activity can be better evaluated.

Two GDEs of the Pt NW and PtNi NW arrays (200°C, AL) were tested, with and without prior coating of Nafion® ionomer (0.6 mg_{Naf} cm^{-2}). Cleaning CVs and slower scan CVs were firstly conducted whereby the catalyst surface area was determined. Figure 5.20 shows the slow scan CVs from which the ECSA was calculated. Very small ECSA and double layer capacitive charging were found for those GDEs without ionomer (4.2 m^2 g_{Pt}^{-1} for Pt NW

arrays and 5.5 m^2 g$_{Pt}^{-1}$ for PtNi NW arrays*), indicating that the hydrophobic GDL results in poor penetration of the liquid electrolyte and so most catalysts remain inactive. With ionomer larger ECSAs than in the MEA test were found with values of 26.8 and 29.0 m^2 g$_{Pt}^{-1}$ for the Pt NW and PtNi NW array GDEs, respectively.
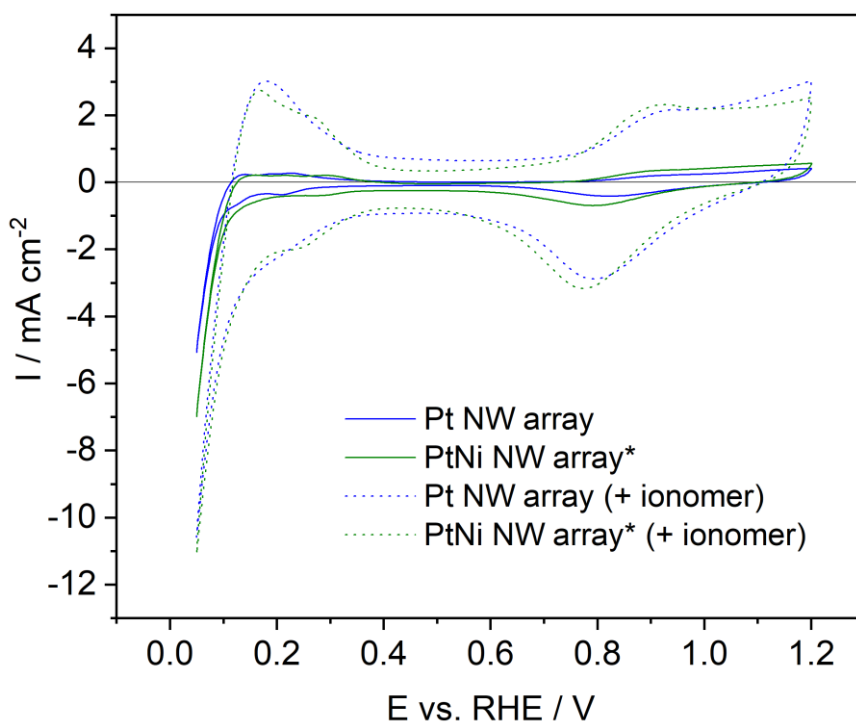
Figure 5.20: CVs of the Pt NW array and PtNi NW array* GDEs with/without ionomer coating.

After this test the electrolyte was saturated with O$_2$ and the OCP was monitored until it reached a plateau. Table 5.1 lists the OCP values for all GDEs. It can be seen that the OCP of each GDE was lower when ionomer is present, which can be ascribed to the lower O$_2$ solubility in the ionomer thin film as compared to that in the liquid electrolyte [201,202]. Nevertheless, the increased ECSA improves the catalytic performance as shown by the kinetic region of the linear sweep voltammograms (LSVs) (Figure 5.21). Table 5.1 lists the specific activities at 0.9 V vs. RHE. These activities are not comparable to most RDE data because here the GDE is used rather than the catalyst thin film and no rotation can be used

to minimize other influences. For the Pt NW arrays, the measured specific activity with and without ionomer are very similar; 19.0 and 19.9 μA cm_{Pt}^{-2} respectively. PtNi NW array* without ionomer showed a 3.10 fold increase in specific activity (61.7 μA cm_{Pt}^{-2}) as compared to Pt NW arrays, clearly demonstrating enhanced catalytic activity of the ORR on the alloyed PtNi NW surface. However, the specific activity of PtNi NW array* with ionomer is 49.8 μA cm_{Pt}^{-2}. While the enhancement for PtNi observed by ex-situ GDE the measurement is much larger than that exhibited in the MEA test, an unfavourable interaction between Ni and the ionomer layer is clearly reducing catalytic activity in addition to increased mass transport resistances in the MEA test.
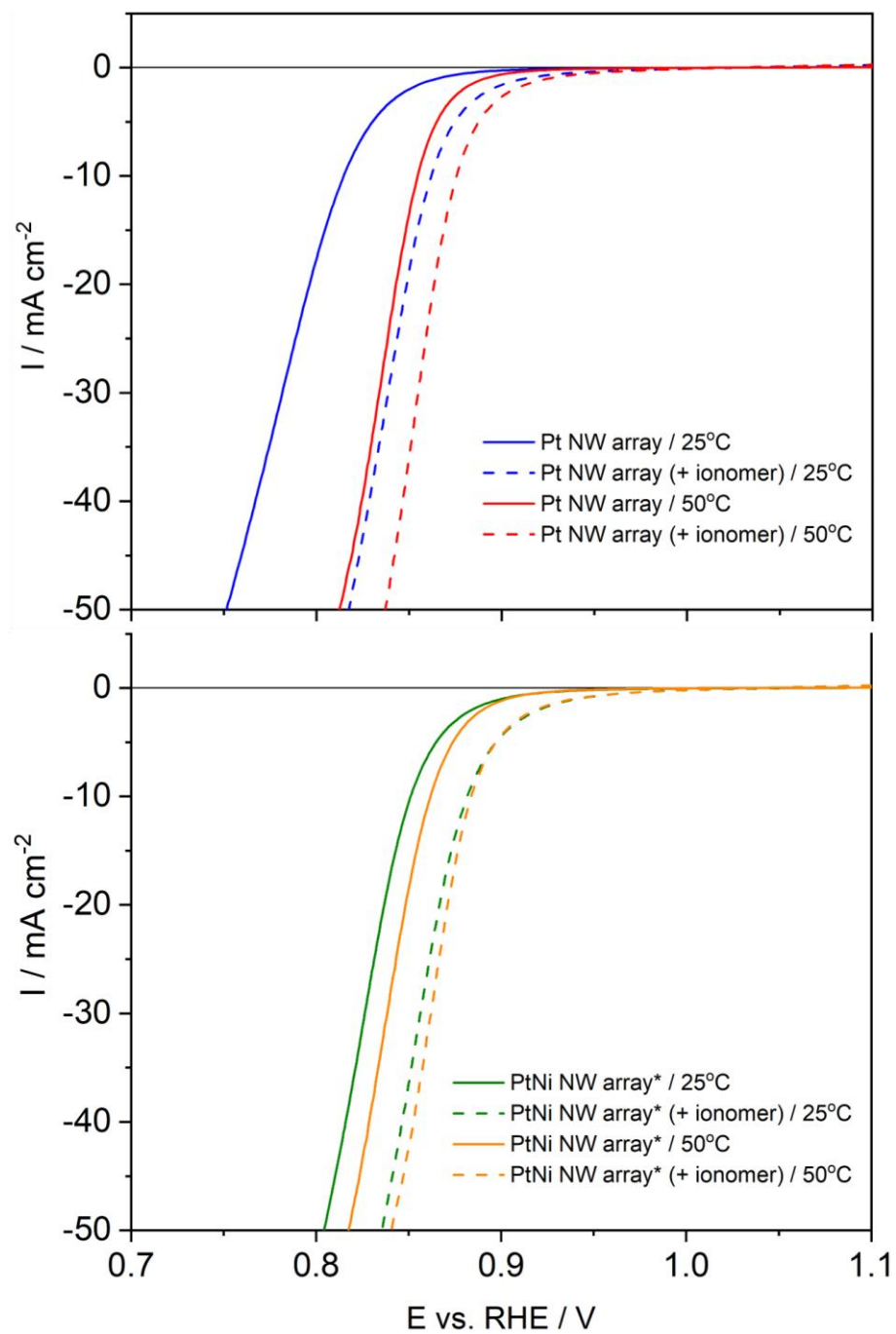
Figure 5.21: Corrected LSVs between 1.2–0.4 V vs. RHE for the Pt NW array and PtNi NW array* GDEs with/without ionomer coating at temperatures of 25 and 50°C. The kinetic region (1.1–0.7 V vs. RHE) is shown.

Table 5.1: ECSA, OCP and kinetic analysis of the ex-situ tested GDEs:

Sample	ECSA m² g$_{Pt}$⁻¹	OCP V	Mass activity (0.9 V vs. RHE) / mA mg$_{Pt}$⁻¹	Specific activity (0.9 V vs. RHE) / μA cm$_{Pt}$⁻²
Pt NW array	4.2	1.044	0.832	19.9
PtNi NW array*	5.5	1.062	3.39	61.7
Pt NW array (0.6 mg$_{Naf}$ cm⁻²)	26.8	1.029	5.08	19.0
PtNi NW array* (0.6 mg$_{Naf}$ cm⁻²)	29.0	1.056	14.4	49.8
Pt NW array / 50°C	3.3	1.041	1.89	60.4
PtNi NW array* / 50°C	2.4	1.030	3.97	162.1
Pt NW array (0.6 mg$_{Naf}$ cm⁻²) / 50°C	25.9	1.024	8.65	33.4
PtNi NW array* (0.6 mg$_{Naf}$ cm⁻²) / 50°C	31.3	1.039	13.9	44.5

To understand this further, ex-situ GDE measurements were also performed at 50°C. Similar ECSAs were obtained at the higher temperature, but there were key changes observed to the LSVs in the kinetic region (Figure 5.21). The activities are listed in Table 5.1 and Figure 5.22 shows the relative improvements in specific activity for each GDE at the elevated temperature. The Pt NW array GDE gained a 3.04-fold increase in specific activity whereas the PtNi NW array* GDE samples increased less (2.63-fold with respect to the activity at 25°C). The reduced increase for PtNi is thought to be due to Ni leaching out of the NWs causing lattice relaxation of the NWs. However, this gap is more pronounced with an ionomer coating. Where the Pt NW array (+ ionomer) GDE gained a 1.76-fold increase in specific activity through the higher temperature, the PtNi NW array* (+ ionomer) showed a reduced activity as compared to that obtained at 25°C. Even though O$_2$ permeability through the ionomer layer is a key factor in the high current density region of the polarisation curves, the region in which specific activity is acquired is often assumed to have negligible mass transport limitations. In this was the measured current corresponds to the activity inherent of the catalyst surface. These results suggest otherwise, where synergistic effects of Ni leaching and ionomer contamination result in a reduced activity of PtNi NW array* GDEs at

elevated temperature. Such phenomena can be used to explain the much reported disparity between the RDE measurement and MEA test (including that reported in Chapter 4), leading to the conclusion that either the alloyed component needs to be much more stabilised, or greater emphasis should be made on using these catalysts in ionomer free GDEs where at least the later contribution can be mitigated [203].
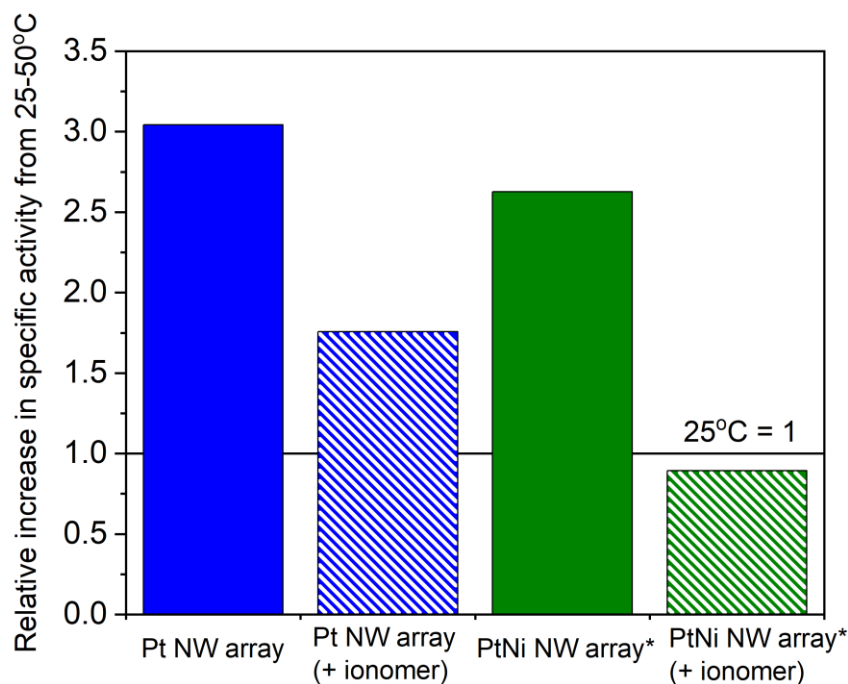
Figure 5.22: Relative increases in specific activity measured at 50°C with respect to 25°C for the GDEs (0.9 V vs. RHE).

5.6. Conclusions

The synthesis methodology of the PtNi NW/C catalysts in Chapter 4 was successfully adapted for the fabrication of the PtNi NW array GDEs. An optimal annealing temperature of 200°C was established. Cross-sectional SEM and ICP-MS analyses show that using a wet chemical impregnation method, Ni deposits primarily at the carbon fibre/MPL interface. Significant reductions in the electrode performance observed can be ascribed to ionomer contamination and ion exchange in the PEM. Acid leaching partially mitigates these effects but low optimal ionomer content was still required for the PtNi NW array GDEs. With these

refinements the PtNi NW array GDE showed ×1.07 and ×1.22 power density of the Pt NW array and Pt/C GDEs, respectively. However, the AST showed that the catalytic activity enhancements of the PtNi NW array GDE cannot withstand extensive operation, and after 3000 CV cycles similar power performance to the Pt NW array GDE was found. Attempts should be made to better elucidate and refine the Pt alloy structure of these NWs in future. The ex-situ GDE test demonstrated the much enhanced catalytic performance of the PtNi NW array* GDE as compared to the Pt NW array GDE. However, this catalytic enhancement is mainly exhibited at low measurement temperature where ionomer contamination from Ni is limited. In particular a reduction in performance was observed for the PtNi NW array* GDE at the higher temperature when ionomer is coated on the surface. This is concluded to be the primary cause of the disparity reported on the catalyst performance obtained from the RDE measurement and the MEA test in the literature, indicating that alloy stability is paramount for both durability and immediate catalytic performances in PEMFCs.

6. Gas diffusion electrodes from short Pt nanorods grown on nitrided carbon nanotube arrays

Some data has been re-analysed and acquired since publication

Besides improving the catalyst metal composition to improve the power performance of 1D nanostructure array electrodes, in this chapter, nitrided carbon nanotube (N-CNT) arrays are introduced as a catalyst support for the in-situ growth of 1D Pt nanostructures to improve the distribution of the catalyst and performance of the GDEs.

6.1. Introduction

With regards to improving the oxygen reduction reaction (ORR) catalytic activity, methods are not limited to changing the metal composition or structure. Support-catalyst interactions mean that by changing the catalyst support, further enhancements in catalytic activity can be made in alternative supports to conventional carbon blacks [204]. While the search for alternative supports includes looking at non-carbonaceous supports such as metal-oxides to circumvent carbon corrosion issues at a high cell potential, a penalty in electron conductivity is often suffered [5,28,122].

Lots of success has been made with alternative carbonaceous supports such as carbon nanotubes (CNTs) and graphene, which can improve both the catalytic activities and stability of the supported Pt catalysts through enhanced electrical conductivity and metal-support interactions [26,27,123]. A hindering factor with these supports is their inert pristine surfaces, which are difficult to deposit the metal catalyst on. Suitable anchoring sites can be provided through surface functionalisation such as the incorporation of surface organic groups [125], metallic seed particles [126,127] or heteroatom dopants [39,128]. In particular, the use of heteroatom doped carbon materials has been shown to increase the binding energy of precious metals to the support surface [130], changing d-band electronic structure of the supported metals and hence improving the catalytic activities [129]. Hetero-atom doping can also induce catalytically active sites on the support through the formation of defect sites [128].

While both graphene and CNT supports have shown improvements in catalyst ORR activity, the use of graphene in a working PEMFC suffers the issue of aggregation and stacking, hindering the effective transport of reactant gases [132,205]. CNTs have demonstrated good performance in working fuel cells. For example, Tang *et al.* sputter coated Pt nanoparticles onto CNTs fabricated directly on the carbon paper by thermal chemical vapour deposition (CVD) and achieved a maximum power density of 595 mW cm^{-2} with a Pt loading of 0.04 mg_{Pt} cm^{-2} (under O_2 gas) [134]. Promising PEMFC performance was also reported for electrodes with Pt supported on CNT arrays, which were fabricated by CVD on quartz or Al substrates and transferred onto the Nafion® membrane during membrane electrode assembly (MEA) fabrication [135,136]. Performance enhancement in these works was more pronounced at the high current density region and was attributed to effective gas and proton transportation throughout the ordered CNTs alongside improved water management characteristics as a direct result of the CNTs hydrophobic properties.

Inspired by these works as well as the improvement in the catalyst activities and PEMFC performance of the Pt NW electrodes, there is clear incentive for the development of GDEs composed of Pt NWs supported on hetero-atom functionalised CNTs in a simple and scalable way. To meet this end, this work demonstrates GDEs from short Pt nanorods in-situ grown on nitrogen doped CNT (N-CNT) arrays. CNT arrays were grown directly on the GDL surface using plasma enhanced CVD (PECVD). Nitriding was achieved using active surface screen plasma (ASP) treatment. The formic acid reduction approach was then used to grow short Pt nanorods onto the N-CNTs. The performance was then evaluated by single cell test showing much enhanced mass transport characteristics in comparison to conventional Pt/C and the Pt NW GDEs presented in Chapter 5.

6.2. Pt/N-CNT GDE catalyst layer (CL) structure

SEM was used to examine the GDL surface before and after the growth of CNTs (Figure 6. 1). Figure 6.1a shows the surface of the untreated Sigracet 39BC GDL, which having a mesoporous layer (MPL) contained carbon nano-spheres of diameter 30–50 nm in aggregates of 100-500 nm. Part of this aggregation is attributable to the 5% poly tetrafluoroethylene (PTFE) coated in the MPL to prevent water flooding during fuel cell operation. After CNT growth and nitriding, Figure 6.1b shows a thin porous layer on-top of the GDL. While the ordering is not as vertically aligned as can be achieved by CVD on a planar substrate [135], the N-CNTs clearly protrude from the surface in a similar way to Pt NW arrays (Figure 6.1c) so we still describe it as N-CNT array in this chapter [32].
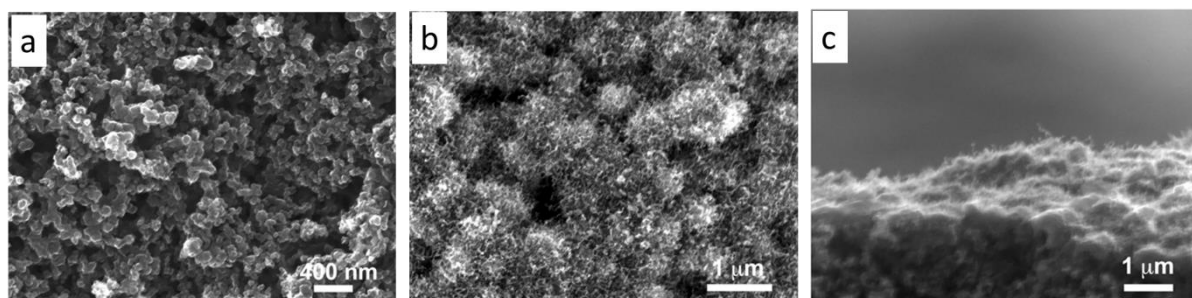
Figure 6.1: Surface SEM images of **(a)** 39 BC GDL and **(b and c)** N-CNT array GDL. **(c)** shows the cross-section SEM image of the N-CNT array GDL.

Figure 6.2a and 6.2b show the top down and cross-sectional SEM images of the Pt/C GDE, respectively, showing a compact CL. A similar structure is seen with the NW GDE (Figure 6.2c) where the ultrathin nature of the NWs shows no visible changes to the GDE morphology on a mesoporous scale.
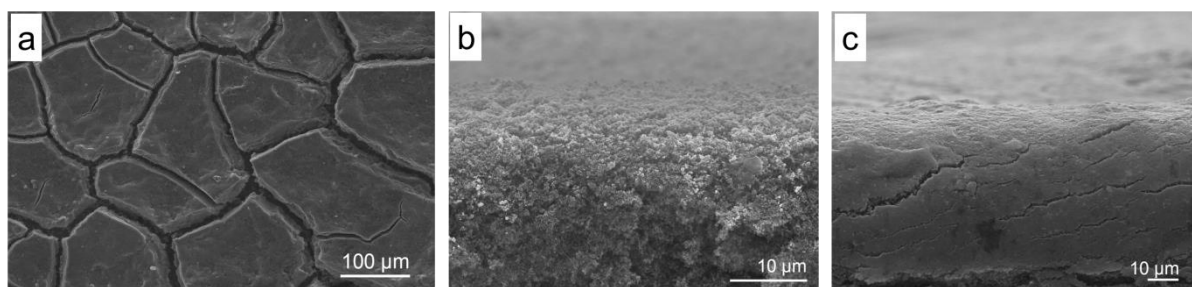
Figure 6.2: (a) Surface and **(b)** cross sectional SEM images of the Pt/C nanoparticle GDE and **(c)** Pt NW GDE.

To quantitatively analyse the porosity of the prepared GDEs, Hg porosimetry was conducted on the 39 BC GDL as well as the Pt/C, Pt NW array and Pt/N-CNT array GDEs. The pore size distribution data (Figure 6.3) indicates a similar meso-pore size distribution pattern for the 39 BC GDL, Pt/C and Pt NW array electrodes, but the Pt/N-CNT array GDE shows a higher fraction of larger macropores with a peak in the range 315–360 nm, as a result of the open CL structure shown in the SEM images.
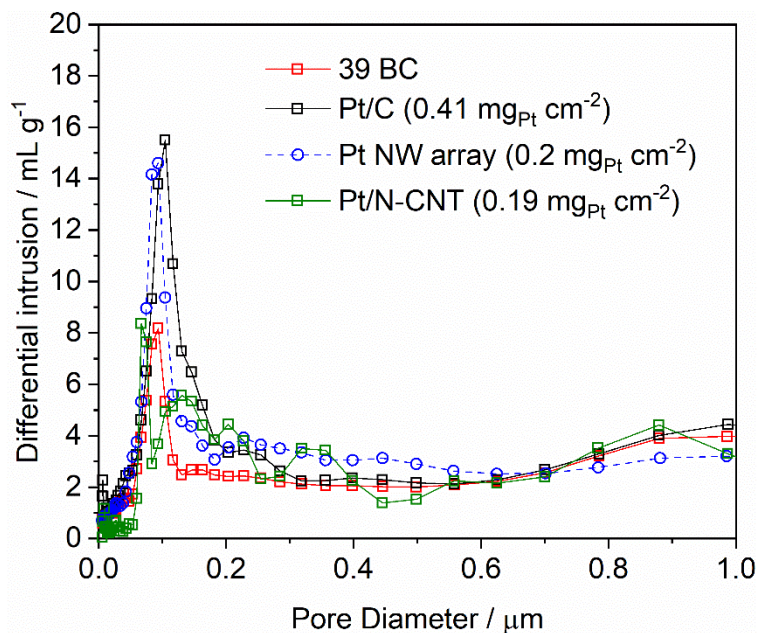
Figure 6.3: Pore size distribution of the 39 BC GDL, Pt/C, Pt NW array and Pt/N-CNT GDEs obtained by Hg porosimetry.

After GDE fabrication, some of the Pt/N-CNT array CL was scraped off and imaged using high resolution transmission electron microscopy (HR-TEM). The entwined N-CNTs are hundreds of nm long, multi-walled and have an average diameter of around 10–20 nm (Figure 6.4a). This result is very similar to the CNT structure obtained by Shen *et al.* who used a PECVD technique with an Al foil substrate [136]. From Figures 6.4b and 6.4c, it can be seen that short Pt nanorods and NPs are grown on the surface of the N-CNTs. The good Pt dispersion is thought to have been aided by defects induced by the nitriding process, which provides the initial nucleation sites for the Pt seeds to form [107], as well as the high reaction temperature (i.e. 40 °C) employed, which has been shown to improve the NW dispersion on the GDL surface [32]. As a result of the highly dispersed Pt seeds, the short nanorods have lengths up to just 10 nm and ultrathin diameters of ca. 3–4 nm, in comparison to the typical long NW variants achieved at the low reaction temperature [109,179]. The smaller length agrees with work by Sui *et al.* where the prior introduction of Pt seeds before the NW growth produced more dispersed but shorter NWs [165]. Figure 6.4d shows a HR-

141

TEM image of the Pt on N-CNT, and an inter-lattice spacing of 0.23 nm is observed as typical with the preferential growth of the NRs in the <111> direction. The ability to resolve this also indicates the highly crystalline nature of the formed Pt NRs.
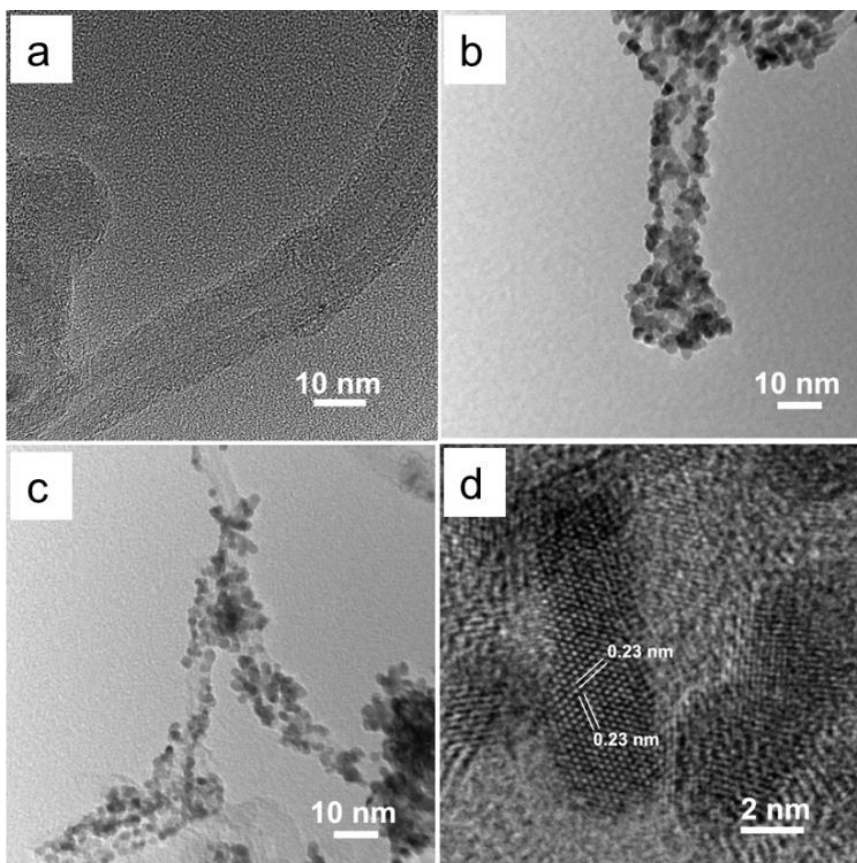
Figure 6.4: (a) TEM images of the N-CNTs supported on the GDL surface, **(b,c)** Pt/N-CNTs scraped off the GDE surface and **(d)** HR-TEM images of Pt nanorods demonstrating the inter-lattice spacing of single crystal Pt nanorods growing along the <111> direction.

6.3. Pt/N-CNT GDE structure characterisation

Thermal gravimetric analysis (TGA) analysis was utilised to determine the Pt loading of the Pt/N-CNT GDE. 1 cm^2 GDE pieces were used and so the left-over mass corresponds to the Pt loading in mg cm^{-2}. Figure 6.5 shows the TGA plots where the big drop in 300–850°C is caused by the combustion of the carbon GDL and CNT support. The drop occurred at a slower rate than the TGA plot of the PtNW/C GDE in Chapter 4 due to the use of the mixed

air and N_2 gas flow. The remaining material was Pt and hence Pt loadings of 0.41 mg_{Pt} cm^{-2}

and 0.19 mg_{Pt} cm^{-2} were determined for the Pt/C and Pt/N-CNT GDEs, respectively. While a

loading of 0.4 mg_{Pt} cm^{-2} was expected for the Pt/N-CNT GDE, the high CNT deposition

temperature possibly resulted in the decomposing of the PTFE binder in the MPL thus

making the structure loose, then some of CNTs with deposited catalysts might be washed

away in the post cleaning process.
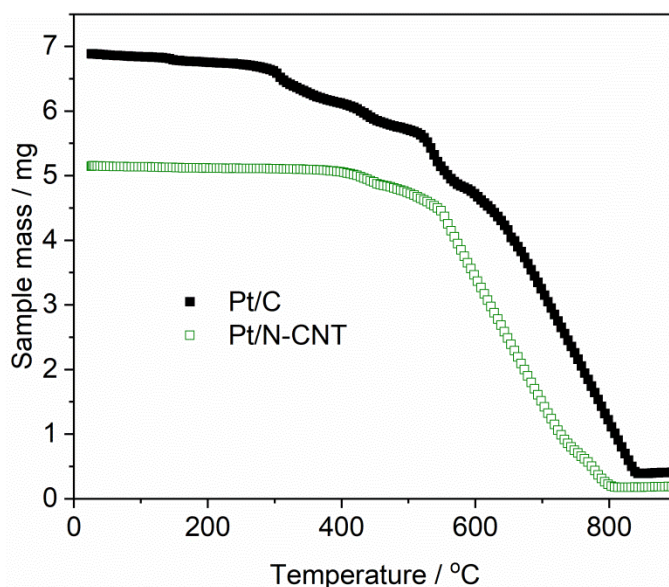
Figure 6.5: TGA plot of the Pt/C and Pt/N-CNT GDEs in a 60 mL min^{-1} flow of air and N_2 (2:1

volume ratio) in the range 25–900°C. The heating rate was 10°C min^{-1}.

XRD patterns of the Pt/C, N-CNT GDL and Pt/N-CNT GDEs are shown in Figure 6. The

amorphous carbon and complex composition of the GDL induced a large background noise,

together with the low Pt loadings giving low intensities for the Pt peaks (Figure 6.6a). The

peaks in the 2θ range of 12–25° and 26.6° result from amorphous carbon and graphitic

carbon, respectively [192]. The Pt peaks presented are indexed to JCPDS-04-0802. The

crystalline nature of the Pt/N-CNT was further confirmed by the XRD pattern of Pt grown on

N-CNT arrays made on a Si substrate (Figure 6.6b) where a very strong peak intensity was

recorded, further indicating the large influence of the substrate used. The XRD pattern of the

Pt/N-CNT GDE shows a higher intensity compared to the Pt/C GDE demonstrating a higher degree of crystallinity with the nanorods (*cf.* nanoparticles).
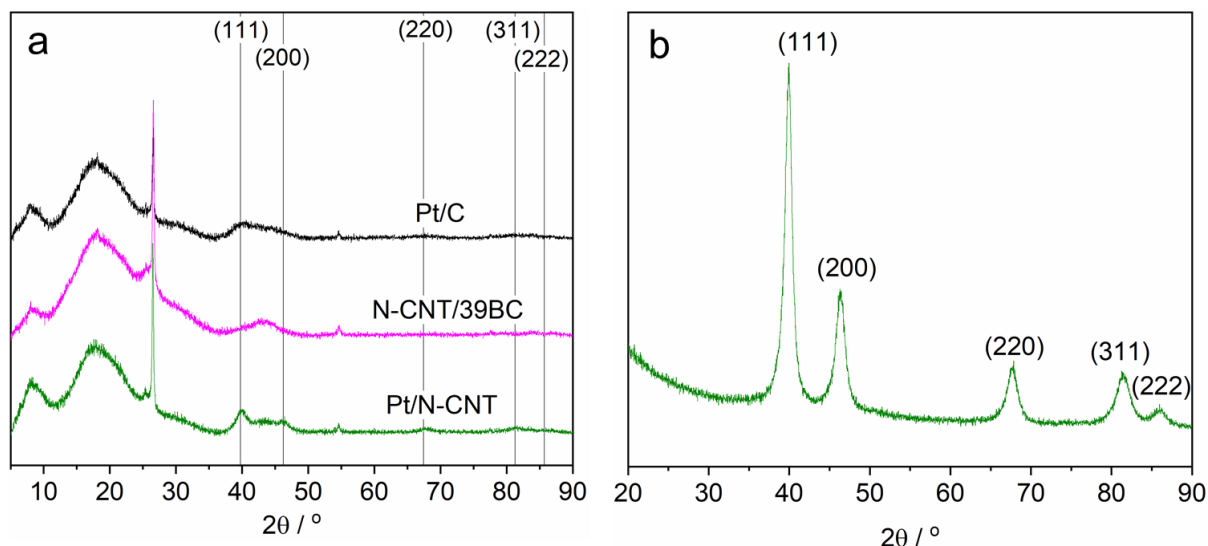
Figure 6.6: XRD diffraction patterns of **(a)** the Pt/C, N-CNT/39BC and Pt/N-CNT GDL/GDEs and **(b)** Pt/N-CNT grown on Si wafer.

To confirm the nitriding process and elements in the Pt/N-CNT catalysts, XPS was conducted on the GDEs and GDLs at various stages of the Pt/N-CNT GDE fabrication. The survey spectra are presented in Figure 6.7. It can be seen that with the process and the adding of materials, the F(KLL) and F(1s) peaks show a clear decrease (ca. 840 eV and 700 eV, respectively). In the high resolution scan of the C1s region this is also accompanied with a low contribution of the CF_3 and CF_2 peaks of about 5 at. %, instead of 27-35 at. % with the 39 BC and CNT/39BC GDLs (Figure 6.7). This suggests that the nitriding process degraded the PTFE on the surface in the GDL.
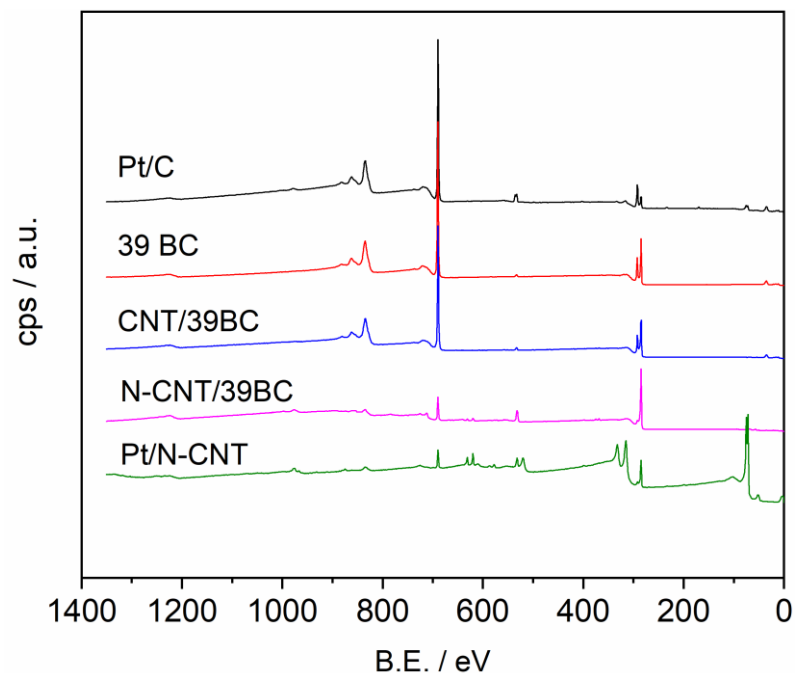
Figure 6.7: Survey XPS spectra for the Pt/C and the Pt/N-CNT GDE at various stages of the fabrication.

The introduction of nitrogen into the CNT structure was confirmed by the high resolution scan of the N1s region where peaks were observed for the N-CNT/39BC, Pt/N-CNT and Pt/C catalysts (Figure 6.8). N1s peaks were fitted with characteristic peaks for pyrridinic (398.1 eV), pyrrolic (399.4 eV), quaternary (400.8 eV) and pyridinic N-oxide (403.4 eV) [39,206]. Quaternary and pyrrolic N peaks are the largest contributors in the spectrum of N-CNT/39BC. Pyridinic N with the addition of M-N peaks (397.2 eV) becomes more prominent after the growth of Pt onto the N-CNT surface. The increase in pyridinic N here suggests that while Pt deposition occurs on the hetero-atom dopants or defects induced by such dopants [207], the Pt growth also induces defects that promote further nucleation. Nanorod lengths therefore remain short and extended NW structures as seen on amorphous carbon are not observed [34].
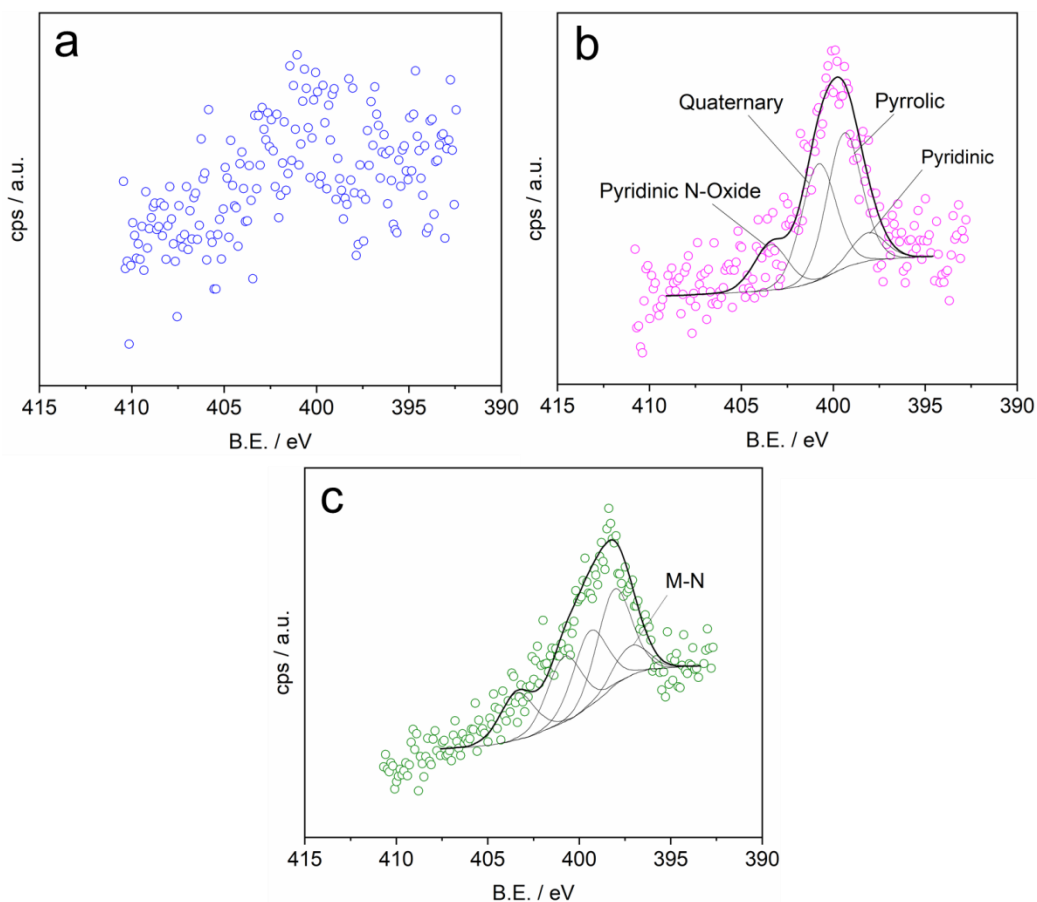
Figure 6.8: N1s XPS spectra for **(a)** CNT/39BC, **(b)** N-CNT/39BC and **(c)** the Pt/N-CNT GDE.

Figure 6.9 shows the Pt4f XPS spectra for the Pt/C and Pt/N-CNT GDEs. The intensity of the peaks for Pt/N-CNT GDE are much higher than that for Pt/C indicating that most of the Pt is present at the surface of the former GDE. This is consistent with the XPS of the Pt NW GDE in Chapter 5. Analysis indicates that Pt within Pt/N-CNTs is composed almost entirely of Pt(0) whereas Pt within Pt/C is composed of 56 at. % Pt(0), 34 at. % Pt(II) and 10 at. % Pt(IV). A small Pt(0) 7/2 peak shift of around 0.25 eV to lower binding energies is also observed for the Pt/N-CNT GDE which is similar to that of the Pt NW GDE in Chapter 5 and so differences in oxide proportion could be an artefact of the 1D crystal structure.
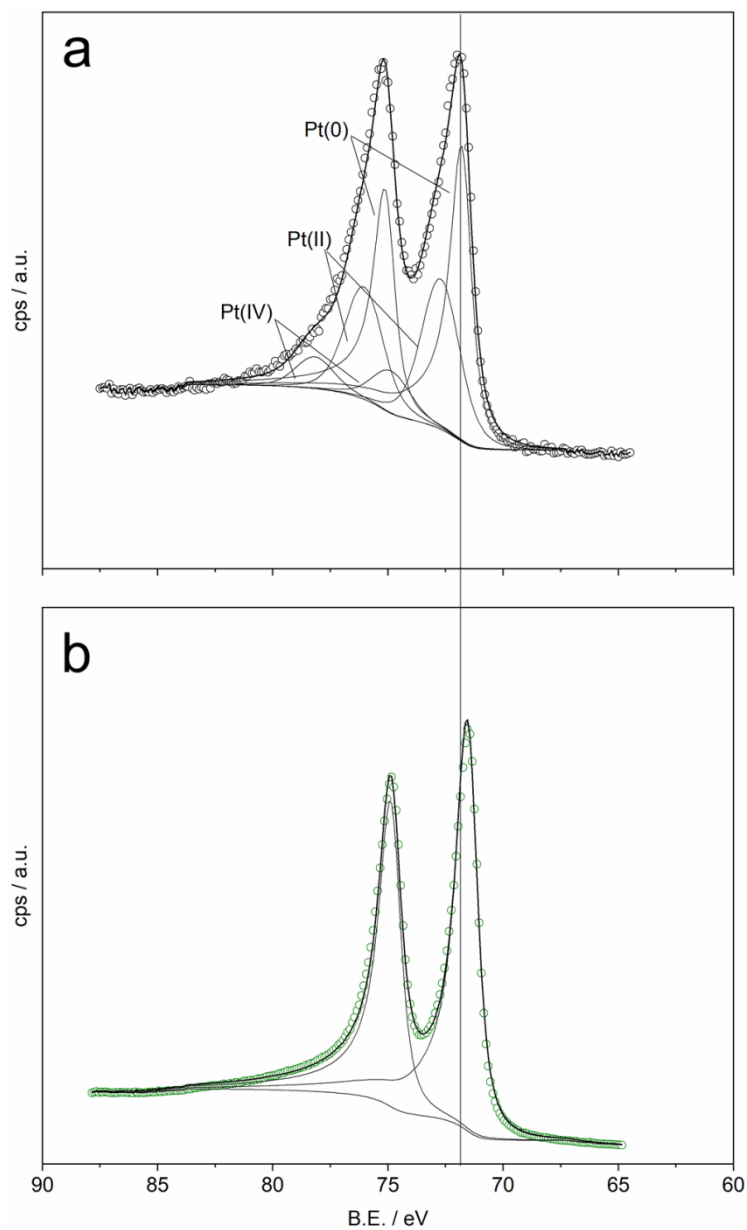
Figure 6.9: Pt4f XPS spectra of **(a**) Pt/C and **(b)** Pt/N-CNT GDEs.

The C1s spectra for the Pt/N-CNT GDE is presented in Figure 6.10. While C1s spectra of graphene sheets typically shows sp^2 or sp^3 hybridisation, no such analysis was possible with the GDE due to the abundance of mesoporous carbon from the original 39 BC GDL. Therefore, the C1s scan was fitted with a single symmetrical peak at approximately 284.8 eV, typical of sp^3 hybridisation.
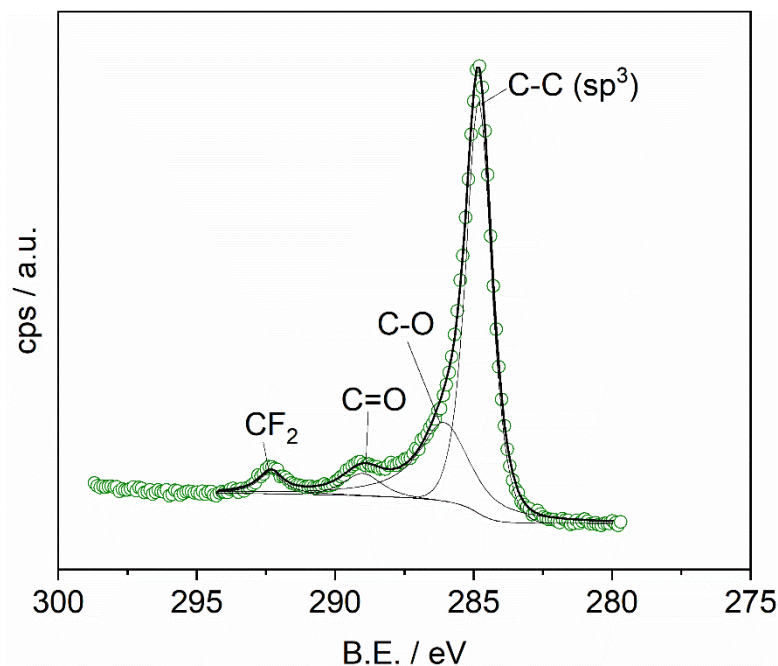
Figure 6.10: C1s XPS spectrum of Pt/N-CNT GDE.

6.4. Pt/N-CNT GDE single cell performance

The catalytic performance of the Pt/N-CNT GDE in comparison to the Pt/C and Pt NW array GDEs was evaluated by an MEA test using a polarisation curve recorded according to the EU harmonised protocol to mirror the conditions expected in automotive applications [168]. The Pt/N-CNT GDE with the lower Pt loading is compared with the Pt/C GDE with 0.41 mg_{Pt} cm^{-2} and Pt NW array GDE with 0.312 mg_{Pt} cm^{-2}. Figure 6.11a shows the polarisation and power density curves for the Pt/C, Pt NW array and Pt/N-CNT GDEs. At 0.6 V, the power densities recorded are 0.442, 0.504, and 0.544 W cm^{-2}, respectively. Therefore, with around half of the Pt loading, the Pt/N-CNT GDE achieves a 1.23-fold increase in power output in comparison to the Pt/C GDE, and a 1.08-fold increase to the Pt NW array GDE. Figure 6.11b demonstrates this improvement further when the current is normalised to the Pt electrochemical effective surface area within the electrode, clearly showing the Pt/N-CNT GDE to be the superior one. Included in this figure are also Pt/C and Pt NW array GDEs with optimal loadings of 0.2 mg_{Pt} cm^{-2} to show that the performance enhancement from the Pt/N-

CNT GDE is mainly contributable to reduced mass transport through increased CL meso-porosity.
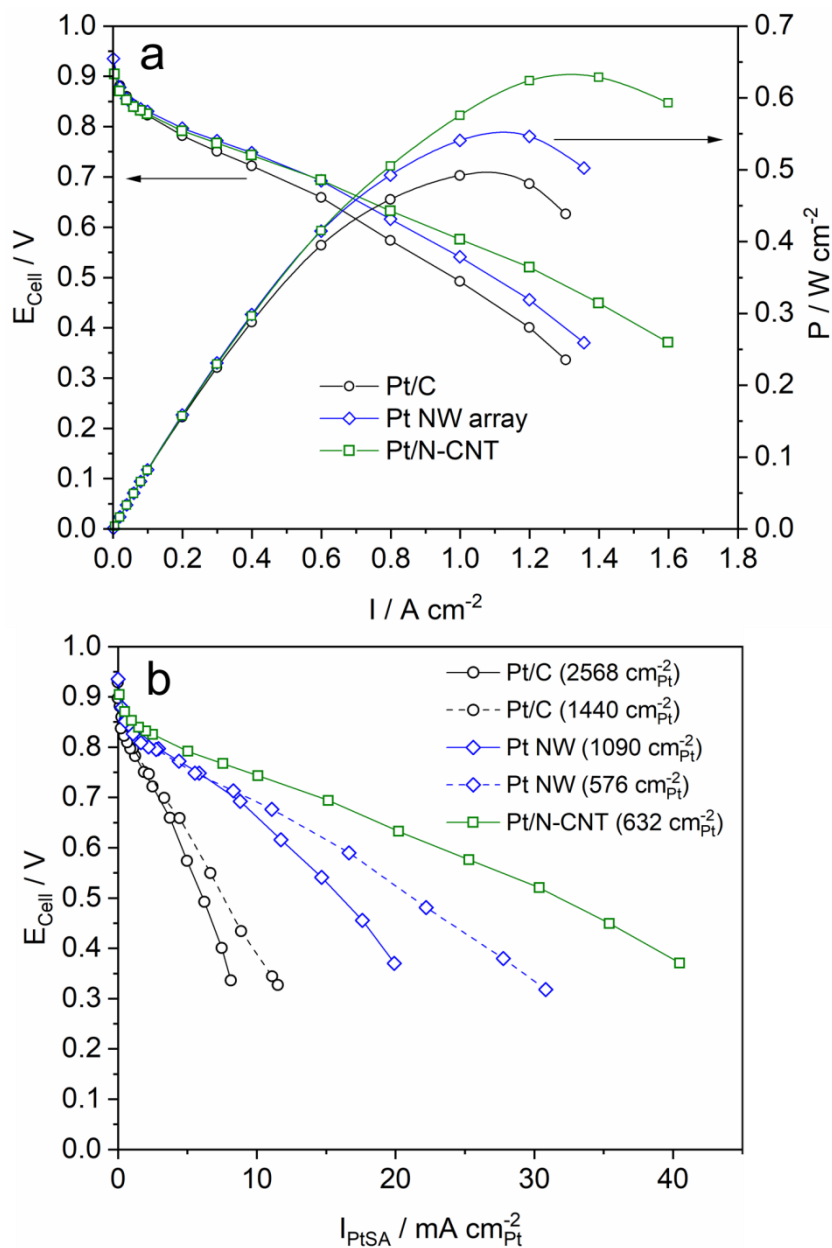
Figure 6.11: (a) Polarisation and power density curves of the MEAs with the Pt/C, Pt NW array and Pt/N-CNT GDEs. **(b)** Normalised polarisation curve of the GDEs including Pt/C (TKK) and Pt NW array electrodes with a catalyst loading of 0.2 mg$_{Pt}$ cm^{-2}. The current is normalised to Pt surface area, which is quoted in the legend.

EIS was recorded to further analyse this claim and it was first conducted in the kinetic loss region of 30 mA cm^{-2}. Figure 6.12a—the corresponding Nyquist plot—shows that the charge transfer and internal resistances for all GDEs were very similar. However, at high currents/low voltages (Figures 6.12b and 6.12c), the charge transfer losses follow the order of Pt/N-CNT < Pt NW array < Pt/C indicating improved ORR kinetics for the Pt NWs and further enhancement by using the N-CNTs. This improvement in kinetics is not as observable at high potentials because much of the potential drop is because of the lower open circuit potential (OCP) as a result of the smaller catalyst electrochemical surface area. At low frequencies the mass transfer losses for the Pt/N-CNT and Pt NW array GDEs are much reduced in comparison to the Pt/C GDE as a result of the thin and highly porous CL structure. This is because in the MEAs with the Pt/N-CNT and Pt NW array GDEs, the catalyst distribution is closer to the PEM (*cf.* the Pt/C GDE), hence the migration path for the protons is reduced and there is a smaller proton transport resistance. Secondly, the thinner CL and highly porous structure reduces the gaseous reactant transport losses and improve the catalyst exposure for a high catalyst utilisation ratio.
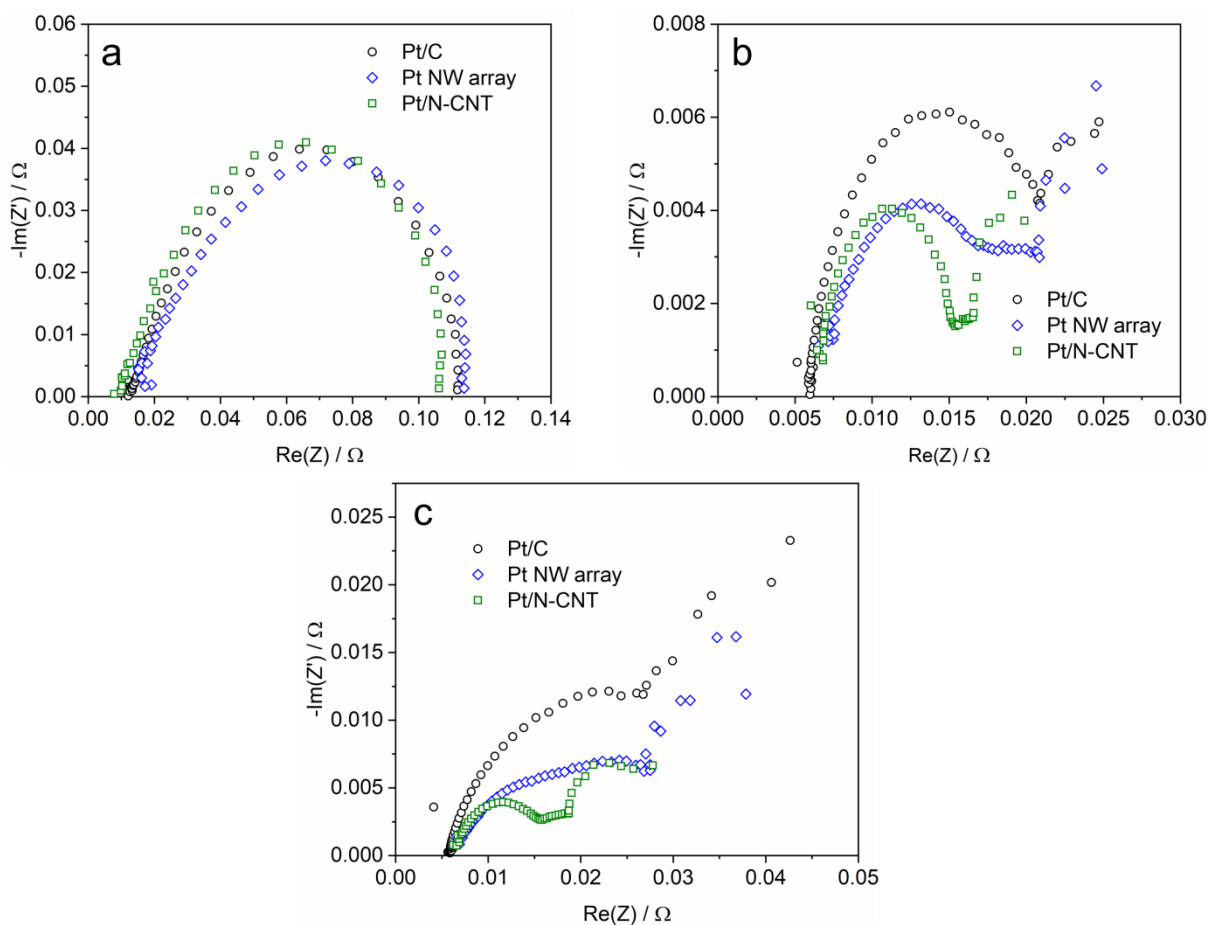
Figure 6.12: EIS of the MEA with the Pt/C, Pt NW array and Pt/N-CNT GDEs recorded at **(a)** 30 mA cm^{-2}, **(b)** 0.65 V and **(c)** 0.5 V.

Additionally, the reduced impedance for the Pt/N-CNT GDE in comparison to the Pt NW array one cannot just be ascribed to the CL thickness but the clear difference in porosity afforded by the Pt/N-CNT CL. Porosity effects is an increasingly appreciated consideration for GDE development where, for example, Garsany *et al.* recently conducted a study on replacing Nafion® ionomer with a shorter side chain alternative, Aquivion [29]. The inability of the Aquivion to penetrate the micro-pores of the carbon support allowed these regions to retain their natural hydrophobicity. This aided in the effective removal of product water and hence the transportation of reactant gases. Additionally, with regards to micropores, it has been shown that Pt trapped too deep within the micro-pores of high surface area carbon

supports can even be inactive to the ORR due to a lack of proton accessibility [120]. The SEM analysis (Figure 6.1) indicates that the N-CNTs protrude from the GDL surface where minimal Pt are in the microporous regime but rather reside in mesopores and macropores – where Hg porosity measurements showed a larger pore size distribution - with good access to both protons and reactant gases. This is thought to be another primary source of the much improved PEMFC performance in comparison to both the Pt/C and Pt NW array GDEs.

To measure the ECSA of each GDE, cathode CV scans were conducted in the MEA in the potential range 0.05–1.2 V vs. RHE at a scan rate of 20 mV s^{-1} (Figure 6.13) and the hydrogen desorption region was used to determine the charge transferred in the process. For the Pt/C electrode an ECSA of 40.1 m^2 g$_{Pt}^{-1}$ was obtained, and 21.8 and 21.9 m^2 g$_{Pt}^{-1}$ was found for the Pt NW array and for Pt/N-CNT GDEs, respectively. The lower ECSA of the NWs results from the 1D nanostructure of the Pt nanorod and NW which have a lower surface to bulk ratio, which agrees with data acquired in our group before [35].
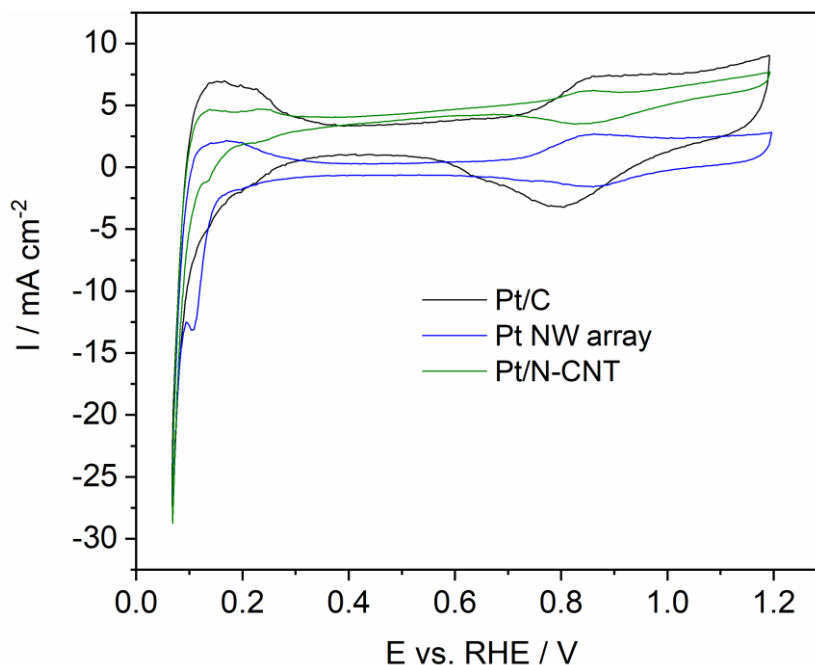
Figure 6.13: CVs for the Pt/C, Pt NW array and Pt/N-CNT GDEs in the potential range 0.05–1.2 V vs. RHE recorded at a scan rate of 20 mV s^{-1}.

Specific and mass activities of the catalyst in the MEA were also obtained under US DoE test conditions and accounted for internal resistance and H_2 crossover [184]. Figure 6.14 shows both the originally recorded and corrected polarisation curves from which the current densities at 0.9 V were taken for calculation. As is the same with the polarisation curves recorded under air, the lower ECSA and overall Pt loading, i.e. the lower absolute Pt electrochemical surface area results in an OCP order of Pt/N-CNT < Pt NW array < Pt/C. Despite this factor, the mass activities taken at 0.9 V were 0.065, 0.062 and 0.060 A mg_{Pt}^{-1} for the Pt/N-CNT, Pt NW array and Pt/C GDEs, respectively. The specific activities were found to be 296.2, 284.86 and 129.31 μA cm_{Pt}^{-2} for the respective order of Pt/N-CNT > Pt NW array > Pt/C GDEs indicating the increased activity of the Pt/N-CNT catalyst in the electrode towards the ORR. The increase in activity can be attributed primarily to inherent improvements in ORR activity of the nanorods with a boost provided by a synergistic metal-support interaction. An MEA with a cathode from the N-CNT/GDL without Pt was tested but no power performance was recorded, indicating that the enhanced power performance of the Pt/N-CNT GDE is not due to any catalytic activity by the N-CNT array support.
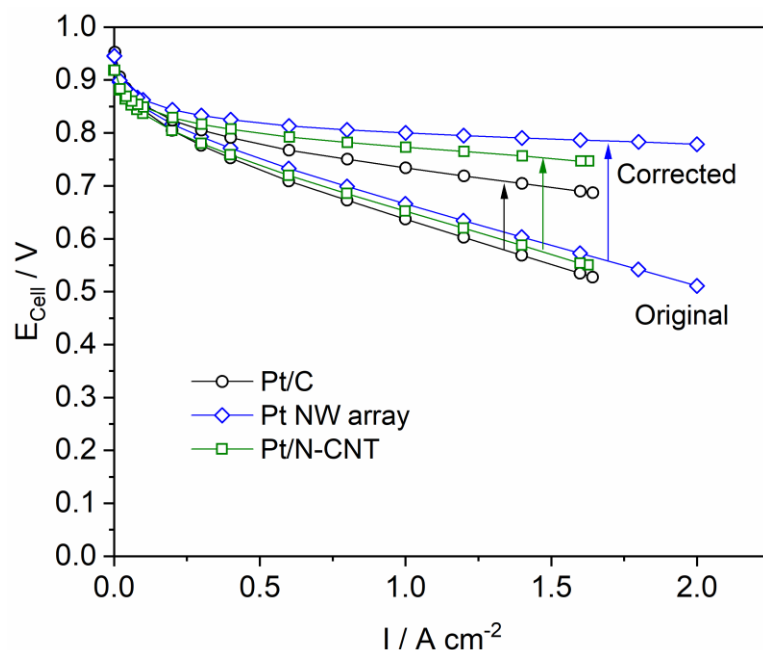
Figure 6.14: Original and corrected (H_2 cross over and internal resistance) polarisation curves for the Pt/C, Pt NW array and Pt/N-CNT GDEs under O_2 at DoE testing conditions.

The Tafel plot (and one normalised to Pt ECSA) are shown in Figure 6.15. Above 0.2 A cm^{-2}, the lower Tafel slopes indicates smaller potential losses for the Pt/N-CNT and Pt NW array electrodes compared to the Pt/C GDE (Figure 6.15a). While a slope transition at a low potential is attributable to a decrease in Pt oxide coverage [159,208], alternative Tafel slopes at a high potential indicate differences in the rate determining step for the ORR [13]. The evidence for this is confirmed by the Pt4f XPS spectra (Figure 6.9), which shows little to no oxide for the Pt NW and Pt/N-CNT GDEs unlike the Pt/C GDE. The CV spectrum also indicates that the 1D catalysts have a more positive redox potential for Pt oxide. Both suggest a reduced susceptibility to Pt oxide formation in contrast to Pt/C – possibly due to a different exposure of crystal facets - and so the rate determining step could have shifted away from the oxygen dissociation step. Alternatively, the lower Tafel slopes demonstrated for the Pt/C in the previous works on the thin-film CL with the RDE measurement and low Pt loadings indicate that aside from the catalyst composition, the CL structure may also play a considerable role in the ORR kinetics whereby mass transport effects cannot be fully omitted

[32,147,199]. Because of the large impact on PEMFC performance, this needs to be better understood with future research. The overall shift in Tafel plot between the Pt NW array and Pt/N-CNT GDEs can be attributed to the difference in surface area as demonstrated by Tafel plots normalised to Pt ECSA (Figure 6.15b).
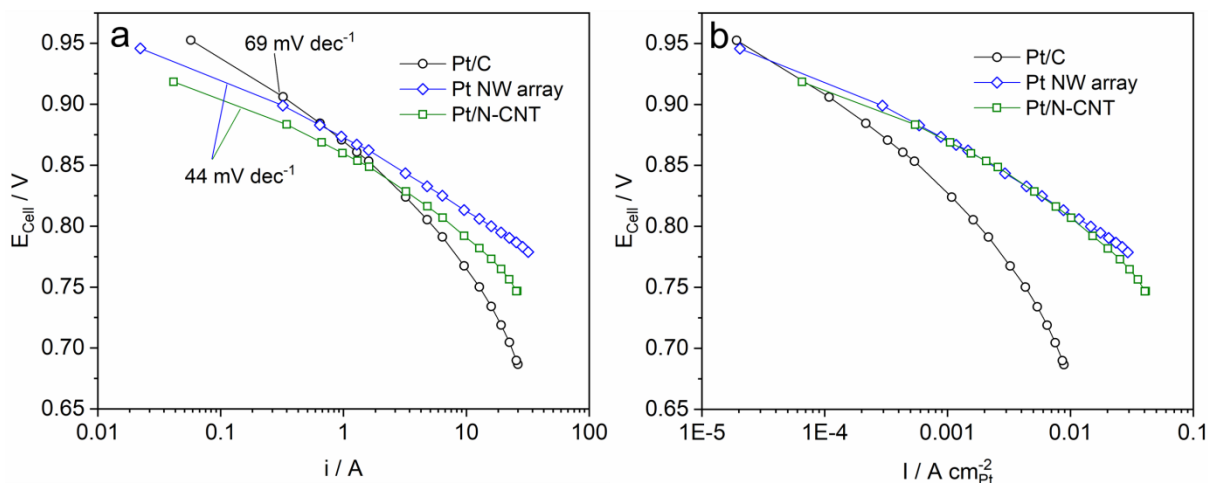
Figure 6.15: (a) Tafel plot and **(b)** Tafel plot normalised to Pt electrochemical surface area based on the kinetic region of the corrected polarisation curves in Figure 6.14.

6.5. Accelerated stress test Pt/N-CNT GDEs

CNT supports have been previously shown to have a higher resistance to carbon corrosion compared to mesoporous carbon [209]. In addition, 1D single crystal nanostructures have also been demonstrated to have better stability to AST in comparison to NP analogues because of enhanced surface properties [108,200]. The durability of the three GDEs were evaluated in this research using 3000 AST cycles in the potential range 0.6–1.2 V vs. RHE (N_2 supplied at the cathode). The Pt/N-CNT GDE has a smaller surface area loss of 41% compared to 76% for the Pt/C GDE (Figure 6.16a). The Pt NW array GDE showed a loss of 51% indicating that both the 1D morphology and N-CNT support indeed improve the stability of the catalyst to surface area loss. After the AST the power performance for the Pt/N-CNT

GDE is still higher than the Pt/C GDE with power density of 0.339 and 0.308 W cm^{-2} at 0.6 V, respectively (Figure 6.16b), corresponding to a power density decline of 38 and 30%, respectively. The higher decline for the Pt/N-CNT GDE in the power density in comparison to a smaller one in the ECSA loss is potentially due to electrode structure degradation as a result of different contact between Nafion® ionomer with the 1D structures in comparison to that with the NPs [200]. Additionally, the smaller initial ECSA and the logathrimic nature of the OCP on Pt surface area means that a smaller loss for the Pt/N-CNTs results in a larger drop in potential. The former suggestion is supported by virtue that the Pt NW array GDE only suffered a 24% drop in the power density with a final value of 0.383 W cm^{-2} post the AST (despite similar ECSAs the Pt loading and hence absolute Pt surface area is larger for the Pt NW array than for the Pt/N-CNT GDE). The combination of a larger absolute Pt surface area compared to the Pt/N-CNT GDE and increased stability compared to the Pt/C GDE endows the Pt NW GDE with the best durability in terms of performance. Even so, the Pt/N-CNT GDE post AST still performs the best at the high current densities as a result of the CL mesoporous structure. These results further stress the need to improve N-CNT anchoring to the GDL substrate whereby minimal material loss would lead to even higher fuel cell performances and perhaps better durability in comparison to the commercial Pt/C GDEs and Pt NW array GDEs.
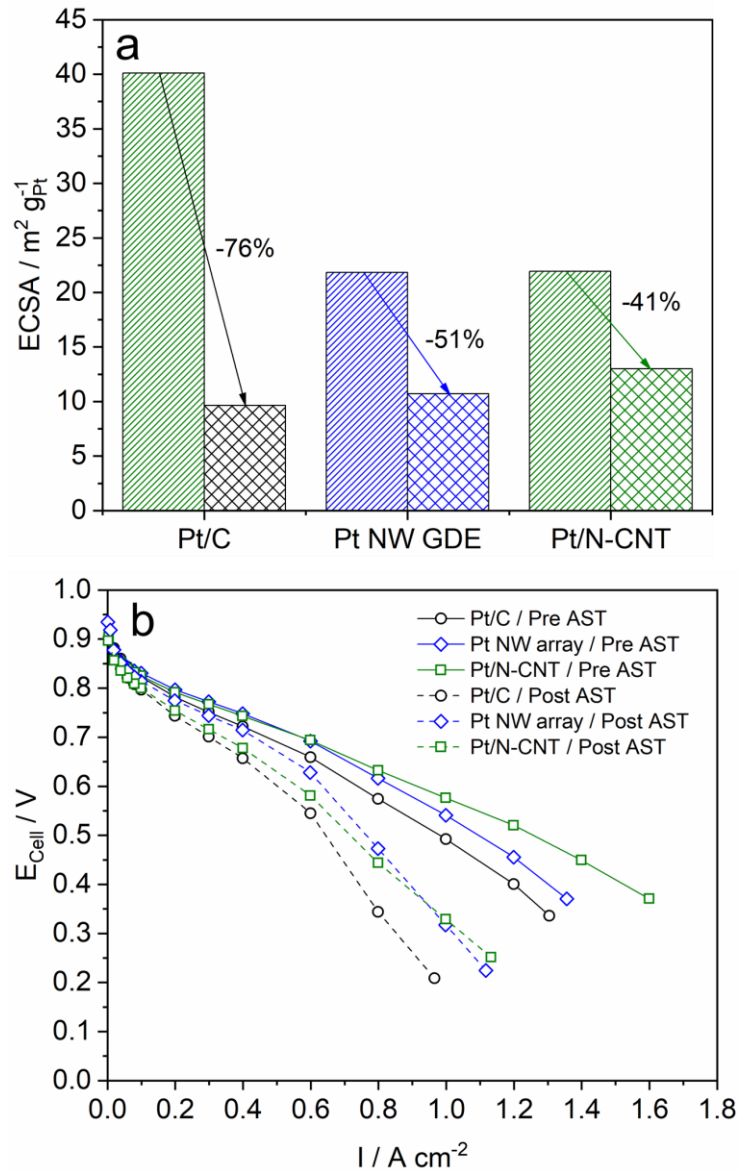
Figure 6.16: (a) ECSAs and **(b)** polarisation curves for the GDEs before and after the AST.

6.6. Conclusions

High performance GDEs were demonstrated with the advances in both alternative carbon support and 1D Pt nanostructures through the development of a simple and scalable method of developing the Pt/N-CNT array GDEs. The direct deposition of the CNT arrays onto the GDL substrate afforded a unique porous and open structure onto which 1D Pt nanorods could be grown to form a thin CL. The ASP treatment to nitride the CNTs provided suitable anchoring sites for the successful growth of Pt nanorods and good distribution as confirmed

by TEM and XPS analyses. However, the anchoring of the CNTs to the GDL substrate needs to be much improved. Higher power performance was observed for the Pt/N-CNT GDE in single cell PEMFC test in comparison to both the Pt/C and Pt NW array GDEs. This improvement was ascribed to the beneficial support-catalyst interaction as per the Pt4f XPS peak shift, and reduced mass transport resistances via an increase in meso-porosity shown by Hg porosimetry measurements. The AST showed an increased stability of the Pt/N-CNT GDE as a result of the highly stable nanorods in comparison to NPs, but also an increase in Pt stability afforded by the N-CNT support. In relation to the overall thesis, this work there highlights the significance of CL structure on overall electrode performance and thus will be further summarised together with the NW composition changes as a method of improving NW array GDEs in the final chapter.

7. Conclusions and Outlook

This thesis focuses on improving the performance of Pt-based 1D hybrid nanostructure array gas diffusion electrodes (GDEs) through two separate methodologies: Alloying of Pt with Ni to improve the catalytic activities of the catalysts, and the use of nitrogen doped carbon nanotubes (N-CNTs) as an alternative support to tune the morphology and distribution of 1D Pt nanostructures resulting in an advanced electrode structure. The morphology, structure and composition of the catalysts, together with their distribution and behaviour in the catalyst layer (CL) were investigated based on the catalytic performance using the half-cell measurement and membrane electrode assembly (MEA) test in proton exchange membrane fuel cells (PEMFCs).

In Chapter 4, a method was developed for the fabrication Pt_3Ni nanowires (NWs), utilising the formic acid reduction method so that the procedure could be easily translated to fabricate PtNi NW array GDEs. To maintain the NW morphology, the Pt NW/C catalysts were firstly synthesised (NWs with average diameter 3.40 nm formed in agglomerates measuring an average 120 nm on the diagonal) and Ni was then successfully incorporated into the structure by means of an impregnation-thermal annealing method. It was shown by a maximum 0.002 Å reduction in lattice constant calculated from XRD spectra, that while the high annealing temperatures induced a greater degree of alloying in the PtNi NWs, the ultrathin morphology of the NWs is highly susceptible to sintering at the temperature as low as 250°C. Without the capability to use the conventional high annealing temperature employed in the development of highly ordered PtNi NP catalysts, the degree of annealing and thus enhancements in catalytic activity were limited in the PtNi NW catalysts. A comparatively modest 1.78-fold increase in the mass activity vs. Pt NW/C was demonstrated by rotating disk electrode (RDE) measurement in 0.1 M $HClO_4$ aqueous electrolyte. However, very poor power performance was recorded in the MEA test in single cells which was ascribed to ionomer contamination by surface Ni species of the PtNi/C catalysts resulting in exacerbated mass transport losses.

To reduce Ni contamination, an acid leaching step was thus employed to remove unalloyed and surface Ni from the PtNi NW catalysts during the adaptation to the PtNi NW array GDEs in Chapter 5. The power performance was much improved in the MEA test and a 1.07-fold increase in the power density vs. the Pt NW array GDE was recorded (0.541 and 0.504 W cm^{-2} respectively, at E_{Cell} = 0.6 V). However, a slightly worse stability was demonstrated for this GDE where ECSA loss was 60%, and after the accelerated stress testing (AST), the PtNi NW GDE showed only the same power performance to that of the Pt NW array GDE. Ex-situ GDE measurement was also performed in 0.1 M HClO$_4$ aqueous electrolyte to understand the catalytic behaviour of the GDE. The results indicated that the PtNi NW array GDE showed much enhanced ORR activities (3.10-fold larger specific and 4.07-fold larger mass activity for PtNi in comparison to pure Pt NWs) under less aggressive conditions than in the PEMFC operation environment where Ni leaching and ionomer contamination were less prominent issues. Inclusion of ionomer and an elevation in the measurement temperature showed reduced benefits, and a reduced activity was recorded for the PtNi NW GDEs. The results suggested negative Ni/ionomer interactions as a leading cause, in agreement with previous work on the disparity between the catalyst performance of novel ORR catalysts recorded by the half-cell RDE measurement and MEA test. This work further demonstrates that if the Ni is better stabilised in the Pt NW array GDE then significant improvements in PEMFC performance are obtainable.

In addition to the catalyst composition study, a further work on the alteration of the CL structure using N-CNT arrays as catalyst support for 1D Pt nanostructures showed greater improvements in the electrode power performance. Plasma enhanced chemical vapour deposition (PECVD) followed by active screen plasma treatment (ASP) were used to grow N-CNT arrays on the surface of the gas diffusion layer (GDL). This was followed by use of the formic acid reduction method to grow 1D Pt nanostructures uniformly distributed on the N-CNT surface. The 1D Pt nanostructures are short nanorods with a diameter of 3–4 nm and a

length in the range of 5–10 nm. Hg porosity measurements indicated that while the Pt NW array GDE has a similar porous distribution to the conventional GDE made with the Pt/C nanoparticle catalysts, the Pt/N-CNT had a high fraction of macropores in the range of 315–360 nm, leading to much improved mass transport properties. The improved distribution of Pt nanostructures, and the highly porous CL, together with the metal-support interaction boost the ORR catalytic activities, and much enhanced power performance was recorded for the Pt/N-CNT array GDE in the MEA test (0.544 W cm^{-2}) at a lower loading of 0.19 mg$_{Pt}$ cm^{-2} in comparison to both Pt/C and Pt NW array GDEs. However, the adhesion of the CNTs to the GDL surface was weak and needs to be rectified in future work.

With regards to mass transport losses with the CL in the PEMFC operation, contributions can be roughly separated into Fickian and non-Fickian components whereby the former is heavily dependent on the porosity of the CL [19]. With a high degree of meso-porosity Fickian gas transport was much improved in the Pt/N-CNT array GDE and is thus considered to be one of the main reasons of the improved power performance in comparison to the other GDEs, in addition to improved mass transport due to the thinness of the CL which provides a reduction in the mean free path of the O_2 reactants, protons and electrons.

The US DoE has the 2020 target of 0.10 mg$_{Pt}$ cm^{-2} for precious group metal (PGM) loading at the cathode; however, the inverse relationship of the non-Fickian transport resistance to Pt surface is hindering advancements. Much of this resistance depends on the O_2 permeability through the ionomer thin film coated on the catalyst surface and thus lots of research efforts have been conducted in finding alternative ionomers [29,210,211]. Ionomer-free CLs could also be an answer where protons can transport via a thin water film formed on the catalyst surface in fuel cell operation [31,158], which provides added bonus of avoiding of the adsorption of sulphate from ionomer onto the catalyst surface which is considered as a leading inhibitor of ORR kinetics in PEMFCs. The catalyst-ionomer interactions in the NW array CL are little known and so this should be evaluated as well as the possibility of using

such CLs in an ionomer free PEMFC. PtNi is known to be more hydrophilic than pure Pt and thus could be a more likely candidate to retain the thin water film required for ionomer-free CLs (of course, a highly stable Ni in the catalyst structure with an excellent tolerance to the leaching is also necessary). Additionally the removal of ionomer means that ionomer contamination would no longer be an issue and thus the enhancement in inherent ORR catalytic activities demonstrated in the ex-situ GDE test could be fully realised in a working PEMFC.

Aside from successfully improving the Pt NW array GDEs, this thesis therefore provides numerous promising avenues for future work, listed as follows:

- Finding ways to improve the stability of Ni in the PtNi NW array electrodes. This could be through optimisation of the acid leaching process or through advanced methods to impregnate the Pt surface more selectively with Ni (e.g. under potential deposition).
- Improving the anchoring of CNT arrays to the GDL surface through further optimisation of the PECVD technique, e.g. reducing the deposition temperature close to 350°C, below the PTFE decompose temperature, thereby ensuring less wasted Pt precursor in the NW growth.
- Deconvolution of the mass transport losses, e.g. by recently developed EIS fitting technique, in the Pt NW and Pt/N-CNT GDEs to measure the Fickian and Non-Fickian contributions. This will help to ascertain the true impact of each CL structure and thus guide future development.
- Modelling of the catalyst-ionomer interface within the NW array systems.
- Evaluation of the performance of the PtNi NW and Pt/N-CNT array systems with ultra-low Pt loadings.
- Investigations into whether either system could be use in an ionomer-free environment.

- Finally, evaluation into the scalability and potential cost effectiveness of both GDE technologies as an alternative commercial GDE technology.

REFERENCES

[1]   D. MacKay, "Sustainable Energy — without the hot air," UIT Cambridge Ltd, 2009.

[2]   "Emissions Gap Report 2018," United Nations Environment Programme, 2018.

[3]   L. Andaloro, A. Arista, G. Agnello, G. Napoli, F. Sergi, V. Antonucci, "Study and design of a hybrid electric vehicle (Lithium Batteries-PEM FC)", *Int. J. Hydrogen Energy*. **42** (2017) 3166–3184.

[4]   T. Hua, R. Ahluwalia, L. Eudy, G. Singer, B. Jermer, N. Asselin-Miller, S. Wessel, T. Patterson, J. Marcinkoski, "Status of hydrogen fuel cell electric buses worldwide", *J. Power Sources*. **269** (2014) 975–993.

[5]   P. Mardle, S. Du, "Materials for PEMFC Electrodes", *Ref. Modul. Mater. Sci. Mater. Eng.* (2017) 1–13.

[6]   Frano Barbir, "PEM Fuel Cells - Theory and Practice," Elsevier, 2013.

[7]   J. Zaidi, T. Matsuura, "Polymer Membranes for Fuel Cells," Springer, 2009.

[8]   A. El-kharouf, R. Steinberger-Wilckens, N. Rees, "Gas Diffusion Layer Materials and their Effect on Polymer Electrolyte Fuel Cell Performance - Ex Situ and In Situ", *Fuel Cells*. **14** (2014) 735–741.

[9]   P.J. Hamilton, B.G. Pollet, "Polymer Electrolyte Membrane Fuel Cell (PEMFC) Flow Field Plate : Design , Materials and Characterisation", *Fuel Cells*. **10** (2010) 489–509.

[10]   X. Li, I. Sabir, "Review of bipolar plates in PEM fuel cells: Flow-field designs", *Int. J. Hydrogen Energy*. **30** (2005) 359–371.

[11]   D.J.L. Brett, N.P. Brandon, "Review of Materials and Characterization Methods for Polymer Electrolyte Fuel Cell Flow-Field Plates", *J. Fuel Cell Sci. Technol.* **4** (2007) 29–44.

[12]   A.J. Bard, L.R. Faulkner, "Electrochemical Methods Fundamentals and Applications," John Wiley & Sons, Inc., 2001.

[13]   T. Shinagawa, A.T. Garcia-esparza, K. Takanabe, "Insight on Tafel slopes from a microkinetic analysis of aqueous electrocatalysis for energy conversion", *Nat. Publ. Gr.* **5** (2015) 13801.

[14]   G. Hinds, E. Brightman, "In situ mapping of electrode potential in a PEM fuel cell", *Electrochem. Commun.* **17** (2012) 26–29.

[15]   S.A. Vilekar, R. Datta, "The effect of hydrogen crossover on open-circuit voltage in polymer electrolyte membrane fuel cells", **195** (2010) 2241–2247.

[16]   A. Dicks, J. Larminie, "Fuel Cell Systems Explained," Wiley, 2003.

[17]   C. Simon, F. Hasché, H.A. Gasteiger, "Influence of the Gas Diffusion Layer Compression on the Oxygen Transport in PEM Fuel Cells at High Water Saturation Levels", *J. Electrochem. Soc.* **164** (2017) F591–F599.

[18]   J. Huang, Z. Li, J. Zhang, "Review of characterization and modeling of polymer

electro- lyte fuel cell catalyst layer : The blessing and curse of ionomer", *Front. Energy.* **11** (2017) 334–364.

[19]   A. Kongkanand, M.F. Mathias, "The Priority and Challenge of High-Power Performance of Low-Platinum Proton-Exchange Membrane Fuel Cells", *J. Phys. Chem. Lett.* **7** (2016) 1127–1137.

[20]   D. Papageorgopoulos, "Fuel Cell R&D Overview," in: 2019 Annu. Merit Rev. Peer Eval. Meet., US DoE - Fuel Cells Technologies Office, 2019.

[21]   Y. Nie, L. Li, Z. Wei, "Recent advancements in Pt and Pt-free catalysts for oxygen reduction reaction", *Chem. Soc. Rev.* **44** (2015) 2168–2201.

[22]   S. Mukerjee, S. Srinivasan, M.P. Soriaga, J. Mcbreen, "Role of Structural and Electronic Properties of Pt and Pt Alloys on Electrocatalysis of Oxygen Reduction", *J. Electrochem. Soc.* **142** (1995) 1409–1421.

[23]   I.E.L. Stephens, J. Rossmeisl, I. Chorkendorff, "Toward sustainable fuel cells", *Science.* **354** (2016) 1378–1380.

[24]   Q. Jia, J. Li, K. Caldwell, D.E. Ramaker, J.M. Ziegelbauer, R.S. Kukreja, A. Kongkanand, S. Mukerjee, "Circumventing Metal Dissolution Induced Degradation of Pt-Alloy Catalysts in Proton Exchange Membrane Fuel Cells : Revealing the Asymmetric Volcano Nature of Redox Catalysis", *ACS Appl. Nano Mater.* **6** (2016) 928–938.

[25]   S. Sharma, B.G. Pollet, "Support materials for PEMFC and DMFC electrocatalysts - A review", *J. Power Sources.* **208** (2012) 96–119.

[26]   H. Tang, J.H. Chen, Z.P. Huang, D.Z. Wang, Z.F. Ren, L.H. Nie, Y.F. Kuang, S.Z. Yao, "High dispersion and electrocatalytic properties of platinum on well-aligned carbon nanotube arrays", *Carbon N. Y.* **42** (2004) 191–197.

[27]   R. Kou, Y. Shao, D. Wang, M.H. Engelhard, J. Hun, J. Wang, V. V Viswanathan, C. Wang, Y. Lin, Y. Wang, I.A. Aksay, J. Liu, "Enhanced activity and stability of Pt catalysts on functionalized graphene sheets for electrocatalytic oxygen reduction", *Electrochem. Commun.* **11** (2009) 954–957.

[28]   E. Antolini, E.R. Gonzalez, "Ceramic materials as supports for low-temperature fuel cell catalysts", *Solid State Ionics.* **180** (2009) 746–763.

[29]   Y. Garsany, W.A. Iii, M.B. Sassin, R.M.E. Hjelm, B.D. Gould, K.E. Swider-lyons, "Improving PEMFC Performance Using Short-Side-Chain Low-Equivalent-Weight PFSA Ionomer in the Cathode Catalyst Layer", *J. Electrochem. Soc.* **165** (2018) F381–F391.

[30]   X. Yan, F. Zhang, H. Zhang, H. Tang, M. Pan, P. Fang, "Improving Oxygen Reduction Performance by Using Protic Poly (Ionic Liquid) as Proton Conductors", *ACS Appl. Mater. Interfaces.* **11** (2019) 6111–6117.

[31]   M.K. Debe, "Tutorial on the Fundamental Characteristics and Practical Properties of Nanostructured Thin Film (NSTF) Catalysts", *J. Electrochem. Soc.* **160** (2013) 522–534.

[32]   Y. Lu, S. Du, R. Steinberger-Wilckens, "Temperature-controlled growth of single-crystal Pt nanowire arrays for high performance catalyst electrodes in polymer

electrolyte fuel cells", *Appl. Catal. B Environ.* **164** (2015) 389–395.

[33]   S. Du, "Pt-based nanowires as electrocatalysts in proton exchange fuel cells", *Int. J. Low-Carbon Technol.* **7** (2012) 44–54.

[34]   S. Du, "A Facile Route for Polymer Electrolyte Membrane Fuel Cell Electrodes with in situ Grown Pt Nanowires", *J. Power Sources.* **195** (2010) 289–292.

[35]   S. Du, K. Lin, S.K. Malladi, Y. Lu, S. Sun, Q. Xu, R. Steinberger-Wilckens, H. Dong, "Plasma nitriding induced growth of Pt-nanowire arrays as high performance electrocatalysts for fuel cells", *Sci. Rep.* **4 : 6439** (2014) 1–6.

[36]   H.S. Wroblowa, Yen-Chi-Pan, G. Razumney, "Electroreduction of oxygen: A new mechanistic criterion", *J. Electroanal. Chem. Interfacial Electrochem.* **69** (1976) 195–201.

[37]   N. Ramaswamy, N. Hakim, S. Mukerjee, "Degradation mechanism study of perfluorinated proton exchange membrane under fuel cell operating conditions", *Electrochem. Commun.* **53** (2008) 3279–3295.

[38]   E. Yeager, "Electrocatalysts for O2 reduction", *Electrochim. Acta.* **29** (1984) 1527–1537.

[39]   M.A. Molina-garcía, N. V Rees, ""Metal-free " electrocatalysis : Quaternary-doped graphene and the alkaline oxygen reduction reaction", *Appl. Catal. A, Gen.* **553** (2018) 107–116.

[40]   J.K. Nørskov, J. Ressmeisl, A. Logadottir, L. Lindqvist, J.R. Kitchin, T. Bligaard, H. Jonsson, "Origin of the overpotential for oxygen reduction at a fuel cell cathode", *J. Phys. Chem. B.* **108** (2004) 17886–17892.

[41]   V. Viswanathan, H.A. Hansen, J. Rossmeisl, J.K. Nørskov, "Universality in oxygen reduction electrocatalysis on metal surfaces", *ACS Catal.* **2** (2012) 1654–1660.

[42]   J. Greeley, J. Rossmeisl, A. Hellman, J.K. Nørskov, "Theoretical Trends in Particle Size Effects for the Oxygen Reduction Reaction", *Z. Phys. Chem.* **221** (2007) 1379–1391.

[43]   A. Kabasawa, H. Uchida, M. Watanabe, "Influence of decomposition products from perfluorosulfonic acid membrane on fuel cell performance", *Electrochem. Solid-State Lett.* **11** (2008) 190–193.

[44]   J. Liu, Y. Huang, "Oxygen Reduction Reaction on PtCo Nanocatalyst: (Bi)sulfate Anion Poisoning", *Nanoscale Res. Lett.* **13** (2018) 1–6.

[45]   N.M. Markovic, H.A. Gasteiger, P.N. Ross, "Oxygen reduction on platinum low-index single-crystal surfaces in sulfuric acid solution. Rotating ring - Pt(hkl) disk studies", *J. Phys. Chem.* **99** (1995) 3411–3415.

[46]   V. Stamenkovic, B.S. Mun, K.J.J. Mayrhofer, P.N. Ross, N.M. Markovic, J. Rossmeisl, J. Greeley, J.K. Nørskov, "Changing the Activity of Electrocatalysts for Oxygen Reduction by Tuning the Surface Electronic Structure", *Angew. Chemie.* **118** (2006) 2963–2967.

[47]   V.R. Stamenkovic, B.S. Mun, M. Arenz, K.J.J. Mayrhofer, C.A. Lucas, G. Wang, P.N. Ross, N.M. Markovic, "Trends in electrocatalysis on extended and nanoscale Pt-

bimetallic alloy surfaces", *Nat. Mater.* **6** (2007) 241–247.

[48]   J. Greeley, I.E.L. Stephens, a S. Bondarenko, T.P. Johansson, H. a Hansen, T.F. Jaramillo, J. Rossmeisl, I. Chorkendorff, J.K. Nørskov, "Alloys of platinum and early transition metals as oxygen reduction electrocatalysts", *Nat. Chem.* **1** (2009) 552–556.

[49]   V. Tripković, E. Skúlason, S. Siahrostami, J.K. Nørskov, J. Rossmeisl, "The oxygen reduction reaction mechanism on Pt(111) from density functional theory calculations", *Electrochim. Acta*. **55** (2010) 7975–7981.

[50]   V. Tripkovic, T. Vegge, "Potential- and Rate-Determining Step for Oxygen Reduction on Pt(111)", *J. Phys. Chem. C.* **121** (2017) 26785–26793.

[51]   D. Eberle, B. Horstmann, "Oxygen Reduction on Pt(111) in Aqueous Electrolyte: Elementary Kinetic Modeling", *Electrochim. Acta*. **137** (2014) 714–720.

[52]   D. Banham, T. Kishimoto, Y. Zhou, T. Sato, K. Bai, J. Ozaki, Y. Imashiro, S. Ye, "Critical advancements in achieving high power and stable nonprecious metal catalyst – based MEAs for real-world proton exchange membrane fuel cell applications", *Sci. Adv.* **4** (2018) 1–8.

[53]   K. Kinoshita, "Particle Size Effects for Oxygen Reduction on Highly Dispersed Platinum in Acid Electrolytes", *J. Electrochem. Soc.* **137** (1990) 845–848.

[54]   M.L. Sattler, P.N. Ross, "The surface structure of Pt crystallites supported on carbon black", *Ultramicroscopy*. **20** (1986) 21–28.

[55]   P. Parthasarathy, A. V. Virkar, "Electrochemical Ostwald ripening of Pt and Ag catalysts supported on carbon", *J. Power Sources*. **234** (2013) 82–90.

[56]   E. Padgett, V. Yarlagadda, M.E. Holtz, M. Ko, B.D.A. Levin, R.S. Kukreja, J.M. Ziegelbauer, R.N. Andrews, J. Ilavsky, A. Kongkanand, D.A. Muller, "Mitigation of PEM Fuel Cell Catalyst Degradation with Porous Carbon Supports", *J. Electrochem. Soc.* **166** (2019) 11–17.

[57]   L. Zhang, K. Doyle-Davis, X. Sun, "Pt-Based electrocatalysts with high atom utilization efficiency: From nanostructures to single atoms", *Energy Environ. Sci.* **12** (2019) 492–517.

[58]   H.C. Brown, C.A. Brown, "Reaction of Sodium Borohydride with Platinum Metal Salts in the Presence of Decolorizing Carbon-A Supported Platinum Catalyst of Markedly Enhanced Activity for Hydrogenations", *J. Am. Chem. Soc.* **84** (1962) 2827.

[59]   K. Park, J. Choi, B. Kwon, S. Lee, Y. Sung, H. Kim, A. Wieckowski, "Chemical and electronic effects of Ni in Pt/Ni and Pt/Ru/Ni alloy nanoparticles in methanol electrooxidation", *J. Phys. Chem. B*. **106** (2002) 1869–1877.

[60]   J.R.C. Salgado, E. Antolini, E.R. Gonzalez, "Pt-Co/C electrocatalysts for oxygen reduction in H-2/O-2 PEMFCs synthesized by borohydride method", *J. Electrochem. Soc.* **151** (2004) A2143–A2149.

[61]   E. Antolini, J.R.C. Salgado, a. M. dos Santos, E.R. Gonzalez, "Carbon-Supported Pt-Ni Alloys Prepared by the Borohydride Method as Electrocatalysts for DMFCs", *Electrochem. Solid-State Lett.* **8** (2005) A226–A230.

[62]   A. Islam, M.A.K. Bhuiya, M.S. Islam, "A Review on Chemical Synthesis Process of

Platinum Nanoparticles", *Asia Pacific J. Energy Environ.* **1** (2014) 107–121.

[63]   J. Jiang, A. Kucernak, "Electrooxidation of small organic molecules on mesoporous precious metal catalysts II: CO and methanol on platinum-ruthenium alloy", *J. Electroanal. Chem.* **543** (2003) 187–199.

[64]   F. Fievet, J.P. Lagier, M. Figlarz, "Preparing Monodisperse Métal Powders in Micrometer and Submicrometer Sizes by the Polyol Process", *MRS Bull.* (1989) 29–34.

[65]   S. Harish, S. Baranton, C. Coutanceau, J. Joseph, "Microwave assisted polyol method for the preparation of Pt/C, Ru/C and PtRu/C nanoparticles and its application in electrooxidation of methanol", *J. Power Sources.* **214** (2012) 33–39.

[66]   H. Li, S. Zhang, S. Yan, Y. Lin, Y. Ren, "Pd/C catalysts synthesized by microwave assisted polyol method for methanol electro-oxidation", *Int. J. Electrochem. Sci.* **8** (2013) 2996–3011.

[67]   Y. Chen, Z. Liang, F. Yang, Y. Liu, S. Chen, "Ni-Pt core-shell nanoparticles as oxygen reduction electrocatalysts: Effect of Pt shell coverage", *J. Phys. Chem. C.* **115** (2011) 24073–24079.

[68]   E.I. Santiago, L.C. Varanda, H.M. Villullas, "Carbon-supported Pt-Co catalysts prepared by a modifled polyol process as cathodes for PEM fuel cells", *J. Phys. Chem. C.* **111** (2007) 3146–3151.

[69]   C. Wang, H. Daimon, T. Onodera, T. Koda, S. Sun, "A general approach to the size- and shape-controlled synthesis of platinum nanoparticles and their catalytic reduction of oxygen", *Angew. Chemie - Int. Ed.* **47** (2008) 3588–3591.

[70]   G.A. Tritsaris, J. Greeley, J. Rossmeisl, J.K. Nørskov, "Atomic-scale modeling of particle size effects for the oxygen reduction reaction on Pt", *Catal. Letters.* **141** (2011) 909–913.

[71]   R. Loukrakpam, P. Chang, J. Luo, B. Fang, D. Mott, I.T. Bae, H.R. Naslund, M.H. Engelhard, C.J. Zhong, "Chromium-assisted synthesis of platinum nanocube electrocatalysts", *Chem. Commun.* **46** (2010) 7184–7186.

[72]   E. Antolini, J.R.C. Salgado, L.G.R.A. Santos, G. Garcia, E.A. Ticianelli, E. Pastor, E.R. Gonzalez, "Carbon supported Pt-Cr alloys as oxygen-reduction catalysts for direct methanol fuel cells", *J. Appl. Electrochem.* **36** (2006) 355–362.

[73]   Y. Zhou, D. Zhang, "Nano PtCu binary and PtCuAg ternary alloy catalysts for oxygen reduction reaction in proton exchange membrane fuel cells", *J. Power Sources.* **278** (2015) 396–403.

[74]   M. Shao, Q. Chang, J.-P. Dodelet, R. Chenitz, "Recent Advances in Electrocatalysts for Oxygen Reduction Reaction.", *Chem. Rev.* **116** (2016) 3594–3657.

[75]   Y. Yu, W. Yang, X. Sun, W. Zhu, X.Z. Li, D.J. Sellmyer, S. Sun, "Monodisperse MPt (M = Fe, Co, Ni, Cu, Zn) nanoparticles prepared from a facile oleylamine reduction of metal salts", *Nano Lett.* **14** (2014) 2778–2782.

[76]   C. Wang, M. Chi, D. Li, D. Van Der Vliet, G. Wang, Q. Lin, J. F. Mitchell, K.L. More, N.M. Markovic, V.R. Stamenkovic, "Synthesis of homogeneous Pt-bimetallic nanoparticles as highly efficient electrocatalysts", *ACS Catal.* **1** (2011) 1355–1359.

[77]   J. Wu, J. Zhang, Z. Peng, S. Yang, F.T. Wagner, H. Yang, "Truncated octahedral Pt3Ni oxygen reduction reaction electrocatalysts", *J. Am. Chem. Soc.* **132** (2010) 4984–4985.

[78]   J. Zhang, H. Yang, J. Fang, S. Zou, "Synthesis and oxygen reduction activity of shape-controlled Pt3Ni nanopolyhedra", *Nano Lett.* **10** (2010) 638–644.

[79]   M.K. Carpenter, T.E. Moylan, R. Singh, M.H. Atwan, M.M. Tessema, M.K. Carpenter, R.S. Kukreja, "Solvothermal Synthesis of Platinum Alloy Nanoparticles for Oxygen Reduction Electrocatalysis Solvothermal Synthesis of Platinum Alloy Nanoparticles for Oxygen Reduction Electrocatalysis", *J. Am. Chem. Soc.* **134** (2012) 8535–8542.

[80]   C. Cui, L. Gan, H. Li, S. Yu, M. Heggen, P. Strasser, "Octahedral PtNi Nanoparticle Catalysts : Exceptional Oxygen", *Nano Lett.* **12** (2012) 5885–5889.

[81]   R.K. Ahluwalia, D.D. Papadias, N.N. Kariuki, J.K. Peng, X. Wang, Y. Tsai, D.G. Graczyk, D.J. Myers, "Potential dependence of pt and co dissolution from platinum-cobalt alloy PEFC catalysts using time-resolved measurements", *J. Electrochem. Soc.* **165** (2018) 3024–3035.

[82]   P. Yu, M. Pemberton, P. Plasse, "PtCo/C cathode catalyst for improved durability in PEMFCs", *J. Power Sources.* **144** (2005) 11–20.

[83]   D. Banham, S. Ye, K. Pei, J.I. Ozaki, T. Kishimoto, Y. Imashiro, "A review of the stability and durability of non-precious metal catalysts for the oxygen reduction reaction in proton exchange membrane fuel cells", *J. Power Sources.* **285** (2015) 334–348.

[84]   F.D. Coms, "The Chemistry of Fuel Cell Membrane Chemical Degradation", *ECS Trans.* **16** (2008) 235–255.

[85]   J.S. Walker, N. V Rees, P.M. Mendes, "Progress towards the ideal core @ shell nanoparticle for fuel cell electrocatalysis for fuel cell electrocatalysis", *J. Exp. Nanosci.* **13** (2018) 276–289.

[86]   J. Zhang, F.H.B. Lima, M.H. Shao, K. Sasaki, J.X. Wang, J. Hanson, R.R. Adzic, "Platinum monolayer on non-noble metal-noble metal core-shell nanoparticles electrocatalysts for O2 reduction", *J. Phys. Chem. B.* **109** (2005) 11973.

[87]   Y. Ma, P.B. Balbuena, "Pt surface segregation in bimetallic Pt3M alloys: A density functional theory study", *Surf. Sci.* **602** (2008) 107–113.

[88]   M. Chi, C. Wang, Y. Lei, G. Wang, D. Li, K.L. More, A. Lupini, L.F. Allard, N.M. Markovic, V.R. Stamenkovic, "Surface faceting and elemental diffusion behaviour at atomic scale for alloy nanoparticles during in situ annealing", *Nat. Commun.* **6** (2015) 1–9.

[89]   G. Wang, H. Wu, D. Wexler, H. Liu, O. Savadogo, "Ni@Pt core-shell nanoparticles with enhanced catalytic activity for oxygen reduction reaction", *J. Alloys Compd.* **503** (2010) 2–5.

[90]   P. Strasser, S. Koh, T. Anniyev, J. Greeley, K. More, C. Yu, Z. Liu, S. Kaya, D. Nordlund, H. Ogasawara, M.F. Toney, A. Nilsson, "Lattice-strain control of the activity in dealloyed core–shell fuel cell catalysts", *Nat. Chem.* **2** (2010) 454–460.

[91]   P. Mani, R. Srivastava, P. Strasser, "Dealloyed Pt-Cu Core-Shell Nanoparticle

Electrocatalysts for Use in PEM Fuel Cell Cathodes", *J. Phys. Chem. C.* **1** (2008) 2770–2778.

[92] P. Mani, R. Srivastava, P. Strasser, "Dealloyed binary PtM3 (M=Cu, Co, Ni) and ternary PtNi3M (M=Cu, Co, Fe, Cr) electrocatalysts for the oxygen reduction reaction: Performance in polymer electrolyte membrane fuel cells", *J. Power Sources.* **196** (2011) 666–673.

[93] J. Snyder, I. McCue, K. Livi, J. Erlebacher, "Structure/Processing/Properties Relationships in Nanoporous Nanoparticles As Applied to Catalysis of the Cathodic Oxygen Reduction Reaction", *J. Am. Chem. Soc.* **134** (2012) 8633–8645.

[94] J. Snyder, K. Livi, J. Erlebacher, "Oxygen reduction reaction performance of [MTBD][beti]-encapsulated nanoporous NiPt alloy nanoparticles", *Adv. Funct. Mater.* **23** (2013) 5494–5501.

[95] C. Wang, M. Chi, D. Li, D. Strmcnik, D. Van Der Vliet, G. Wang, V. Komanicky, K.C. Chang, A.P. Paulikas, D. Tripkovic, J. Pearson, K.L. More, N.M. Markovic, V.R. Stamenkovic, "Design and synthesis of bimetallic electrocatalyst with multilayered Pt-skin surfaces", *J. Am. Chem. Soc.* **133** (2011) 14396–14403.

[96] Q. Shao, F. Li, Y. Chen, X. Huang, "The Advanced Designs of High-Performance Platinum-Based Electrocatalysts : Recent Progresses and Challenges", *Adv. Mater. Interfaces.* **1800486** (2018) 1–24.

[97] Multi-Year Research, Development, and Demonstration Plan: 3.4 Fuel Cells, US Department of Energy (DOE), 2017.

[98] C. Chen, Y. Kang, Z. Huo, Z. Zhu, W. Huang, H.L. Xin, J.D. Snyder, D. Li, J.A. Herron, M. Mavrikakis, M. Chi, K.L. More, Y. Li, N.M. Markovic, G.A. Somorjai, P. Yang, V.R. Stamenkovic, "Highly Crystalline Multimetallic Nanoframes with Three-Dimensional Electrocatalytic Surfaces", *Science.* **343** (2014) 1339–1343.

[99] S. Du, C. Koenigsmann, S. Sun, One-Dimensional Nanostructures for PEM Fuel Cell Applications, Elsevier, 2017.

[100] S.M. Choi, J.H. Kim, J.Y. Jung, E.Y. Yoon, W.B. Kim, "Pt nanowires prepared via a polymer template method: Its promise toward high Pt-loaded electrocatalysts for methanol oxidation", *Electrochim. Acta.* **53** (2008) 5804–5811.

[101] W.C. Choi, S.I. Woo, "Bimetallic Pt-Ru nanowire network for anode material in a direct-methanol fuel cell", *J. Power Sources.* **124** (2003) 420–425.

[102] Y. Piao, H. Lim, J.Y. Chang, W.Y. Lee, H. Kim, "Nanostructured materials prepared by use of ordered porous alumina membranes", *Electrochim. Acta.* **50** (2005) 2997–3013.

[103] Y. Song, R.M. Garcia, R.M. Dorin, H. Wang, Y. Qiu, E.N. Coker, W.A. Steen, J.E. Miller, J.A. Shelnutt, "Synthesis of Platinum Nanowire Networks Using a Soft Template", *Nano Lett.* **7** (2007) 3650–3655.

[104] J. Chen, T. Herricks, M. Geissler, Y. Xia, "Single-Crystal Nanowires of Platinum can be Synthesized by Controlling the Reaction Rate of a Polyol Process.", *J. Am. Chem. Soc.* **126** (2004) 10854–5.

[105] S. Sun, D. Yang, D. Villers, G. Zhang, E. Sacher, J.P. Dodelet, "Template- And surfactant-free room temperature synthesis of self-assembled 3D Pt nanoflowers from

single-crystal nanowires", *Adv. Mater.* **20** (2008) 571–574.

[106] S. Puri, V. Wadhawan, Kinetics of Phase Transitions, CRC Press, 2009.

[107] S. Sun, F. Jaouen, J.P. Dodelet, "Controlled growth of Pt nanowires on carbon nanospheres and their enhanced performance as electrocatalysts in PEM fuel cells", *Adv. Mater.* **20** (2008) 3900–3904.

[108] S. Sun, G. Zhang, D. Geng, Y. Chen, R. Li, M. Cai, X. Sun, "A highly durable platinum nanocatalyst for proton exchange membrane fuel cells: Multiarmed starlike nanowire single crystal", *Angew. Chemie - Int. Ed.* **50** (2011) 422–426.

[109] H. Meng, Y. Zhan, D. Zeng, X. Zhang, G. Zhang, F. Jaouen, "Factors Influencing the Growth of Pt Nanowires via Chemical Self-Assembly and their Fuel Cell Performance", *Small.* **11** (2015) 3377–3386.

[110] L. Bu, J. Ding, S. Guo, X. Zhang, D. Su, X. Zhu, J. Yao, J. Guo, G. Lu, X. Huang, "A General Method for Multimetallic Platinum Alloy Nanowires as Highly Active and Stable Oxygen Reduction Catalysts", *Adv. Mater.* **27** (2015) 7204–7212.

[111] L. Bu, X. Zhang, X. Shen, D. Su, G. Lu, X. Zhu, J. Yao, J. Guo, S. Guo, X. Huang, "Surface engineering of hierarchical platinum-cobalt nanowires for efficient electrocatalysis", *Nat. Commun.* **7** (2016) 1–10.

[112] N. Zhang, L. Bu, S. Guo, J. Guo, X. Huang, "Screw Thread-Like Platinum-Copper Nanowires Bounded with High-Index Facets for Efficient Electrocatalysis", *Nano Lett.* **16** (2016) 5037–5043.

[113] K. Jiang, D. Zhao, S. Guo, X. Zhang, X. Zhu, J. Guo, G. Lu, X. Huang, "Efficient oxygen reduction catalysis by subnanometer Pt alloy nanowires.", *Sci. Adv.* **3** (2017) 1–8.

[114] J. Mao, W. Chen, D. He, J. Wan, J. Pei, J. Dong, Y. Wang, P. An, Z. Jin, W. Xing, H. Tang, Z. Zhuang, X. Liang, Y. Huang, G. Zhou, L. Wang, D. Wang, Y. Li, "Design of ultrathin Pt-Mo-Ni nanowire catalysts for ethanol electrooxidation", *Sci. Adv.* (2017) 1–9.

[115] Q. Shao, K. Lu, X. Huang, "Platinum Group Nanowires for Efficient Electrocatalysis", *Small Methods.* **1800545** (2019) 1800545–1800566.

[116] M. Li, M. Li, Z. Zhao, T. Cheng, A. Fortunelli, C. Chen, R. Yu, L. Gu, B. Merinov, Z. Lin, E. Zhu, T. Yu, Q. Jia, J. Guo, L. Zhang, W.A.G. Iii, Y. Huang, X. Duan, "Ultrafine jagged platinum nanowires enable ultrahigh mass activity for the oxygen reduction reaction", *Science.* **9050** (2016) 1414–1419.

[117] R. Zacharia, S. ullah Rather, S.W. Hwang, K.S. Nahm, "Spillover of physisorbed hydrogen from sputter-deposited arrays of platinum nanoparticles to multi-walled carbon nanotubes", *Chem. Phys. Lett.* **434** (2007) 286–291.

[118] T.M. Day, P.R. Unwin, J. V. Macpherson, "Factors controlling the electrodeposition of metal nanoparticles on pristine single walled carbon nanotubes", *Nano Lett.* **7** (2007) 51–57.

[119] T. Matsumoto, T. Komatsu, K. Arai, T. Yamazaki, M. Kijima, H. Shimizu, Y. Takasawa, J. Nakamura, "Reduction of Pt usage in fuel cell electrocatalysts with carbon nanotube electrodes", *Chem. Commun.* (2004) 840–841.

[120] V. Yarlagadda, M.K. Carpenter, T.E. Moylan, R.S. Kukreja, R. Koestner, W. Gu, L. Thompson, A. Kongkanand, "Boosting Fuel Cell Performance with Accessible Carbon Mesopores", *ACS Energy Lett.* **3** (2018) 618–621.

[121] K. Kodama, A. Shinohara, N. Hasegawa, K. Shinozaki, R. Jinnouchi, T. Suzuki, T. Hatanaka, Y. Morimoto, "Catalyst Poisoning Property of Sulfonimide Acid Ionomer on Pt (111) Surface", *J. Electrochem. Soc.* **161** (2014) F649–F652.

[122] N. Macauley, D.D. Papadias, J. Fairweather, D. Spernjak, D. Langlois, R. Ahluwalia, K.L. More, R. Mukundan, R.L. Borup, "Carbon Corrosion in PEM Fuel Cells and the Development of Accelerated Stress Tests", *J. Electrochem. Soc.* **165** (2018) F3148–F3160.

[123] A. Rubio, J.A. Alonso, P.M. Ajayan, "Improved Charge Transfer at Carbon Nanotube Electrodes", *Adv. Mater. Commun.* **11** (1999) 154–157.

[124] G.G. Wildgoose, C.E. Banks, R.G. Compton, "Metal nanoparticles and related materials supported on Carbon nanotubes: Methods and applications", *Small.* **2** (2006) 182–193.

[125] P. Luksirikul, K. Tedsree, M.G. Moloney, M.L.H. Green, "Electron Promotion by Surface Functional Groups of Single Wall Carbon Nanotubes to Overlying Metal Particles in a Fuel-Cell Catalyst", *Angew. Chemie - Int. Ed.* **51** (2012) 6998–7001.

[126] S. Du, Y. Lu, R. Steinberger-Wilckens, "PtPd nanowire arrays supported on reduced graphene oxide as advanced electrocatalysts for methanol oxidation", *Carbon N. Y.* **79** (2014) 346–355.

[127] S. Du, Y. Lu, S.K. Malladi, Q. Xu, R. Steinberger-Wilckens, "A simple approach for PtNi–MWCNT hybrid nanostructures as high performance electrocatalysts for the oxygen reduction reaction", *J. Mater. Chem. A.* **2** (2014) 692–698.

[128] R. Imran Jafri, N. Rajalakshmi, S. Ramaprabhu, "Nitrogen doped graphene nanoplatelets as catalyst support for oxygen reduction reaction in proton exchange membrane fuel cell", *J. Mater. Chem.* **20** (2010) 7114–7117.

[129] J. He, X. He, L. Liu, B. Hu, F. Bai, P. Zhang, "Tailoring Carbon Materials Substrate to Modify the Electronic Structure of Platinum for Boosting Its Electrocatalytic Activity", *J. Electrochem. Soc.* **165** (2018) F247–F252.

[130] L. Zhang, Z. Xia, "Mechanisms of Oxygen Reduction Reaction on Nitrogen-Doped Graphene for Fuel Cells", *J. Phys. Chem. C.* **115** (2011) 11170–11176.

[131] L. Qu, Y. Liu, J.-B. Baek, L. Dai, "Nitrogen-doped reduced-graphene oxide as an efficient metal-free electrocatalyst for oxygen reduction in fuel cells", *RSC Adv.* **3** (2013) 3990–3995.

[132] P. Mardle, O. Fernihough, S. Du, "Evaluation of the Scaffolding Effect of Pt Nanowires Supported on Reduced Graphene Oxide in PEMFC Electrodes", *Coatings.* **8** (2018) 48–56.

[133] S. Park, Y. Shao, H. Wan, P.C. Rieke, V. V. Viswanathan, S.A. Towne, L. V. Saraf, J. Liu, Y. Lin, Y. Wang, "Design of graphene sheets-supported Pt catalyst layer in PEM fuel cells", *Electrochem. Commun.* **13** (2011) 258–261.

[134] Z. Tang, C. Kok, K. Keat, Z. Tian, D.H.C. Chua, J. Lin, "Enhanced catalytic properties

from platinum nanodots covered carbon nanotubes for proton-exchange membrane fuel cells", *J. Power Sources.* **195** (2010) 155–159.

[135] J. Liu, Y. Yuan, G. Goenaga, D. Liu, "Performance Improvement of Fuel Cell using Platinum Functionalized Aligned Carbon Nanotubes Performance Improvement of Fuel Cell using Platinum Functionalized Aligned Carbon Nanotubes", *NSTI-Nanotech.* **3** (2010) 805–808.

[136] Y. Shen, Z. Xia, Y. Wang, C. Kok, J. Lin, "Pt coated Vertically Aligned Carbon Nanotubes as Electrodes for Proton Exchange Membrane Fuel Cells", *Procedia Eng.* **93** (2014) 34–42.

[137] K. Gong, F. Du, Z. Xia, M. Durstock, L. Dai, "Nitrogen-Doped Carbon Nanotube Arrays with High Electrocatalytic Activity for Oxygen Reduction", *Science.* **323** (2009) 760–764.

[138] J. Shui, M. Wang, F. Du, L. Dai, "N-doped carbon nanomaterials are durable catalysts for oxygen reduction reaction in acidic fuel cells", *Sci. Adv.* **1** (2015) 1–8.

[139] S.C. Gallo, C. Charitidis, H. Dong, "Surface functionalization of carbon fibers with active screen plasma", *J. Vac. Sci. Technol. A. Vacuum, Surfaces, Film.* **35** (2017) 21404–21413.

[140] S. Louisia, Y.R.J. Thomas, P. Lecante, M. Heitzmann, M. Rosa Axet, P.A. Jacques, P. Serp, "Alloyed Pt3M (M = Co, Ni) nanoparticles supported on S- and N-doped carbon nanotubes for the oxygen reduction reaction", *Beilstein J. Nanotechnol.* **10** (2019) 1251–1269.

[141] S.M. Alia, B.A. Larsen, S. Pylypenko, D.A. Cullen, D.R. Diercks, K.C. Neyerlin, S.S. Kocha, B.S. Pivovar, "Platinum-coated nickel nanowires as oxygen-reducing electrocatalysts", *ACS Catal.* **4** (2014) 1114–1119.

[142] S.A. Mauger, K.C. Neyerlin, S.M. Alia, C. Ngo, S.K. Babu, K.E. Hurst, S. Pylypenko, S. Litster, B.S. Pivovar, "Fuel cell performance implications of membrane electrode assembly fabrication with platinum-nickel nanowire catalysts", *J. Electrochem. Soc.* **165** (2018) F238–F245.

[143] E. Antolini, J.R.C. Salgado, E.R. Gonzalez, "The stability of Pt-M (M = first row transition metal) alloy catalysts and its effect on the activity in low temperature fuel cells. A literature review and tests on a Pt-Co catalyst", *J. Power Sources.* **160** (2006) 957–968.

[144] T. Okada, J. Dale, Y. Ayato, O.A. Asbjørnsen, M. Yuasa, I. Sekine, "Unprecedented Effect of Impurity Cations on the Oxygen Perfluorinated Ionomer", *Langmuir.* **15** (1999) 8490–8496.

[145] J. Braaten, A. Kongkanand, S. Litster, "Oxygen Transport Effects of Cobalt Cation Contamination of Ionomer Thin Films in Proton Exchange Membrane Fuel Cells", *ECS Trans.* **80** (2017) 283–290.

[146] M.S. Wilson, S. Gottesfeld, "Thin-film catalyst layers for polymer electrolyte fuel cell electrodes", *J. Appl. Electrochem.* **22** (1992) 1–7.

[147] H.A. Gasteiger, J.E. Panels, S.G. Yan, "Dependence of PEM fuel cell performance on catalyst loading", **127** (2004) 162–171.

[148] K. Kudo, Y. Morimoto, "Analysis of Oxygen Transport Resistance of Nafion thin film on Pt electrode", *ECS Trans.* **50** (2012) 1487–1494.

[149] D. Chen, A. Kongkanand, J. Jorne, "Proton Conduction and Oxygen Diffusion in Ultra-Thin Nafion Films in PEM Fuel Cell : How Thin?", *J. Electrochem. Soc.* **166** (2019) 24–33.

[150] T. Suzuki, K. Kudo, Y. Morimoto, "Model for investigation of oxygen transport limitation in a polymer electrolyte fuel cell", *J. Power Sources.* **222** (2013) 379–389.

[151] K. Kudo, T. Suzuki, Y. Morimoto, "Analysis of Oxygen Dissolution Rate from Gas Phas into Nafion Surface and Development of an Agglomerate Model", *ECS Trans.* **33** (2010) 1495–1502.

[152] R. Jinnouchi, K. Kudo, N. Kitano, Y. Morimoto, "Molecular Dynamics Simulations on O2 Permeation through Nafion Ionomer on Platinum Surface", *Electrochim. Acta.* **188** (2016) 767–776.

[153] A. Sode, N.J.C. Ingle, M. Mccormick, D. Bizzotto, E. Gyenge, S. Ye, S. Knights, D.P. Wilkinson, "Controlling the deposition of Pt nanoparticles within the surface region of Nafion", *J. Memb. Sci.* **376** (2011) 162–169.

[154] N.J.C. Ingle, A. Sode, I. Martens, E. Gyenge, D.P. Wilkinson, D. Bizzotto, "Synthesis and Characterization of Diverse Pt Nanostructures in Nafion", *Langmuir.* **30** (2014) 1871–1879.

[155] I. Martens, B.A. Pinaud, L. Baxter, D.P. Wilkinson, D. Bizzotto, "Controlling Nanoparticle Interconnectivity in Thin-Film Platinum Catalyst Layers", *J. Phys. Chem. C.* **120** (2016) 21364–21372.

[156] M.K. Debe, a. J. Steinbach, G.D. Vernstrom, S.M. Hendricks, M.J. Kurkowski, R.T. Atanasoski, P. Kadera, D. a. Stevens, R.J. Sanderson, E. Marvel, J.R. Dahn, "Extraordinary Oxygen Reduction Activity of Pt3Ni7", *J. Electrochem. Soc.* **158** (2011) B910–B918.

[157] L. Gancs, T. Kobayashi, M.K. Debe, R. Atanasoski, A. Wieckowski, "Crystallographic characteristics of nanostructured thin-film fuel cell electrocatalysts: A HRTEM study", *Chem. Mater.* **20** (2008) 2444–2454.

[158] J. Liu, I. V. Zenyuk, "Proton transport in ionomer-free regions of polymer electrolyte fuel cells and implications for oxygen reduction reaction", *Curr. Opin. Electrochem.* **12** (2018) 202–208.

[159] M.K. Debe, "Effect of Electrode Surface Area Distribution on High Current Density Performance of PEM Fuel Cells", *J. Electrochem. Soc.* **159** (2012) B53–B66.

[160] A. Kongkanand, M. Dioguardi, C. Ji, E.L. Thompson, "Improving Operational Robustness of NSTF Electrodes in PEM Fuel Cells", *J. Electrochem. Soc.* **159** (2012) 405–411.

[161] A. Kongkanand, J.E. Owejan, S. Moose, M. Dioguardi, M. Biradar, R. Makharia, "Development of Dispersed-Catalyst/NSTF Hybrid Electrode", *J. Electrochem. Soc.* **159** (2012) F676–F682.

[162] A. Kongkanand, J. Zhang, Z. Liu, Y.H. Lai, P. Sinha, E.L. Thompson, R. Makharia, "Degradation of PEMFC observed on NSTF electrodes", *J. Electrochem. Soc.* **161**

(2014) 744–753.

[163] S. Du, B. Millington, B.G. Pollet, "The effect of Nafion ionomer loading coated on gas diffusion electrodes with in-situ grown Pt nanowires and their durability in proton exchange membrane fuel cells", *Int. J. Hydrogen Energy*. **36** (2011) 4386–4393.

[164] Y. Lu, S. Du, R. Steinberger-Wilckens, "Three-dimensional catalyst electrodes based on PtPd nanodendrites for oxygen reduction reaction in PEFC applications", *Appl. Catal. B Environ.* **187** (2016) 108–114.

[165] S. Sui, Z. Wei, K. Su, A. He, X. Wang, Y. Su, X. Hou, S. Raffet, S. Du, "Pt nanowire growth induced by Pt nanoparticles in application of the cathodes for Polymer Electrolyte Membrane Fuel Cells (PEMFCs)", *Int. J. Hydrogen Energy*. **43** (2018) 20041–20049.

[166] S. Moniri, T. Van Cleve, S. Linic, "Pitfalls and best practices in measurements of the electrochemical surface area of platinum-based nanostructured electro-catalysts", *J. Catal.* **345** (2017) 1–10.

[167] Y. Garsany, O. a Baturina, K.E. Swider-Lyons, S.S. Kocha, "Experimental Methods for Quantifying the Activity of Platinum Electrocatalysts for the Oxygen Reduction Reaction", *Anal. Chem.* **82** (2010) 6321–6328.

[168] G. Tsotridis, A. Pilenga, G. De Marco, T. Malkow, EU Harmonised Test Protocols for PEMFC MEA Testing in Single Cell Configuration for Automotive Applications; JRC Science for Policy report, 2015.

[169] S.M. Alia, S. Pylypenko, A. Dameron, K.C. Neyerlin, S.S. Kocha, B.S. Pivovar, "Oxidation of Platinum Nickel Nanowires to Improve Durability of Oxygen-Reducing Electrocatalysts", *J. Electrochem. Soc.* **163** (2016) F296–F301.

[170] S.M. Alia, C. Ngo, S. Shulda, M.-A. Ha, A.A. Dameron, J.N. Weker, K.C. Neyerlin, S.S. Kocha, S. Pylypenko, B.S. Pivovar, "Exceptional Oxygen Reduction Reaction Activity and Durability of Platinum–Nickel Nanowires through Synthesis and Post-Treatment Optimization", *ACS Omega*. **2** (2017) 1408–1418.

[171] B. Pivovar, Extended Surface Electrocatalyst Development, in: 2017 DOE Hydrog. Fuel Cells Progr. Rev., 2017.

[172] M.C. Elvington, H.R. Colón-Mercado, "Pt and Pt/Ni "Needle" Eletrocatalysts on Carbon Nanotubes with High Activity for the ORR", *Electrochem. Solid-State Lett.* **15** (2012) K19–K22.

[173] S. Mukerjee, S. Srinivasan, M.P. Soriaga, J. McBreen, "Effect of Preparation Conditions of Pt Alloys on Their Electronic, Structural, and Electrocatalytic Activities for Oxygen Reduction-XRD,XAS and Electrochemical Studies", *J. Phys. Chem.* **99** (1995) 4577–4589.

[174] S. Zignani, V. Baglio, D. Sebastián, A. Saccà, I. Gatto, A. Aricò, "Towards Highly Performing and Stable PtNi Catalysts in Polymer Electrolyte Fuel Cells for Automotive Application", *Materials*. **10** (2017) 317.

[175] V. Stamenković, T.J. Schmidt, P.N. Ross, N.M. Marković, "Surface composition effects in electrocatalysis: Kinetics of oxygen reduction on well-defined Pt3Ni and Pt3Co alloy surfaces", *J. Phys. Chem. B*. **106** (2002) 11970–11979.

[176] V. Stamenković, T.J. Schmidt, P.N. Ross, N.M. Marković, "Surface segregation effects in electrocatalysis: Kinetics of oxygen reduction reaction on polycrystalline Pt3Ni alloy surfaces", *J. Electroanal. Chem.* **554–555** (2003) 191–199.

[177] A. Chandan, M. Hattenberger, A. El-Kharouf, S. Du, A. Dhir, V. Self, B.G. Pollet, A. Ingram, W. Bujalski, "High temperature (HT) polymer electrolyte membrane fuel cells (PEMFC)-A review", *J. Power Sources.* **231** (2013) 264–278.

[178] A.C. Fernandes, V.A. Paganin, E.A. Ticianelli, "Degradation study of Pt-based alloy catalysts for the oxygen reduction reaction in proton exchange membrane fuel cells", *J. Electroanal. Chem.* **648** (2010) 156–162.

[179] P. Mardle, S. Du, "Annealing Behaviour of Pt and PtNi Nanowires for Proton Exchange Membrane Fuel Cells", *Materials.* **11** (2018) 1473–1485.

[180] P. Mardle, X. Ji, J. Wu, S. Guan, H. Dong, S. Du, "Thin film electrodes from Pt nanorods supported on aligned N-CNTs for proton exchange membrane fuel cells", *Appl. Catal. B Environ.* **260** (2020) 118031–118038.

[181] Xpsfitting.com, "X-ray Photoelectron Spectroscopy (XPS) Reference Pages - Platinum", (n.d.).

[182] J.-H. Choi, K.-W. Park, B.-K. Kwon, Y.-E. Sung, "Methanol Oxidation on Pt/Ru, Pt/Ni, and Pt/Ru/Ni Anode Electrocatalysts at Different Temperatures for DMFCs", *J. Electrochem. Soc.* **150** (2003) A973–A978.

[183] T. Sato, T. Nakamura, F. Ozawa, "Thermal Decomposition of Nickel Hydroxide", *J. Appl. Chem. Biotechnol.* **25** (1975) 583–590.

[184] H.A. Gasteiger, S.S. Kocha, B. Sompalli, F.T. Wagner, "Activity benchmarks and requirements for Pt, Pt-alloy, and non-Pt oxygen reduction catalysts for PEMFCs", *Appl. Catal. B Environ.* **56** (2005) 9–35.

[185] Y. Garsany, I.L. Singer, K.E. Swider-Lyons, "Impact of film drying procedures on RDE characterization of Pt/VC electrocatalysts", *J. Electroanal. Chem.* **662** (2011) 396–406.

[186] H.A. Hansen, J. Rossmeisl, J.K. Nørskov, "Surface Pourbaix diagrams and oxygen reduction activity of Pt, Ag and Ni(111) surfaces studied by DFT", *Phys. Chem. Chem. Phys.* **10** (2008) 3607–3608.

[187] R.G. Milazzo, S.M.S. Privitera, D. D'Angelo, S. Scalese, S. Di Franco, F. Maita, S. Lombardo, "Spontaneous galvanic displacement of Pt nanostructures on nickel foam: Synthesis, characterization and use for hydrogen evolution reaction", *Int. J. Hydrogen Energy.* **43** (2018) 7903–7910.

[188] T. Okada, H. Satou, M. Yuasa, "Effects of Additives on Oxygen Reduction Kinetics at the Interface between Platinum and Perfluorinated Ionomer", *Langmuir.* **19** (2003) 2325–2332.

[189] W.W. McNeary, C. Ngo, A.E. Linico, J.W. Zack, A.M. Roman, K.M. Hurst, S.M. Alia, J.W. Medlin, S. Pylypenko, B.S. Pivovar, A.W. Weimer, "Extended Thin-Film Electrocatalyst Structures via Pt Atomic Layer Deposition", *ACS Appl. Nano Mater.* **1** (2018) 6150–6158.

[190] S. Shulda, J.N. Weker, C. Ngo, S.M. Alia, S.A. Mauger, K.C. Neyerlin, B.S. Pivovar, S. Pylypenko, "2D and 3D Characterization of PtNi Nanowire Electrode Composition and

Structure", *ACS Appl. Nano Mater.* **2** (2019) 525–534.

[191] SGL, "SIGRACET Fuel Cell Components", (2019).

[192] W. Ren, D. Li, H. Liu, R. Mi, Y. Zhang, L. Dong, L. Dong, "Lithium storage performance of carbon nanotubes with different nitrogen contents as anodes in lithium ions batteries", *Electrochim. Acta.* **105** (2013) 75–82.

[193] K. Hongsirikarn, J.G. Goodwin, S. Greenway, S. Creager, "Effect of cations (Na+, Ca2+, Fe3+) on the conductivity of a Nafion membrane", *J. Power Sources.* **195** (2010) 7213–7220.

[194] M.K. Debe, "Electrocatalyst approaches and challenges for automotive fuel cells", *Nature.* **486** (2012) 43–51.

[195] E.B. Easton, P.G. Pickup, "An electrochemical impedance spectroscopy study of fuel cell electrodes", *Electrochim. Acta.* **50** (2005) 2469–2474.

[196] C.M. Zalitis, D. Kramer, A.R. Kucernak, "Electrocatalytic performance of fuel cell reactions at low catalyst loading and high mass transport.", *Phys. Chem. Chem. Phys.* **15** (2013) 4329–4340.

[197] M. Markiewicz, C. Zalitis, A. Kucernak, "Performance measurements and modelling of the ORR on fuel cell electrocatalysts - The modified double trap model", *Electrochim. Acta.* **179** (2015) 126–136.

[198] Y. Lu, S. Du, R. Steinberger-Wilckens, "One-dimensional nanostructured electrocatalysts for polymer electrolyte membrane fuel cells—A review", *Appl. Catal. B Environ.* **199** (2016) 292–314.

[199] A.E.S. Sleightholme, D.P. Wilkinson, D. Bizzotto, S. Ye, E.L. Gyenge, "Nafion Film-Templated Platinum Electrodes for Oxygen Reduction", *Electrocatalysis.* **1** (2010) 22–27.

[200] B. Li, D.C. Higgins, Q. Xiao, D. Yang, C. Zhng, M. Cai, Z. Chen, J. Ma, "The durability of carbon supported Pt nanowire as novel cathode catalyst for a 1.5 kW PEMFC stack", *Appl. Catal. B Environ.* **162** (2015) 133–140.

[201] A. Parthasarathy, S. Srinivasan, A.J. Appleby, C.R. Martin, "Temperature Dependence of the Electrode Kinetics of Oxygen Reduction at the Platinum / Nation | Interface--A Microelectrode Investigation", **139** (1992) 2530–2537.

[202] J. Snyder, T. Fujita, M.W. Chen, J. Erlebacher, "Oxygen reduction in nanoporous metal-ionic liquid composite electrocatalysts.", *Nat. Mater.* **9** (2010) 904–7.

[203] D.F. van der Vliet, C. Wang, D. Tripkovic, D. Strmcnik, X.F. Zhang, M.K. Debe, R.T. Atanasoski, N.M. Markovic, V.R. Stamenkovic, "Mesostructured thin films as electrocatalysts with tunable composition and surface morphology", *Nat. Mater.* **11** (2012) 1051–1058.

[204] S. Sharma, B.G. Pollet, "Support materials for PEMFC and DMFC electrocatalysts - A review", *J. Power Sources.* **208** (2012) 96–119.

[205] K. Cheng, D. He, T. Peng, H. Lv, M. Pan, S. Mu, "Porous graphene supported Pt catalysts for proton exchange membrane fuel cells", *Electrochim. Acta.* **132** (2014) 356–363.

[206] S. Hou, X. Cai, H. Wu, X. Yu, M. Peng, K. Yan, D. Zou, "Nitrogen-doped graphene for dye-sensitized solar cells and the role of nitrogen states in triiodide reduction", *Energy Environ. Sci.* **6** (2013) 3356–3362.

[207] J. Zhu, G. He, L. Liang, Q. Wan, P. Kang, "Direct anchoring of platinum nanoparticles on nitrogen and phosphorus-dual-doped carbon nanotube arrays for oxygen reduction reaction", *Electrochim. Acta*. **158** (2015) 374–382.

[208] N.P. Subramanian, T.A. Greszler, J. Zhang, W. Gu, R. Makharia, "Pt-Oxide Coverage-Dependent Oxygen Reduction Reaction (ORR) Kinetics", *J. Electrochem. Soc.* **159** (2012) B531–B540.

[209] E. Antolini, "Carbon supports for low-temperature fuel cell catalysts", *Appl. Catal. B Environ.* **88** (2009) 1–24.

[210] J. Peron, Z. Shi, S. Holdcroft, "Hydrocarbon proton conducting polymers for fuel cell catalyst layers", *Energy Environ. Sci.* **4** (2011) 1575–1591.

[211] H. Zhang, J. Liang, B. Xia, Y. Li, S. Du, "Ionic liquid modified Pt/C electrocatalysts for cathode application in proton exchange membrane fuel cells", *Front. Chem. Sci. Eng.* (2019) 695–701.